First-Principles Studies of Transition Metal Chalcogenides and Oxide Heterostructures for Spintronic Applications

Sonali Kakkar

FIRST-PRINCIPLES STUDIES OF TRANSITION METAL CHALCOGENIDES AND OXIDE HETEROSTRUCTURES FOR SPINTRONIC APPLICATIONS

SONALI KAKKAR

A thesis submitted for the partial fulfillment of the

degree of Doctor of Philosophy

Institute of Nano Science and Technology, Mohali,
Knowledge City, Sector-81, SAS Nagar, Manauli PO, Mohali 140306, Punjab, India

Indian Institute of Science Education and Research, Mohali,
Knowledge City, Sector-81, SAS Nagar, Manauli PO, Mohali 140306, Punjab, India

April 2023

Dedicated to my Parents

Declaration

The work presented in this thesis has been carried out by me under the guidance of Dr. Chandan Bera at the Institute of Nano Science and Technology, Mohali. This work has not been submitted in part or in full for a degree, a diploma, or a fellowship to any other university or institute. Whenever contributions of others are involved, every effort is made to indicate this clearly, with due acknowledgement of collaborative research and discussions. This thesis is a bona fide record of original work done by me and all sources listed within have been detailed in the bibliography.

Sonali Kakkar
(Candidate)

In my capacity as the supervisor of the candidate's thesis work, I certify that the above statements by the candidate are true to the best of my knowledge.

Dr. Chandan Bera
(Thesis Supervisor)

Acknowledgment

A Ph.D. is only the beginning of an academic's never-ending quest for knowledge. By God's grace, I consider myself fortunate to have had unconditional affection, immeasurable support, and encouragement from several people, without the help of whom the work presented in this thesis would not have been possible. I would like to take this opportunity, as I am about to submit this work, to express my profound gratitude and appreciation to everyone who helped to make my Ph.D. thesis possible.

Foremost, I would like to express my sincere gratitude to my supervisor **Dr. Chandan Bera** for all the support and encouragement he has given me during my Ph.D. tenure. Without his guidance and constant feedback, this Ph.D. would not have been possible.

I would also thank my thesis and annual review committee members: **Dr. Suvankar Chakraverty** and **Dr. Md. Ehesan Ali** for their time, helpful feedback, insightful comments, and encouragement.

Along with this, I would like to extend my heartfelt thanks to my collaborators **Dr. Suvankar Chakraverty**, **Dr. Vinayak B. Kamble** (IISER Thiruvananthapuram), **Dr. Jesús Carrete Montaña** (TU Wien, Austria) and **Dr. Surendra Singh** (Bhabha Atomic Research Centre, Mumbai) for giving me the opportunity to work with them on collaborative projects and thus, enhancing my knowledge base.

I want to thank my fellow lab mates (PETr group) for the thought-provoking conversations and for making these graduation years fun-filled. **Parrydeep Kaur** deserves special thanks for helping me on the incredible journey of my Ph.D. through her unwavering emotional support. She has helped me to navigate the research problems by stirring up scientific discussions and providing useful insights. My deep admiration to **Raveena Gupta** for her tremendous help, worthy inputs to my research, and for always being very supportive with her self-motivated and courageous nature. She is ever eager to help when needed. I am also very grateful to **Dr. Ajit Singh** and **Baljinder Kaur** for helping me in different ways at different stages of my Ph.D. All of them have been a constant pillar of patience and encouragement for me in this lab since the beginning. Of course, a big thanks to **Naveen Khaliya, Gourav Rana, Ajay Partap Singh Rana**, **Ayushi Jain**, **Bibek Ranjan Satpathy** and **Nidhi Pandey** for being the source of constant energy, fun, laughter, and enthusiasm in the group. Our loud laughters, cheers, and chats over lunch and tea sessions at ”Hub ch” will be dearly missed by me. Playing ”Dumb-Charades” with you guys has so many wonderful and joyful memories attached to it. You guys made every event or occasion pleasant and fun-filled with your cheerfulness and jokes over all these years and helped remind me that there is more to life than physics.

A good support system is essential for survival during a Ph.D. tenure. I'm lucky to have batchmates like **Mamta Raturi**, **Gagandeep Kaur**, **Dr. Rakesh Mishra**, **Arpna Jaryal**, **Manish**, **Priyanka**, **Chirag**, **Dr. Navpreet Kaur**, **Dr. Deepak Chauhan**, and **Kritika Sood**. A big and warm thanks to such great friends for life Mamta and Gagan who always had my back, during the ups and downs of my Ph.D. life. I would always be indebted for the unconditional emotional support, love, and affection. I will greatly miss our sleepovers, get-togethers, outings, long walks, and phone calls.

I am grateful to **Dr. Gurpreet Kaur**, my roommate for the majority of my time in Ph.D. and the oldest (and most reliable) buddy in INST. She has been a part of my beautiful and golden memories since our M.Sc days, and she will always hold a special place in my heart. Her tenacity and energy have motivated me throughout. I will miss our hour-long chats about every aspect of the Ph.D. and life in general. The most special part of our silly fights was the subsequent reconciliation, which I will always remember. The constant joshing of each other and ensuing long and loud laughters will live on in my memories. She has been and always will be a lifelong friend.

I am thankful to my colleagues and friends, **Dr. Ashish Bhatt**, **Dr. Prabhleen Kaur**, **Dr. Deepika Rani**, **Dr. Ruchi Tomar**, **Dr. Vianni Chopra**, **Dr. Shefali Sartaliya**, **Dr. Nandan Ghorai**, **Dr. Tanmay Goswami**, **Manvi Sachdeva**, **Ruchi Verma**, **Neeshu**, **Jyoti Saini**, **Pinky**, **Manpreet Kaur**, and **Anamika** for being there for help and constant motivation.

Special thanks go to past members of our lab, **Dr. Prabhjot Kaur**, **Dr. R Lenin**, **Dr. Akariti Sharma**, **Kalpana**, **Samarjit** and **Harwinder**. Dr. Prabhjot Kaur deserves special recognition for her encouragement, support, and engaging discussions that significantly aided my research work in the initial days.

Some people have been the constants throughout and just one phone call away, **Gonika**, **Dr. Anisha**, **Neha**, **Jyoti**, **Seema** - thank you.

I would acknowledge the Department of Science and Technology (DST) and the Institute of Nano Science and Technology (INST), Mohali, India, for providing me with the Ph.D. fellowship, supercomputing facilities, and the infrastructural support which made it possible for me to carry out research-related activities and finish this thesis. I am thankful to the Centre for Development in Advanced Computing (CDAC), Pune, India for providing its supercomputing facilities.

Special regards to my Mama-Mami, and Nana-nani for all the love, moral support, and encouragement in these five years. You people were always there with everything possible just to bring a smile to my face. Thanks for providing me a home away from home, where all the worries just fade away in the company of my sweet baby sisters Neeshika and Ananya.

None of this would have ever been possible without the unconditional love and support of my family, whom I can't thank enough; my mother and brother who have always been there with their love, affection, and care. Thank you for always believing in me and encouraging me to follow my dreams. My father deserves the deepest gratitude for having instilled such values and tenacity in me; your blessings illuminate every gloom and give me the utmost courage as each day of my life passes. This one is just for you: your profound love, teachings in integrity, truthfulness, and honesty no matter what, and eternal blessings. Each day that passes, I miss you, Papa.

Lastly, I bow down to the Almighty for giving me the strength and patience to pursue this path.

Sonali Kakkar

Abstract

Spintronics focuses on active control and manipulation of the spin degree of freedom of electrons to get beyond the limitations of the semiconductor-based electronic industry. New device concepts that use an electric field or spin-polarized current result in quick and energy-efficient magnetic switching, in contrast to magnetic field-driven magnetic switching. In spintronic devices, spin polarization is controlled either by magnetic layers or via spin-orbit coupling (SOC). The era of spintronics began with the discovery of giant magnetoresistance (GMR). Certain spintronics-based technologies, such as spin-transfer-torque magnetoresistive random-access memory (STT-MRAM), have been put into use on a commercial scale. The efficient use of these spintronic devices, however, still has certain challenges to overcome. Therefore, it is imperative to discover and design innovative materials featuring outstanding and distinctive spin-based mechanisms. 2D magnetic materials in transition metal chalcogenides (TMC) provide unique physical paradigms and encourage the development of cutting-edge spintronic devices. The features of 2D TMC span a broad range, including topological phases, semimetals, half-metals, and Mott insulators, to mention a few. Beyond ferromagnetism, there are other magnetic states such as antiferromagnets, and quantum spin liquids. Similarly, atomically tailored oxide heterostructures create a powerful platform offering whole new opportunities for electronics and spintronics. They manifest phenomena encompassing the Rashba physics, magnetic ordering, and enhancement of SOC among others owing to the reconstruction of the spin, orbital, lattice, and charge states at the interfaces. It is possible to create oxide-based magnetic tunnel junctions (MTJ), and interface-based magnetoelectric spintronic devices using multiferroic oxides. Additionally, spin-orbit-based mechanisms in oxide heterostructures provide a new spintronics dimension out of which the Rashba physics emerges as a strong candidate.

It is widely acknowledged that first-principles density functional theory (DFT) is an efficient method for designing functional materials and elucidating underlying mechanisms of experimental phenomena. This thesis focuses on using state-of-the-art first-principles calculations based on DFT to unveil the electronic, spintronic, and topological characteristics in materials picked from the strongly correlated class of TMC and oxide heterointerfaces. The aim is to identify multifunctional materials with intrinsic magnetic ordering and high SOC-driven exotic phenomena in conjunction with the low dimensionality for future low-power-consumption quantum electronics and spintronics.

The thesis consists of five chapters and has been organized in the following framework:

Chapter 1 begins with a succinct backdrop of the study. The next section of this chapter provides an overview of strongly correlated materials, including Mott-Hubbard and charge-transfer insulators. After that, it provides a quick review of 2D magnetic TMC and oxide heterostructures, two classes of strongly correlated materials. We have also included a brief history of magnetism in solids and the exchange interactions that mediate the magnetic ordering in order to provide some understanding of magnetism in solid-state systems. The concept of SOC has then been explained, with emphasis placed on the Rashba effect and its emergence in oxide heterostructures, followed by a short description of SOC-driven topological states, particularly the quantum anomalous Hall effect (QAHE). Towards the end of chapter 1, the theoretical background of various computational methods useful in understanding the calculation of results presented in this thesis has been provided.

Chapter 2 infers to the ab initio study of electronic and ground state magnetic properties in bulk and layered transition metal chalcogenides. In this context, the first section of this chapter investigates the electronic structure and magnetic ordering in triclinic $CuSeO_3$. The electronic structure suggests that $CuSeO_3$ in the triclinic phase is a charge-transfer insulator. We find the non-collinear antiferromagnetic configuration as the ground-state magnetic ordering. This can be attributed to the hybridization of Cu-d and O-p orbitals, giving rise to Cu-O-Cu superexchange interactions. We observe a spiral spin texture in the reciprocal space with a finite out-of-plane spin component. Spintronics of such non-collinear antiferromagnetic charge transfer insulating states is a relatively new and rapidly developing field of physics. In the following section of this chapter, the vdW layered transition metal ternary chalcogenide CoAsS with strong electron correlations is explored for its potential in spintronics. The dynamically stable CoAsS monolayer via its rich magnetic and electronic phase diagram has been demonstrated as a quasi-2D magnetic material. Because of the broken time-reversal symmetry and SOC, a topological state with a non-trivial Chern number is revealed at the critical Coulomb parameter using Kubo's approach. These results make the CoAsS monolayer very appealing for low-power-consumption nanoelectronics and spintronics.

Chapter 3 focuses on the emergent phenomena in perovskite oxide heterostructures based on polar perovskite oxide $LaVO_3$ (LVO). In this regard, the first section of the chapter explores the electronic properties in the heterostructure between a Mott insulator LVO and a band insulator $SrTiO_3$ (STO) with two distinct orientations (001) and (111). The electronic structure confirms that this heterointerface comprising two bulk insulators is n-type metallic in both orientations. Because of the peculiar orbital reconstruction at the two interfaces, we notice the difference in orbital occupation as well as orbital degeneracies. Furthermore, the Fermi surface reveals fourfold/sixfold symmetry as well as the presence/absence of open orbits in the (001)/(111) orientations. Thus, unique orbital-occupation and degeneracies due to orbital reconstruction as well as symmetry of Fermi surface highlights the important role played by crystal field in determining the electronic properties in LVO/STO heterostructure. In the subsequent section of this chapter, we have examined the (001) and (111) surfaces of polar perovskite oxide $KTaO_3$ (KTO) terminated with the Ta atoms for electronic and spintronic properties. We observed the presence of 2DEG with parabolic bands near the Fermi level at both the surfaces of KTO. The distribution of 2DEG is primarily contained in the surface layers of KTO in the 5d orbitals of Ta atoms. Due to the significant SOC of Ta atoms and the breaking of inversion symmetry at the surfaces, the Rashba spin splitting is visible in the bands. The spin texture on the Fermi surface and constant energy contours corroborate the 2D nature of the Rashba spin splitting on the (001) surface, While a complicated spin structure is seen on the surface of (111)-KTO. The final section of this chapter is devoted to the emergent properties in polar-polar heterostructure of perovskite oxides LVO and KTO depending on the crystal orientation. The charge transfer from the surface layers to the interfacial region due to the electronic reconstruction mechanism results in high carrier density 2DEG. Momentum-dependent Rashba spin splitting is seen in the electronic bands originating from the symmetry-breaking electric field. We demonstrate the orbital dependence of the Rashba effect in this heterostructure on account of orbital reconstruction at the interface. Spin-splitting is larger at the crossing regions of the d_{xy} and $d_{xz/yz}$ sub-bands. Further, the spin texture of the Rashba-split bands highlights the complexity of the orientation-dependence in the LVO/KTO heterostructure.

Chapter 4 is based on a theoretical understanding of high-mobility, conducting, and spin-polarized 2DEG at the EuO/TaO_2 interface of a ferromagnetic insulator EuO and non-magnetic polar perovskite KTO. The presence of proximity-induced Zeeman exchange splitting and the Rashba spin-orbit field in the EuO/KTO superlattice warrants a thorough examination of the system's detailed electronic band structure to look for the possibility of non-trivial quantum phenomena. 2DEG is confined on the KTO side particularly at the interfacial TaO_2 layer in the d_{xy} orbitals of Ta due to orbital reconstruction as confirmed by distributions of spin and charge density. The substantial exchange splitting (0.73 eV) between the two spin channels of interfacial Ta-5d_{xy} orbitals due to the proximity effect of ferromagnetic EuO results in a spin-polarized 2DEG at the interface. The band crossing points between the majority and minority spin bands open a gap when SOC is turned on. The large spikes of the Berry curvature at the momenta of SO-induced gaps and integral Chern number demonstrate the non-trivial band topology. We observe the Rashba-type spin texture of the bands having the SO-induced gap showing single spin winding of electron spin with opposite chirality without noticing the conventional Rashba splitting in the bands. The magnetic easy axis is perpendicular to the interfacial plane. Hence our findings suggest that EuO/KTO system has potential in low-power quantum electronics, spintronics, and spin-orbitronics.

The final chapter, **chapter 5**, concludes this thesis by summarising the key findings of the different studies presented in the individual chapters. It also provides a prospective future research outlook by steering the characteristics of various 2D materials and probing further emergent phenomena at the interface of oxide heterostructures for spintronic applications.

Contents

Title Page **i**

Declaration **v**

Acknowledgement **vii**

Abstract **xi**

1 Introduction **1**

- 1.1 Background 1
- 1.2 Strongly correlated materials 2
  - 1.2.1 Mott-Hubbard and charge-transfer insulators 3
  - 1.2.2 Two-dimensional transition metal chalcogenides 5
  - 1.2.3 Oxide heterostructures 6
- 1.3 Magnetism in solids 9
- 1.4 Magnetic ordering and exchange interactions 10
  - 1.4.1 Exchange interactions in metals 13
  - 1.4.2 Exchange interactions in insulators 14
- 1.5 Spin-orbit coupling/interaction 16
  - 1.5.1 Rashba effect 17
  - 1.5.2 Topological states of matter and quantum anomalous Hall effect 19
- 1.6 Computational methodology 21
  - 1.6.1 Theoretical background 21
  - 1.6.2 Density Functional theory (DFT) 22
    - 1.6.2.1 Kohn-Sham formalism 23
    - 1.6.2.2 Exchange-correlation functionals 24
    - 1.6.2.3 DFT+U: Extension to DFT for strongly correlated systems 26

1.7 Organization of thesis 33

2 Electronic and magnetic properties of 3d transition-metal chalcogenides 37

2.1 Non-collinear antiferromagnetic insulating state in triclinic $CuSeO_3$ . . 37
  2.1.1 Introduction 37
  2.1.2 Computational methodology 39
  2.1.3 Magnetic properties 39
  2.1.4 Electronic properties 41
  2.1.5 Conclusions 43
2.2 Electronic and magnetic properties in layered ternary chalcogenide CoAsS 44
  2.2.1 Introduction 44
  2.2.2 Methodology 45
  2.2.3 Structural properties 46
  2.2.4 Phonon dispersion 47
  2.2.5 Electronic structure 48
  2.2.6 Magnetic properties 51
  2.2.7 Chern number and quantum anomalous Hall effect 55
  2.2.8 Conclusion 56

3 Emergent properties in LVO-based perovskite oxide heterostructures 57

3.1 Introduction 57
3.2 Electronic properties in (001) and (111) LVO/STO heterostructures . . . 58
  3.2.1 Computational methodology 59
  3.2.2 Electronic structure 59
  3.2.3 Fermi surface 62
  3.2.4 Conclusion 62
3.3 Rashba effect in 2DEG at KTO (001) and (111) surfaces 63
  3.3.1 Computational methodology 64
  3.3.2 KTO (001) surface 65
  3.3.3 KTO (111) surface 68
  3.3.4 Conclusion 71
3.4 Rashba splitting in (001) and (111) LVO/KTO heterostructures 72
  3.4.1 Computational methodology 73
  3.4.2 Structural properties 74
  3.4.3 Electronic properties 75
  3.4.4 Electrostatic potential and charge transfer 82
  3.4.5 Spin texture 85

3.4.6 Interface energetics 87
3.4.7 Conclusions 88

4 Spin-polarized 2DEG at EuO/KTO interface 89
4.1 Introduction 89
4.2 Computational Methodology 91
4.3 Electronic structure 92
4.4 Spin and Charge density 97
4.5 Rashba SOC and Berry curvature 100
4.6 Conclusions 103

5 Summary and Future Outlook 105
5.1 Summary 105
5.2 Future Outlook 108

List of Abbreviations

SOC	Spin-orbit coupling
DFT	Density functional theory
GMR	Giant magnetoresistance
NM	Non-magnetic
FM	Ferromagnetic
AFM	Antiferromagnetic
STT-MRAM	Spin-transfer-torque magnetoresistive random-access memory
MTJ	Magnetic tunnel junctions
TB	Tight-binding
TRS	Time reversal symmetry
TMC	Transition metal chalcogenides
TMDC	Transition metal dichalcogenides
2DEG	Two dimensional electron gas
vdW	Van der Waals
KS	Kohn-Sham
DOS	Density of states
VASP	Vienna Ab initio Simulation Package
PAW	Projector augmented wave
LDA	Local-Density Approximation
GGA	Generalized Gradient Approximation
FLL	Fully localized limit
MAE	Magnetic anisotropy energy
PMA	Perpendicular magnetic anisotropy

List of Figures

1.1 Schematic of (top) charge-transfer (C-T) and (bottom) Mott-Hubbard (M-H) insulators, decided by the competition between Coulomb repulsion U_{dd} (between d electrons) and charge-transfer energy Δ_{CT}. Figure reproduced from Ref.[1] with permission from American Physical Society. 4

1.2 Schematic of electronic and atomic reconstructions at the n- and p- type interfaces of the LAO/STO heterostructure, respectively. Figure reproduced from Ref.[2] with permission from Springer Nature. 8

1.3 Wave functions for the H_2 molecule. (a) The spatially symmetric bonding orbital (spin singlet state S = 0), which corresponds to the sum of the two atomic orbitals is of lower energy than the (b) spatially antisymmetric antibonding orbital (spin triplet state S = 1), which corresponds to the difference between the two atomic orbitals[3,4]. 13

1.4 Electron delocalization in d orbitals which are nearly empty, nearly filled, and half-filled, respectively[4]. 14

1.5 A typical superexchange in a magnetic oxide. The up and down arrows show the spins of the electrons over transition metal (M) (single unpaired electron) and oxygen (O) atoms. The ferromagnetic coupling of spins on M atoms has ground state (i), but the exclusion principle prohibits the delocalization of spins as in (ii) & (iii) configurations. The antiferromagnetic coupling of spins on M atoms has ground state (iv), which can be delocalized over the M-O-M unit as given in the excited configurations (v) and (vi), thus lowering the kinetic energy[3,4]. 15

1.6 Rashba effect (a) bands showing spin splitting due to the Rashba effect with horizontally displaced parabolas (b) spin texture of the Rashba-split bands in the reciprocal space with clockwise/anticlockwise spins of outer/inner Rashba-split bands[5,6]. 18

1.7 A schematic diagram of edge channels in a magnetic sample with QAHE in real space. The black arrow represents the spontaneous magnetization in the sample along the z direction. A chiral QAHE channel appears at the edge of the sample (in-plane red arrows), and the spin of this conductive channel is fully polarized (red arrows perpendicular to the plane)[7,8]. 19

2.1 Magnetic structures of triclinic $CuSeO_3$ corresponding to non-collinear (a) AFM (NC)-I (b) AFM (NC)-II configurations. The corresponding atoms are marked in the figure. 40

2.2 The spin texture of triclinic $CuSeO_3$ in the k_x-k_y plane, the color bar shows the out-of-plane spin component. 41

2.3 Electronic band structure of triclinic $CuSeO_3$ along the high symmetry path X-Γ-Y|L-Γ-Z|N-Γ-M|R-Γ in the ground state magnetic configuration. 42

2.4 Total and orbital-projected DOS of triclinic $CuSeO_3$ in the ground state magnetic configuration. 43

2.5 Crystal structure of orthorhombic CoAsS (space group $Pca2_1$) showing (a) the top view, the pentagonal building blocks, and the monolayer. (b) the side view of the CoAsS unit cell; the shaded portion highlights the tetrahedral arrangement of transition metal atom Co. Yellow, green, and blue colors represent S, As, and Co atoms, respectively. (c) first Brillouin zone with the high symmetry points marked on it; shaded portion represents the 2D Brillouin zone corresponding to the monolayer. 47

2.6 Calculated phonon dispersion spectra of CoAsS for (a) bulk and (b) monolayer, along the high symmetry paths Γ-X-S-Y-Γ-Z-T-R-U-Z and Γ-Y-S-X-Γ, respectively. 48

2.7 Electronic band structure of bulk CoAsS with and without SOC (a) in the NM state within DFT, (b) in the AFM-G state within the DFT+U approach using $U = 6.8$ eV. Blue and red colors represent the plots with and without SOC, respectively. 49

2.8 Electronic band structure of monolayer CoAsS with and without SOC in the NM state within DFT. Blue and red colors represent the plots with and without SOC, respectively. 49

2.9 Electronic band structure of monolayer CoAsS with and without SOC (a) and (b) in AFM-G ($U = 6.8$ eV) and FM ($U = 8.2$ eV) states, respectively within the DFT+U approach. Blue and red colors represent the plots with and without SOC, respectively. 50

2.10 Total and orbital decomposed DOS plots for d orbitals (e_g and t_{2g}) of Co, p orbitals of As and S atoms for bulk and monolayer CoAsS. (a) Non-spin-polarized plot within the DFT approach in the NM state. (b) and (c) spin-polarized plot for AFM-G ($U = 6.8$ eV) and FM phase ($U = 8.2$ eV), respectively within DFT+U approach. The vertical black dashed line corresponds to the Fermi energy E_f. 50

2.11 (a) Magnetic structures of CoAsS in AFM-A, AFM-C, AFM-G, and FM configurations. Up and down arrows on Co atoms represent up and down spin states, respectively. Variation of (b) magnetic moment on Co atom μ (in μ_B), the energy difference between FM and competing AFM phase ΔE_{AFM-FM}, and band gap (E_g) in eV with U for bulk and monolayer CoAsS. 53

2.12 Charge density difference ($\Delta\rho_{AFM-FM}$) plots of CoAsS monolayer at $U = 4$ eV (upper panel) and $U = 8.2$ eV (lower panel) in ac (left) and bc (right) planes; Co, As, and S atoms are marked on the plot. The color bar on the right side indicates a positive charge density difference (higher charge density for AFM state) with red color, while the rest of the colors stipulate negative charge density difference (higher charge density for FM state). 54

2.13 (a) Contour plot of the Berry curvature distribution of the valence bands projected to k_x-k_y plane and (b) variation of charge Hall conductivity with $E - E_f$ for FM state of CoAsS monolayer. The inset in (b) shows the magnified view of the quantized portion of Hall conductivity. 56

3.1 (a) Crystal structure and (b) The total and orbital-projected DOS onto the 3d orbitals of Ti atoms along with the layerwise contribution to the Ti-3d orbital-projected DOS from the first four TiO_2 layers (labeled as $1-4$) as we go away from the interface for (001)-oriented LVO/STO heterostructure. The atoms La, O, V, Sr, and Ti are marked in the figure. 60

3.2 (a) Crystal structure and (b) The total and orbital-projected DOS onto the 3d orbitals of Ti atoms along with the layerwise contribution to the Ti-3d orbital-projected DOS from the first four Ti layers (labeled as $1-4$) as we go away from the interface for (111)-oriented LVO/STO heterostructure. The atoms La, O, V, Sr, and Ti are marked in the figure. 61
3.3 Calculated Fermi surface plots of (a) (001)- and (b) (111)- oriented LVO/STO heterostructures in (001) and (111) planes, respectively; where different colors represent different bands. 62
3.4 (a) Crystal structure of bulk KTO in cubic pm–3m space group with atoms K, Ta, and O marked on it. (b) Electronic band structure of bulk KTO along high symmetry path Γ-Y-M-Γ-Z-R-A-Z with orbital projection on the atoms. 63
3.5 (a) Electronic band structure of KTO (001) surface with atomic projection on atoms K, Ta, and O along high symmetry path Y-Γ-M including SOC (b) Layer-wise projected DOS on the atomic layers shown in the background of the plot. The black dashed line indicates the Fermi level E_f. 66
3.6 The planar average of the electrostatic potential (oscillating green curve) along the z-direction (perpendicular to the surface) and the macroscopic average of electrostatic potential (red curve) of (001) surface of polar KTO. The crystal structure is shown in the background; where magenta, brown, and red spheres represent K, Ta, and O atoms, respectively. The Fermi energy (E_f) is set to zero. 67
3.7 Constant energy contour plots of spin-texture (a)-(c) on Fermi surface (d)-(f) corresponding to a cut at energy ($E-E_F$) = –0.2 eV for each spin component along the cartesian axis (S_x, S_y, and S_z) calculated in k_x-k_y plane for KTO (001) surface. The colors indicate the modulus as well as the orientation (up(red) or down(blue)) of the spin polarization. . . . 68
3.8 (a) Electronic band structure of KTO (111) surface with atomic projection on atoms K, Ta, and O along high symmetry path M-Γ-K including SOC (b) Layer-wise projected DOS on the atomic layers shown in the background of the plot. The black dashed line indicates the Fermi level E_f. 69

3.9 The planar average of the electrostatic potential (oscillating green curve) along the z-direction (perpendicular to the surface) and the macroscopic average of electrostatic potential (red curve) of (111) surface of KTO. The crystal structure of (111) surface slab is shown within the plot in the background; where magenta, brown, and red spheres represent K, Ta, and O atoms, respectively. The Fermi energy (E_f) is set to zero. . . 70
3.10 Constant energy contour plots of spin-texture (a)-(c) on Fermi surface (d)-(f) corresponding to a cut at energy ($E-E_F$) = 0.6 eV for each spin component along the cartesian axes (S_x, S_y, and S_z) calculated in k_x-k_y plane for KTO (111) surface. The insets in (d)-(f) show the zoomed-in portions of the spin texture for the Rashba-split band. The colors indicate the modulus as well as the orientation (up(red) or down(blue)) of the spin polarization. 72
3.11 Side view of the crystal structure of slabs of LVO/KTO heterostructure in (001) orientation with (a)-(b) asymmetric and symmetric terminations of surfaces of KTO. 74
3.12 Side view of crystal structures of slabs of LVO/KTO heterostructure in (111) orientation with (a)-(b) asymmetric and symmetric terminations of surfaces of KTO. 76
3.13 Electronic structure of (001)-oriented LVO/KTO heterostructure (a)-(b) Calculated total as well as orbital projected DOS and band structure along the high symmetry path Y-Γ-M with SOC for asymmetric and symmetric terminations, respectively. Bands showing the prominent Rashba spin splitting are highlighted in red. 77
3.14 Band structures of (001)-oriented LVO/KTO heterostructure having symmetric termination of KTO with electron spin projections along the (a) y, (b) z, and (c) x-direction, respectively. Red and blue colors represent the positive and negative components of spin projections, respectively. . 77
3.15 Electronic structure of (111)-oriented LVO/KTO heterostructure (a)-(b) Calculated total as well as orbital projected DOS and band structure along high symmetry path M-Γ-K with SOC for asymmetric and symmetric terminations, respectively. Bands showing the prominent Rashba spin splitting are highlighted in red. 78

3.16 Calculated d-orbital projected band structures on 5d and 3d orbitals of Ta and V atoms, respectively with SOC along high symmetry path (a) Y-Γ-M for (001)- and (b) M-Γ-K for (111)- oriented LVO/KTO heterostructures, respectively with asymmetric termination. The radius of the circles represents the weight of the d orbitals. The colors of the individual d orbitals are indicated in the plot. 80
3.17 (a)-(b) Calculated band structure plots with atomic projection including SOC along high symmetry path (a) Y-Γ-M for (001)- and (b) M-Γ-K for (111)- oriented LVO/KTO heterostructures, respectively with asymmetric termination. The radius of the circles represents the weight of the individual atoms with the colors of the individual atoms indicated in the plot. 80
3.18 (a) Superlattice structure of LVO/KTO with two identical n-type interfaces LaO/TaO_2 (highlighted by dashed lines). (b) band structure plot with SOC along high symmetry path Y-Γ-M for LVO/KTO superlattice model in (001) orientation. 82
3.19 (a)-(b) The planar average of the electrostatic potential (oscillating green curves) along the z-direction (perpendicular to the interface) and the macroscopic average of electrostatic potential (red curves) of (001)-oriented LVO/KTO HS for asymmetric and symmetric terminations, respectively. The crystal structures of corresponding HS systems are shown within the plots in the background; where green, cyan, magenta, brown, and red spheres represent La, V, K, Ta, and O atoms, respectively. The Fermi energy (E_F) is set to zero. The charge density difference plots of the corresponding HS systems are also shown; the yellow-colored regions designate electron accumulation, whereas the blue color reflects electron depletion in the HS. The zoomed-in charge density difference at the interfacial region for symmetric termination is also shown in the inset of (b). 83

3.20 (a)-(b) The planar average of the electrostatic potential (oscillating green curves) along the z-direction (perpendicular to the interface) and the macroscopic average of electrostatic potential (red curves) of (111)-oriented LVO/KTO HS for asymmetric and symmetric terminations, respectively. The crystal structures of corresponding HS systems are shown within the plots in the background; where green, cyan, magenta, brown, and red spheres represent La, V, K, Ta, and O atoms, respectively. The Fermi energy (E_F) is set to zero. The charge density difference plots of the corresponding HS systems are also shown; the yellow-colored regions designate electron accumulation, whereas the blue color reflects electron depletion in the HS. 84

3.21 Spin-texture on constant energy contour plots corresponding to a cut at energy (E-E_F) (a) 0.32 eV, (b) 0.23 eV for each spin component along the cartesian axis (S_x, S_y, and S_z) calculated in k_x-k_y plane for the heterointerface LVO/KTO in (001) orientation for asymmetric and symmetric terminations, respectively. The colors indicate the modulus as well as the orientation (up(red) or down(blue)) of the spin polarization. 86

3.22 Spin-texture on constant energy contour plots corresponding to a cut at energy (E-E_F) (a) 0.02 eV, and (b) -0.11 eV for each spin component along the cartesian axis (S_x, S_y, and S_z) calculated in k_x-k_y plane for the (111)-oriented LVO/KTO heterointerface for asymmetric and symmetric terminations, respectively. The colors indicate the modulus as well as the orientation (up(red) or down(blue)) of the spin polarization. . . . 87

4.1 Total as well as atomic and orbital projected DOS in bulk EuO with spin-polarization. 93

4.2 Spin-polarized electronic band structure of bulk EuO along the high symmetry path Γ-X-W-L-Γ-K-X. Red and blue lines correspond to the majority and minority spin states, respectively. 94

4.3 Spin-polarized DOS (a) Total DOS along with the orbital projection on the corresponding atoms, (b) Layer-wise projected DOS on the atomic layers shown in the background of the plot. 95

4.4 Spin-polarized electronic band structure (a) Band structure plot of the EuO/KTO superlattice along the high symmetry path Y-Γ-M-X in the 2D Brillouin zone as shown in the inset, with red and blue lines representing up and down spin, respectively. (b) d-orbital projected band structure plot along the path Y-Γ-M with the value of exchange splitting in the d_{xy} orbitals indicated in the figure. 96
4.5 Band structure along M'-Γ-M path with the band crossing points of majority and minority spin states, α_1 and α_2 are zoomed in the inset. . . 97
4.6 Spin density distribution of the EuO/KTO superlattice with red (up spin) and blue (down spin) isosurfaces. The inset of the figure shows the top view of the interfacial TaO_2 layer with the induced spin density in d_{xy} orbitals. 98
4.7 (a) Layer decomposition of electron occupation in the 2DEG (b) Differential charge density plot of the EuO/KTO superlattice. The yellow color represents electron accumulation, while the blue color represents electron depletion. 99
4.8 The band structure of the EuO/KTO superlattice with SOC with the orbital character of the bands marked in the figure. 100
4.9 The Berry curvature along the high symmetry path M'-Γ-M along with the bands having the Rashba spin-orbit gap opened at the crossing points α_1 and α_2. The zoomed-in spin-orbit gaps are shown in the inset. 102
4.10 The spin texture of the bands with the Rashba spin-orbit gap on the constant energy contour in reciprocal space. A portion of the anticlockwise helical spin of the outer band labeled 1 is zoomed in the inset. 103

List of Tables

1.1 The seven ages of magnetism[9] 10

2.1 Optimized lattice parameters (Å) of $CuSeO_3$ and the magnetic moment values on Cu ions located at different positions in the unit cell for AFM (NC)-II configuration. 40

2.2 Comparison of total energies of various magnetic configurations with respect to the reference configuration (E_0 = 0 eV), ΔE (meV). 41

2.3 Total energy (in eV) for NM, AFM-A, AFM-G, AFM-C and FM states for bulk and monolayer CoAsS for U = $4-10$ eV. Values in bold represent the most stable (lowest energy) state. 52

2.4 Exchange coupling constant J (in meV) and critical temperature T_C (in K) for U = $4-10$ eV for bulk (b) and monolayer (m) CoAsS. 52

3.1 Rashba parameters viz. Rashba coupling constant α_R (eVÅ), Rashba splitting energy E_R (meV), and Rashba momentum offset K_R (Å^{-1}) for (001)- and (111)- oriented LVO/KTO heterointerface slabs for the cases of asymmetric and symmetric terminations of KTO. 79

CHAPTER 1

Introduction

”The laws of physics is the canvas God laid down on which to paint his masterpiece.”

Dan Brown

1.1 Background

Given the saturation of size and data processing speed of contemporary electronic devices, a move away from the prevalent charge-based electronics is urgently required. Spintronics is the most promising alternative information technology that can overcome these limitations due to its multifunctional characteristics. This is achieved via increasing the memory and processing power of the next-generation nanoelectronic devices while reducing power consumption by leveraging the intrinsic charge and spin degrees of freedom of electrons. The spin current is transported with reduced heating loss, which results in less dissipation. Moreover, the great storage density of the devices is further ensured by the use of electron spins. Further, spintronic devices process data more quickly and use less electricity because changing the spin state requires less energy. In spintronic devices, spin polarization is controlled either by magnetic layers or via spin-orbit coupling (SOC). The era of spintronics began with the discovery of giant magnetoresistance (GMR)[10], which earned Albert Fert and Peter Grünberg the

2007 Nobel Prize in Physics. The spin valve, which has two ferromagnetic (FM) metals and a non-magnetic (NM) metal between them, displays the GMR effect. The relative magnetic configuration of the two ferromagnetic metals determines the resistance of the spin valve, which can switch between two values (high or low). The device's resistance is low or high in a parallel or antiparallel configuration of the ferromagnetic metals, suggesting that magnetic sensors and storage devices may be able to store a bit. Spin-transfer-torque magnetoresistive random-access memory (STT-MRAM)[11], for example, is one spintronics-based technology that has been commercially adopted. There are still several challenges that must be overcome for these spintronic devices to operate effectively. As a result, research into new multifunctional materials is ongoing, and advancements in the field are heavily reliant on the exploration and identification of novel material systems. An appealing framework for investigating materials suitable for spintronic devices is offered by emerging 2D materials in the transition metal chalcogenides (TMC) and oxide heterostructures, both of which are members of the strongly correlated materials family. This is due to their distinctive physical and multifunctional features at low dimensionality[12–18]. This theoretical thesis focuses on the exploration of spintronic phenomena in the two strongly correlated families of TMC and oxide heterostructures, particularly in the low dimensional realm.

1.2 Strongly correlated materials

Due to their pervasiveness in several cutting-edge topics in condensed matter physics, strongly correlated materials are currently receiving a great deal of attention in both theoretical and applied research[19]. Usually, the repulsive interactions between electrons have relatively little impact on the electronic, mechanical, and thermal properties of materials. The electronic states in these materials are principally derived from delocalized s and p orbitals. This, coupled with the Pauli exclusion principle, causes electron kinetic energy to predominate over electron-electron interaction. This results in well-known electronic states such as metals, semiconductors, band insulators, and semimetals as predicted by band theory. However, there are several materials whose electronic, magnetic, and optical properties are largely determined by electron-electron interactions. These materials, often termed as strongly correlated systems, are composed of rare-earth and transition elements with partially filled 3d-, 4f- or 5f- electronic shells with local magnetic moments. This causes the d and f electrons in the materials to interact strongly with one another and with itinerant electronic states, giving rise to anomalous features and diversity of physical phenomena[20]. Strong correlation effects of d or f electrons are responsible for a variety of phenomena, such as the colossal magnetoresistance effects found in manganese oxides, high-temperature superconductivity seen in layered copper oxides and iron pnictides, and heavy fermion phenomena seen in actinide or lanthanide intermetallic compounds, to name a few[21]. In addition to this, one of the main issues in condensed matter physics is the quantitative explanation of the electronic structure of strongly correlated electrons. Conventional band theory predicts metallic characteristics while failing to account for the insulating behaviors of such materials that have been seen in experimental studies. The insulating states in strongly correlated materials can be differentiated into Mott-Hubbard and charge-transfer insulators, which are further described below.

1.2.1 Mott-Hubbard and charge-transfer insulators

While strongly correlated materials exhibit insulating behavior in experimental measurements, standard band theories predict them to be metallic. Nevil Mott identified this fundamental mistake in the band theory and stressed the importance of interelectron forces, which result in the bandgap in these incorrectly predicted conductors called to be Mott insulators[22]. Strong Coulomb repulsion between electrons described by the term “U” causes them to localize in atomic-like orbitals called Mott localization, which drives the system in an insulating state. The bandgap exists between bands of similar characters i.e., between sub orbitals of the same orbitals, for example, 3d characters. When electrons are strongly localized, they are unable to move freely between atoms and must instead “hop” from one to the next using a mechanism between neighboring atoms. The amplitude of this “hopping” mechanism, called t, is proportional to the bandwidth of the valence electronic states. The competition between the Coulomb potential U between electrons and the transfer integral t between adjacent atoms determines whether an energy gap will occur. The Hubbard model is used to describe the correlated systems by incorporating the on-site repulsion, which originates from the Coulomb repulsion between electrons in the same atomic orbitals and can therefore explain the metal-to-insulator transition in these systems. As a result, the inclusion of on-site Coulomb repulsion U_{dd} (between d electrons without any loss of generality) separates the metallic bands into two distinct sets of Hubbard bands, (Upper (UHB) and

Lower Hubbard bands (LHB)). Therefore, a large band gap is opened in these systems which is in line with the experimental data[23,24].

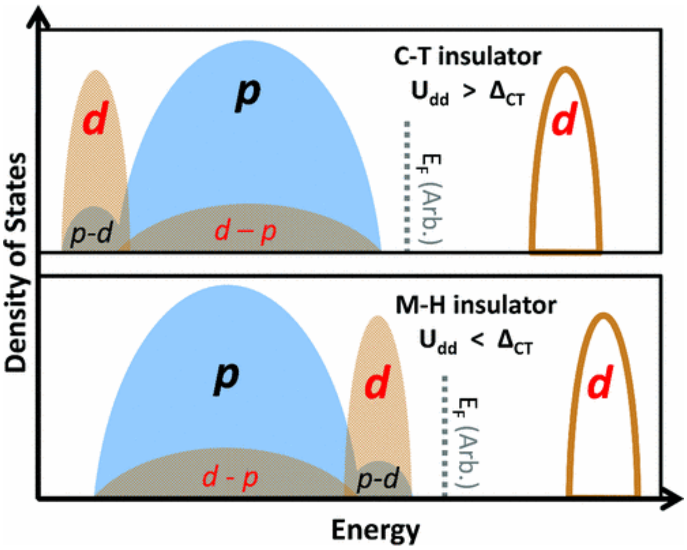

Figure 1.1: Schematic of (top) charge-transfer (C-T) and (bottom) Mott-Hubbard (M-H) insulators, decided by the competition between Coulomb repulsion U_{dd} (between d electrons) and charge-transfer energy Δ_{CT}. Figure reproduced from Ref.[1] with permission from American Physical Society.

In addition to the electron-electron correlations, the electronic structure of the late transition metal oxides, including the cuprate superconductors is further complicated by the hybridization between the transition-metal d states and O p bands that are situated between the lower and upper Hubbard bands formed by the transition-metal d orbitals. Therefore, to obtain a comprehensive understanding of the electronic characteristics of strongly correlated systems, the p orbitals of the anions or the ligands surrounding the transition metal ions or rare earth elements should be taken into account. An electron can be moved from the p orbitals of the anion or the ligands to the corresponding transition metal elements of the compound for a cost of Δ_{CT}, or charge-transfer energy. It is interesting to note that the categorization of transition metal compounds exhibiting insulating behavior can be addressed from the Zaanen-Sawatzky-Allen diagram as depicted in the seminal study in 1985[25]. The charge-transfer energy between the transition metal-3d and anion-p states Δ_{CT}, and the Coulomb interaction of the transition metal 3d electrons U_{dd} are both depicted in this picture[25,26] as key factors influencing the basic electronic structure. A comparison of the value of U_{dd} with Δ_{CT} determines whether the insulator is of the Mott-Hubbard or charge-transfer type based on the energy distributions of the d orbitals for the transition metals and the p orbitals of the neighboring anions (or ligands). The two types of insulators are shown pictorially in Fig. 1.1.

1.2.2 Two-dimensional transition metal chalcogenides

In recent years, the 2D TMC family of strongly correlated materials has rapidly grown and demonstrated a wide range of unique electronic and optical features, as well as more recently, magnetism. Since the successful exfoliation of monolayer graphene in 2004[27], the demand for device downsizing has spurred researchers to investigate 2D materials for uses in spintronics. describe the effect of dimensionality of magnetism, highlighting the importance of low dimensional ma netism in brief, write one short paragraph on this from review of 2d magnetism. Few-layered TMCs have received a lot of attention among these 2D materials due to their diverse properties. They range from semiconductors (MX_2; M = Mo, W, and X = S, Se, Te) through half-metals (VX_2, X = S, Se), and metals TaX_2, NbX_2, X = S, Se), giving them numerous opportunities for use in the integrated circuits, photoelectronic, and electronics[28,29]. As a result, many researchers have worked to promote their use in spintronic devices. However, the majority of these lack intrinsic magnetic properties, which has limited their use in spintronics. One efficient method to induce magnetic moments in these materials is to create crystal flaws like defects[30,31], edge-states[32–35], or dislocations at the grain boundaries[36]. These methods can contribute unpaired electrons and produce magnetic moments. Other techniques for inducing magnetism include adding magnetic and non-magnetic dopants[37–39] or adsorbing atoms[40,41], phase structure engineering[42], making ternary alloys[43], forming Janus structures[43], strain engineering[44,45]. However, it is very challenging to accurately control doping, strain, defects, and structural phases in experiments. Therefore, investigating 2D materials with inherent magnetism is crucial for their use in modern spintronics.

Atomically thin intrinsic magnetic materials have piqued interest for a long time. The forbidden long-range magnetic ordering in 2D materials at finite temperatures with isotropic and short-range exchange interaction, as hypothesized by Mermin and Wagner, deceived scientists and slowed the discovery of many such materials for a long time[46]. However, the limitations imposed by Mermin Wagner's theorem are inapplicable in the Ising system or a system with anisotropy. This was recognized by the researchers time and again, eventually leading to the discovery of 2D magnets at a slow pace. Three different types of atomically thin magnets have emerged from time to time, namely, Quasi-2D magnets obtained from the bulk[47–50], ultrathin magnetic films composed of conventional transition metal magnets[51–58], and vdW magnetic materials, as demonstrated by David et al.[59]. But only after the vdW magnets in the TMC family were discovered, the family of 2D magnetic materials was flooded, as several promising 2D magnets were found. Through ab initio calculations, it was proposed in 2012 that the pure VX_2 (X = S, Se) monolayers exhibited magnetic ordering, which could be tuned by applying strain[60]. Later, it was predicted that 2D MPX_3 (M = V, Cr, Mn, Fe, Co, Ni, Cu, Zn, and X = S, Se, Te) transition metal chalcogenophosphates would possess magnetic ordering ranging from antiferromagnetic to ferromagnetic. Furthermore, detailed research is done on the magnetic ground states of transition-metal trichalcogenide monolayers based on Mn and Cr[61–66]. Several monolayer materials, notably chromium trihalides (CrX_3, X = F, Cl, Br, and I) have been theoretically investigated[67–69]. An Ising-type antiferromagnetic (AFM) ordering in monolayer $FePS_3$ was experimentally demonstrated in 2016[70]. In 2017, the intrinsic long-range ferromagnetic ordering in pristine $Cr_2Ge_2Te_6$[71] and CrI_3[72] atomic layers was experimentally verified, putting to rest long-held assumptions. Since then, a variety of monolayer magnets have been experimentally proven[73–76]. Furthermore, the electronic spectrum of 2D TMC spans a broad range, including topological phases, semimetals, half-metals, Mott-Hubbard, and charge-transfer insulators[12–16]. Likewise, the spectrum of magnetic properties extends beyond ferromagnetism to encompass antiferromagnetism, ferrimagnetism, multiferroic behavior, and quantum spin liquids[77–81].

1.2.3 Oxide heterostructures

An incredible variety of physical phenomena occur in oxide heterostructures, featuring perovskite oxides, which are a subclass of transition metal oxides and a member of the family of strongly correlated electron systems. The transition metal s electrons are transferred to the oxygen ions owing to high electronegativity, while the remaining strongly correlated d electrons determine their physical characteristics, including electrical transport, magnetic states, optical response, and structural properties. Atomically well-defined and sharp interfaces of perovskite oxide heterostructures with proper crystal orientation and lattice mismatch manifest phenomena non-existent in constituting oxides. Strong interactions between the charge, spin, orbital, and lattice degrees of freedom give rise to novel solid-state phenomena including magnetism, Mott transitions, superconductivity, and multiferroicity, among others[17,18,82,83].

$LaAlO_3/SrTiO_3$ (LAO/STO) interface serves as the landmark oxide interface in the oxide heterostructures family. The discovery of high mobility two-dimensional electron gas (2DEG) at the interface of (001)-oriented LAO/STO in 2004, served as a milestone in this field[84]. It remains unclear if this conducting electron gas originates from an external mechanism caused by oxygen vacancies in the STO or from a property of the polar LAO thin film. Several mechanisms were put forth in an effort to comprehend the "real" cause of the conducting interface of two insulating oxides. However, the precise cause of the conductivity is still up for debate and is influenced by the external conditions affecting the growth of the heterostructure. Among the various hypothesized mechanisms for conduction are the polar catastrophe, oxygen vacancies, cation intermixing, and cation stoichiometry[84–86]. The atomically precise termination layer at the interface of the model oxide heterostructure system of LAO/STO created by Ohtomo and Hwang in Bell Laboratories has two potential interfacial configurations of $AlO_2/LaO/TiO_2$ or $AlO_2/SrO/TiO_2$. The two interfacial structures with electron and hole doping were found to be conducting with carrier mobility of more than $10,000\ cm^2V^{-1}s^{-1}$ and insulating, respectively. In the simple ionic limit, the interface between the charged and neutral planes of LAO and STO, respectively exhibits an excess/deficiency of $1/2$ in units of electronic charge e per 2D unit cell for the two different interfacial configurations. This polar discontinuity at the atomically abrupt interface between the two oxides with valence mismatch causes the divergence in the electrostatic potential with the increase in the thickness of the film, which is known as a "polar catastrophe". To overcome this electrostatic instability, there is electronic/atomic redistribution at the interface. Through electronic reconstruction, the additional $1/2$ electron at the n-type $AlO_2/LaO/TiO_2$ interface is accommodated in the 3d orbitals of Ti in STO resulting in the valence of $Ti^{3.5}$. Whereas at the p-type $AlO_2/SrO/TiO_2$ interface, the extra $1/2$ hole is accommodated by the introduction of oxygen vacancies on the STO side through atomic reconstruction. This explains why the LAO/STO interface was found to be conducting in the experiments. Fig. 1.2 schematically shows this electronic/atomic reconstruction at the n- and p- type interfaces of LAO/STO[2]. Since then, the LAO/STO heterointerface has received considerable attention because of its potential to exhibit a wide range of phenomena on a single platform. Emergent magnetism at the interface of two non-magnetic oxides with significant negative magnetoresistance and magnetic hysteresis of sheet resistance at low temperatures thrilled the spintronic community[87]. Additionally, the electron gas at the LAO/STO interface transitions to the superconducting phase via the Berezinskii-Kosterlitz-Thouless (BKT) transition at $\cong 200 mK$, which is characteristic of a 2D electron system[88]. Moreover, there is a significant gate-tunable Rashba spin-orbit interaction as a result of the interfacial breaking of inversion symmetry[89,90].

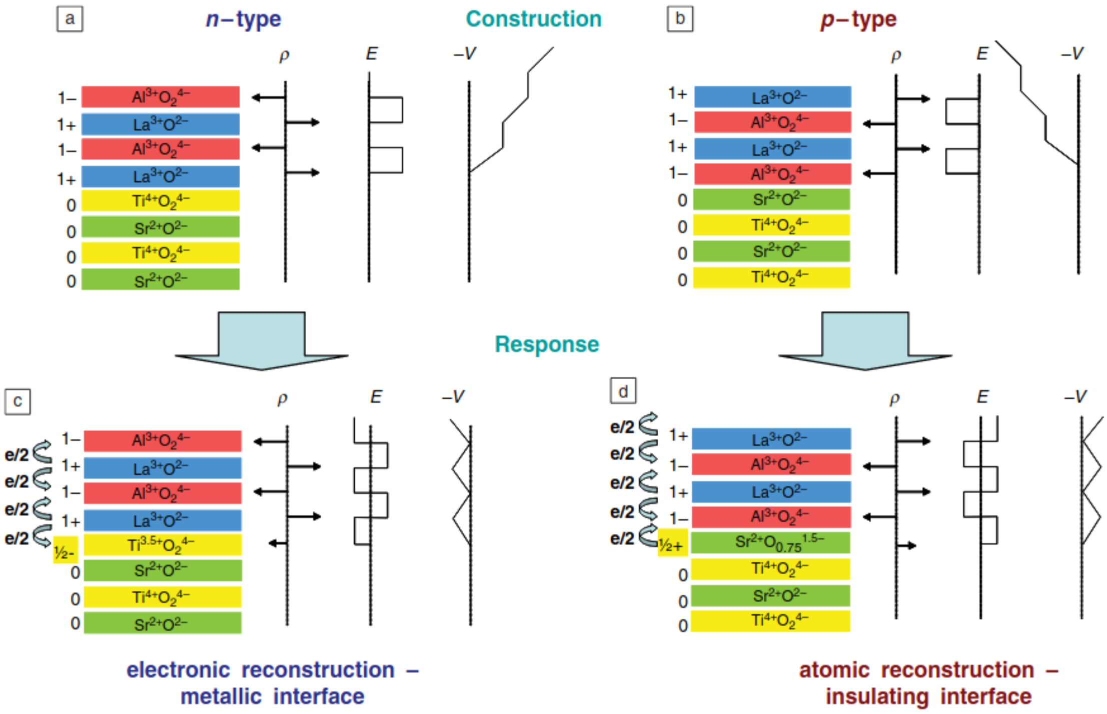
a
n–type
Construction
b
p–type
ρ
E
–V
1–
1+
0
Al3+O2 4–
La3+O2–
Ti4+O2 4–
Sr2+O2–
Response
c
d
e/2
½–
½+
Ti3.5+O2 4–
Sr2+O0.75 1.5–
electronic reconstruction – metallic interface
atomic reconstruction – insulating interface

Figure 1.2: Schematic of electronic and atomic reconstructions at the n- and p- type interfaces of the LAO/STO heterostructure, respectively. Figure reproduced from Ref.[2] with permission from Springer Nature.

In the past few decades, rapid advancements in atomistic scale precision thin film deposition techniques, such as pulsed laser deposition (PLD) and molecular beam epitaxy (MBE), have provided unprecedented access to the new physics emerging at oxide interfaces. These oxide heterostructures provide an excellent platform for the exploration of critical functionalities for spintronic applications. For example, it is possible to create oxide-based magnetic tunnel junctions (MTJ) for use in highly efficient, miniature MRAM devices. The half-metallic interface of the oxide heterostructure with large spin polarization is utilized as MTJ, together with $La_{0:75}Sr_{0:25}MnO_3$ (LSMO) electrodes and an insulating substrate as the tunneling barrier[91–94]. Further, magnetization in interface-based magnetoelectric spintronic devices is electrically controlled in heterostructures made of multiferroic materials[83,95–97]. For complex oxide heterostructures, STO has emerged as the material of choice for use as the substrate material, inheriting the majority of its features[98–107]. A few examples of STO-based heterostructures include $LaGaO_3$ (LGO)/STO[108], $NdAlO_3$ (NAO)/STO[109], $LaFeO_3$ (LFO)/STO[110], γ-Al_2O_3/STO[111]. Replacement of the perovskite LAO with spinel structured γ-Al_2O_3 led to record-high electron mobility of more than 105 cm^2 at 2 K, surpassing the initial mobility value of 103 $cm^2V^{-1}s^{-1}$ in LAO/STO system. Apart from the STO-based oxide heterostructures, several other heterostructures have been created[83,95–97,112]. The 5d perovskite oxide $KTaO_3$ (KTO) has lately gained attention as a possible contender for STO as it hosts low dimensional electron gas with high electron mobility and strong SOC, almost an order of magnitude greater than STO[13,113–117]. Some of the oxide heterostructures based on the KTO substrate include $LaTiO_3$ (LTO)/KTO, amorphous-LAO/KTO, $LaVO_3$ (LVO)/KTO, and EuO/KTO[13,118–123]. Additionally, spin-orbit-based mechanisms in oxide heterostructures provide a new spintronics dimension through direct and inverse spin Hall effects as well as Rashba-Edelstein effects allowing low-power electrical control of magnetism[89,124,125]. One standout candidate in this regard is the Rashba physics in oxide interfaces[90,126–129], which is described in more detail later in this chapter.

After reviewing the pertinent material family, the following sections cover the key principles and concepts about magnetism and SOC required to comprehend the field of spintronics.

1.3 Magnetism in solids

The history of magnetism dates back to 1088 with the discovery of the nautical compass[9]. The unification of electricity and magnetism was brought about by Hans-Christian Oersted's unintentional discovery of the magnetic field by a current-carrying wire in 1820. The well-known Maxwell equations inspired by the laws of electromagnetic induction (1821) and the magneto-optic Faraday effect (1845) used the distribution of magnetic poles or electric currents to model the magnetism of ferromagnetic materials.

The force that the E and B have on charges and currents is described by the Lorentz force law. These two theoretical concepts establish a connection between the electric and magnetic fields, E and B, and the free-space electric charge and current densities, ρ and j are the cornerstones of classical electromagnetism. However, a significant question was raised by the abnormally high current density required in a magnetized iron bar with substantial magnetization. The molecular field hypothesis (1907) proposed by Pierre Weiss for ferromagnetism suffered a similar fate. The development of quantum mechanics and the applications of relativity to the problem of ferromagnetism as interpreted by classical physics led to the beginning of modern physics. The fascinating history of magnetism consisting of seven eras is listed in Table 1.1. We are currently living in the seventh era, also known as the age of spintronics. Conventional charge-based electronics is gradually transitioning to spintronics, which makes use of the electron's spin characteristic by manipulating and utilizing spin currents.

Period	Dates	Icon	Drivers	Materials
Ancient period	-2000–1500	Compass	State, geomancers	Iron, lodestone
Early modern age	1500–1820	Horseshoe magnet	Navy	Iron, lodestone
Electromagnetic age	1820–1900	Electromagnet	Industry/infrastructure	Electrical steel
Age of understandingine	1900–1935	Pauli matrices	Academic	(Alnico)
High-frequency age	1935–1960	Magnetic resonance	Military	Ferrites
Age of applications	1960–1995	Electric screwdriver	Consumer market	Sm-Co, Nd-Fe-B
Age of spin electronics	1995–	Read head	Consumer market	Multilayers

Table 1.1: The seven ages of magnetism[9]

1.4 Magnetic ordering and exchange interactions

The number and orientation of spins of electrons affect the magnetic characteristics of an ion or atom. The collective effect of all the spins of the atoms decides the macroscopic magnetic properties of a solid. Pauli paramagnetism, diamagnetism, spin glasses, antiferromagnetism, ferrimagnetism, and ferromagnetism are a few examples of the various magnetic properties that materials can typically display. In transition metal compounds with d states, the same d electrons often control both the electronic and magnetic properties, but in inner transition metal compounds with f states, the f electrons control the magnetism, and the d or s electrons control the electronic properties. As a result of the strong correlation between individual electrons in these compounds, an ion's spin can better be described by its total spin rather than the spins of its individual electrons. Whereas the exchange interaction effect strongly correlates the atomic spins of neighboring ions with each other. These exchange interactions, inherently based on the combination of electron-electron repulsion and quantum mechanics, are at the root of magnetic order. The exchange symmetry of electrons places limitations on the permitted states during the exchange of identical particles. According to the Pauli principle, no two electrons can have the same four quantum numbers. To describe exchange interaction, consider H_2 molecule with two Hydrogen atoms H_a and H_b, each having one electron with position coordinates $\mathbf{r}_1$ and $\mathbf{r}_2$ rotating around the respective proton[3]. The total wave function of H_2 molecule $\Psi(\mathbf{r}_1, \mathbf{r}_2)$ is the product of the spatial and spin parts of the wavefunction and must be antisymmetric under the exchange of electrons (fermions). As a result, the antisymmetric spin part (singlet state χ_S) corresponds to the symmetric spatial part (with higher charge density between the atoms) and the symmetric spin part (triplet state χ_T) corresponds to the antisymmetric spatial part (decreased charge density between the atoms). The total wavefunctions for the singlet and triplet states are:

$$\Psi_S = \frac{1}{\sqrt{2}}[\psi_a(\mathbf{r_1})\psi_b(\mathbf{r_2}) + \psi_a(\mathbf{r_2})\psi_b(\mathbf{r_1})]\chi_S \tag{1.1}$$

$$\Psi_T = \frac{1}{\sqrt{2}}[\psi_a(\mathbf{r_1})\psi_b(\mathbf{r_2}) - \psi_a(\mathbf{r_2})\psi_b(\mathbf{r_1})]\chi_T \tag{1.2}$$

If χ_S and χ_T are assumed to be normalized, the energy of the two states follows from:

$$E_{S,T} = \int \Psi^*_{S,T}\hat{\mathscr{H}}\Psi_{S,T}d\mathbf{r_1}d\mathbf{r_2} \tag{1.3}$$

The difference between the two energies $E_S - E_T$ can be written in terms of the exchange integral as defined by

$$2\mathrm{J} = E_S - E_T = 2\int \psi_a^*(\mathbf{r_1})\psi_b^*(\mathbf{r_2})\mathscr{H}\psi_a(\mathbf{r_2})\psi_b(\mathbf{r_1})d\mathbf{r_1}d\mathbf{r_2} \tag{1.4}$$

$E_S - E_T$ can be parametrized using $\mathbf{S_1}.\mathbf{S_2}$, the spin operators for the two electrons. For singlet (triplet) state, $\mathbf{S_1}.\mathbf{S_2}$ = -$\frac{3}{4}$ ($\frac{1}{4}$). Hence, the effective Hamiltonian $\hat{\mathscr{H}}$ = $\frac{1}{4}(E_S + 3E_T) - (E_S - E_T)\mathbf{S_1}.\mathbf{S_2}$ has a spin-dependent term written by:

$$\hat{\mathscr{H}}^{spin} = -2\mathrm{J}\mathbf{S_1}.\mathbf{S_2} \tag{1.5}$$

For J > 0, $E_S > E_T$ favoring the triplet state (S = 1), indicating the preference for the parallel spins. For J < 0, $E_S < E_T$ i.e. antiparallel alignment of spins (singlet state with S = 0) is preferred. Heisenberg generalized the above Hamiltonian to many-electron atomic spins and gave the Hamiltonian:

$$\hat{\mathscr{H}}_{Heisenberg} = -2\sum_{i>j} \mathrm{J_{ij}}\mathbf{S_i}.\mathbf{S_j} \tag{1.6}$$

Here, $\mathrm{J_{ij}}$ is the exchange constant between spins $\mathbf{S_i}$ and $\mathbf{S_j}$ and can be simplified to J for nearest neighbor spins and 0, otherwise.

The Coulomb repulsion between electrons on the same atom pushes the electrons apart, stabilizing an antisymmetric spatial state or a triplet spin state with J > 0, in accordance with Hund's rule. J is predicted to be negative when the electrons are from separate atoms, stabilizing the singlet state with the antiparallel alignment of spins. As a result, a symmetric spatial state known as the bonding state is formed. This can be explained by the energy level of a particle in a box of length L ($1/L^2$ dependence). Kinetic energy is lowered with greater lengths resulting in more stability. This is because it increases the freedom of the electrons to move about the atoms rather than being confined to a single atom which forms the bonds between the atoms. The molecular orbitals are bonding (spatially symmetric) or antibonding (spatially antisymmetric) as shown in Fig. 1.3. The exchange interactions in metals and insulators are explained in the next sections:

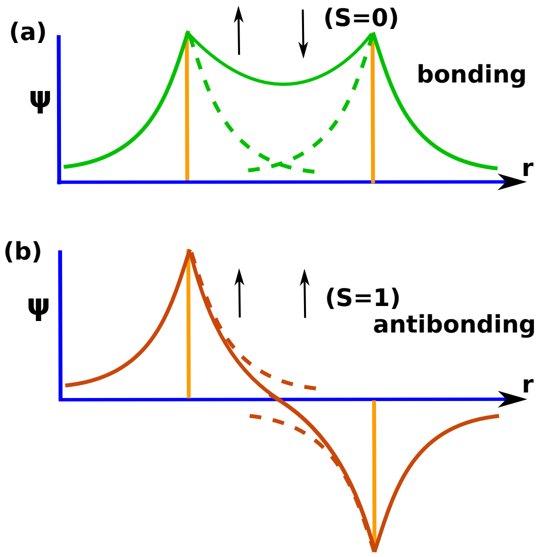

Figure 1.3: Wave functions for the H_2 molecule. (a) The spatially symmetric bonding orbital (spin singlet state S = 0), which corresponds to the sum of the two atomic orbitals is of lower energy than the (b) spatially antisymmetric antibonding orbital (spin triplet state S = 1), which corresponds to the difference between the two atomic orbitals[3,4].

1.4.1 Exchange interactions in metals

Direct exchange interaction is the interaction of magnetic atoms through the overlap of their atomic orbitals that occurs in the absence of any intervening atom. The tight-binding (TB) model Hamiltonian for the one-electron wave function in the 3d metallic series is $\mathscr{H} = \sum_{ij} t_{ij} c_i^\dagger c_j$, where t_{ij} is the interatomic transfer integral and c and $c^\dagger$ are the creation and annihilation operators for electrons, respectively. When only nearest neighbor interactions are taken into account, t_{ij} is equal to t, and the band's bandwidth W in the TB model is given by $2Zt$, where Z is the number of immediate neighbors. Since $Z = 8 - 12$ and t is approximately 0.1 eV for 3d transition metals, the W is of the order of a few eV. Further, the sign of the exchange interaction is determined by the occupation level of the conduction bands. The half-filled bands favor antiferromagnetic interaction, while almost-empty or almost-filled bands are responsible for ferromagnetic interaction through the delocalization of d orbitals as shown pictorially (Fig. 1.4). Additionally, an increase in t results in a rise in the bandwidth W, which delocalizes the electrons irrespective of spin. The critical condition for the appearance of magnetic ordering $U/W > (U/W)_{critical}$ is met, when $W < W_{critical}$ for Coulomb interaction U, at which the exchange is greatest. Interatomic distance also affects the direct exchange interaction with ferromagnetic exchange favored at larger spacing.

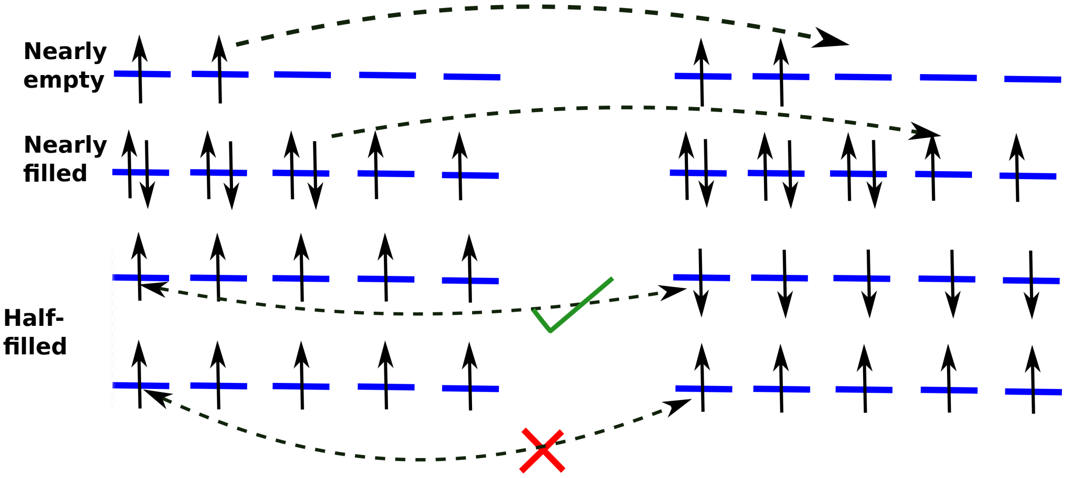

Figure 1.4: Electron delocalization in d orbitals which are nearly empty, nearly filled, and half-filled, respectively[4].

Other exchange interactions that contribute to magnetic ordering in metals include RKKY (Ruderman, Kittel, Kasuya, and Yosida) interaction which involves the conduction electrons mediating the exchange between the localized magnetic moments on the neighboring atoms, coupling of the spins s of the conduction electrons with core spins S in metals through s-d interaction. Another ferromagnetic exchange interaction called the double exchange mechanism exists in certain oxides having magnetic ions exhibiting two mixed valence states.

1.4.2 Exchange interactions in insulators

The direct overlap of the 3d orbitals of the cations (Mn^{2+}, Fe^{3+}) in insulators, primarily oxide systems, is insufficient to explain long-range exchange interactions. Through the hybridization of p-d orbitals in these systems, non-magnetic oxygen ions mediate the superexchange interaction between magnetic ions as given by the Heisenberg Hamiltonian. This interaction is described by $\sim -t^2$/U, where t is the hopping/transfer integral ($\propto W$), and U is the Coulomb interaction. The two magnetic ions having one unpaired electron (without any loss of generality) each separated by an oxygen ion having two outermost electrons in p orbitals favors the antiferromagnetic coupling in contrast to the ferromagnetic one. The antiferromagnetic state is stabilized by the delocalization of electrons over the oxygen ion and two magnetic ions (M-O-M unit), which lowers the kinetic energy. This can be explained with the help of Fig. 1.5.

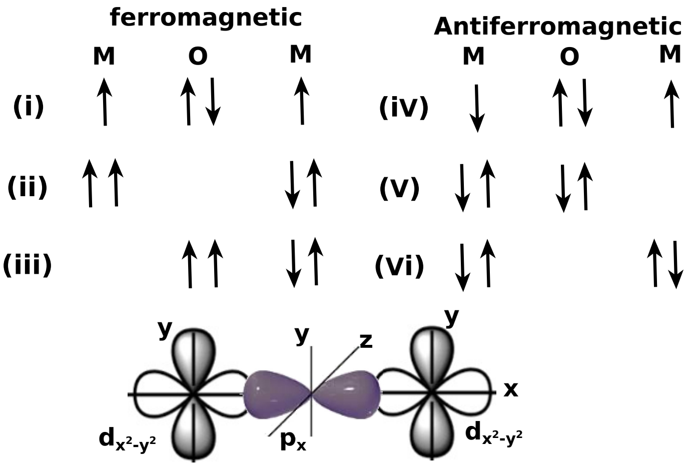

Figure 1.5: A typical superexchange in a magnetic oxide. The up and down arrows show the spins of the electrons over transition metal (M) (single unpaired electron) and oxygen (O) atoms. The ferromagnetic coupling of spins on M atoms has ground state (i), but the exclusion principle prohibits the delocalization of spins as in (ii) & (iii) configurations. The antiferromagnetic coupling of spins on M atoms has ground state (iv), which can be delocalized over the M-O-M unit as given in the excited configurations (v) and (vi), thus lowering the kinetic energy[3,4].

Furthermore, according to the Goodenough-Kanamori rules, the interatomic separation, M-O-M bond angle, orbital occupancy, and symmetry all of these affect the strength and sign of superexchange interaction.

(a) With the singly occupied 3d-orbitals on the two magnetic ions directed towards each other with a $120^\circ - 180^\circ$ M-O-M bond angle, the exchange interaction is stronger antiferromagnetic.

(b) When the singly occupied 3d-orbitals on the two magnetic ions can have zero overlap due to the symmetry of orbitals with $\sim 90^\circ$ M-O-M bond angle, the exchange interaction is weakly ferromagnetic.

(c) With vacant or doubly occupied 3d orbitals of the same symmetry on one magnetic ion and singly occupied 3d orbitals on the other magnetic ion, the exchange interaction is weakly ferromagnetic.

The Superexchange is generally antiferromagnetic rather than ferromagnetic because the overlap integrals are typically greater than zero.

In addition to the inherent magnetism, SOC is at the heart of the rich phenomena observed in condensed matter systems for spintronics applications. As a result of the interplay between SOC and low dimensionality, new phases of matter have appeared, such as chiral spin textures and spin-polarized surface and interface states. The following section discusses the concept of spin-orbit interaction and some of the associated phenomena, including the Rashba effect and quantum anomalous Hall effect (QAHE).

1.5 Spin-orbit coupling/interaction

The spin-orbit interaction couples the orbital motion of electrons to their spin. Due to the nucleus's Coulomb potential, an electron encounters an electric field **E** as it moves in its permitted orbit with momentum p around the positively charged nucleus. To put it another way, the nucleus is rotating with momentum **–p** around the electron in the rest frame of the electron. This can be visualized as a current loop with an electron at its center. A magnetic field is created at the location of the electron by this current loop. Therefore, if the electron is considered to be moving at relativistic speed, or at a velocity similar to the velocity of light in a vacuum, the electric field **E** of the nucleus is viewed as an effective magnetic field $\mathbf{B}_{eff}$ given by $\mathbf{B}_{eff}$ = $(\mathbf{v}\times\mathbf{E})/c^2$ in the rest frame of the electron. The energy or Hamiltonian corresponding to the interaction between the electron's spin magnetic moment and $\mathbf{B}_{eff}$ is provided by:

$$H = \mu_B(\boldsymbol{\sigma}.\mathbf{B_{eff}}) \tag{1.7}$$

Here, μ_B is Bohr magneton and $\boldsymbol{\sigma}$ is Pauli spin vector. When $\mathbf{B}_{eff}$ is taken into account, this formula is simplified to

$$H = \mu_B \boldsymbol{\sigma}.\frac{(\mathbf{v}\times\mathbf{E})}{c^2} \tag{1.8}$$

The energy correction or perturbation term connects the electron's spin, $\boldsymbol{\sigma}$, to its orbital motion, which is indicated by orbital velocity, **v**. This is referred to as spin-orbit coupling or interaction. The SOC in real solid-state materials is depicted in an oversimplified manner by this atomic SOC. Due to the screening effect, conduction electrons in actual solids barely experience the electric field of nuclei, yet the presence of an internal or external potential gradient ∇V in the solids results in SOC[130]. Two categories- the Dresselhaus and the Rashba SOC, can be made based on the origin of the potential gradient in the solid. First discovered in zinc-blende $III-V$ semiconductor compounds lacking a center of inversion, such as GaAs or InSb, Dresselhaus SOC results from the absence of a center of inversion in a solid[131]. The Rashba SOC develops as a result of the structure inversion asymmetry found at surfaces or interfaces in heterostructures. The Rashba SOC effect is particularly appealing for spintronic applications which is discussed in more detail below.

1.5.1 Rashba effect

The Rashba effect is a manifestation of the spin-orbit interaction in actual solid-state materials. It depicts the momentum-dependent spin-splitting in the electronic bands at surfaces or interfaces as a result of the combined action of SOC and the breaking of inversion symmetry. The well-known Bychkov-Rashba Hamiltonian[132] describes the Rashba interaction for nearly free electrons with parabolic band dispersion written as

$$H_R = \alpha_R(\vec{k} \times \vec{\sigma}).\hat{z}, \tag{1.9}$$

Here α_R is the Rashba coupling constant which depends upon the strength of SOC and inversion asymmetry, $\vec{k}$ the momentum, $\vec{\sigma}$ is the vector of the Pauli spin matrices, and $\hat{z}$ is the unit vector along the direction of the symmetry-breaking field. This results in linear spin-splitting in the parabolic energy bands with the expression,

$$\varepsilon_k = \frac{\hbar^2 k^2}{2m} \pm \alpha_R k, \tag{1.10}$$

It is a surface- or interface-driven SOC mechanism that lifts the spin degeneracy of the electronic energy bands at the non-zero wave vector k as shown in Fig. 1.6 (a). In a Rashba system, the momentum and spin degrees of freedom are locked perpendicular to each other as depicted in Fig. 1.6 (b). Three parameters describing the strength of the Rashba effect are α_R, E$_R$ (Rashba splitting energy), and momentum offset K$_R$. The values of E$_R$ and K$_R$ for the Rashba-split band can be calculated from the band itself, while α_R is calculated from E$_R$ and K$_R$ using the relation, $\alpha_R = 2E_R/K_R$.

The Rashba effect has enormous implications for the creation of high-performance next-generation spintronic devices since the accompanying spin splitting enables electrical control of spin without the requirement for an external magnetic field. Further, the

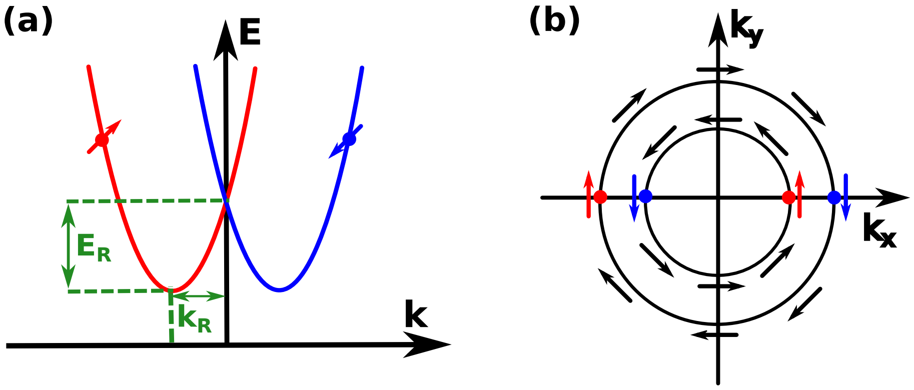

Figure 1.6: Rashba effect (a) bands showing spin splitting due to the Rashba effect with horizontally displaced parabolas (b) spin texture of the Rashba-split bands in the reciprocal space with clockwise/anticlockwise spins of outer/inner Rashba-split bands[5,6].

perovskite oxides are characterized by the presence of d electrons and high-Z elements with strong SOC. Therefore, the presence of SOC and the symmetry-breaking electric field normal to the heterointerface in oxide heterostructures lifts the spin degeneracy (associated with the spatial inversion symmetry) that causes the Rashba effect at the surfaces/interfaces[128,129,133]. At the LAO/STO interface, a significant Rashba SOC in the 2DEG is obtained, which is further adjustable with gate voltage[89,90,90,126,127]. Effective spin-to-charge interconversion in 2DEG at these interfaces driven by the Rashba effect has gained a lot of interest recently. Lesne et al.[134], demonstrated the spin-charge conversion achieved with exceptional efficiency at low temperatures in the 2DEG at the LAO/STO interface using the Rashba effect. High mobility 2DEG offers higher momentum relaxation times than those present in conventional metal-metal interfaces, resulting in a higher figure of merit ($\lambda_{IREE} \sim \alpha R\tau$). Additionally, Wang et al. used the direct Rashba-Edelstein effect to obtain an efficiency of $\sim$ 6.3 in charge-to-spin conversion in the LAO/STO at ambient temperature[135]. At the interfaces of STO-based oxide heterostructures, the Rashba SOC adjustable with optical gating offers another efficient method for adjusting the transport characteristics of electrons in solids[136,137]. A further demonstration of the external electric field-tunable Rashba effect at polar perovskite surfaces and interfaces was made by Shananavas et al.[116], using DFT and the TB model.

1.5.2 Topological states of matter and quantum anomalous Hall effect

Topological states of quantum matter are the appearance of quantum phenomena at the macroscopic scale in solid-state materials[135]. The first demonstration of a topologically non-trivial state of matter is the integral quantum Hall effect (IQHE)[138]. Irrespective of experiment's geometrical specifics or the flaws in its materials, the 2DEG demonstrated quantization of the Hall conductance at very low temperatures and high magnetic fields. The longitudinal resistance is zero, and the hall conductance is quantized in plateaus of Ce^2/h (C is called Chern number, h is Planck's constant, and e is the electronic charge). Another topologically non-trivial state of matter known as the QAHE is the quantized Hall conductivity in the absence of an external magnetic field[139]. The practical realization of QAHE remains hindered for several years after F.D.M. Haldane presented the first TB model for the quantization of Hall conductance on a periodic 2D graphitic honeycomb lattice in 1988[140]. In a QAH material that is insulating in the bulk, current only flows along the edges of the sample in the unidirectional lanes known as chiral edge states shown schematically in Fig. 1.7. These edge states are robust and provide dissipaton-free current transport which is valuable for low-power and high-speed next-generation electronics. This robustness is related to the topology of the material characterized by the topological invariants. A material's topology is a geometric characteristic that is undisturbed by continuous deformations and unaffected by factors like sample size, shape, and disorder.

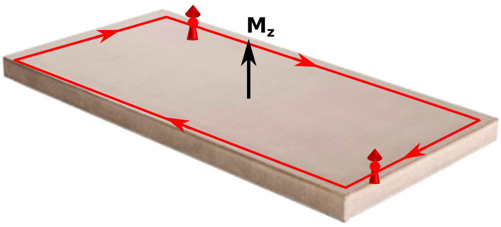

Figure 1.7: A schematic diagram of edge channels in a magnetic sample with QAHE in real space. The black arrow represents the spontaneous magnetization in the sample along the z direction. A chiral QAHE channel appears at the edge of the sample (in-plane red arrows), and the spin of this conductive channel is fully polarized (red arrows perpendicular to the plane)[7,8].

In order to comprehend the accurate quantization of Hall conductance, it is important to remember that a material's electronic energy band structure mostly dictates its physical properties. The characteristics of the material would not have an impact on the physical attributes related to the topological invariant for the energy bands of a solid. In QAHE, a topological invariant known as the Chern number[141] can be obtained from the integration of Berry curvature in the 2D Brillouin zone as

$$C = \frac{1}{2\pi} \sum_{n} \int_{BZ} d^2k \Omega_n(k), \tag{1.11}$$

here $\Omega_n(k)$ is the Berry curvature of the n^{th} Bloch band and according to Kubo formula[142,143] can be modified as

$$\Omega_n(k) = -\sum_{m \neq n} \frac{2Im(< \psi_{nk}|V_x|\psi_{mk} >< \psi_{mk}|V_y|\psi_{nk} >)}{(\omega_n - \omega_m)^2}, \tag{1.12}$$

here, $E_n = \hbar\omega_n$ is the eigenvalue of the n^{th} eigenstate of ψ_{nk} at a particular k point, and $V_{x/y}$ is the velocity operator.

The quantized Hall conductivity $\sigma_{xy} = Ce^2/h$ that is carried by the 1D chiral edge states generating dissipationless transport is determined by the sum of the Chern numbers of all the occupied bands. QAHE, a combined effect of spin-orbit coupling and intrinsic magnetization has fetched a great deal of interest recently[144–146]. In experiments, one of the techniques to realize the QAHE state is through the quantum spin Hall effect (QSHE)[147], which is the quantized counterpart of the spin Hall effect (SHE) realized in HgTe/CdTe[148,149] and InAs/GaSb[150,151] quantum wells. In time-reversal invariant systems with SOC, SHE happens when opposite spins accumulate on the opposing lateral surfaces in a direction perpendicular to the electric field without the presence of an external magnetic field. In a topological insulator with a non-zero topological invariant Z_2, the quantized spin-Hall conductance and zero charge-Hall conductance may provide a route to the QAH state by breaking the time-reversal symmetry[98]. Creating heterostructures out of materials with strong SOC and inherent magnetism from two distinct materials is another method for obtaining QAHE. Zhang et al. predicted that the CdO/EuO quantum well would support the stoichiometric quantum anomalous Hall state without magnetic doping[152]. In light of the fact that the 4d and 5d elements of transition metals have strong SOC and large magnetic moments, transition metal oxides offer another potential family of materials to exploit in the quest for the QAH effect. Materials for QAH state have been proposed in a variety of transition metal oxide heterostructures, such as pyrochlore $A_2B_2O_7$ heterostructures[153] and perovskite bilayer ABO_3 heterostructures[154–156].

1.6 Computational methodology

DFT is currently a well-established framework and the method of choice for quantum mechanical electronic structure calculations on the most difficult problems in the fields of physics, materials sciences, and chemistry as compared to the wavefunction-based methods (Schrödinger theory). It explains the behavior of matter by addressing the quantum mechanics of many-body systems such as atoms, molecules, and solids. The central idea behind DFT is to use electron probability density $\rho(\vec{r})$ as a fundamental variable to characterize the energies of electronic systems.

1.6.1 Theoretical background

The wave function that emerges from the electronic structure theory holds all the necessary details about a system. All the physical quantities of interest, such as energy values, can be calculated by applying the corresponding operators to the wave function and computing the expectation values. One approach to determining the wave function is the wave function theory, which was first proposed by Erwin Schrodinger in 1925. The nuclear dynamics are constrained by the Born-Oppenheimer approximation, which makes things a little easier, so the Schrodinger equation for electrons is given by:

$$H\psi = E\psi \tag{1.13}$$

expanding the electron Hamiltonian operator,

$$H = \sum_{i=1}^{N} \frac{-\hbar^2}{2m}\nabla_i^2 - Ze^2 \sum_{R} \frac{1}{|r_i - R|} + \frac{1}{2}\sum_{i\neq j} \frac{e^2}{|r_i - r_j|} = \hat{T} + \hat{V_{ne}} + \hat{V_{ee}} \tag{1.14}$$

The kinetic energy of the system of N electrons is represented by the first term in the equation above. The second term is the nuclear-attraction term (also known as the one-electron potential term), frequently referred to as the external potential in DFT. The final term is the inter-electronic interaction or electron correlation (two-electron potential term). The wave function of a complex system with many electrons is quite complicated since it depends on three spatial coordinates and the spin coordinate of each electron in the system. It is an antisymmetric product of orbitals, which are linear combinations of basis functions. As a result, as the system gets larger, it becomes nearly impossible to correctly solve the equations. Another difficult aspect of wave functions is their physical interpretation. The wave function can be physically understood by using the probability density given by $|\psi|^2$. Walter Kohn and Pierre Hohenberg introduced the DFT method, a novel approach based on electron density, in 1964. They proved through theorems that the electron density, which only requires three spatial coordinates, contains all of the information in a system.

1.6.2 Density Functional theory (DFT)

Two theorems formulated by Hohenberg and Kohn in 1964 laid the meticulous foundation for current DFT techniques.

The ground state wave function can be written as a unique functional of the ground state electron density, i.e. $\Psi_0 = \Psi[n_0]$. Hence, the ground state energy E can be represented as a functional of the ground state density in the following way:

$$E_0\left[\Psi\left[\mathrm{n}_0\right]\right] = <\Psi\left[\mathrm{n}_0\right]\left|\hat{T} + \hat{V}_{ne} + \hat{V}_{ee}\right|\Psi\left[\mathrm{n}_0\right]> \tag{1.15}$$

The external potential V_{ext} is determined by the ground-state electron density $\rho(\vec{r})$ within a small additive constant. According to the fundamentals of quantum mechanics, we know $V_{ext} \rightarrow H \rightarrow \Psi \rightarrow \rho$. The first HK theorem demonstrates the inverse route as $\rho \rightarrow V_{ext} \rightarrow H \rightarrow \Psi$. Hence, it establishes a one-to-one mapping between the ground-state densities and wave functions in many-electron systems.

There exists a universal functional of the density, $F_{HK}[\rho']$, such that for any well-behaved density $\rho'(\vec{r})$ that integrates to the proper number of electrons N, the density follows the variational principle and the energy functional satisfies the following relation:

$$E_0 \leq E\left[\rho'\right] = F_{HK}\left[\rho'\right] + \int \rho'(\vec{r})V_{ext}(\vec{r})d\vec{r} \tag{1.16}$$

in which E_0 is the ground-state energy and the equality holds when the density ρ', is the exact ground-state density ρ_0', for the external potential V_{ext}. Although the HK theorems are quite powerful, they do not provide a practical way to determine a system's ground-state density.

1.6.2.1 Kohn-Sham formalism

In 1965, Kohn and Sham developed a straightforward approach for performing DFT calculations that preserves the essence of DFT. The difficulty of determining trial densities and calculating energy from trial densities was addressed by KS formalism with the inclusion of atomic orbitals. It results in the practical use of DFT by taking into consideration a fictitious system of non-interacting electrons that has the same ground state density as the real system of interacting electrons. The addition of a small correction factor takes into account the kinetic energy difference between the real and fictitious (non-interacting) systems. Now, the kinetic energy of the non-interacting system can be calculated exactly by adding one-electron kinetic energy of occupied one-electron orbitals. The electronic energy in the KS approach can be written in the abbreviated form:

$$E = T + V_{ne} + V_{ee} + V_{xc} \tag{1.17}$$

which is the sum of kinetic energy of non-interacting electrons, nuclear-electron interaction, electron-electron repulsion, and exchange-correlation energy. The exchange-correlation energy includes the effects of quantum mechanical exchange and correlation, correction for classical self-interaction errors, and the difference in kinetic energy between non-interacting and real systems. In the KS approach, density is defined as the sum of the occupied orbitals in an orbital basis set, with basis functions χ :

$$\rho(r) = \sum_{i=1}^{N} |\chi_i(r)|^2 \tag{1.18}$$

N is the number of electrons obtained from the density by:

$$N = \int \rho(r) dr \tag{1.19}$$

Now, the energy functional in this basis set can be written as:

$$E[\rho(r)] = \sum_i^N \left(\langle \chi_i | -\frac{1}{2}\nabla_i^2 | \chi_i \rangle - \langle \chi_i | \sum_k^{nuclei} \frac{Z_k}{|r_i - r_k|} | \chi_i \rangle \right) + \sum_i^N \langle \chi_i | + \frac{1}{2} \int \frac{\rho(r')}{|r_i - r'|} dr' | \chi_i \rangle + E_{xc}[\rho(r)] \tag{1.20}$$

The first two terms in the above expression are identical to that in Hamiltonian in WFT, if χ_i are occupied molecular orbitals. The next term involves the integration of the interaction between density and the orbitals which determine the density using Eq. 1.18 and the orbitals are in turn obtained by solving Eq. 1.21 involving the density in expression 1.22. This demands reaching the self-consistency till the point where calculating the expression 1.18 from the orbitals, regenerates the density used in 1.22 to evaluate the orbitals by 1.21. Therefore, the key objective is to determine the orbitals χ_i that minimize the energy functional in Eq. 1.20 as well as satisfy the following eigenvalue equation of KS operators:

$$h_i^{KS} \chi_i = \varepsilon_i \chi_i \tag{1.21}$$

The KS operator is a one-electron operator that includes terms corresponding to kinetic energy, nuclear-electron attraction for all nuclei, electron-electron repulsion with density appearing self-consistently, and an exchange-correlation term.

$$h_i^{KS} = -\frac{1}{2}\nabla_i^2 - \sum_k^{nuclei} \frac{Z_k}{|r_i - r_k|} + \int \frac{\rho(r')}{|r_i - r'|} dr' + V_{xc} \tag{1.22}$$

In Eq. 1.22, V_{xc} is the functional derivative of the exchange-correlation energy which presents the key challenge in the DFT approach.

$$V_{xc} = \frac{\partial E_{xc}}{\partial \rho} \tag{1.23}$$

It must be emphasized that the orbitals χ must give the exact density (minimum must correspond to the real system) since Eq. 1.20 is exact.

1.6.2.2 Exchange-correlation functionals

Since the explicit form of the exchange-correlation functional is unknown, an approximation must be made. This section briefly discusses two widely used types of exchange-correlation functionals, Local-Density Approximation (LDA) and Generalized Gradient Approximation (GGA).

Local Density Approximations

All other density-based approximations are fundamentally based on the LDA for the approximate exchange-correlation functionals. The LDA is the most used functional and is based on an electron gas with uniform density, where the motion of the electron is taken into account under a positive, ionic background charge distribution to preserve charge neutrality. In LDA, the exchange-correlation energy at a position r per particle in the ideal homogeneous electron gas with electron density n(r) remains constant. In this approximation, the exchange-correlation functional E_{XC}[n(r)] has the following form:

$$\begin{aligned} E_{XC}^{LDA}[n(r)] = \int n(r)\varepsilon_{XC}^{hom} n(r)dr = \int n(r)[\varepsilon_{X}^{hom} n(r) + \varepsilon_{C}^{hom} n(r)]dr \\ = E_{X}^{LDA}[n(r)] + E_{C}^{LDA}[n(r)] \end{aligned} \tag{1.24}$$

The exchange-correlation functional E_{XC}[n(r)] in LDA assumption splits into two parts, the exchange part $E_X^{LDA}[n(r)]$ and the effective correlation contribution $E_C^{LDA}[n(r)]$. The exchange part gives the exchange energy of an electron in a homogeneous electron gas of a particular density n(r), and initially deduced by Bloch and Dirac around the late 1920s. The exchange part $E_X^{LDA}[n(r)]$ in the exchange-correlation functional E_{XC}[n(r)] can be derived analytically for a system of uniform electron gas with density n(r):

$$E_{X}^{LDA}[n(r)] = \int n(r)\varepsilon_{X}^{hom} n(r)dr = -\frac{3}{4}\left(\frac{3}{\pi}\right)^{1/3} \int n(r)^{4/3} dr \tag{1.25}$$

where ε_X^{hom} is the homogeneous electron density for the exchange part in LDA.

$$\varepsilon_{X}^{hom} = -\frac{3}{4}\left(\frac{3}{\pi}\right)^{1/3} n(r)^{1/3} \tag{1.26}$$

The accuracy of exchange energy in LDA, $\sim 10\%$. The underestimation of exchange energy in LDA formalism and the overestimation of correlation energy error partially cancel one another and provide a quite fair accuracy for ionization energies of atoms, dissociation energies of molecules, and cohesive energies $\sim 10-20\%$. The LDA works well for systems with slowly varying electron density.

But the LDA fails miserably for heavy fermions and systems that are primarily dominated by electron-electron interactions. With rapid density variation, the LDA tends to underestimate bond length by $1-2\%$, vibrational frequencies of molecules within $5-10\%$ accuracy, overestimate the binding energies by $10-50\%$, and largely underestimate the fundamental transition energy gaps or bandgap of solids by up to $\sim 50\%$ [157,158].

Generalized Gradient Approximations

Since the exchange-correlation energy of a homogeneous electron distribution widely differs for a real material with non-local density variations, the first extension beyond the LDA formalism is the use of not only the information about the density n(r) at a particular point r in space, but to also enrich the exchange energy with gradient correction of the charge density, $\nabla n(r)$ that accounts for the non-homogeneity of the actual electron density. Thus, the exchange-correlation energy in generalized gradient approximation (GGA) becomes [159],

$$E_{XC}^{GGA}[n(r),n(r')] = \int f[n(r),n(r'),\nabla n(r),\nabla n(r')]dr \tag{1.27}$$

The GGA is found to give much better results than LDA in predicting material properties to their approximate real values in the KS method. The overcorrection of the local electronic density of uniform electron gas by gradient-corrected density largely reduces the ground state properties such as lattice constants being smaller by $< 0.6\%$ than experiment value, and bandgap underestimation problem of LDA within 0.2 eV of its experimental value in GGA [160,161].

1.6.2.3 DFT+U: Extension to DFT for strongly correlated systems

The two most used exchange-correlation energy approximations, LDA and GGA, are based on an expansion around the homogeneous limit of an interacting electron gas. As a result, they perform effectively in situations where the electronic charge density changes gradually and is easily met by delocalized atomic states like s or p orbitals. These methods, however, pose serious issues when applied to strongly correlated systems, which include systems with transition metal, lanthanide, or actinide elements with partially filled d- or f-shells. This issue can be traced to the propensity of exchange-correlation functionals to excessively delocalize valence electrons and to overly stabilize metallic ground states[162] as a result of incomplete cancellation of electronic self-interaction contained in the Hartree term. Thus, there is still a “fragment” of the original electron which may lead to increased self-interaction and an excessive delocalization of the wave functions[162]. Therefore, DFT dramatically fails to anticipate the characteristics of systems whose ground state is characterized by a more pronounced localization of electrons and predicts metallic ground states in many Mott insulating transition metal oxides.

The DFT+U method, developed by Anisimov et al.[22], formulated to improve the description of the ground state of correlated systems, is inspired by the Hubbard model. It is often termed as LDA+U which stands for a Hubbard, “+U” correction to approximate DFT functionals, such as LDA, Local Spin Density Approximation (LSDA), or GGA. The principal objective of the U correction is to use an additional Hubbard-like term to treat the strong on-site Coulomb interaction of localized electrons. Hence, the Hubbard model is employed to characterize the strongly correlated electronic states of localized d or f orbitals of transition metal and rare earth elements while taking the remaining valence electrons into account at the level of “regular” approximate DFT functionals. Within LDA+U, a system’s total energy can be expressed as follows:

$$E_{LDA+U}[\rho(r)] = E_{LDA}[\rho(r)] + E_{Hub}[n^{i\sigma}_{mm'}] - E_{dc}[n^{i\sigma}] \tag{1.28}$$

where $\rho(r)$ is the electronic density, E_{Hub} is the term that contains the Hubbard Hamiltonian to describe correlated states, and E_{LDA} represents the standard DFT total energy functional being corrected. $n^{i\sigma}_{mm'}$ are occupation numbers of localized orbitals (i.e. density matrix elements) identified by the atomic site index i, state index m (such as running through the eigenstates of L_z for a specific angular quantum number l), and by the spin σ. $n^{i\sigma}$ is the sum of the occupations corresponding to all m and m' orbitals. Because of the additive Hubbard term, it is necessary to eliminate from the E_{LDA}, an approximate estimate of electron correlation effects, including the on-site correlation energy between electrons in these m and m' orbitals. Therefore, a “double-counting” factor (E_{dc}) must be deducted from the LDA’s total energy that approximates the electronic interactions as a mean field. E_{dc} term is not uniquely defined and different formulations can be applied to various systems. The fully localized limit (FLL) formulation[163–165], which applies to systems with more localized electrons on atomic orbitals, is the most widely used of these formulations due to its ability to expand the width of the KS orbitals and to effectively capture Mott localization. Based on this formulation, the LDA+U can be written as:

$$E_{LDA+U}[\rho(r)] = E_{LDA}[\rho(r)] + \sum_i \left[\frac{U^i}{2} \sum_{m,\sigma \neq m'\sigma'} n_m^{i\sigma} n_{m'}^{i\sigma'} - \frac{U^i}{2} n^i (n^i - 1) \right] \tag{1.29}$$

The dependence on the occupation number is anticipated since the Hubbard correction is only used in the states where correlation effects are the most prominent. The occupation number is calculated as the projection of occupied KS orbitals on the states of a localized basis set:

$$n_{mm'}^{i\sigma} = \sum_{k,v} f_{kv}^{\sigma} \left\langle \psi_{kv}^{\sigma} | \phi_{m'}^{i} \right\rangle \left\langle \phi_{m}^{i} | \psi_{kv}^{\prime\sigma} \right\rangle \tag{1.30}$$

where the coefficients f_{kv}^{σ} represent the occupations of KS states (labeled by k-point, band, and spin indices), determined by the Fermi-Dirac distribution of the corresponding single-particle energy eigenvalues. This formulation allows for the Mott localization of electrons on certain atomic states while reducing the fractional occupancy of localized orbitals[162].

Rotationally invariant formulation:

The formulation in Eq. 1.29, while able to capture the essence of the LDA+U method, is not invariant under rotation of the atomic orbital basis set employed to determine the occupancy numbers $n_m^{i\sigma}$. Calculations using this functional are thus adversely impacted by an unfavorable dependence on the particular unitary transformation of the localized basis set employed to define the atomic occupations [Eq. 1.30]. Therefore, rotationally invariant formulation, the unitary-transformation invariant of LDA+U[165] is regarded as the most complete formulation of the LDA+U in which the electronic interactions are totally orbital dependent. A more general expression, adopted from the HF method, was given for E_{Hub} and E_{dc}:

$$E_{Hub}[\{n^i_{mm'}\}] = \frac{1}{2}\sum_{\{m\},\sigma,i} \{\langle m,m''|V_{ee}|m',m'''\rangle n^{i\sigma}_{mm'} n^{i-\sigma}_{m''m'''} + (\langle m,m'''|V_{ee}|m',m'''\rangle - \langle m,m''|V_{ee}|m''',m'\rangle) \times n^{i\sigma}_{mm'} n^{i\sigma}_{m''m'''}\} \tag{1.31}$$

$$E_{dc}[\{n^i_{mm'}\}] = \sum_i \left\{ \frac{U^i}{2} n^i(n^i-1) - \frac{J^i}{2}[n^{i\uparrow}(n^{i\uparrow}-1) + n^{i\downarrow}(n^{i\downarrow}-1)] \right\} \tag{1.32}$$

In Eq. 1.31, the V$_{ee}$ integrals describe electron-electron interactions that are depicted as the integrals of the Coulomb kernel on the wave functions of the localized basis set (such as d atomic states), denoted by the index m:

$$\langle m,m''|V_{ee}|m',m'''\rangle = \int d\mathbf{r} \int d\mathbf{r}' \psi^*_{im}(\mathbf{r})\psi_{im'}(\mathbf{r}) \frac{e^2}{|\mathbf{r}-\mathbf{r}'|} \psi^*_{im''}(\mathbf{r}')\psi_{im'''}(\mathbf{r}') \tag{1.33}$$

Assuming that atomic (e.g., d or f) states are chosen as the localized basis, these integrals can be factorized in radial and angular contributions. Thus, matrix elements of operator V$_{ee}$ can be expressed via complex spherical harmonics and effective Slater integral parameters F^k:

$$\langle m,m''|V_{ee}|m',m'''\rangle = \sum_k a_k(m,m',m'',m''')F^k \tag{1.34}$$

where k = 0,2,......,2l (l being the angular quantum number of the localized manifold with -l $\leq$ m $\leq$ l). The a$_k$ represents the angular factors and corresponds to the products of Clebsh-Gordan coefficients:

$$a_k(m,m',m'',m''') = \frac{4\pi}{2k+1} \sum_{q=-k}^{k} \langle lm|Y_{kq}|lm'\rangle \langle lm''|Y^*_{kq}|lm'''\rangle \tag{1.35}$$

where Y_{kq} are complex spherical harmonics. The quantities F^k are the (Slater) integrals involving the radial part of the atomic wave functions R$_{nl}$ (n indicating the atomic shell they belong to).

For d electrons, only F^0, F^2, and F^4 are required to calculate the V$_{ee}$ matrix elements, while f electrons also need F^6. The effective Coulomb and exchange interactions, U and J, can be calculated as atomic averages of the corresponding Coulomb integrals over the localized states of the same manifold (in this example atomic orbitals of fixed l), which is consistent with the definition of the dc term [Eq. 1.32] as the mean-field approximation of the Hubbard correction (Eq. 1.31). For d orbitals it is easy to obtain:

$$U = \frac{1}{(2l+1)^2} \sum_{m,m'} \langle m, m' | V_{ee} | m, m' \rangle = F^0 \tag{1.36}$$

$$J = \frac{1}{2l(2l+1)} \sum_{m \neq m', m'} \langle m, m' | V_{ee} | m', m \rangle = \frac{F^2 + F^4}{14} \tag{1.37}$$

A simpler formulation:

However, a simplified formulation that maintains rotational invariance, provided by Dudarev et al., is based on the full rotationally invariant formulation with fully orbital-dependent electronic interactions and has been shown to be equally effective[164]. This is accomplished by keeping only the lowest order Slater integrals F^0 and ignoring all the higher order ones: F^2 = F^4 = J = 0. This simplification is equivalent to assuming that $a_0(m,m',m'',m''') = \delta_{m,m'}\delta_{m'',m'''}$. Using these conditions in Eqs. 1.31 and 1.32, one easily obtains:

$$\begin{aligned} E_U[\{n^{i\sigma}_{mm'}\}] =& E_{Hub}[\{n^i_{mm'}\}] - E_{dc}[\{n^i\}] \\ =& \sum_i \frac{U^i}{2} \left[(n^i)^2 - \sum_\sigma Tr[(\mathbf{n}^{i\sigma})^2] \right] - \sum_i \frac{U^i}{2} n^i(n^i - 1) \\ =& \sum_{i,\sigma} \frac{U^i}{2} Tr[\mathbf{n}^{i\sigma}(1 - \mathbf{n}^{i\sigma})] \end{aligned} \tag{1.38}$$

Due to its dependency on the trace of occupation matrices and on their products, the reduced functional in Eq. 1.38 still maintains the rotational invariance of the one in Eqs. 1.31 and 1.32. In contrast, this formulation loses the formal similarity to the HF energy functional and only one interaction parameter (U^i) is required to express the corrective functional. As a result of the simplified LDA+U approach's spin-diagonal form in Eq. 1.38, it has become common practice to assign the Coulomb interaction U an effective value that includes the exchange correction, U$_{eff}$ = U–J[164], where the "J" parameter is the exchange interaction term that takes into account Hund's rule coupling.

Optimizing the U value

LDA+U largely depends on the numerical value of the U_{eff} (referred to as "U" for simplicity). The value of U can either be theoretically computed or semiempirically adjusted to fit the experimental electronic structure. However, the semiempirical way of determining the U parameter is unable to capture changes in the on-site electronic interaction under changing physical conditions as well as the dependence of U on the volume, structure, or magnetic phase of the crystal. As an alternative, Hubbard U can be determined from first principles[166], using a self-consistent method such as through a linear response method as presented by Cococcioni et al.[167]. The choice of the optimum U value can be greatly influenced by the parameters used in DFT calculations, such as pseudopotentials, basis sets, cutoff energy, and k-point sampling. In addition, the used exchange-correlation functionals (LDA or GGA), and the fitted experimental characteristics all affect U value[168]. Moreover, due to the high computational cost of ab initio calculations of U as well as the fact that computed U is not always superior to empirical ones, semiempirical tuning is found to be the most widely used method by researchers. However, in this practice, caution should be exercised while using the semiempirical approach.

Successes and failures of DFT+U:

The fundamental benefit of the DFT+U approach is its easy implementation on the existing DFT codes, which results in a little increase in computational complexity over the standard DFT computations. It is easier in terms of theoretical formulation and practical implementations with significantly reduced computational cost when compared to other corrective approaches like the hybrid functionals and post-Hartree-Fock methods. Moreover with almost the same predictive power, it can even capture features of certain materials that cannot be captured by other higher-level or precise calculations. In addition to electronic structure, the U correction can improve the description of physical properties such as magnetic and structural characteristics of correlated systems.

However, one of the shortcomings of the DFT+U method is its failure to accurately anticipate the characteristics of systems with more delocalized electrons, such as metals. Although theoretical U calculation methods exist, they have much higher computational costs than semiempirical methods. On the other hand, despite the convenience of the semiempirical tuning of U, Hubbard correction's potential cannot be completely utilized, since it cannot be used to study systems with variations of on-site electronic interactions. In order to realize the full potential of the U correction, further advancements to the ab initio calculation of U are thus still needed, with lower computational costs.

1.7 Organization of thesis

The thesis consists of five chapters and has been organized in the following framework:

Chapter 1 begins with a succinct backdrop of the study. The next section of this chapter provides an overview of strongly correlated materials, including Mott-Hubbard and charge-transfer insulators. After that, it provides a quick review of 2D magnetic TMC and oxide heterostructures, two classes of strongly correlated materials. We have also included a brief history of magnetism in solids and the exchange interactions that mediate the magnetic ordering in order to provide some understanding of magnetism in solid-state systems. The concept of SOC has then been explained, with emphasis placed on the Rashba effect and its emergence in oxide heterostructures, followed by a short description of SOC-driven topological states, particularly the quantum anomalous Hall effect (QAHE). Towards the end of chapter 1, the theoretical background of various computational methods useful in understanding the calculation of results presented in this thesis has been provided.

Chapter 2 infers to the ab initio study of electronic and ground state magnetic properties in bulk and layered transition metal chalcogenides. In this context, the first section of this chapter investigates the electronic structure and magnetic ordering in triclinic $CuSeO_3$. The electronic structure suggests that $CuSeO_3$ in the triclinic phase is a charge-transfer insulator. We find the non-collinear antiferromagnetic configuration as the ground-state magnetic ordering. This can be attributed to the hybridization of Cu-d and O-p orbitals, giving rise to Cu-O-Cu superexchange interactions. We observe a spiral spin texture in the reciprocal space with a finite out-of-plane spin component. Spintronics of such non-collinear antiferromagnetic charge transfer insulating states is a relatively new and rapidly developing field of physics. In the following section of this chapter, the vdW layered transition metal ternary chalcogenide CoAsS with strong electron correlations is explored for its potential in spintronics. The dynamically stable CoAsS monolayer via its rich magnetic and electronic phase diagram has been demonstrated as a quasi-2D magnetic material. Because of the broken time-reversal symmetry and SOC, a topological state with a non-trivial Chern number is revealed at the critical Coulomb parameter using Kubo's approach. These results make the CoAsS monolayer very appealing for low-power-consumption nanoelectronics and spintronics.

Chapter 3 focuses on the emergent phenomena in perovskite oxide heterostructures based on polar perovskite oxide $LaVO_3$ (LVO). In this regard, the first section of the chapter explores the electronic properties in the heterostructure between a Mott insulator LVO and a band insulator $SrTiO_3$ (STO) with two distinct orientations (001) and (111). The electronic structure confirms that this heterointerface comprising two bulk insulators is n-type metallic in both orientations. Because of the peculiar orbital reconstruction at the two interfaces, we notice the difference in orbital occupation as well as orbital degeneracies. Furthermore, the Fermi surface reveals fourfold/sixfold symmetry as well as the presence/absence of open orbits in the (001)/(111) orientations. Thus, unique orbital-occupation and degeneracies due to orbital reconstruction as well as symmetry of Fermi surface highlights the important role played by crystal field in determining the electronic properties in LVO/STO heterostructure. In the subsequent section of this chapter, we have examined the (001) and (111) surfaces of polar perovskite oxide $KTaO_3$ (KTO) terminated with the Ta atoms for electronic and spintronic properties. We observed the presence of 2DEG with parabolic bands near the Fermi level at both the surfaces of KTO. The distribution of 2DEG is primarily contained in the surface layers of KTO in the 5d orbitals of Ta atoms. Due to the significant SOC of Ta atoms and the breaking of inversion symmetry at the surfaces, the Rashba spin splitting is visible in the bands. The spin texture on the Fermi surface and constant energy contours corroborate the 2D nature of the Rashba spin splitting on the (001) surface, While a complicated spin structure is seen on the surface of (111)-KTO. The final section of this chapter is devoted to the emergent properties in polar-polar heterostructure of perovskite oxides LVO and KTO depending on the crystal orientation. The charge transfer from the surface layers to the interfacial region due to the electronic reconstruction mechanism results in high carrier density 2DEG. Momentum-dependent Rashba spin splitting is seen in the electronic bands originating from the symmetry-breaking electric field. We demonstrate the orbital dependence of the Rashba effect in this heterostructure on account of orbital reconstruction at the interface. Spin-splitting is larger at the crossing regions of the d_{xy} and $d_{xz/yz}$ sub-bands. Further, the spin texture of the Rashba-split bands highlights the complexity of the orientation-dependence in the LVO/KTO heterostructure.

Chapter 4 is based on a theoretical understanding of high-mobility, conducting, and spin-polarized 2DEG at the EuO/TaO_2 interface of a ferromagnetic insulator EuO and non-magnetic polar perovskite KTO. The presence of proximity-induced Zeeman exchange splitting and the Rashba spin-orbit field in the EuO/KTO superlattice warrants a thorough examination of the system's detailed electronic band structure to look for the possibility of non-trivial quantum phenomena. 2DEG is confined on the KTO side particularly at the interfacial TaO_2 layer in the d_{xy} orbitals of Ta due to orbital reconstruction as confirmed by distributions of spin and charge density. The substantial exchange splitting (0.73 eV) between the two spin channels of interfacial Ta-5d_{xy} orbitals due to the proximity effect of ferromagnetic EuO results in a spin-polarized 2DEG at the interface. The band crossing points between the majority and minority spin bands open a gap when SOC is turned on. The large spikes of the Berry curvature at the momenta of SO-induced gaps and integral Chern number demonstrate the non-trivial band topology. We observe the Rashba-type spin texture of the bands having the SO-induced gap showing single spin winding of electron spin with opposite chirality without noticing the conventional Rashba splitting in the bands. The magnetic easy axis is perpendicular to the interfacial plane. Hence our findings suggest that EuO/KTO system has potential in low-power quantum electronics, spintronics, and spin-orbitronics.

The final chapter, **chapter 5**, concludes this thesis by summarising the key findings of the different studies presented in the individual chapters. It also provides a prospective future research outlook by steering the characteristics of various 2D materials and probing further emergent phenomena at the interface of oxide heterostructures for spintronic applications.

CHAPTER 2

Electronic and magnetic properties of 3d transition-metal chalcogenides

"If you thought that science was certain —well, that is just an error on your part."

Richard Feynman

2.1 Non-collinear antiferromagnetic insulating state in triclinic $CuSeO_3$

2.1.1 Introduction

Due to the unusual features that result from highly correlated d-band electrons, transition metal compounds such as oxides and chalcogenides have recently gained interest among the scientific community. Electronic correlations are expected to be particularly strong in 3d transition metals and weaken as one moves to 4d, and 5d transition metals due to an increase in the size of the d orbitals. The electronic behavior of these compounds is also significantly influenced by the p states of the anions. Depending on the relative strength of Coulomb interaction of the TM 3d electrons (U_{dd}) and the charge-transfer energy between TM-3d and anion-p states (Δ_{CT}), two types of insulators, namely, Mott-Hubbard and charge-transfer insulators are realized[1,169,170]. In addition to their intriguing electronic characteristics, TM compounds also manifest novel magnetic states arising from partially filled d bands on the TM ions. The various magnetic states include ferromagnetism, antiferromagnetism, multiferroicity, etc[171–176]. Furthermore, unusual long-range magnetic orderings, such as non-collinear states can be produced by magnetic frustration, which can result from either the geometry of the crystal lattice or from the competition between distinct magnetic interactions.

Recently, copper-based materials such as $CuFeO_2$[177–182] and Cu_2OSeO_3[183–188] have shown potential as spintronics materials due to their coupled magnetic order with electronic degrees. So far, three structural phases (i.e. orthorhombic, triclinic, and monoclinic) are reported for $CuSeO_3$[189,190]. There are several reports on monoclinic and orthorhombic phases of $CuSeO_3$ suggesting the presence of anisotropic exchange interaction along with an additional exchange term beyond the coupled linear tetramer model. Such interaction causes helical spin texture in monoclinic $CuSeO_3$ with a transition to the induced ferromagnetic state under the application of an external magnetic field above 40T at 1.6K[191]. A ferromagnetic ground state can be stabilized below 25K, by interchanging "Cu" and "Se" atoms ($CuSeO_3$ to $SeCuO_3$), keeping the crystal symmetry the same[192–195]. Some reports suggest that $SeCuO_3$ possesses antiferromagnetic ordering with T_N = 7K due to intertetramer coupling in the system[196,197]. The orthorhombic phase of $CuSeO_3$ shows a ferromagnetic state at $T_C \approx 26K$ in an applied magnetic field of around 1T[198,199]. Although the monoclinic and orthorhombic phases are thoroughly investigated by various groups, there is a lack of investigation on the triclinic phase of $CuSeO_3$.

In the present work, we have explored the ground state magnetic ordering and electronic structure of $CuSeO_3$ in the triclinic phase. The strong electron correlations in the 3d orbitals of Cu drive the system to an insulating state. The band gap between the d orbitals of Cu and the p orbitals of O is understood to be a charge-transfer gap. Furthermore, the hybridization between the Cu-3d orbitals and O-p orbitals results in the superexchange interactions responsible for the stability of the antiferromagnetic ordering. The lowest energy non-collinear antiferromagnetic configuration results from the competition between various magnetic orderings. The spiral magnetic spin texture in the reciprocal space further makes this material desirable for spintronic applications.

2.1.2 Computational methodology

Electronic and magnetic properties of triclinic $CuSeO_3$ were investigated using DFT within Vienna Ab initio Simulation Package (VASP). To account for the exchange-correlation effects, Perdew-Burke-Ernzerhof revised for solids (PBEsol) functional was used within GGA[200] with projector augmented wave (PAW) potentials[201,202]. A kinetic energy cut–off of 550 eV was used for the plane wave basis set. For geometry relaxation and static calculations, the DFT+U method was employed. In the DFT+U method, Hubbard parameter U was used to account for the strong on-site Coulombic interactions between localized 3d electrons of Cu within Dudarev's approach[164] where only the difference U_{eff} (U–J) is meaningful. A value of 10 eV was kept fixed for U_{eff} (U-J) for 3d orbitals of Cu. $9 \times 9 \times 9$ k-point mesh with gamma centered scheme was used for relaxation and static calculations. For the density of states (DOS) calculation, an $11 \times 11 \times 11$ k-point mesh was used. To find the ground state magnetic ordering, spin-polarized and non-collinear SOC calculations were performed for collinear and non-collinear magnetic structures, respectively. The spin texture in the reciprocal space was calculated with PyProcar code[203].

2.1.3 Magnetic properties

The calculated values of optimized lattice parameters of triclinic $CuSeO_3$ are listed in Table 2.1. To explore the ground state magnetic ordering, we calculated the total energy of the $CuSeO_3$ assuming the different spin configurations such as ferromagnetic, ferrimagnetic, and collinear as well as non-collinear antiferromagnetic orderings. Two different antiferromagnetic configurations with Cu spins arranged in a non-collinear fashion were compared for relative stability. One is termed AFM (NC)-I in which the spins of Cu atoms lying in (100) planes are non-collinear AFM while there is interplanar AFM coupling between the adjacent planes along the 'a' axis of the crystal. The second one is termed AFM (NC)-II, in which the Cu spins in (010) planes are non-collinear AFM and there is interplanar AFM coupling between the adjacent (010) planes along the 'b' axis of the crystal. Magnetic structures depicting the AFM (NC)-I and II configurations are shown in Fig. 2.1 (a) and (b), respectively. Calculations of total energy reveal that AFM (NC)-II has the lowest energy and thus is the most stable and hence taken as the reference configuration (E_0 = 0 eV). Table 2.1 gives the magnetic moment

Lattice constants (Å)	Magnetic moment on Cu ions (μ_B)
a=4.71727	corner atoms: 1.199 2.181 0
b=8.72755	edge-centered: 1.158 -2.181 0
c= 10.45690	interior atoms: -1.179 0 0

Table 2.1: Optimized lattice parameters (Å) of $CuSeO_3$ and the magnetic moment values on Cu ions located at different positions in the unit cell for AFM (NC)-II configuration.

values for the Cu atoms at various locations in the unit cell for the non-collinear ground state. Table 2.2 indicates the difference between the total energy for various magnetic configurations and the energy of the reference configuration. In addition, we find that the ferrimagnetic configuration is almost equally stable as the antiferromagnetic configuration in which Cu spins are arranged in a collinear manner. Further, we calculate the spin texture of the triclinic $CuSeO_3$ in the k_x-k_y plane as shown in Fig. 2.2. The arrows show the in-plane spin components and the color bar shows the out-of-plane spin component. The presence of the out-of-plane spin component in the form of spirals is seen in the spin texture. Therefore, antiferromagnetic ordering of non-collinear Cu spins with a spiral magnetic spin texture is revealed in triclinic $CuSeO_3$.

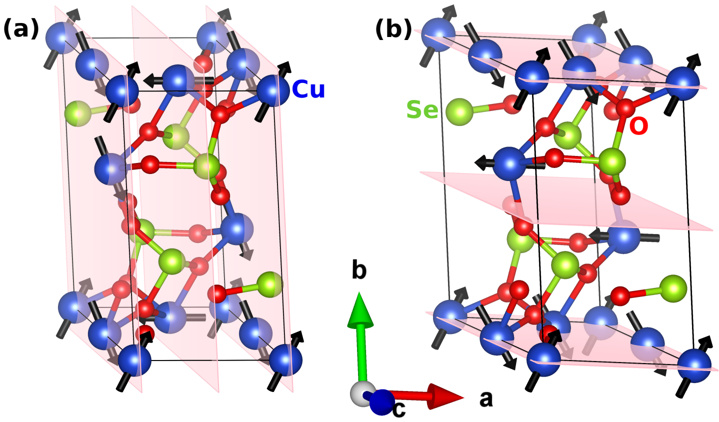

Figure 2.1: Magnetic structures of triclinic $CuSeO_3$ corresponding to non-collinear (a) AFM (NC)-I (b) AFM (NC)-II configurations. The corresponding atoms are marked in the figure.

Magnetic Ordering	ΔE (meV)
Non magnetic	157.254
Ferromagnetic	69.599
Ferrimagnetic	43.392
AFM(coll.)	43.377
AFM (NC)-I	0.76
AFM (NC)-II	0

Table 2.2: Comparison of total energies of various magnetic configurations with respect to the reference configuration (E_0 = 0 eV), ΔE (meV).

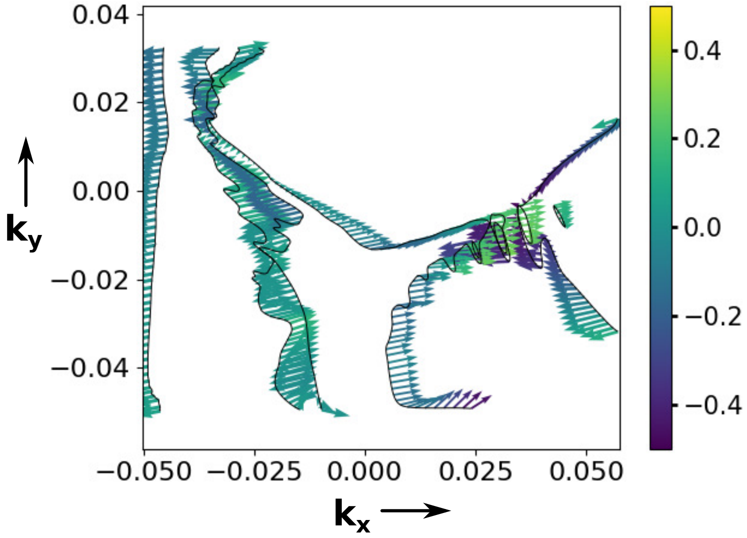

Figure 2.2: The spin texture of triclinic $CuSeO_3$ in the k_x-k_y plane, the color bar shows the out-of-plane spin component.

2.1.4 Electronic properties

To investigate the electronic behavior of triclinic $CuSeO_3$, the electronic band structure for the ground state magnetic configuration is calculated along high symmetry path X-Γ-Y|L-Γ-Z|N-Γ-M|R-Γ in the first Brillouin zone as shown in Fig. 2.3. Experimentally, $CuSeO_3$ is found to be an insulator with a band gap of 3.90 eV at room temperature[204]. For many transition metal oxides containing ions with partly filled d orbitals, DFT predicts metallic states as opposed to the experimentally found insulating states. The comparably weak spatial extension of 3d orbitals in the Cu leads to large electronic Coulomb repulsions and thus electronic correlations play an important role in this compound. Therefore, the electronic structure was calculated in the framework of DFT+U, where Hubbard parameter U accounts for the strong electron correlations between the localized 3d electrons. Without incorporating the Hubbard U parameter in the geometry optimization calculations, we observed the partially filled valence band with few empty states and an energy gap of 2.24 eV between the valence band and the next empty conduction band (even with higher U values) for the ground state magnetic ordering. When geometry optimization is performed including Hubbard U for Cu 3d electrons, an indirect band gap of 2.60 eV is opened between the valence and conduction bands indicating metal-to-insulator transition.

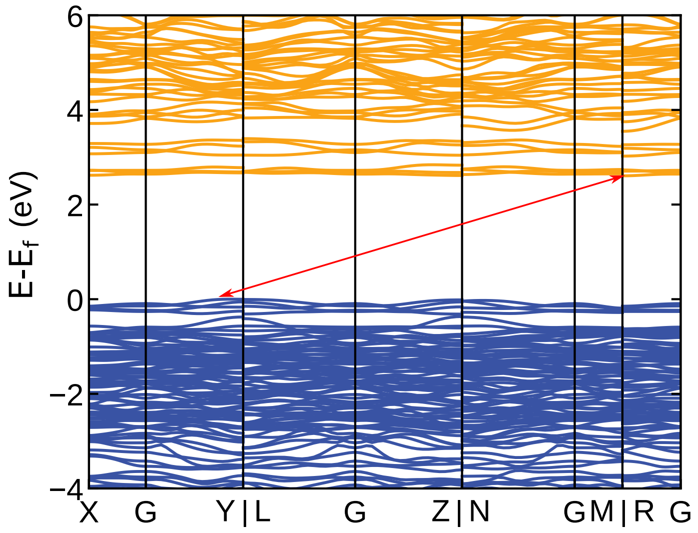

Figure 2.3: Electronic band structure of triclinic $CuSeO_3$ along the high symmetry path X-Γ-Y|L-Γ-Z|N-Γ-M|R-Γ in the ground state magnetic configuration.

To gain further information on the origin of the insulating state in the ground state magnetic configuration in this material, the total and orbital-projected DOS is shown in Fig. 2.4. As shown in the plot, the valence band is dominated by O-p states in contrast to the conduction band which is dominated by Cu-d states. Additionally, below the Fermi level, a Cu-d band is present beneath the O-p dominant band. Hubbard U opens a gap between the Cu-d and O-p bands by separating the occupied and unoccupied Cu d bands. As a result, the band gap can be described as between the p and d states implying that the triclinic $CuSeO_3$ is a charge-transfer insulator. Furthermore, Cu-d bands are present in the valence band throughout the entire range of O-p states, with a lower density of states and there is a small hybridization between Cu-d and O-p orbitals.

Similarly, O-p states with a lower density of states are present in the conduction band region in addition to the Cu-d orbitals. Thus, the hybridization of Cu-d and O-p orbitals gives rise to Cu-O-Cu superexchange interactions which are responsible for the stability of the non-collinear antiferromagnetic configuration. In addition to this, Se-p and O-p orbitals hybridize in the valence band region, and there is no direct hybridization of Cu-d and Se-p orbitals, which is also reflected in the crystal structure of CuSeO$_3$. Cu atoms are only directly linked to O atoms and there is no direct connection between Cu atoms and Se atoms, the linkage is instead mediated by O atoms.

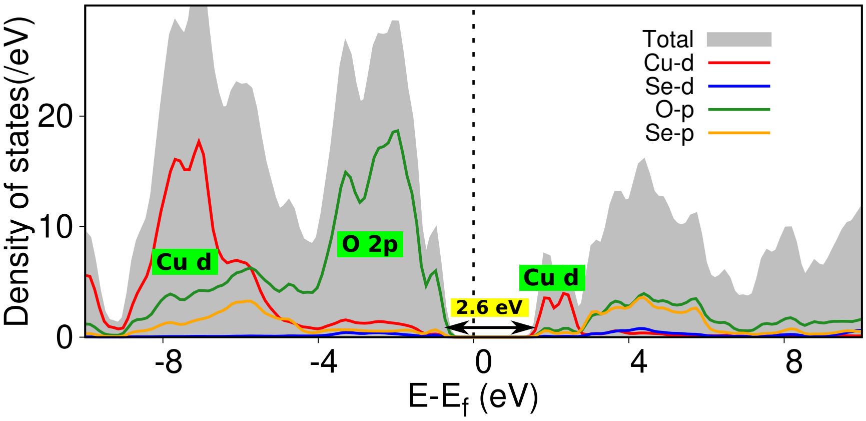

Figure 2.4: Total and orbital-projected DOS of triclinic CuSeO$_3$ in the ground state magnetic configuration.

2.1.5 Conclusions

In conclusion, we studied the triclinic phase of CuSeO$_3$ with DFT calculations for electronic and magnetic properties. The total energy analyses of the different spin configurations show that the magnetic structure with an intraplanar (in (010) planes) non-collinear AFM coupling of Cu spins and an interplanar AFM spin coupling (among (010) planes) is preferred. The band structure and DOS analysis reveal that it is a charge-transfer insulator with an energy gap of 2.60 eV between the occupied O-p and unoccupied Cu-d bands. The spin texture in the reciprocal space shows the spiral magnetic texture. Spintronics of such non-collinear antiferromagnetic charge-transfer insulating states is a relatively new and rapidly developing field of physics. Moreover, artificial lattice distortion in this material may even lead towards the realization of multiferroicity along with skyrmionic spin texture.

It should be observed that triclinic $CuSeO_3$ exhibits a bulk structure without any layers. Due to their exceptional features and enormous potential for scalable device applications, vdW materials have attracted a lot of scientific interest over the past few decades. They are composed of layers of covalently bonded atoms that are weakly held together by vdW forces. They can be exfoliated down to the monolayer limit and are capable of exhibiting emergent phenomena that are only observed in the 2D limit. In the following section, a transition-metal ternary chalcogenide CoAsS, characterized by vdW layers is investigated in both the bulk and monolayer limits.

2.2 Electronic and magnetic properties in layered ternary chalcogenide CoAsS

2.2.1 Introduction

Due to their peculiar physics, thin layered materials with vdW gaps are attracting a lot of attention as potential candidates for use in the areas of electronics, optoelectronics, catalysis, and spintronics[154,205–207]. A number of thin layered materials such as black phosphorus, hexagonal boron nitride, and transition metal dichalcogenides (TMDC)[208–213] have been proven good for electronic transport next to graphene. In their pristine state, TMDC monolayers are non-magnetic; they only acquire magnetic properties when exposed to external effects. This includes strain, electric field, doping with transition metal atoms, adsorption of non-metal atoms on the surface, and defects such as structural defects, adatoms, impurities, point defects, and vacancy defects[36,214–220]. The control of external factors for the intended magnetic ordering, however, restricts the applicability in device fabrication. We, therefore, require materials with intrinsic magnetic ordering, in which manipulating these extrinsic factors are not needed. It has been observed that VS_2 and VSe_2 monolayers possess intrinsic FM ordering in their pristine states[221] which can be enhanced with applied strain[60]. Similarly, materials with atomically thin layers, such as CrI_3, $CrBr_3$, and $CrCl_3$, have intrinsic ferromagnetism down to the monolayer limit[72,222–224]. A few other magnetic materials that fall within this category are $GdTe_3$[225], $MnSe_2$[74], and $RuCl_3$[226]. It is interesting to note that ternary layered chalcogenides offer a distinct class of materials with a vdW gap and can be exfoliated into a monolayer or a few layers[227,228]. Recently, an iron-based vdW material Fe_4GeTe_2 showing a practically room-temperature FM order, as well as a large magnetization, and strong conductivity has been realized[229]. Gong et.al[71] reported long-range intrinsic FM ordering in clean $Cr_2Ge_2Te_6$ atomic layers by using scanning magneto-optic Kerr microscopy. Further investigations of magnetic properties in 2D ternary materials include Fe_3GeTe_2[75,230], $FePS_3$[70,73], MAX_3 (M = V, Cr, Mn, Fe, Co, Ni; A = Si, Ge, Sn; X = S, Se, Te)[231], and $CrXTe_3$ (X = Si, Ge)[63,232].

In the present section, we have extensively studied the electronic, magnetic, and topological properties of layered ternary chalcogenide CoAsS with first-principles calculations. Including on-site Coulomb interactions with the Hubbard U parameter, we find magnetic ordering in bulk as well as monolayer CoAsS. As we increase U, the most stable magnetic ordering changes from AFM to FM. The dynamically stable CoAsS monolayer via its rich magnetic and electronic phase diagram has been demonstrated as a quasi-2D magnetic material. We have also investigated the possibility of the QAHE in the FM state of the CoAsS monolayer due to the broken time-reversal symmetry and SOC. A topological state with a non-trivial Chern number is revealed at the critical Coulomb parameter using Kubo's approach. At the critical U value, the interplay of electron-electron correlation, spin-orbit coupling, and low dimensionality gives the non-zero Chern number.

2.2.2 Methodology

The first-principles calculations based on DFT were performed using the PAW method as implemented within the VASP[201,202,233]. GGA with PBE exchange-correlation functional was used[200]. DFT and DFT+U formalisms were used to analyze the electronic and magnetic properties for comparison with and without SOC. In the DFT+U method, Hubbard U correction was used to account for strong on-site Coulombic interactions between localized 3d electrons of transition metal Co within Dudarev's approach,[164] where only the difference U_{eff} (U–J) is meaningful. A value of 0.89 eV was kept fixed for J, while U was varied to see the effect on electronic and magnetic properties. We have explored the influence of U in the range of 1-10 eV on the aforementioned properties. Such values of U for strongly correlated 3d orbitals of the Co atom have already been studied in the literature for other compounds of Co[234,235]. The structure optimization was done with the gamma-centered k-point mesh of $9 \times 9 \times 9$ for the bulk unit cell and $9 \times 9 \times 1$ for the monolayer unit cell to get more converged results. Self-consistent calculations of charge density were done with the same k-mesh. A kinetic energy cut-off of 400 eV was used for the plane-wave basis set. A vacuum of 19 Å was used to avoid interlayer interactions between periodic images in the case of the monolayer. Phonon dispersion spectra were calculated with PHONOPY package[236] and VASP code. Spin-polarized calculations were done to study the magnetic properties. Further, the Chern number and Hall conductivity calculations were performed using the VASPBERRY code[237] which is also interfaced with VASP.

To obtain the exchange interaction coupling constants, the total energy calculated for various magnetic ordered states are mapped onto Heisenberg Hamiltonian as given by

$$H = -\frac{1}{2}\sum_{i,j} J_{ij} S_i . S_j, \tag{2.1}$$

where J_{ij} is the exchange coupling constant between sites i and j; S_i and S_j are spin operators at sites i and j, respectively. The critical temperature for the magnetic transition is calculated using mean-field approximation with the equation as

$$T_C = \frac{2}{3}|J|\frac{z}{K_B}S(S+1), \tag{2.2}$$

where J is the magnitude of exchange coupling constant, z is the number of nearest neighbors of ion, K_B is the Boltzmann constant, and S is the spin operator.

2.2.3 Structural properties

The bulk interlayer vdW gap of non-centrosymmetric orthorhombic CoAsS (space group Pca2_1) is 3.80 Å, which is quite large, making experimental exfoliation into single or multilayers easy and practically feasible. Top and side views of the unit cell of the crystal structure of CoAsS are given in Fig. 2.5. In a layer, Co atoms are sandwiched between As and S atoms in a trigonal prismatic structure, with two S and one As atom above and below the plane of the Co atom. As seen in Fig 2.5, each Co atom is in a tetrahedral arrangement having bonds with two S and two As atoms. The optimized lattice parameters of the bulk unit cell are $a = 4.8390$ Å, $b = 7.1659$ Å, and $c = 6.3679$ Å. While for monolayer the corresponding values are $a = 4.8292$ Å and $b = 7.1582$ Å. On moving from bulk to monolayer, the lattice constant decreases by 0.2%. The three atoms Co, As, and S have Wyckoff positions of 'a' and a site point group of C_1 (non-centrosymmetric and polar).

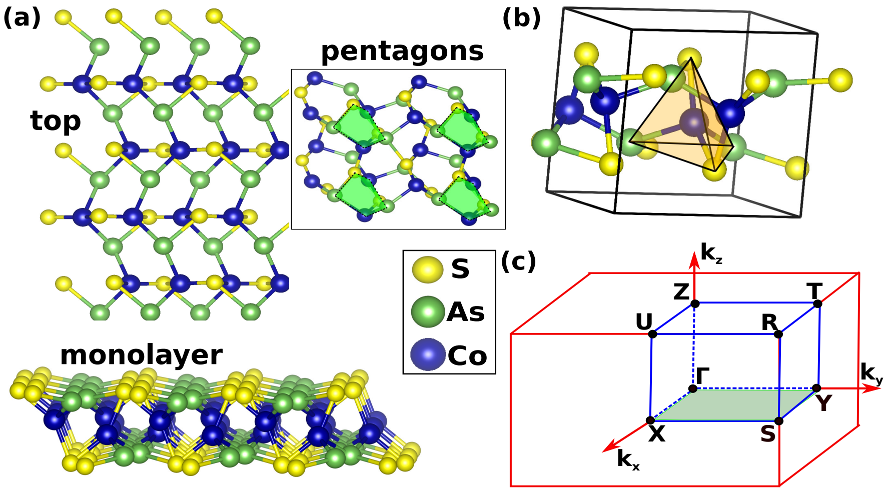

Figure 2.5: Crystal structure of orthorhombic CoAsS (space group $Pca2_1$) showing (a) the top view, the pentagonal building blocks, and the monolayer. (b) the side view of the CoAsS unit cell; the shaded portion highlights the tetrahedral arrangement of transition metal atom Co. Yellow, green, and blue colors represent S, As, and Co atoms, respectively. (c) first Brillouin zone with the high symmetry points marked on it; shaded portion represents the 2D Brillouin zone corresponding to the monolayer.

Due to the absence of vdW interactions, the distance between the upper and lower atomic planes of the S atom is reduced from bulk to monolayer by 0.12%. Nearest-neighbor intralayer Co-Co distance of 2.513 Å in bulk is decreased to 2.507 Å in monolayer. Co atoms are arranged in puckered pentagonal layers as shown in Fig. 2.5. It is important to note that the transition metal atoms are not directly bonded to each other and they are linked via S or As atoms in a zigzag pattern.

2.2.4 Phonon dispersion

In order to assess the dynamical stability, phonon dispersion calculations of optimized CoAsS structures have been carried out for bulk and monolayer. Phonon band spectra are calculated along the paths Γ-X-S-Y-Γ-Z-T-R-U-Z and Γ-Y-S-X-Γ for bulk and monolayer, respectively. As shown in Fig. 2.6 (a) and (b), the absence of imaginary vibrational frequencies at all wave vectors confirms the dynamical stability of this structure in both cases. In the case of the monolayer, a quadratic acoustic mode is also observed which confirms the 2D nature of the material.

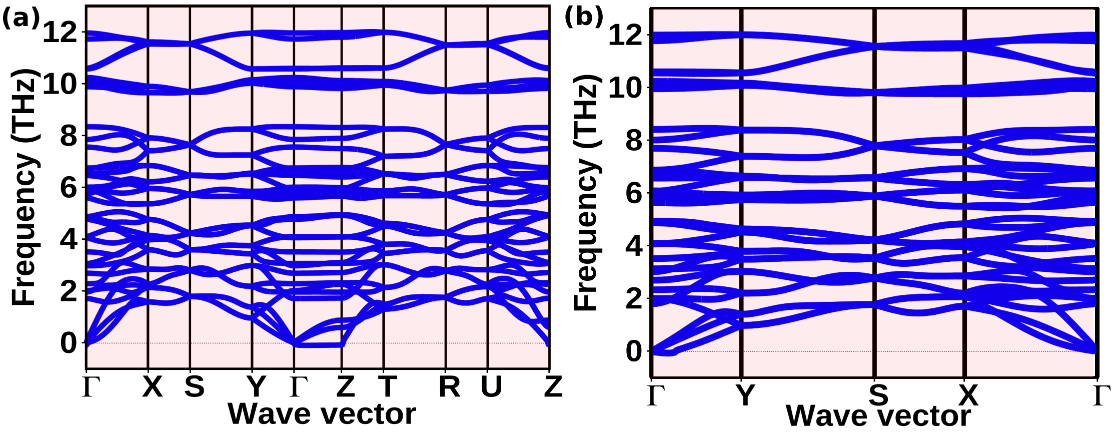

Figure 2.6: Calculated phonon dispersion spectra of CoAsS for (a) bulk and (b) monolayer, along the high symmetry paths Γ-X-S-Y-Γ-Z-T-R-U-Z and Γ-Y-S-X-Γ, respectively.

2.2.5 Electronic structure

To determine the electronic band structure of bulk and monolayer CoAsS, GGA and GGA+U methods are used with and without SOC. We observe that the material is magnetic in the ground state for both bulk and monolayer forms using the DFT+U method. Band structures for bulk along high symmetry path Γ-X-S-Y-Γ-Z-U-R-T-Z with DFT and DFT+U methods are shown in Fig. 2.7 (a) and (b), respectively. It is evident from Fig. 2.7 (a) that GGA predicts metallic behavior with a zero band gap for the bulk CoAsS. In this method, SOC has little impact because bands are almost degenerate both with and without SOC. Fig. 2.7 (b) depicts the plot for GGA+U for the bulk case and demonstrates no modification in terms of the band gap from Fig. 2.7 (a), but the bands are split and shifted by the addition of SOC. While the observed shifting of bands corresponding to the d orbitals of the Co atom is the only notable change in the bulk band structure, the monolayer, on the other hand, exhibits a variation in electronic structure depending on the U value and the magnetic state considered. Fig. 2.8 shows the electronic band structure of the monolayer in the non-magnetic state calculated along the high symmetry path Γ-Y-S-X-Γ, with and without SOC. Band structures for AFM-G (U = 6.8 eV) and FM (U = 8.2 eV) states are shown in Fig. 2.9 (a) and (b), respectively. In the single-layer CoAsS AFM-G state, an indirect band gap of 0.21 eV can be seen at U = 6.8 eV, and the system exhibits a metal-to-insulator transition (MIT). The conduc-

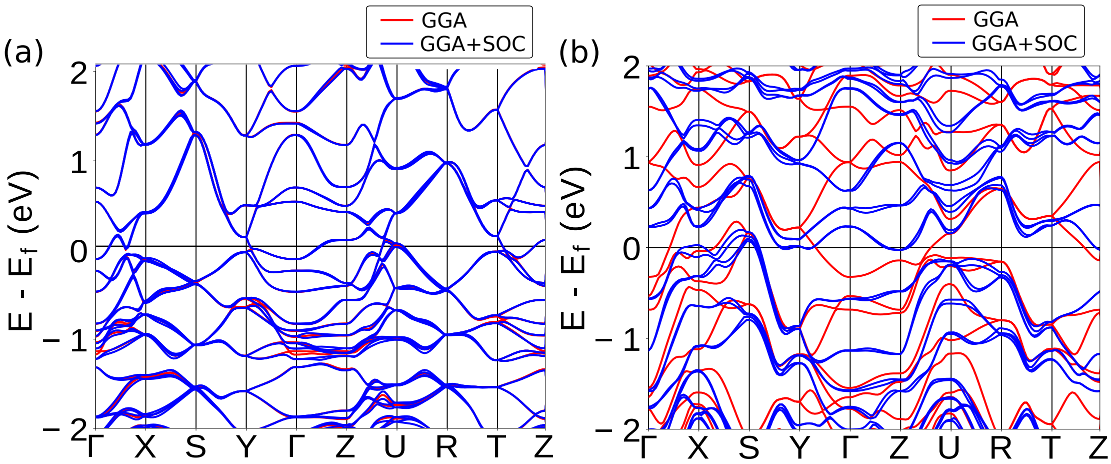

Figure 2.7: Electronic band structure of bulk CoAsS with and without SOC (a) in the NM state within DFT, (b) in the AFM-G state within the DFT+U approach using $U = 6.8$ eV. Blue and red colors represent the plots with and without SOC, respectively.

tion band minimum (CBM) is along the Y-S direction and the valence band maximum (VBM) is at the S point (see Fig. 2.9 (a)). This band gap is decreased as a result of the band-splitting when the effect of SOC is taken into account. SOC breaks the degeneracy and splits the band in high symmetry direction at the Γ-points in the metallic FM state (U = 8.2 eV) as seen in Fig. 2.9 (b).

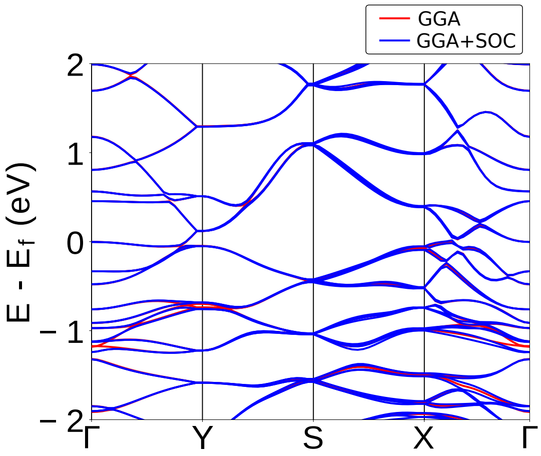

Figure 2.8: Electronic band structure of monolayer CoAsS with and without SOC in the NM state within DFT. Blue and red colors represent the plots with and without SOC, respectively.

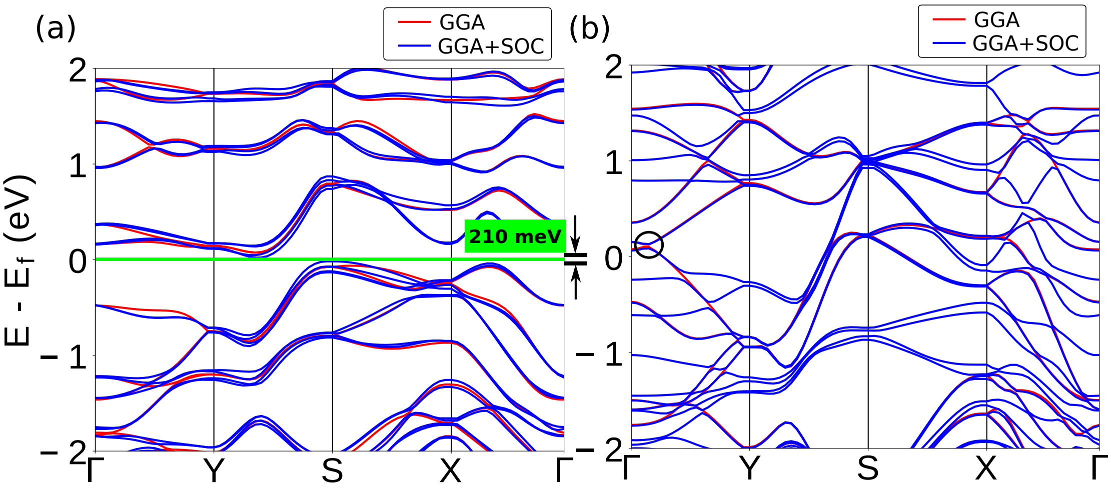

Figure 2.9: Electronic band structure of monolayer CoAsS with and without SOC (a) and (b) in AFM-G ($U = 6.8$ eV) and FM ($U = 8.2$ eV) states, respectively within the DFT+U approach. Blue and red colors represent the plots with and without SOC, respectively.

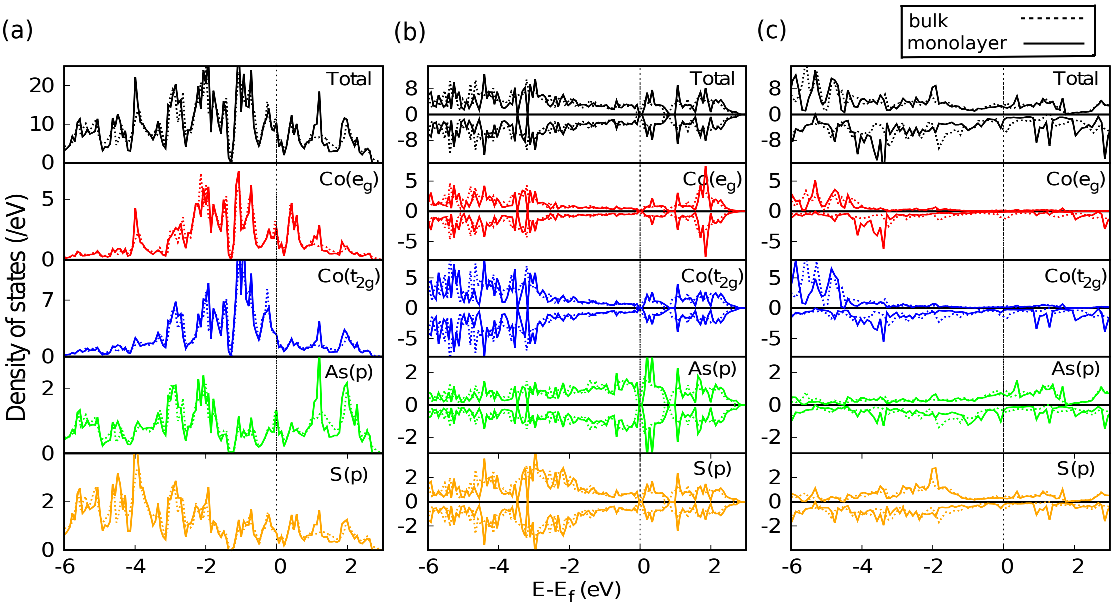

Figure 2.10: Total and orbital decomposed DOS plots for d orbitals (e_g and t_{2g}) of Co, p orbitals of As and S atoms for bulk and monolayer CoAsS. (a) Non-spin-polarized plot within the DFT approach in the NM state. (b) and (c) spin-polarized plot for AFM-G ($U = 6.8$ eV) and FM phase ($U = 8.2$ eV), respectively within DFT+U approach. The vertical black dashed line corresponds to the Fermi energy E_f.

To gain further insight into the role of atomic orbitals in the electronic properties of CoAsS, we have calculated the total and orbital decomposed density of states for d orbitals of Co, as well as p orbitals of As and S atoms for the non-spin-polarized and spin-polarized case within DFT and DFT+U approaches, respectively. Fig. 2.10 (a) shows the total and orbital decomposed non-spin-polarized DOS plot for bulk as well as the monolayer of CoAsS calculated within DFT. Due to the tetrahedral arrangement of Co atoms, we have plotted the contribution of t_{2g} and e_g orbitals of Co separately. The angle of the tetrahedron formed by As and S atoms around the Co atom is distorted from the standard tetrahedral angle of 109.5°, making it a deformed tetrahedron. It is evident from the non-spin-polarized DOS plot of Fig. 2.10 (a) that the distortion is large and there is a mixing of the t_{2g} and e_g orbitals. Due to fully filled t_{2g} and partially filled e_g orbitals, the contributions of t_{2g} and e_g are greater in valence band and conduction band, respectively. The presence of d orbitals of Co as well as p orbitals of As and S close to the Fermi level results in p-d hybridization. Fig. 2.10 (b) and (c) show spin-polarized DOS plot for the AFM-G phase ($U = 6.8$ eV) and FM phase ($U = 8.2$ eV), respectively for bulk and monolayer within DFT+U. Compared to Fig. 2.10 (a), d orbitals of Co shift away from the Fermi level due to the Coulombic repulsion. Exchange splitting is large in the FM ground state magnetic ordering for $U = 8.2$ eV as shown in Fig. 2.10 (c).

2.2.6 Magnetic properties

Without accounting for Hubbard U corrections, the lack of any local magnetic moments suggests that both the bulk and monolayer CoAsS are non-magnetic. Magnetic moments localized on Co d orbitals, along with a small moment on As atoms in the opposite direction to that on Co atom is observed in CoAsS when Hubbard U is taken into account for Co d orbitals. To determine the magnetic ordering in the ground state as a function of U, total energy analysis has been done for different magnetic structures. The various magnetic structures include NM, FM (intralayer FM interaction is assumed between the Co atoms), and three distinct AFM (intralayer AFM interaction between Co atoms is taken into account) configurations, namely AFM-A, AFM-C, and AFM-G are shown in Fig. 2.11 (a). Since interlayer coupling was not taken into account in the calculations for the bulk case, only intralayer aspects of the magnetic properties of the bulk and monolayer differ due to variations in the lattice constants and bond lengths. In

U	**NM**		**AFM-A**		**AFM-G**		**AFM-C**		**FM**	
———-	bulk	monolayer	bulk	monolayer	bulk	monolayer	bulk	monolayer	bulk	monolayer
4	−51.6034	−54.0863	−54.1603	−54.0857	−54.2142	−54.1440	**−54.2208**	**−54.1443**	−54.1335	−54.0866
5	−50.7942	−50.7260	−50.7700	−50.6621	−51.1569	−51.0895	**−51.2192**	**−51.1129**	−51.1629	−51.0379
6	−47.5225	−47.4611	−47.5900	−47.6564	−48.6412	**−48.5225**	**−48.6534**	−48.5168	−48.5870	−48.4562
6.8	−44.9880	−44.9318	−46.8247	−46.7141	**−46.9297**	**−46.8242**	−46.9054	−46.6845	−46.7213	−46.5831
8	−41.3620	−41.3098	−44.5630	−44.4376	−44.6247	−44.4876	**−44.8004**	**−44.6306**	−44.7458	−44.6197
9	−38.5469	−38.4941	−42.9232	−42.4602	−42.9398	−42.8000	−43.0241	−42.7428	**−43.1502**	**−43.0176**
10	−35.9841	−35.9345	−41.6042	−41.5153	−41.5056	−41.5153	−41.5137	−41.2506	**−41.7693**	**−41.6254**

Table 2.3: Total energy (in eV) for NM, AFM-A, AFM-G, AFM-C and FM states for bulk and monolayer CoAsS for U = 4 – 10 eV. Values in bold represent the most stable (lowest energy) state.

U		4	5	6	6.8	8	9	10
J	b	-43.66	-28.16	-33.20	-92.04	-27.31	63.03	127.79
	m	-28.8	-37.4	-30.3	-50.7	-5.4	137.35	187.40
T_C	b	672.36	433.66	511.28	1417.41	420.57	970.66	1967.96
	m	443.52	575.96	466.62	780.78	83.16	2115.19	2885.96

Table 2.4: Exchange coupling constant J (in meV) and critical temperature T_C (in K) for U = 4 – 10 eV for bulk (b) and monolayer (m) CoAsS.

the AFM-A configuration, the zigzag chain of Co atoms is arranged ferromagnetically and antiferromagnetically along the a- and b-axes, respectively, so that AFM ordering extends along the *b*-axis of the crystal. In AFM-G configuration, the zigzag chain of Co atoms is coupled ferromagnetically and antiferromagnetically along *b*- and *a*-axes, respectively, therefore the AFM ordering extends along the *a*-axis of the crystal. Whereas, in AFM-C configuration, Co atoms are coupled antiferromagnetically the along *a*- as well as the *b*- axes of the crystal. It is important to note that depending on the value of the Hubbard U parameter used, magnetic configurations vary in their relative stability. Table 2.3 contains the values of total energy for the various magnetic structures at varying values of U. It clearly shows that AFM interactions are more prevalent for U$\leq$ 8 eV, while for U $>$ 8 eV, FM interactions predominate.

We have also calculated the values of exchange coupling constant (J) and critical temperature (T_C) for U in the range of 4 – 10 eV for bulk and monolayer, from eq. (2.1)

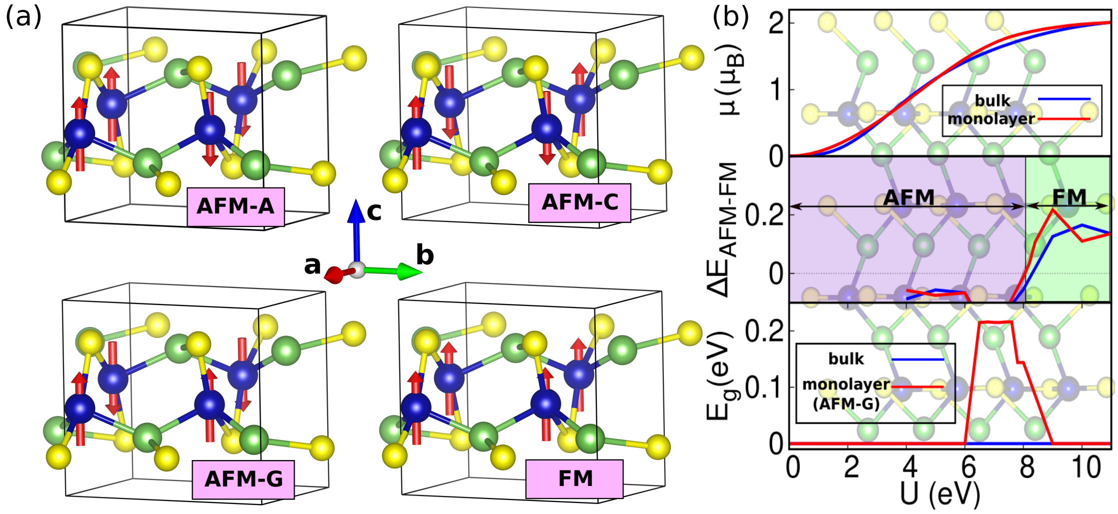

Figure 2.11: (a) Magnetic structures of CoAsS in AFM-A, AFM-C, AFM-G, and FM configurations. Up and down arrows on Co atoms represent up and down spin states, respectively. Variation of (b) magnetic moment on Co atom μ (in μ_B), the energy difference between FM and competing AFM phase ΔE_{AFM-FM}, and band gap (E_g) in eV with U for bulk and monolayer CoAsS.

and eq. (2.2), respectively, and the resulting values are listed in Table 2.4. As can be seen in Table 2.4, the value of J is negative before the AFM-FM transition point ($U = 8.2$ eV), indicating AFM order. While positive values of J after the transition point stipulate FM ordering in the material.

We have shown the variation of local magnetic moment on Co atom (μ), the energy difference between FM and the competing AFM phase ΔE_{AFM-FM} as well as band gap E_g for bulk and monolayer (AFM-G phase) in Fig. 2.11 (b). Magnetic moment increases with an increase in U value due to localization of d orbitals of Co. Band gap for bulk CoAsS is zero for all the U values and all the magnetic phases considered, whereas monolayer shows MIT at $U = 6.5$ eV in AFM-G phase. We observe that the value of the magnetic moment on the Co atom and the ground-state magnetic ordering depends to a great extent on the value of U used for the calculations. For a fixed value of U, the difference between energy values is of the order of meV. We have plotted the energy difference between FM and the competing AFM phase ΔE_{AFM-FM} with U value in Fig. 2.11 (b). For low values of U, the AFM configuration has the lowest energy with a negative value of ΔE_{AFM-FM}. However, at U = 8.2 eV, the energy of the

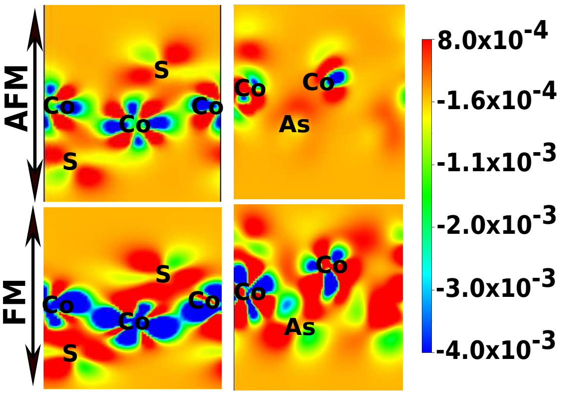

Figure 2.12: Charge density difference ($\Delta\rho_{AFM-FM}$) plots of CoAsS monolayer at $U =$ 4 eV (upper panel) and $U = 8.2$ eV (lower panel) in ac (left) and bc (right) planes; Co, As, and S atoms are marked on the plot. The color bar on the right side indicates a positive charge density difference (higher charge density for AFM state) with red color, while the rest of the colors stipulate negative charge density difference (higher charge density for FM state).

FM state decreases in comparison to the AFM state, causing a transition from AFM to FM configuration.

For scrutinizing the transition from AFM to FM state, we have calculated the charge density difference ($\Delta\rho_{AFM-FM}$) between AFM and FM configurations for $U = 4$ eV (AFM is ground state configuration) and $U = 8.2$ eV (there is AFM-FM transition and ground-state ordering is FM). Fig. 2.12 shows $\Delta\rho_{AFM-FM}$ for U = 4 eV (upper panel) and U = 8.2 eV (lower panel) in ac and bc planes, with the corresponding atoms Co, As, and S marked in the plots. The color bar on the right side shows a positive charge density difference (higher charge density for AFM state) by red color, while the negative charge density difference (higher charge density for FM state) is indicated by the rest of the colors. Comparing the left panel of Fig. 2.12 for charge density difference in the ac plane, it is inferred that for $U = 4$ eV, d orbitals of Co atoms are hybridized with p orbitals of S, which gives stability to AFM state through p-d superexchange interactions mediated by S atoms. For $U = 8.2$ eV, d_{xz} orbitals are filled in FM configuration and the electrons in these orbitals of Co interact with each other providing stability to FM configuration through direct d-d exchange interactions of Co atom.

2.2.7 Chern number and quantum anomalous Hall effect

In systems with broken time-reversal symmetry, SOC in the presence of some specific features in the band structure give rise to the QAH state. This state is characterized by non-trivial edge states that are governed by a non-zero Chern number. The broken time-reversal symmetry due to intrinsic magnetic properties and the gap created near the Γ point in FM state on including SOC raise the potential for hosting non-trivial topological states in CoAsS monolayer. To confirm the non-trivial topology of the CoAsS monolayer, we present in Fig. 2.13 (a) its Berry curvature distribution in the momentum space for FM configuration. It is clear from the plot that the CoAsS monolayer in the FM state with intrinsic magnetization in the xy-plane shows the development of Berry curvature along the $\pm z$-axis, perpendicular to the crystal plane. By performing the integration of Berry curvature over the entire Brillouin zone through Eq. (3), we find the Chern number C = –1. Such a non-zero Chern number (C = –1) and quantized charge Hall conductance σ_{xy} = –(e$^2/h$)C characterize intrinsic QAHE in the FM state of CoAsS monolayer. Chern number C = –1 indicates that CoAsS has one type of quantized current carrying spin along the edge known as chiral edge channel enlarged in the negative z-direction.[238,239], it is believed that 2D materials hosting a topological insulating gap with non-zero Chern number exhibit gapless chiral (one-direction motion of charge carriers) edge states inside the gap that connect the valence and conduction bands.

Further, we have also calculated the energy dependence of anomalous charge Hall conductivity in CoAsS monolayer using Eq. 2.3

$$\sigma_{xy} = -\frac{e^2}{\hbar}\sum_n\sum_k f_n(k)\Omega_n(k), \tag{2.3}$$

where $f_n(k)$ is the Fermi-Dirac distribution function, $\hbar$ is the reduced Planck's constant, and Ω_n(k) is the Berry curvature (from eq. (1.12)). The anomalous charge Hall conductivity vs $E - E_f$ is shown in Fig. 2.13 (b). For the sake of clarity, a magnified view of the quantized platform is shown as an inset in Fig. 2.13 (b), where one can easily find out the quantized nature of Hall conductance. We can consider the CoAsS monolayer has a quantized current carrying minority spin along the edges. Similar to our calculations, a non-zero Chern number and quantized charge Hall conductance are

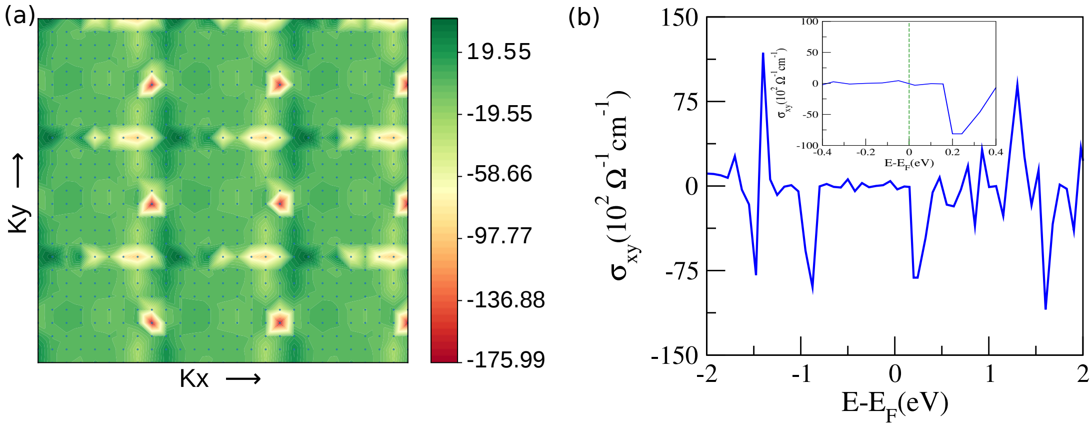

Figure 2.13: (a) Contour plot of the Berry curvature distribution of the valence bands projected to k_x-k_y plane and (b) variation of charge Hall conductivity with $E - E_f$ for FM state of CoAsS monolayer. The inset in (b) shows the magnified view of the quantized portion of Hall conductivity.

also observed in a few Dirac materials[240,241].

2.2.8 Conclusion

In conclusion, the structural, electronic, magnetic, and topological characteristics of the vdW layered ternary chalcogenide CoAsS with strong electron correlations in the orthorhombic phase are thoroughly investigated using DFT and DFT+U functionals. The dynamically stable CoAsS monolayer via its rich magnetic phase diagram has been demonstrated as a quasi-2D magnetic material. We also find the electronic properties to be dependent on the U value as well as the magnetic ordering. The inclusion of U predicted MIT in the CoAsS monolayer in AFM-G state at U = 6.5 eV. Because of the broken time-reversal symmetry and SOC, a topological state with a non-trivial Chern number is revealed at the critical Coulomb parameter using Kubo's approach. Therefore, our theoretical predictions make the CoAsS monolayer very appealing for low-power-consumption nanoelectronics and spintronics.

CHAPTER 3

Emergent properties in LVO-based perovskite oxide heterostructures

"What you learn from a life in science is the vastness of our ignorance."

David Eagleman

3.1 Introduction

Heterointerfaces of transition metal perovskite oxides with similar crystal structures manifest phenomena and functionalities lacking in their bulk constituents due to the reconstruction of the spin, orbital, lattice, and charge states at the interfaces. These phenomena encompass interfacial superconductivity, magnetoresistance, magnetic ordering, enhancement of spin-orbit coupling, magneto-electric coupling, and topological states in oxide heterostructures which open the window for scientific and technological advancement in this expeditiously emerging field[242]. The discovery of 2DEG at the polar/non-polar interface between two bulk insulators LAO/STO[84,243–252] has led to a rigorous study of heterointerfaces of perovskite oxides. Zhong et al. in Ref.[253] performed first-principles DFT calculations and derived tight-binding Hamiltonian for SOC effects at the LAO/STO interface demonstrating notable SOC properties arising from the multiorbital character. They found the biggest SOC effect at the crossing point of the xy and yz (or zx) orbitals as well as the possibility of k-cubic spin splitting in the lowest band around Γ point. In a similar study done by Khalsa et al.[254] using tight-binding-model matrix elements as well as ab initio methods, the Rashba spin-splitting is found to be dependent on atomic SOC strengths combined with processes (polar lattice distortions which alter the metal-oxygen-metal bond angle) in which t_{2g} electrons change orbital character when they hop between metal sites. Soon after various STO-based heterointerfaces hosting 2DEG and two-dimensional hole gas (2DHG) such as STO/LTO[255–257], $LaScO_3$ (LSO)/STO[258], $NdGaO_3$ (NGO) and STO[259] were reported.

3.2 Electronic properties in (001) and (111) LVO/STO heterostructures

Another STO-based oxide heterostructure LVO/STO with a polar perovskite LVO is investigated by Hwang[260] for configuration-dependent transport properties. LVO is a Mott-Hubbard insulator with a band gap of 1.08 eV[154]. It is a polar oxide with alternately charged $(LaO)^{+1}$ and $(VO_2)^{-1}$ planes along (001) direction and $(V)^{+3}$ and $(LaO_3)^{-3}$ planes along (111) direction. The polar/non-polar heterointerface LVO/STO between a Mott-insulator and a band-insulator has been examined for the (001) oriented n-type VO_2/LaO/TiO_2 and p-type VO_2/SrO/TiO_2 interfaces. LVO/STO (110) heterointerface lacking an ionic polar discontinuity has also been investigated. Out of the three interfaces, only the first is found to be conducting and exhibit metallic behavior. He et al. examined the transport characteristics of the compressively strained epitaxial films of two bulk Mott insulators, LTO (bulk gap 0.1 eV) and LVO, on an STO substrate[261]. He demonstrated that the metallic ground state in LVO/STO was qualitatively distinct from that in LTO/STO. Whereas conductivity in LTO/STO is related to the effects of strain-induced electronic structural alterations along with interface effects, metallicity in LVO/STO is interfacial in nature and most likely generated by polarity discontinuities. Moreover, in-plane and out-of-plane magnetoresistance studies were carried out to further explore the reason for the increase in resistivity in LVO/STO films at low temperatures. Even though intriguing phenomena have been demonstrated experimentally, this heterostructure has long lacked a theoretical underpinning.

In this section, we have studied the electronic characteristics at the interface between a Mott insulator (LVO) and a band insulator (STO) in (001) and (111) orientations. The n-type interfaces in this polar/non-polar HS system are $(LaO)^{+}/(TiO_2)^{0}$ and $(LaO_3)^{-3}/(Ti)^{+4}$ in [001] and [111] directions, respectively. The calculated total and Ti-3d orbital projected density of states for the two orientations provide information on the relative d-orbital occupancy at the interface sensitive to the crystalline orientation. Because of the peculiar orbital reconstruction at the two interfaces, we notice the difference in orbital occupation as well as orbital degeneracies. The Fermi surface calculated for the LVO/STO heterostructure emphasizes the variations in symmetry and the presence/absence of open orbits as a result of the orbital polarization and reconstruction in the two orientations.

3.2.1 Computational methodology

To explore the electronic properties in LVO/STO heterostructures with (001) and (111) orientations, first-principles calculations based on DFT implemented in VASP code were performed. To account for exchange-correlation effects PBEsol functional was used within GGA[200] with PAW potentials[201,202]. A kinetic energy cut-off of 520 eV was used for the plane wave basis[233]. For relaxation and static calculations, the Brillouin zone was sampled with a $6 \times 6 \times 1$ gamma-centered k-point grid. For the DOS calculations, $10 \times 10 \times 1$ k-point mesh was used. A stoichiometric thin film model with a vacuum on top of the LVO thin film on an STO substrate was taken into consideration to simulate the heterostructures. The heterostructure was modeled with 4 layers of LVO over the 9 layers of STO with TiO_2 /LaO (Ti/LaO_3) interface for the (001) ((111)) orientation. We employed thin film geometry with a vacuum region of 15 Å to avoid the interaction between adjacent slabs. To account for the electronic correlation between localized electrons of 3d orbitals of Ti and V and to correct the on-site Coulomb interaction, DFT+U calculations were performed using Dudarev's rotationally invariant approach (where only (U–J) is meaningful[164]. Here, U is the on-site Coulomb interaction between localized 3d electrons (Hubbard U) and J is the exchange parameter. Values of U = 5 eV and J = 0.64 eV were used for the Ti atom; U = 3 eV and J = 0 eV were used for the V atom.

3.2.2 Electronic structure

We have computed the total DOS in order to explore the electronic characteristics at the interface of LVO/STO heterostructure. Additionally, the DOS projected onto the 3d

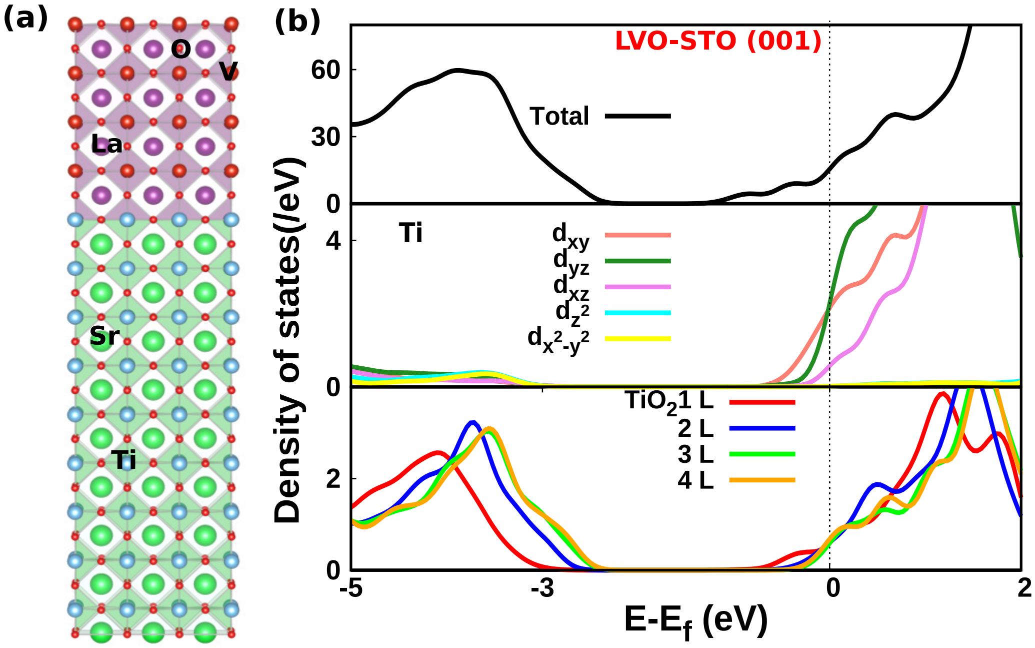

Figure 3.1: (a) Crystal structure and (b) The total and orbital-projected DOS onto the 3d orbitals of Ti atoms along with the layerwise contribution to the Ti-3d orbital-projected DOS from the first four TiO_2 layers (labeled as $1-4$) as we go away from the interface for (001)-oriented LVO/STO heterostructure. The atoms La, O, V, Sr, and Ti are marked in the figure.

orbitals of Ti atoms is calculated to get information about the relative d-orbital occupancy at the Fermi level as well as in valence and conduction band regions. The crystal structure of the LVO/STO heterostructure in the (001) orientation is depicted in Fig. 3.1 (a). For (001)-oriented LVO/STO heterostructure, total DOS confirms the conducting (n-type metallic) heterointerface of two oxide materials, which are insulators in bulk as evident from Fig. 3.1 (b). The DOS projected onto 3d orbitals of Ti atoms suggests that the electrons responsible for conductivity occupy d_{yz} and d_{xz} orbitals which hybridize to give orbital polarization along the z-axis and the effect is only slightly mitigated by d_{xy} orbitals. In addition, we estimated the layerwise contribution to the Ti-3d orbital-projected density of states and Fig. 3.1 (b) (lowermost panel) displays the contribution from the first four TiO_2 layers (labeled as $1-4$) as we go away from the interface. This suggests that the metallic partial DOS persists into deeper layers of STO. Further, the degeneracy between d_{yz} and d_{xz} orbitals for (001)-oriented LVO/STO heterostructure is broken.

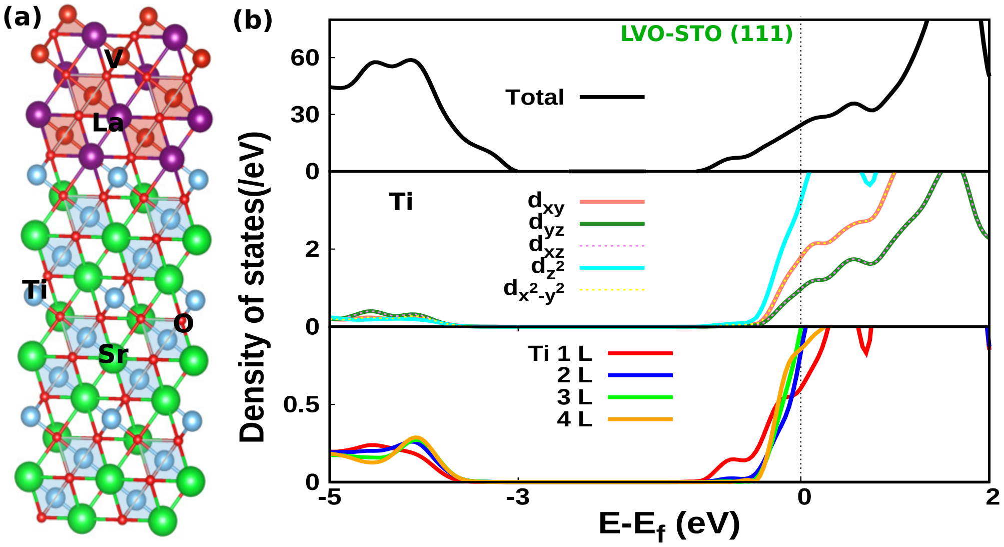

Figure 3.2: (a) Crystal structure and (b) The total and orbital-projected DOS onto the 3d orbitals of Ti atoms along with the layerwise contribution to the Ti-3d orbital-projected DOS from the first four Ti layers (labeled as $1-4$) as we go away from the interface for (111)-oriented LVO/STO heterostructure. The atoms La, O, V, Sr, and Ti are marked in the figure.

Fig. 3.2 (a) illustrates the crystal structure of the LVO/STO heterostructure in the (111) orientation. Total and orbital-projected DOS for (111)-oriented LVO/STO heterostructure in Fig. 3.2 (b) shows the conduction band crosses the Fermi level and valence band separated by a gap, demonstrating n-type conducting behavior. Further, the DOS projected onto the 3d orbitals of Ti atoms reveals that the contribution to the electronic states at the Fermi level comes from d_{z^2} and degenerate d_{yz} and d_{xz} orbitals. Also, there is contribution from the degenerate d_{xy} and $d_{x^2-y^2}$ orbitals to the states at the Fermi level. The different orbital-occupation and enhanced degeneracy in (111) orientation might be related to the orbital reconstruction due to the crystal field in this orientation. Furthermore, we determined the layerwise contribution to the Ti-3d orbital-projected DOS Fig. 3.2 (b) depicts the contribution from the first four Ti layers (labeled as $1-4$) as we go away from the interface, demonstrating that metallic partial DOS penetrates a significant portion of the bulk of STO.

3.2.3 Fermi surface

Next, we calculated the Fermi surface of (001)-oriented LVO/STO heterointerface in (001) plane. The Fermi surface plot as shown in Fig. 3.3 (a) reveals four-fold symmetry due to the crystal symmetry of LVO/STO heterointerface in (001) orientation. Open orbits present in the Fermi surface might be due to the broken degeneracy between the orbitals in this orientation. The Fermi surface calculated for (111)-oriented LVO/STO heterostructure in (111) plane (Fig. 3.3 (b)) shows the six-fold symmetry which is also related to the crystal symmetry in (111) orientation. As the cubic ABO_3 perovskite structure realizes a honeycomb lattice along the (111) direction.

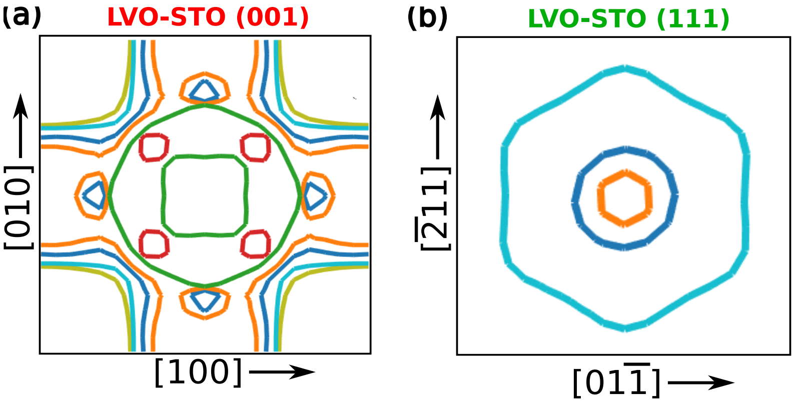

Figure 3.3: Calculated Fermi surface plots of (a) (001)- and (b) (111)- oriented LVO/STO heterostructures in (001) and (111) planes, respectively; where different colors represent different bands.

3.2.4 Conclusion

In conclusion, we have investigated the orientation dependence of electronic properties in polar/non-polar perovskite oxide HS LVO/STO with the n-type interface in (001) and (111) crystallographic orientations. The n-type interfaces in this polar/non-polar HS system are $(LaO)^{+}/(TiO_2)^{0}$ and $(LaO_3)^{-3}/(Ti)^{+4}$ in (001) and (111) directions, respectively. The electronic structure confirms the n-type metallicity in both orientations of this heterointerface comprising two bulk insulators. Because of the peculiar orbital reconstruction at the two interfaces, we notice the difference in orbital occupation as well as orbital degeneracies. Furthermore, the Fermi surface reveals fourfold/sixfold symmetry as well as the presence/absence of open orbits in the (001)/(111) orientations. Thus, unique orbital-occupation and degeneracies due to orbital reconstruction as well as symmetry of Fermi surface highlights the important role played by crystal field in determining the electronic properties in this heterostructure.

In addition to the STO substrate, the use of high-k 5d perovskite oxide, KTO, as a substrate material is currently grabbing attention in oxide heteroepitaxy. KTO has similarities with STO like simpler cubic structure, induced metallicity[262] as well as low-temperature superconductivity with carrier doping[115]. In addition to this, KTO has advantage over STO owing to its excellent mobility, and stronger SOC due to heavier element Ta providing opportunities for new emergent phases[263]. Therefore, in the subsequent sections, we have studied the KTO (001) and (111) surfaces, followed by the heterostructure between LVO and KTO in the (001) and (111) orientations for electronic and spintronic properties.

3.3 Rashba effect in 2DEG at KTO (001) and (111) surfaces

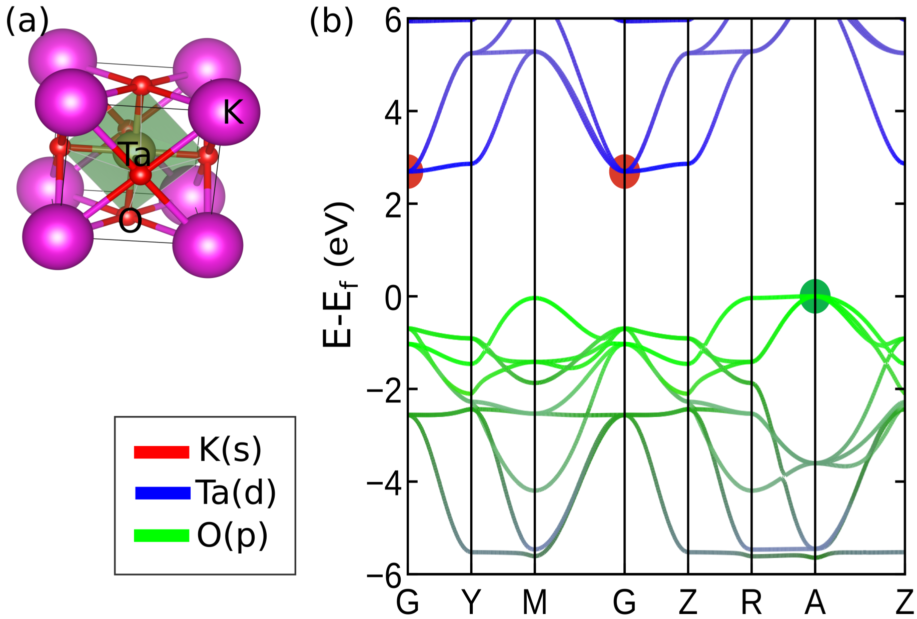

Figure 3.4: (a) Crystal structure of bulk KTO in cubic pm–3m space group with atoms K, Ta, and O marked on it. (b) Electronic band structure of bulk KTO along high symmetry path Γ-Y-M-Γ-Z-R-A-Z with orbital projection on the atoms.

KTO, which is a prototype of polar ABO_3 perovskite oxide is cubic at room temperature with space group Pm–3m. The ABO_3-type crystal structure of cubic KTO is shown in Fig. 3.4 (a). KTO is a wide-band insulator with a bulk gap of 3.64 eV[264]. An indirect band gap of 2.69 eV is obtained with CBM at the Γ point and VBM at the high symmetry point A in our calculations of the orbital-projected electronic band structure for bulk KTO as illustrated in Fig. 3.4 (b). The valence band is made up of O-p states, while the conduction band is made up of Ta-5d states. KTO is a polar perovskite oxide with the structural formula $A^{+}B^{5+}O_3$ consisting of stacks of alternating planes of charged layers $(KO)^{-1}$ and $(TaO_2)^{+1}$. A cleavage of polar perovskite oxides along the charged layers leads to an electrostatic instability termed "polar catastrophe" on the cleaved surfaces, and a charge compensation is required to stabilize these surfaces. This results in the formation of 2DEG/2DHG on the surface with TaO_2/KO termination which causes exciting and useful phenomena at the surface[13,113,114,265–267]. Along (111) crystallographic direction, KTO consists of stacks of alternating planes of charged layers $(Ta)^{+5}$ and $(KO_3)^{-5}$. 2DEG with topological properties at (111) surface of KTO was realized experimentally by Bruno et al.[268]. Moreover, the discovery of the Rashba effect in the 2DEG systems at the perovskite surfaces and interfaces has led to the possibility of tuning its properties by an external electric field[133]. The perovskites are characterized by the presence of high-Z elements and d electrons with strong SOC in contrast to their semiconductor counterparts. The tuning of the Rashba effect on the polar surface of the KTO was demonstrated by Shanavas et al. in 2014 by manipulating the 2DEG with an external electric field[116]. In this section, we have explored the surface electronic properties at the (001) and (111) polar surfaces of KTO terminated with Ta atom.

3.3.1 Computational methodology

The first principle calculations based on DFT were performed using the PAW method as implemented within the VASP[201,202,233]. GGA with PBE exchange-correlation functional was used[200]. Structure relaxation was performed with DFT calculations while electronic properties were investigated within DFT+U formalism with and without SOC. In the DFT+U method, Hubbard correction U was used to account for strong on-site Coulombic interactions between localized d electrons of transition metals Ta within Dudarev's approach[164] where only the difference U_{eff} (U-J) is meaningful. A value of 4 eV were kept fixed for U_{eff} (U–J) for d orbitals of Ta. The structure optimization was done with the gamma-centered k-point mesh of $6 \times 6 \times 1$ to get more converged results. Self-consistent calculations of charge density were done with the same k-mesh. A kinetic energy cut-off of 520 eV was used for the plane-wave basis set. The lattice constants and atomic coordinates were fully relaxed with the convergence criteria for total energy 10^{-3} eV. To simulate the (001) and (111) surfaces terminated by Ta layers, non-stoichimetric slab models with two symmetrical surfaces having thickness of 17 layers (8.5 unit cells) were considered. This corresponded to unequal number of alternate layers of $(KO)^{-1}$ and $(TaO_2)^{+1}$ for (001) surface. While, unequal number of $(Ta)^{+5}$ and $(KO_3)^{-5}$ layers for (111) surface was considered. A vacuum of 19 Å was used for slab models to avoid the interlayer interaction between the adjacent periodic images. SOC was considered in the second-variational method with magnetization along the (001) quantization axis as implemented within VASP. To calculate the energy contour plots of the spin texture in reciprocal space, PyProcar code was used[203].

3.3.2 KTO (001) surface

We examined the formation of 2DEG at the (001) polar surface of KTO with TaO_2 surface termination using first-principles electronic structure calculations. Fig. 3.5 (a) depicts the corresponding band structure along the high symmetry path Y-Γ-M, including SOC, with atomic projection on the atoms K, Ta, and O. The Fermi level is pinned inside the conduction band, and a gap is seen between the valence band and the conduction band, indicating the n-type conductivity at the (001) surface of band insulator KTO. As a result, the creation of 2DEG with nearly parabolic bands near the Fermi level accommodated in the Ta-5d orbitals is illustrated. Furthermore, layer-wise projected DOS on the atomic layers is evaluated in order to gain a better understanding of the distribution of 2DEG in the depth of the slab. The contribution to the states at the Fermi level comes from the TaO_2 layers, while KO layers have no contribution, as evidenced by the DOS projected on atomic layers (depicted in the background of the plot) in Fig 3.5 (b). The electrons responsible for metallic states are mostly accommodated in the two symmetrical TaO_2 surface layers, and their contribution continuously declines as we move toward the bulk of KTO. This 2DEG can be attributed to the electronic reconstruction mechanism at the surface due to the electrostatic instability at the cleaved polar surface. Due to the high SOC of the Ta atom and the breaking of spatial inversion symmetry at

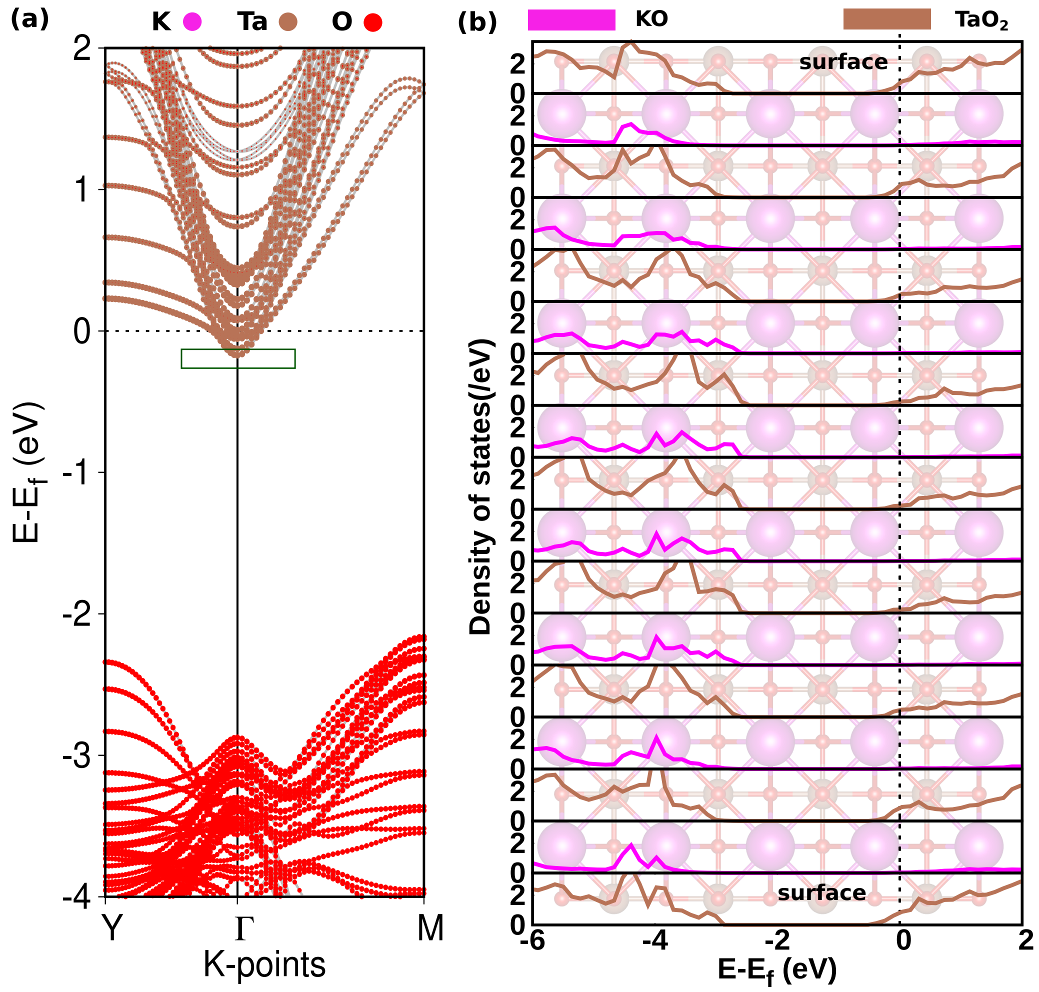

Figure 3.5: (a) Electronic band structure of KTO (001) surface with atomic projection on atoms K, Ta, and O along high symmetry path Y-Γ-M including SOC (b) Layer-wise projected DOS on the atomic layers shown in the background of the plot. The black dashed line indicates the Fermi level E$_f$.

the surface, Rashba spin splitting is visible in the bands. The lowest conduction band exhibiting Rashba splitting is marked in Fig. 3.5 (a).

Next, the electrostatic potential is determined for the (001) surface of KTO with TaO$_2$ termination using first-principles calculations as illustrated in Fig. 3.6. In its raw form, the electrostatic potential is computed with atomic-level resolution and thus oscillates rapidly within the unit cell. The green oscillating line represents the planar average of the electrostatic potential in the z-direction, perpendicular to the surface of

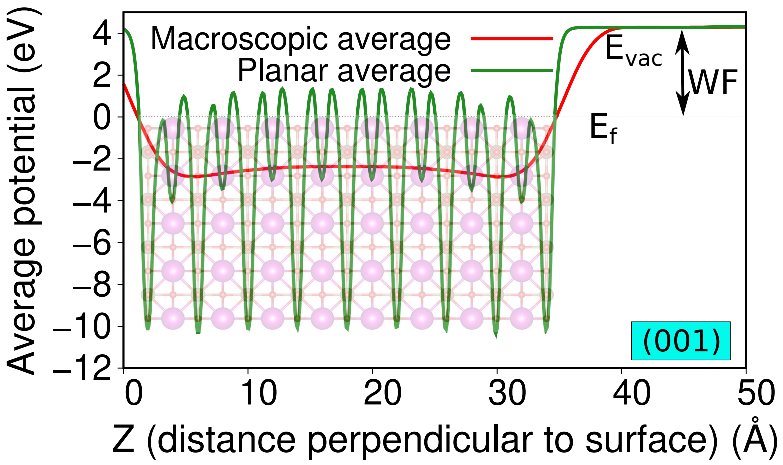

Figure 3.6: The planar average of the electrostatic potential (oscillating green curve) along the z-direction (perpendicular to the surface) and the macroscopic average of electrostatic potential (red curve) of (001) surface of polar KTO. The crystal structure is shown in the background; where magenta, brown, and red spheres represent K, Ta, and O atoms, respectively. The Fermi energy (E_f) is set to zero.

KTO. The macroscopic average or nanosmoothed electrostatic potential in the direction normal to the surface is also shown by the red curve. Fig. 3.6 displays the structure of the KTO (001) surface slab in the background. The macroscopic average potential is not constant throughout the slab, as can be seen in the plot. As we go away from the TaO_2 surface, the slope first rises, then as we approach the other TaO_2 surface, it descends due to the symmetrical TaO_2^+ layers on the opposing surfaces. A value of 4.2 eV has been determined for the work function, which is the difference between the vacuum level and Fermi energy.

The energy contour plots of the spin texture in the reciprocal space (k_x-k_y plane) for the KTO (001) surface have also been calculated in addition to the band structure. The color bar on the right depicts the modulus as well as the orientation of spin polarization, with up (red) and down (blue) spins. Fig. 3.7 (a)-(c) depicts the spin texture at the Fermi surface along the three cartesian axes (S_x, S_y, and S_z). The Fermi surface shows four-fold symmetry which is due to the crystal symmetry in the (001) direction. Similar plots of spin texture for the Rashba-split band (marked in Fig 3.5 (a)) at a cut corresponding to energy (E-E_f) = –0.2 eV along the three cartesian axes (S_x, S_y, and S_z) are presented in Fig. 3.7 (d)-(f). Only the in-plane S_x and S_y spin components are visible in the contour plots of the spin texture, while the out-of-plane S_z spin component is absent. The reverse

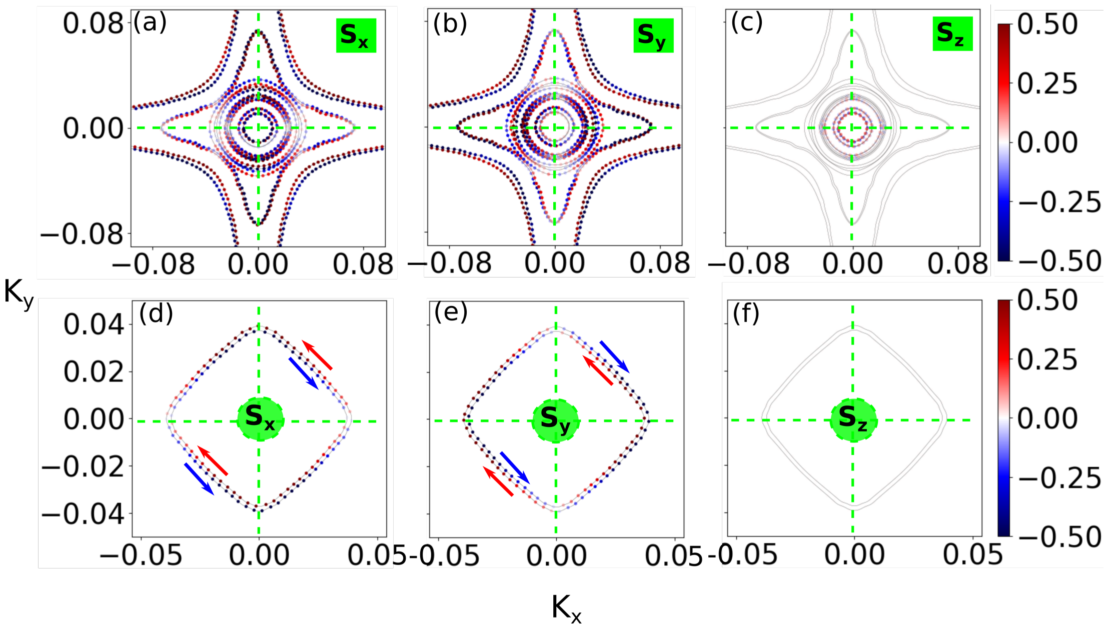

Figure 3.7: Constant energy contour plots of spin-texture (a)-(c) on Fermi surface (d)-(f) corresponding to a cut at energy (E-E$_F$) = –0.2 eV for each spin component along the cartesian axis (S$_x$, S$_y$, and S$_z$) calculated in k$_x$-k$_y$ plane for KTO (001) surface. The colors indicate the modulus as well as the orientation (up(red) or down(blue)) of the spin polarization.

spin orientation for the momentum-dependent spin-split band pair is visible in the spin-texture plots for the bands that exhibit Rashba splitting. A deeper analysis revealed that the S$_x$ component of the spins at the fermi surface is present along the k$_y$ direction but lacking along the k$_x$ direction, with the exception of the two innermost rings/bands. In a similar fashion, the S$_y$ component is present along the k$_x$ direction but missing along the k$_y$ direction. The horizontal and vertical green dashed lines in the plots indicate the two k$_x$ and k$_y$ directions, respectively. In contrast, the S$_z$ component in the k$_x$-k$_y$ plane is completely zero. In other words, spin-momentum locking, a characteristic of the Rashba effect, is demonstrated by the fact that the spins are polarized perpendicular to the direction of the wave vector or momentum.

3.3.3 KTO (111) surface

We studied the formation of 2DEG at the (111) polar surface of KTO with Ta surface termination using first-principles electronic structure calculations. Fig. 3.8 (a) illus-

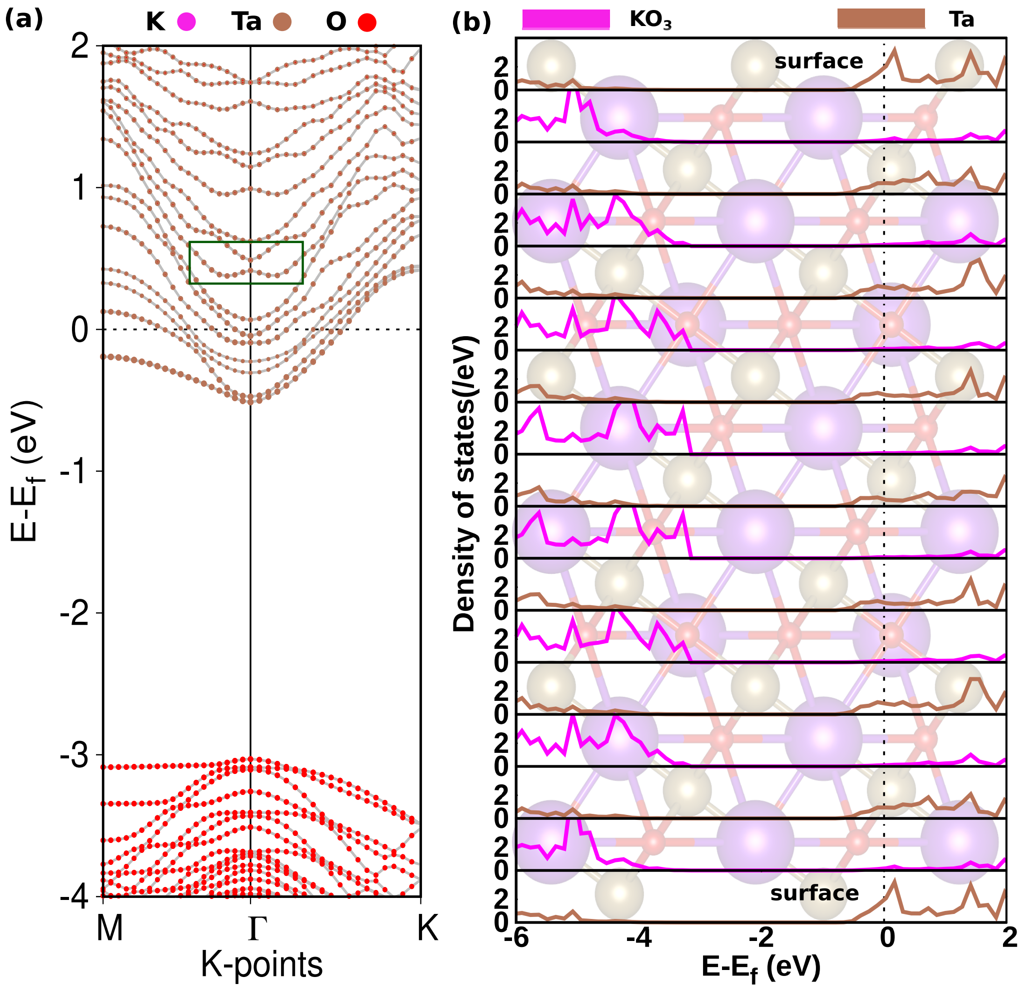

Figure 3.8: (a) Electronic band structure of KTO (111) surface with atomic projection on atoms K, Ta, and O along high symmetry path M-Γ-K including SOC (b) Layer-wise projected DOS on the atomic layers shown in the background of the plot. The black dashed line indicates the Fermi level E_f.

trates the electronic band structure along the high symmetry path M-Γ-K with atomic projection on the K, Ta, and O atoms including SOC. The Fermi level is situated inside the conduction band, and a gap is seen between the valence band and the conduction band illustrating n-type conductivity. A 2DEG with nearly parabolic bands around the Fermi level accommodated in the Ta-5d orbitals at the (111) polar surface of KTO is observed. This 2DEG can be attributed to the electronic reconstruction mechanism at the polar (111) surface due to the electrostatic instability at the surface. A layer-wise projected DOS on the atomic layers is estimated to further provide insight into the distribution of 2DEG in the depth of the (111)-KTO slab. According to the DOS projected on the atomic layers (visible in the plot's backdrop) in Fig. 3.8 (b), the Ta layers contribute to the states at the Fermi level, whereas the KO_3 layers provide no contribution. The two symmetrical Ta surface layers are the primary contributors to the metallic states, and as we approach the bulk of KTO, this contribution steadily decreases. A Rashba spin splitting is observed in the bands and one such Rashba-split band is marked in Fig. 3.8 (a).

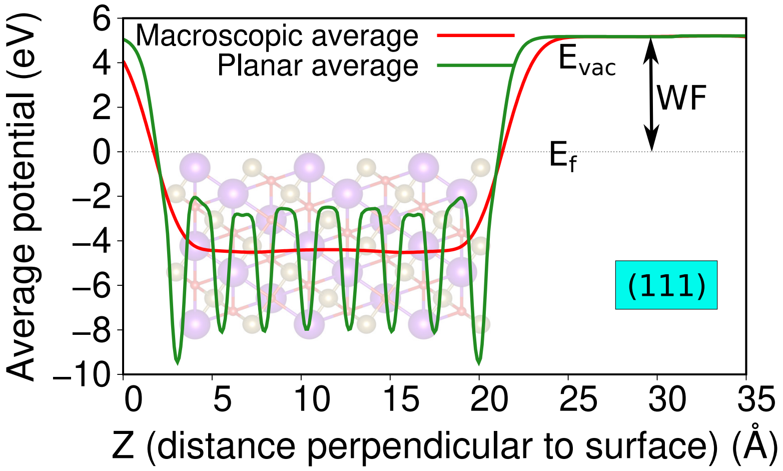

Figure 3.9: The planar average of the electrostatic potential (oscillating green curve) along the z-direction (perpendicular to the surface) and the macroscopic average of electrostatic potential (red curve) of (111) surface of KTO. The crystal structure of (111) surface slab is shown within the plot in the background; where magenta, brown, and red spheres represent K, Ta, and O atoms, respectively. The Fermi energy (E_f) is set to zero.

First-principles calculations are used to determine the electrostatic potential for the (111) surface of KTO with Ta termination, as illustrated in Fig. 3.9. The planar average of the electrostatic potential along the z-direction, perpendicular to the surface of KTO is represented with a green oscillating line. The red curve displays the macroscopic average or nanosmoothed electrostatic potential in the surface-normal direction. In the plot's background, the (111) surface slab of KTO is seen. As we go away from the Ta surface, the slope of macroscopic potential initially rises; as we move toward the other Ta surface, it decreases. However, compared to the (001) surface, the change in slope is minimal. It has been determined that the work function, which is the difference between the vacuum level and Fermi energy, is 5.1 eV.

Next, for the KTO (111) surface, we estimated the energy contour plots of the spin texture in the reciprocal space (k_x-k_y) plane. The color bar on the right depicts the modulus as well as the orientation of spin polarization, with up (red) and down (blue) spins. The spin texture at the Fermi surface along the three cartesian axes (S_x, S_y, and S_z) E_f is depicted in Fig. 3.10 (a)-(c). Because of the crystal symmetry in the (111) direction, the Fermi surface exhibits six-fold symmetry. Likewise, the plots of spin texture for the Rashba-split band (marked in Fig. 3.8 (a)) at a cut corresponding to energy (E-E_f) = 0.6 eV along the three cartesian axes (S_x, S_y, and S_z) are represented in Fig. 3.10 (d)-(f). As can be seen in the insets of the zoomed-in portions of Fig. 3.10 (d)-(f), spin-texture plots for the bands showing the Rashba splitting display the opposite spin orientation for the momentum-dependent spin-split band pair. A deeper analysis reveals that the S_x component is present along the k_y direction but lacking along the k_x direction, with the exception of the innermost ring/band in the Fermi surface. The S_y component is present along the k_x direction but not the k_y direction. The k_x and k_y directions in the plots are indicated by the horizontal and vertical green dashed lines, respectively. Therefore, the spins are polarized perpendicular to the direction of the wave vector or momentum, illustrating spin-momentum locking, a characteristic of the Rashba effect. However, the presence of substantial S_z component reveals complex spin structure as also observed in case of 111-STO 2DEGs. Thus, it can be inferred that the crystal field plays an important role in defining the spin structure of an electronic system.

3.3.4 Conclusion

In conclusion, we have examined the electronic and spintronic properties of the polar perovskite oxide KTO surfaces with the Ta termination in (001) and (111) directions. According to electronic structure calculations, 2DEG is present on both surfaces of KTO, with parabolic bands close to the Fermi level. The in-depth investigation of the distribution of 2DEG reveals that it is primarily accommodated in the 5d orbitals of Ta atoms in the surface layers. Due to the strong SOC of Ta atoms and inversion symmetry breaking at the surface, the Rashba spin splitting is visible in the bands. The work function values for the (001) and (111) surfaces are calculated to be 4.2 eV and 5.1 eV, respectively. Fermi surfaces exhibit four- and six- fold symmetries for the (001)

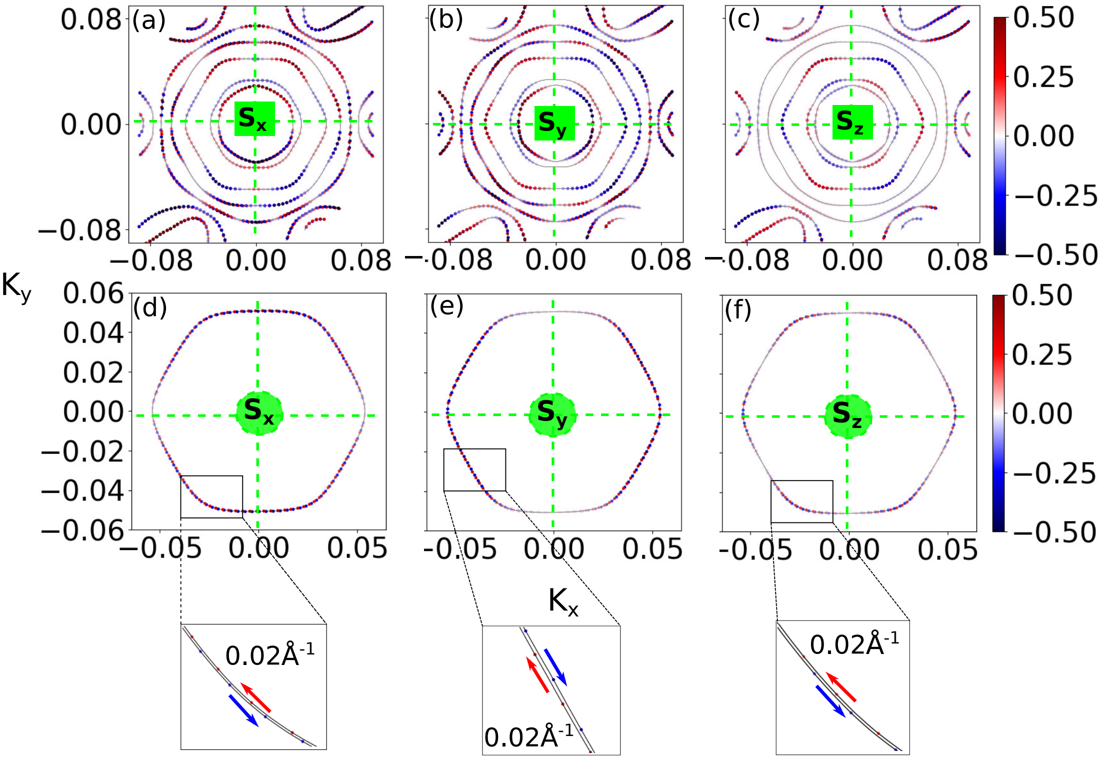

Figure 3.10: Constant energy contour plots of spin-texture (a)-(c) on Fermi surface (d)-(f) corresponding to a cut at energy (E-E$_F$) = 0.6 eV for each spin component along the cartesian axes (S$_x$, S$_y$, and S$_z$) calculated in k$_x$-k$_y$ plane for KTO (111) surface. The insets in (d)-(f) show the zoomed-in portions of the spin texture for the Rashba-split band. The colors indicate the modulus as well as the orientation (up(red) or down(blue)) of the spin polarization.

and (111) surfaces, respectively. The peculiarities of the spin pattern in the two surface directions highlights the important role played by the crystal field in defining the spin structure of an electronic system. In the following section, we have examined the electronic, electrostatic, and spintronic properties in the heterostructure between the polar perovskite oxides LVO and KTO in (001) and (111) orientations.

3.4 Rashba splitting in (001) and (111) LVO/KTO heterostructures

Polar/polar interfaces between perovskite oxides have lately drawn attention in addition to the non-polar/non-polar and polar/non-polar heterostructures[118,119,269]. Very recently, a high mobility 2DEG at the interface of two polar perovskite oxides LVO and KTO is observed with a high SOC in system[120,121]. As a consequence of strong SOC and the Rashba spin splitting, the magneto-transport measurements showed a signature of in-plane anisotropic transverse and longitudinal magnetoresistance in LVO/KTO. The epitaxial growth of LVO thin film on (001) KTO has already been reported experimentally in 2004[270]. However, there is a lack of theoretical studies for this polar/polar conducting heterointerface of LVO/KTO in spite of various exciting phenomena discovered in other heterostructures. Its theoretical study would provide insight into the interplay between SOC, electron correlation of d-orbitals, and interfacial charge transfer. Moreover, the discovery of the Rashba effect in the 2DEG systems at the perovskite surfaces and interfaces has led to the possibility of tuning its properties by an external electric field[133]. The tuning of the Rashba effect on the polar surface of the KTO was demonstrated by Shanavas et al. in 2014 by manipulating the 2DEG with an external electric field[116].

In this section, we have reported orientation-dependent structural, electronic, electrostatic, and spintronic properties of polar-polar heterointerface of two insulators LVO and KTO in (001) and (111) crystal directions for two types of terminations of KTO surface slab, namely, asymmetric and symmetric terminations. The charge transfer from the surface layers to the interfacial region due to the electronic reconstruction mechanism results in high carrier density 2DEG. Due to the high SOC strength of bulk KTO (400 meV)[268] (owing to high-Z Ta atom), momentum-dependent Rashba spin splitting is seen in the electronic bands originating from the symmetry-breaking electric field. The Rashba coefficient α_R in the range of $0.37 - 0.9$ eVÅ is calculated for the spin-split bands, offering a propitious platform for novel spintronic applications based on oxide thin films and heterostructures.

3.4.1 Computational methodology

The first principle calculations based on DFT were performed using the PAW method as implemented within the VASP[201,202,233]. GGA with PBE exchange-correlation functional was used[200]. Structure relaxation was performed with DFT calculations while electronic properties were investigated within DFT+U formalism with and without SOC. In the DFT+U method, Hubbard correction U was used to account for strong on-site Coulombic interactions between localized d electrons of transition metals Ta and V within Dudarev's approach[164] where only the difference U_{eff} (U–J) is meaningful. A value of 4 eV and 3 eV were kept fixed for U_{eff} (U–J) for d orbitals of Ta and V atoms, respectively. The structure optimization was done with the gamma-centered k-point mesh of $6 \times 6 \times 1$ to get more converged results. Self-consistent calculations of charge density were done with the same k-mesh. A kinetic energy cut-off of 520 eV was used for the plane-wave basis set. The lattice constants and atomic coordinates were fully relaxed with the convergence criteria for total energy 10^{-3} eV. A vacuum of 19 Å was used for slab models to avoid the interlayer interaction between the adjacent periodic images. SOC was considered in the second-variational method with magnetization along the (001) quantization axis as implemented within VASP. To calculate the energy contour plots of the spin texture in reciprocal space, PyProcar code was used[203].

3.4.2 Structural properties

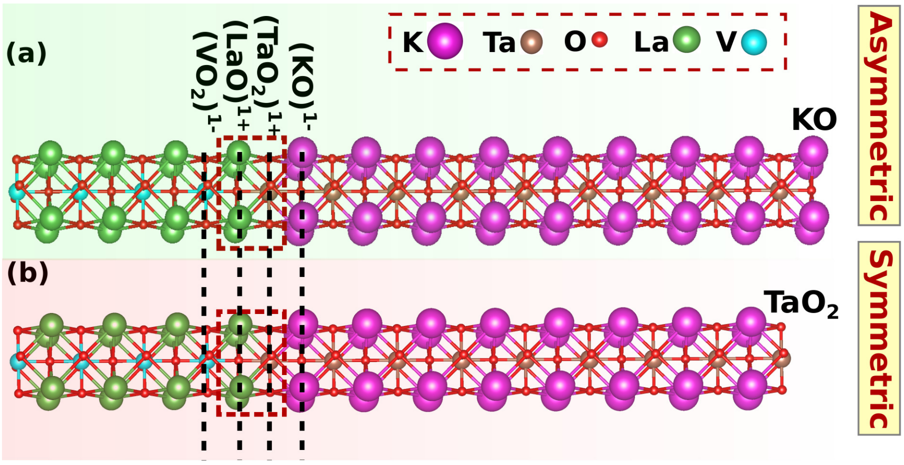

Figure 3.11: Side view of the crystal structure of slabs of LVO/KTO heterostructure in (001) orientation with (a)-(b) asymmetric and symmetric terminations of surfaces of KTO.

Along (001) crystallographic direction, KTO consists of stacks of alternating planes of charged layers $(KO)^{-1}$ and $(TaO_2)^{+1}$, while along (111) crystallographic direction, alternate planes of charged layers $(Ta)^{+5}$ and $(KO_3)^{-5}$. Further, 5d orbitals of Ta are less localized than 3d or 4d orbitals of V, Ti, or Nb in well-studied heterostructures leading to higher electron mobility 2DEG due to the smaller effective mass of the electron. LVO is a Mott-Hubbard insulator with a band gap of 1.08 eV[154]. It is structurally similar to

KTO with $(LaO)^{+1}$ and $(VO_2)^{-1}$ alternate charged planes along (001) direction, while $(V)^{+3}$ and $(LaO_3)^{-3}$ planes along (111) direction. So, the n-type interfaces in this polar/polar HS system are $(LaO)^{+}$/$(TaO_2)^{+}$ and $(LaO_3)^{-3}$/$(Ta)^{+5}$ in (001) and (111) directions, respectively. The geometrical crystal structures for the HS systems studied are shown in Fig. 3.11 and Fig. 3.12 for (001) and (111) orientations, respectively. Lattice constants of bulk KTO and LVO are 3.98 Å and 3.92 Å, respectively with a lattice mismatch of 1.5%, where lattice mismatch is defined as $(a_f$-$a_s)/a_s$; a_f and a_s being lattice constants of unstrained film and substrate, respectively. The negative value of lattice mismatch indicates tensile strain in the film. The HS of LVO/KTO were simulated with slab geometries of LVO and KTO comprising n-type interfaces using the thin film slab model. For symmetric termination where both the terminating surfaces of KTO are the same ($(TaO_2)^{+}$/$(Ta)^{+5}$ in (001)/(111) direction), slabs with an unequal number of $(TaO_2)^{+}$/$(Ta)^{+5}$ and $(KO)^{-}$/$(KO_3)^{-5}$ layers in (001)/(111) direction were used, resulting in a non-stoichiometric system with 8.5 unit cells of KTO and 4 unit cells of LVO. For asymmetric termination of surfaces of KTO, slabs with an equal number of $(TaO_2)^{+}$/$(Ta)^{+5}$ and $(KO)^{-}$/$(KO_3)^{-5}$ layers in (001)/(111) direction were used with 9 unit cells of KTO and 4 unit cells of LVO. In both the symmetric and asymmetric cases, the interfacial layer at the KTO side was composed of Ta atoms. This LVO/KTO heterointerface in (001) orientation has been found to be conducting above the film thickness of three monolayers in the recent experimental report[120].

3.4.3 Electronic properties

By using first-principles electronic structure calculations, we explored the formation of 2DEG in the polar/polar LVO/KTO HS. The total density of states, as well as the projection of s, p, d, and f orbitals, are calculated for LVO/KTO and are shown in Fig. 3.13 and Fig. 3.15 for (001) and (111) orientation, respectively. A gap is observed between the valence band (VB) and the conduction band (CB) and the Fermi level is pinned inside the CB. VB is mainly composed of p orbitals while CB, precisely the metallic states at the Fermi level are composed of d orbitals. We have calculated electronic band structure with and without SOC in LVO/KTO HS along high symmetry path Y-Γ-M for (001) and M-Γ-K for (111) orientation, respectively; Y, M, and K being written in terms of π/2a. The band structure of LVO/KTO with SOC for the asymmetric termination of KTO in (001) orientation is shown in Fig. 3.13 (a). It demonstrates that

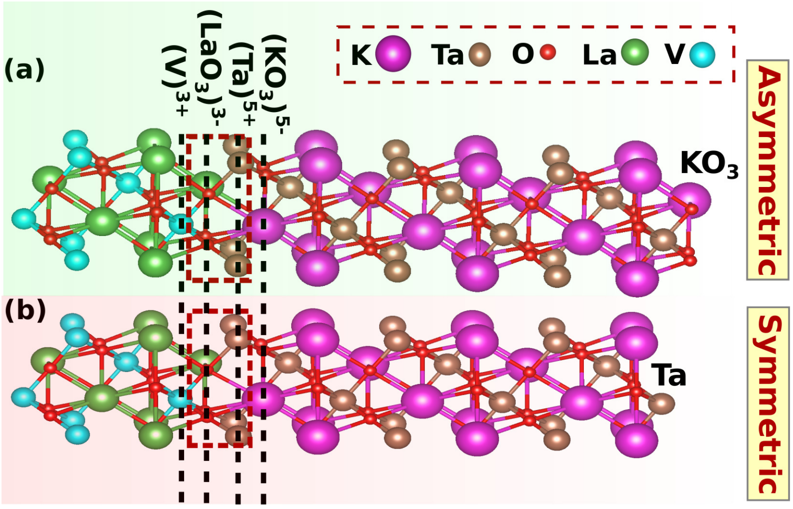

Figure 3.12: Side view of crystal structures of slabs of LVO/KTO heterostructure in (111) orientation with (a)-(b) asymmetric and symmetric terminations of surfaces of KTO.

the system is n-type conducting, and a 2DEG with almost parabolic bands is found close to the Fermi level. This 2DEG can be attributed to the electronic reconstruction mechanism at the interface due to polar discontinuity. At the interface $(LaO)^+/(TaO_2)^+$, there is charge discontinuity which causes a divergence in the electrostatic potential (polar catastrophe) away from the interface. The electrostatic potential energy increases as we move away from the interface due to the internal electric field of LVO. This causes the transfer of electrons from the surface of LVO toward the interface. This mechanism for the formation of 2DEG is similar to that in another polar/polar LTO/KTO system[118].

When SOC is included in the electronic structure calculations, a clear Rashba spin splitting appears for a variety of bands, most notably in the band at energy 0.32 eV ($E-E_f$) highlighted in red color in Fig. 3.13 (a), where E_f is the Fermi energy. At $E-E_f = 0$ and 0.32 eV, the charge carrier densities are determined to be 0.38×10^{14} cm^{-2} and 1.93×10^{14} cm^{-2}, respectively. Furthermore, the Rashba strength of a material is judged by three parameters viz. E_R, α_R, and K_R with the calculated values for the HS system being 4.5 meV, 0.9 eVÅ, and 0.009 Å^{-1}, respectively.

The band structure of LVO/KTO HS for the symmetric termination of KTO in (001) orientation with SOC as shown in Fig. 3.13 (b) emanates the n-type conductivity similar to the asymmetric termination. Also, 2DEG is observed owing to the same mech-

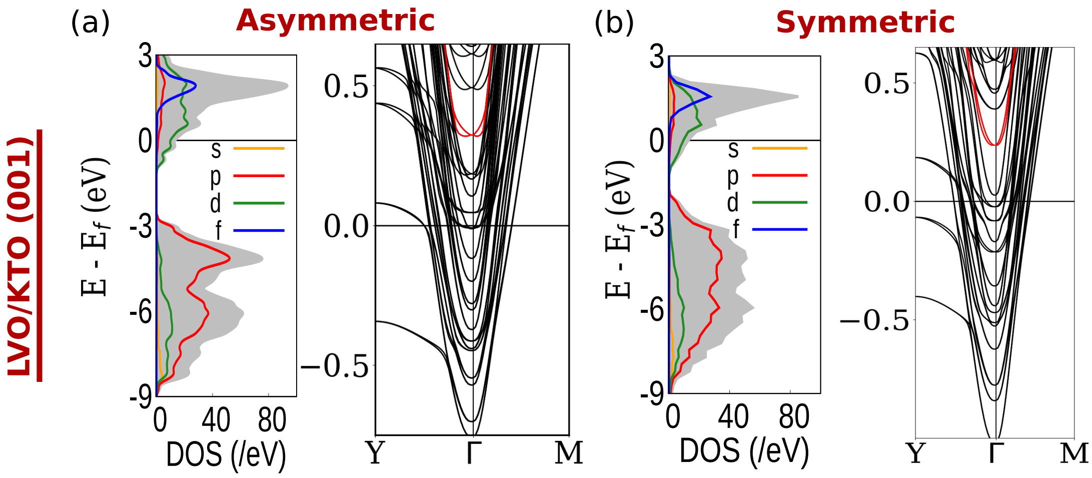

Figure 3.13: Electronic structure of (001)-oriented LVO/KTO heterostructure (a)-(b) Calculated total as well as orbital projected DOS and band structure along the high symmetry path Y-Γ-M with SOC for asymmetric and symmetric terminations, respectively. Bands showing the prominent Rashba spin splitting are highlighted in red.

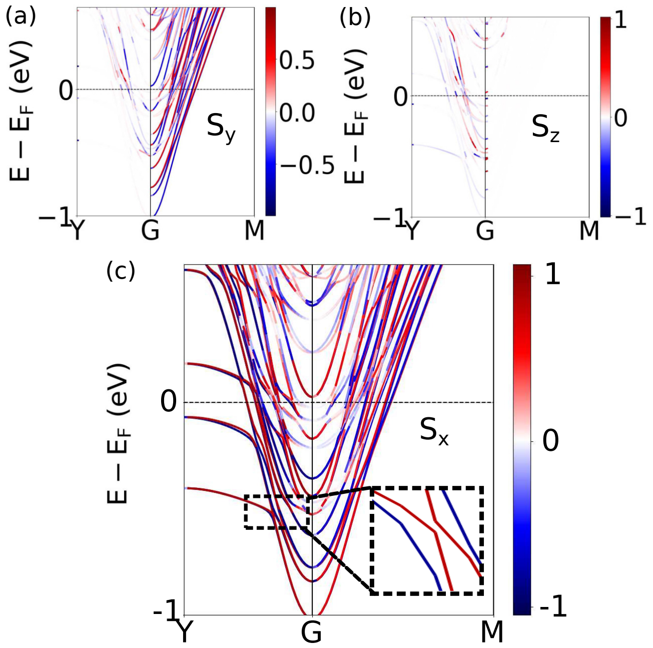

Figure 3.14: Band structures of (001)-oriented LVO/KTO heterostructure having symmetric termination of KTO with electron spin projections along the (a) y, (b) z, and (c) x-direction, respectively. Red and blue colors represent the positive and negative components of spin projections, respectively.

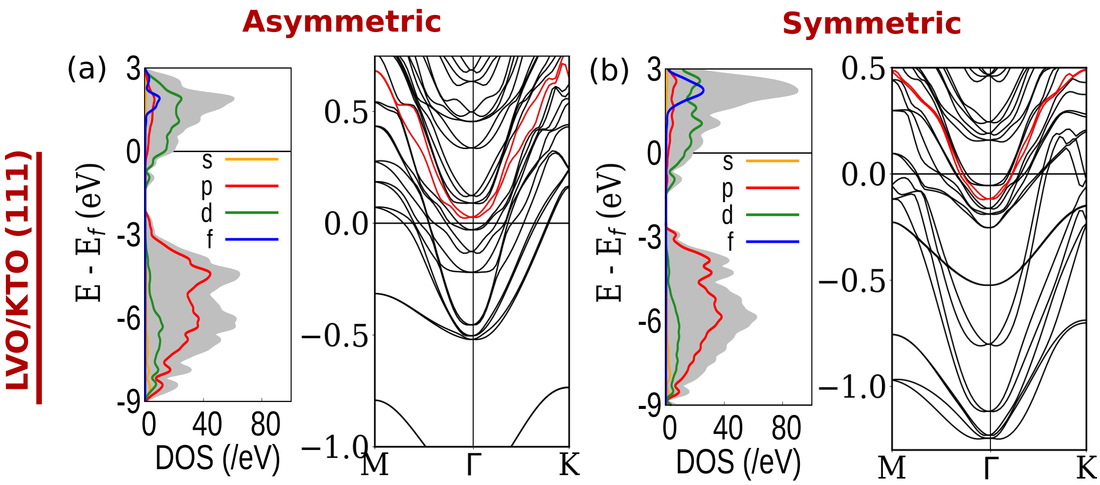

Figure 3.15: Electronic structure of (111)-oriented LVO/KTO heterostructure (a)-(b) Calculated total as well as orbital projected DOS and band structure along high symmetry path M-Γ-K with SOC for asymmetric and symmetric terminations, respectively. Bands showing the prominent Rashba spin splitting are highlighted in red.

anism as in asymmetric termination and the Rashba spin splitting is observed for the bands markedly, at energy (E-E$_f$) 0.23 eV. The charge carrier densities calculated at E-E$_f$ equal to 0 and 0.23 eV are 0.25×10^{14} cm^{-2} and 0.97×10^{14} cm^{-2}, respectively. The evaluated carrier density corresponding to the Rashba-split band at energy (0.23 eV) agrees with the experimentally measured carrier density of 1.02×10^{14} cm^{-2} in LVO/KTO system with a pronounced Rashba effect[120]. The values of the three Rashba parameters E$_R$, α_R, and K$_R$ for the highlighted band (shown in red) come out to be 0.6 meV, 0.37 eV Å, and 0.003 Å^{-1}, respectively. The values of the Rashba coefficient α_R and momentum offset K$_R$ are fairly in agreement with those determined experimentally in LVO/KTO heterointerface[120]. To further analyze the spin polarization caused by the Rashba effect, band structure plots with electron spin projections along the x, y, and z axes are shown in Fig. 3.14. Along the chosen Γ-Y direction, the spins are polarized along the x-direction with vanishing y and z components, as illustrated in these plots. In other words, spins are polarized perpendicular to the direction of the wave vector or momentum, demonstrating spin-momentum locking typical of the Rashba effect. It is important to note that the band-anticrossing region of d$_{xy}$ and d$_{yz/xz}$ orbitals shows larger Rashba-splitting and is zoomed in the inset of Fig. 3.14 (c).

Fig. 3.15 (a) shows the band structure of (111)-oriented LVO/KTO for the asymmetric termination of KTO with SOC stipulating the n-type conductivity in the system. Also, 2DEG is observed in this crystallographic orientation due to charge discontinuity at the n-type interface comprising of $(LaO_3)^{-3}$ and $(Ta)^{+5}$ layers. Remarkable Rashba spin splitting is observed for the band at energy ($E\text{-}E_f$) 0.02 eV. The value of carrier concentration corresponding to the highlighted band is 0.46×10^{14} cm^{-2}. The values of the Rashba parameters E_R, α_R, and K_R are evaluated to be 1.6 meV, 0.7 eVÅ, and 0.004 Å^{-1}, respectively. The band structure of LVO/KTO for the symmetric termination of KTO in (111) orientation with SOC as shown in Fig. 3.15 (b) depicts the conducting heterointerface. Moreover, the Rashba spin splitting is observed in the 2DEG for the band at energy ($E\text{-}E_f$) –0.11 eV. The values of the Rashba parameters E_R, α_R, and K_R in this case, are calculated to be 0.8 meV, 0.39 eVÅ, and 0.004 Å^{-1}, respectively. The value of carrier concentration calculated for the highlighted band is 0.14×10^{13} cm^{-2}. The values of the Rashba parameters for the four cases of LVO/KTO heterointerface are listed in Table 3.1.

Crystallographic orientation	Termination of KTO	α_R (eVÅ)	E_R (meV)	k_R (Å^{-1})
(001)	Asymmetric	0.9	4.5	0.009
	Symmetric	0.3	0.6	0.003
(111)	Asymmetric	0.7	1.6	0.004
	Symmetric	0.3	0.8	0.004

Table 3.1: Rashba parameters viz. Rashba coupling constant α_R (eVÅ), Rashba splitting energy E_R (meV), and Rashba momentum offset K_R (Å^{-1}) for (001)- and (111)-oriented LVO/KTO heterointerface slabs for the cases of asymmetric and symmetric terminations of KTO.

It is noteworthy that Shanavas et al. in 2014, reported α_R of about 0.3 eVÅ for the unrelaxed surface of bare KTO using DFT calculations[116]. It is worth mentioning that the observed values of α_R in LVO/KTO HS are higher than those of other perovskite oxide heterostructures including asymmetric oxide HS LAO//STO/LAO (0.01 – 0.04 eVÅ) depending on STO layer thickness, $(BaOsO_3)_n/(BaTiO_3)_m$ multilayers with or without strain (0.08 – 0.4 eVÅ), $BaIrO_3/BaTiO_3$ (0.7 eVÅ), $BaRuO_3/BaTiO_3$ (0.25 eVÅ), and LTO/STO (0.18 eVÅ)[133,271,272].

Furthermore, the value of the Rashba parameter α_R and the amount of splitting de-

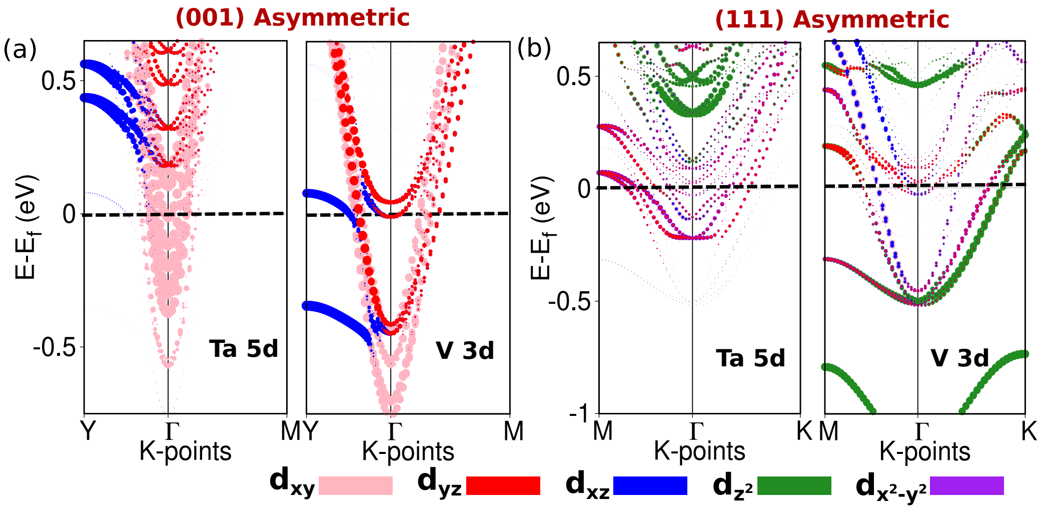

Figure 3.16: Calculated d-orbital projected band structures on 5d and 3d orbitals of Ta and V atoms, respectively with SOC along high symmetry path (a) Y-Γ-M for (001)- and (b) M-Γ-K for (111)- oriented LVO/KTO heterostructures, respectively with asymmetric termination. The radius of the circles represents the weight of the d orbitals. The colors of the individual d orbitals are indicated in the plot.

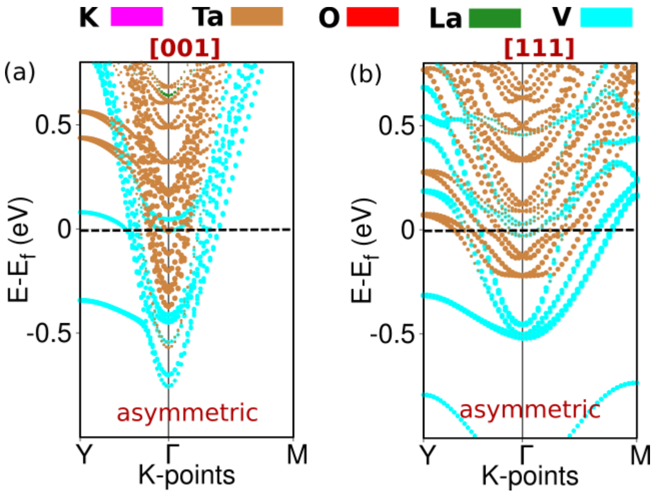

Figure 3.17: (a)-(b) Calculated band structure plots with atomic projection including SOC along high symmetry path (a) Y-Γ-M for (001)- and (b) M-Γ-K for (111)- oriented LVO/KTO heterostructures, respectively with asymmetric termination. The radius of the circles represents the weight of the individual atoms with the colors of the individual atoms indicated in the plot.

pend on the orbital character of the bands in addition to the strength of the spin-orbit coupling. In the case of LVO/KTO HS, the bands that exhibit Rashba splitting are predominantly formed by 5d-orbitals of Ta atom with a little contribution from 3d-orbitals of V atom owing to the high SOC of Ta atom. To investigate the d-orbital composition of the bands showing Rashba splitting, we have plotted the d-orbital projected band structure on 5d and 3d orbitals of Ta and V atoms, respectively for the asymmetric case. As shown in Fig. 3.16 (a) and (b) for the (001)- and (111)- oriented LVO/KTO systems, respectively, we have observed orbital-dependent Rashba splitting. In (001) orientation, electrons occupying heavy bands d_{xz} and d_{yz} present Rashba splitting, whereas light d_{xy} bands are not influenced by the Rashba effect. In (111) orientation, the dz^2 bands in addition to the d_{xz} and d_{yz} bands mainly contribute to the Rashba splitting. The reason for this orbital-dependent splitting of bands is that these orbitals are maximum affected by the symmetry-breaking electric field (along the z-direction) which is responsible for the Rashba effect. This is due to the hybridization of d_{xz} and d_{yz} orbitals to give orbital polarization along the z-direction[273] and the innate shape of d_{z^2} orbitals. Shanavas et. al in Ref.[116] showed that the Rashba spin-orbit interaction in d-electron solids, which originates from the broken inversion symmetry at surfaces or interfaces, is strongly dependent on the orbital characters of the bands involved. Such an orbital dependence of the Rashba splitting is also seen in other works[274]. To determine the atomic composition of the subbands just below E_f, the band structure plots with atomic projection on K, Ta, O, La, and V atoms for the asymmetric case in the (001) and (111) orientations are shown in Fig. 3.17 (a) and (b), respectively. From the plots, it is clear that the contribution to the subbands below E_f from K, O, and La atoms is zero and the corresponding bands have the d-orbital character of Ta and V atoms. Therefore, the electrons reside in the d-orbitals of Ta and V atoms.

In addition, the electronic structure of the superlattice model (without vacuum) in (001) orientation of LVO/KTO has been calculated to study the effect of two terminating surfaces on the band structure. The advantage of the superlattice model is that no vacuum and thus no surfaces are required in the simulation cell, avoiding the contribution of 2DEG from the surfaces. However, experimentally, this type of symmetric structure with two identical interfaces is difficult to create. The thin film layer has a finite thickness and a terminating surface on a substrate slab in most actual implementations[275]. Except for a few bands with a solitary contribution from the surfaces, the band structure without SOC is found to be qualitatively comparable to that of HS with symmetric

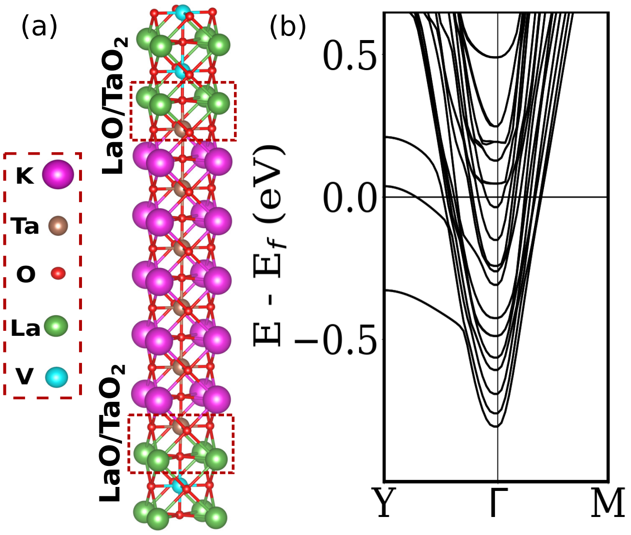

Figure 3.18: (a) Superlattice structure of LVO/KTO with two identical n-type interfaces LaO/TaO$_2$ (highlighted by dashed lines). (b) band structure plot with SOC along high symmetry path Y-Γ-M for LVO/KTO superlattice model in (001) orientation.

termination of KTO slab in (001) orientation. The Rashba splitting was reduced to a minimal amount with SOC, demonstrating that surface layers had a large influence on the Rashba splitting in the bands. Fig. 3.18 depicts the superlattice structure employed in the calculation as well as the corresponding band structure plot including SOC.

3.4.4 Electrostatic potential and charge transfer

When two dissimilar materials are joined to form the heterostructure, the electric dipole at the interface causes the built-in potential or contact potential at the junction. This contact potential is of key significance for the current transport as well as interfacial properties like interfacial charge densities, dipole densities, and band offset[276,277]. The electrostatic potential is calculated by first-principle calculations for the asymmetric and symmetric slabs of (001)- and (111)- oriented LVO/KTO heterointerface and the resulting plots are shown in the upper panels of Fig. 3.19 and Fig. 3.20, respectively. In its raw form, the electrostatic potential is computed with atomic-level resolution and thus oscillates rapidly within the unit cell. The planar average of the electrostatic potential[277] along the z-direction, perpendicular to the interface of LVO/KTO HS is shown with green oscillating lines. Furthermore, red curves show the macroscopic average or nanosmoothed electrostatic potential in the direction normal to the interface. The crystal structures of the corresponding heterointerfaces are shown in the background of the plots.

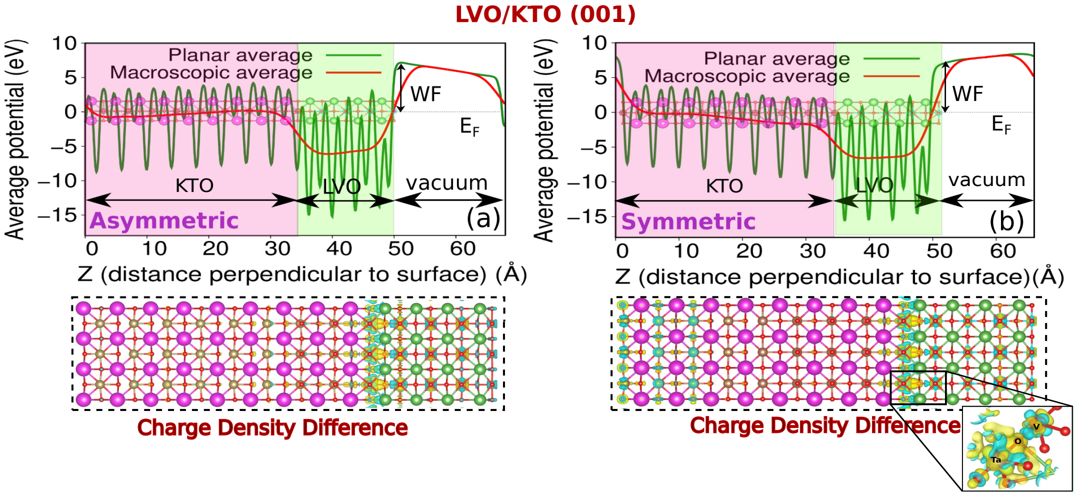

Figure 3.19: (a)-(b) The planar average of the electrostatic potential (oscillating green curves) along the z-direction (perpendicular to the interface) and the macroscopic average of electrostatic potential (red curves) of (001)-oriented LVO/KTO HS for asymmetric and symmetric terminations, respectively. The crystal structures of corresponding HS systems are shown within the plots in the background; where green, cyan, magenta, brown, and red spheres represent La, V, K, Ta, and O atoms, respectively. The Fermi energy (E_F) is set to zero. The charge density difference plots of the corresponding HS systems are also shown; the yellow-colored regions designate electron accumulation, whereas the blue color reflects electron depletion in the HS. The zoomed-in charge density difference at the interfacial region for symmetric termination is also shown in the inset of (b).

The macroscopic average potential is not constant throughout the system. The sloped curves or potential gradients for LVO film as well as KTO substrate in the HS system as inferred from the plots indicate the presence of a residual macroscopic electric field in both polar LVO and KTO. The potential difference ΔV between V_{LVO} and V_{KTO} when calculated for (001) orientation, comes out to be 6.34 eV and 4.80 eV for the asymmetric and symmetric terminations, respectively. The corresponding values for (111) orientation are calculated to be 5.20 eV and 4.54 eV for the instances of asymmetric and symmetric terminations, respectively. The work function, which is the difference between the vacuum level and Fermi energy is calculated to be 7.1 eV and 6.8 eV for the asymmetric and symmetric termination in (001) direction, respectively.

In (111) orientation, for asymmetric and symmetric termination cases, the evaluated values of the work function are 6.1 eV and 6.2 eV, respectively.

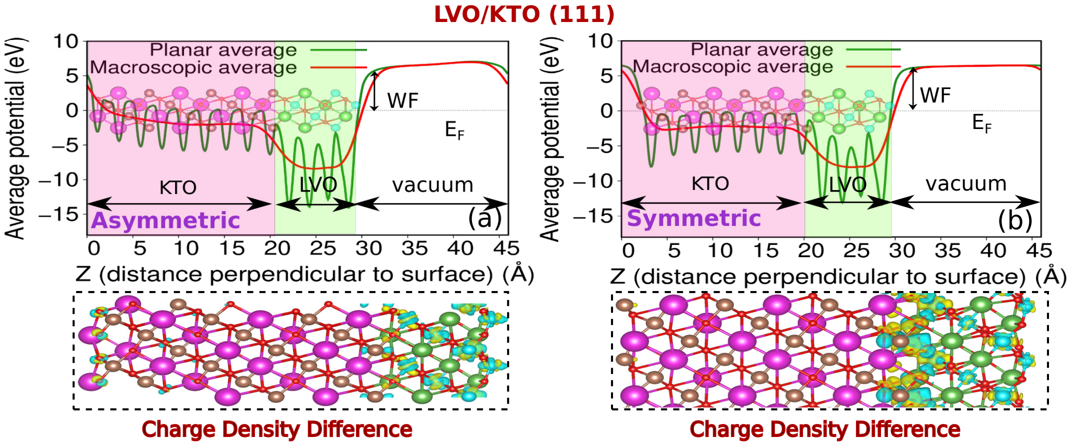

Figure 3.20: (a)-(b) The planar average of the electrostatic potential (oscillating green curves) along the z-direction (perpendicular to the interface) and the macroscopic average of electrostatic potential (red curves) of (111)-oriented LVO/KTO HS for asymmetric and symmetric terminations, respectively. The crystal structures of corresponding HS systems are shown within the plots in the background; where green, cyan, magenta, brown, and red spheres represent La, V, K, Ta, and O atoms, respectively. The Fermi energy (E_F) is set to zero. The charge density difference plots of the corresponding HS systems are also shown; the yellow-colored regions designate electron accumulation, whereas the blue color reflects electron depletion in the HS.

Furthermore, the values of macroscopic average charge carrier densities at individual surfaces and the interface in (001)-oriented LVO/KTO with symmetric termination of KTO are calculated using Maxwell's equation $\nabla.E=\rho/\varepsilon_0$; ε_0 is the permittivity of vacuum. The 2D charge densities (in /cm^2) are produced by integrating the volume charge densities (in /cm^3) along the direction normal to the interface. In (001)-oriented LVO/KTO with symmetric termination of KTO, the carrier densities at the TaO_2 surface, VO_2 surface, and interfacial region are -0.02, 0.012, and -0.012 in the units of 10^{14}/cm^2, respectively. Positive and negative signs represent holes and electrons, respectively. As a result, the presence of holes on the VO_2 surface, as well as electrons at the interfacial region, indicates charge transfer from the latter to the former. Charge density difference plots for the LVO/KTO HS are shown in the lower panels of Fig. 3.19 and Fig. 3.20 for (001) and (111) orientations, respectively to further corroborate the directions of charge transfer as mentioned above. The charge density difference is calculated using the equation

$$\Delta\rho = \rho_{LVO/KTO} - \rho_{LVO} - \rho_{KTO} \tag{3.1}$$

where $\Delta\rho$ is the charge density difference, $\rho_{LVO/KTO}$, ρ_{LVO}, and ρ_{KTO} are the charge densities of the HS system, LVO slab, and KTO slab with the same atomic positions and lattice constants. The LVO and KTO slab models are built in identical LVO/KTO HS with the other part replaced by a vacuum. The yellow-colored regions designate the increased charge density (electron accumulation) upon the formation of HS, whereas the blue color reflects the decrease in charge density (electron depletion) in the HS. In Fig. 3.19 (a), the charge transfer from the surface $(VO_2)^-$ layer to the interfacial $(TaO_2)^+$ and $(VO_2)^-$ layers in (001) orientation for asymmetric termination of the KTO slab is depicted by the corresponding colors. The surface layers of the KTO slab are unaffected by the asymmetric termination in terms of charge transfer. For symmetric termination of the KTO slab, the charge transfer from the surface $(VO_2)^-$ layer to the interfacial $(TaO_2)^+$ and $(VO_2)^-$ layers is observed. The zoomed-in portion of the charge density in the interfacial region is shown in the inset of Fig. 3.19 (b). In addition to the electrons in the orbitals polarized along the z-direction of the V atom in the interfacial VO_2 layer, a distinct accumulation of electrons in d_{xy} orbitals of the Ta atom in the interfacial TaO_2 layer is illustrated in the inset. Also, a few layers from the surface on the KTO side (terminated by $(TaO_2)^+$ layer) participates in the charge transfer upon the formation of the heterostructure. In (111) orientation, the charge transfer from the surface $(V)^{3+}$ layer to the interfacial layers is noticeably observed in Fig. 3.20 (a) and (b) for asymmetric and symmetric cases, respectively. Moreover, the spatial charge distribution in these plots forms hybridized d_{xz} and d_{yz} orbitals, giving orbital polarization along the z-direction as mentioned earlier.

3.4.5 Spin texture

In addition to the band structure analysis, we have also calculated the energy contour plots of the spin texture in the reciprocal space (k_x-k_y plane) for the heterointerface LVO/KTO for the two terminations of the KTO slab in (001) and (111) orientations. The color bar on the right depicts the modulus as well as the orientation of spin polarization, with up (red) and down (blue) spins. For asymmetric termination of the KTO slab in

(001) orientation, the spin texture plots along the three cartesian axes (S_x, S_y, and S_z) at an energy of E-E_f = 0.32 eV are shown in Fig. 3.21 (a). From the plots, it is clear that the 2D Rashba splitting is observed for the band highlighted in red color in the band structure plot in (fig. 3.13). It is explicit that the Rashba bands have spin-polarization in the x-y plane and negligible value of the S_z components. For (001) orientation having symmetric termination of KTO slab, the spin texture plots along the three cartesian axes are shown in Fig. 3.21 (b). It is quite distinct that the 2D Rashba splitting is observed in the contour plot on the plane with energy E-E_f = 0.23 eV similar to the case of asymmetric termination. The bands reveal predominantly in-plane S_x and S_y spin components with almost vanishing out-of-plane S_z component. The splitting in reciprocal space is comparatively larger for the symmetric case as seen from the plots.

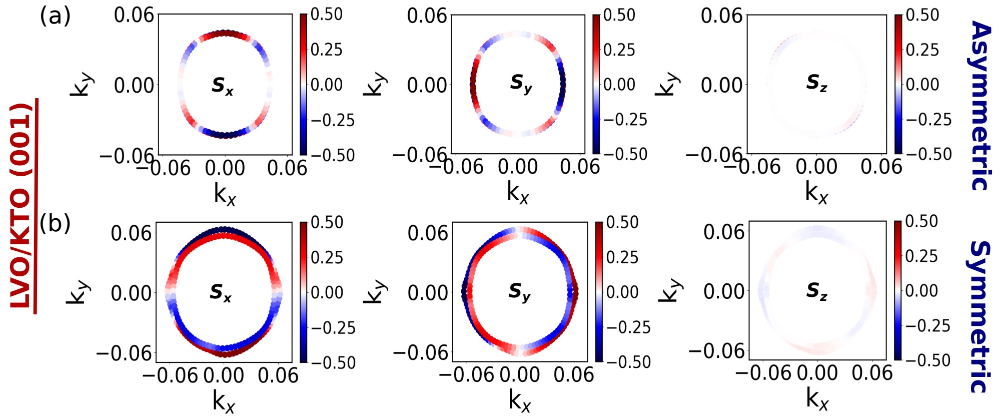

Figure 3.21: Spin-texture on constant energy contour plots corresponding to a cut at energy (E-E_F) (a) 0.32 eV, (b) 0.23 eV for each spin component along the cartesian axis (S_x, S_y, and S_z) calculated in k_x-k_y plane for the heterointerface LVO/KTO in (001) orientation for asymmetric and symmetric terminations, respectively. The colors indicate the modulus as well as the orientation (up(red) or down(blue)) of the spin polarization.

Similar plots of LVO/KTO in (111) orientation in Fig. 3.22 show all three components present in the spin texture plots indicating a complex spin structure. Here, splitting in reciprocal space is more for asymmetric termination, while both the terminations show hexagonal symmetry in (111) orientation. Spin-texture plots for the bands showing the Rashba splitting display the opposite spin orientation for the momentum-dependent spin-split band pair. It should be noted that the spin-texture plots show detailed information like different symmetries viz. four-fold and six-fold symmetries for

(001) and (111) orientations of HS, respectively owing to the symmetry of the crystal structure. As the ring size of the contour plot depends upon the shape of the subband as well as the energy value of the isosurface plot, hence the four cases show different ring sizes due to the distinct energies as well as the shapes of the subbands being considered. As a result of this, there is a difference between the spin textures for the asymmetric and symmetric terminations. Otherwise, other aspects like symmetry and the presence/absence of out-of-plane spin components are similar for the two types of terminations. Thus, only a profound understanding of this elusive competition between the electron-correlations, SOC, and other effects like interfacial confinement as well as crystal orientation would allow us to tune the Rashba splitting in these HS systems.

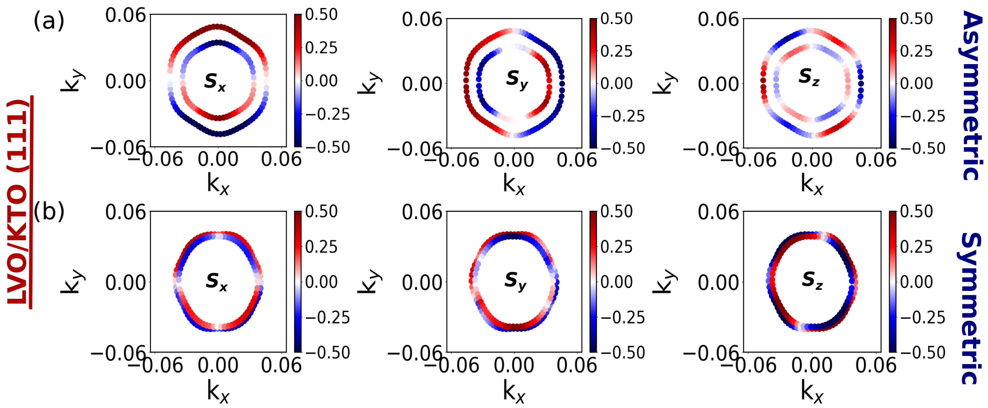

Figure 3.22: Spin-texture on constant energy contour plots corresponding to a cut at energy (E-E$_F$) (a) 0.02 eV, and (b) -0.11 eV for each spin component along the cartesian axis (S$_x$, S$_y$, and S$_z$) calculated in k$_x$-k$_y$ plane for the (111)-oriented LVO/KTO heterointerface for asymmetric and symmetric terminations, respectively. The colors indicate the modulus as well as the orientation (up(red) or down(blue)) of the spin polarization.

3.4.6 Interface energetics

To estimate the interfacial thermodynamic stability of the n-type interfaces in these four HS systems, we have calculated the cleavage energies using the following equation:

$$E_{cleavage} = (E_{slab}^{LVO} + E_{slab}^{KTO} - E_{HS})/A \tag{3.2}$$

; where E$_{slab}^{LVO}$, E$_{slab}^{KTO}$, and E$_{HS}$ are the total energy values of LVO slab, KTO slab, and LVO/KTO HS, respectively. “A” denotes the interfacial area. The LVO and KTO slab models are constructed in the same LVO/KTO HS with the other part replaced by a vacuum. The cleavage energy can be explained as the energy per unit cell required to separate the HS into individual components and its value governs the cohesive strength of the interface between LVO film and KTO substrate, which can affect the thermodynamic stability of the interface. The calculated cleavage energies for the n-type $(LaO)^+/(TaO_2)^+$ interface in (001) LVO/KTO are 0.16 eV^2 and 1.41 eV^2 for asymmetric and symmetric cases, respectively. For $(LaO_3)^{-3}/(Ta)^{+5}$ interface in (111)-oriented HS, the values are 0.75 eV^2 and 0.27 eV^2 for asymmetric and symmetric instances, respectively.

3.4.7 Conclusions

In conclusion, we have investigated the orientation dependence of structural, electronic, electrostatic, and spintronic properties in polar-polar perovskite oxide HS LVO/KTO with the n-type interface for (001) and (111) crystallographic orientations. Electronic structure calculations show an n-type conducting interface and the Rashba spin splitting in the bands with values of α_R in the range of $0.37-0.9$ eVÅ and E_R in the range of $0.6-4.5$ eV owing to the high SOC of Ta atoms and symmetry breaking electric field present in the heterostructure. Orbital-dependent Rashba splitting is noticed due to the occupation of heavy bands d_{yz}/d_{xz} and the additional occupation of d_{z^2} bands in (111) orientation. Spin-splitting is larger at the anticrossing regions of the d_{xy} and $d_{xz/yz}$ subbands. The values of the cleavage energies further confirm the thermodynamic stability of the interfaces in the studied systems. The residual macroscopic electric field present in the two constituent materials, as well as the contact potential at the interface of these heterostructures, can be seen in the electrostatic potential plots. The spin texture on energy contour plots calculated in the reciprocal space confirms the 2D nature of the Rashba spin splitting of 2DEG in (001) orientation, while a complex spin structure is observed in (111) orientation. Thus, our study widens the realm of perovskite-based thin film heterostructures for future spintronic applications maneuvering the Rashba effect with complex spin texture.

CHAPTER 4

Spin-polarized 2DEG at EuO/KTO interface

"God does not play dice with the universe."

Albert Einstein

4.1 Introduction

Spin-polarized 2DEG at the interface of oxide heterointerfaces is gaining considerable attention as a result of its ground-breaking technical evolution in low-power memory and logic devices. Not long ago, it was anticipated and observed that spin-polarized 2DEG was present at the interfaces of non-magnetic perovskite transition-metal oxides with ABO_3 stoichiometry[244,259,278–281]. An alternative way for creating the spin-polarized 2DEG at the interface is to create a heterostructure comprising non-magnetic perovskite oxide and magnetic material[282–284]. Likewise, magnetic interfaces in oxide heterostructures include $GdTiO_3$/STO[285], $SrMnO_3/(LaMnO_3)_1/SrMnO_3$[286], and between $SrRuO_3$ and LSMO[218]. EuO is one of the magnetic materials that has recently been predicted and validated experimentally for producing spin-polarized 2DEG at oxide interfaces[207,287–290]. Additional study into the realization of spin-polarized

2DEG includes the interface of EuO with oxygen-deficient STO[291], and DFT investigations of LAO/EuO heterointerface. The internal electric field of polar LAO drives charge carriers into the 5d-conduction bands of FM EuO[292,293]. Experiments combined with first-principles calculations reveal a substantial positive linear magnetoresistance in the 2DEG at the EuO/STO interface below the Curie temperature of EuO[294]. In addition, the use of a high-k 5d oxide, KTO, as a substrate material is currently attracting interest in oxide heteroepitaxy[120,121,263,295–297]. Very recently, a new type of high-mobility spin-polarized 2DEG has been reported at the interface between EuO and KTO[13,122,123,298]. The spin-polarized 2DEG showed an anomalous Hall effect with a Curie temperature of 70 K[122]. The broken space inversion symmetry at the interface of EuO/KTO HS and significant atomic SOC strength of high-Z element Ta give rise to Rashba spin-orbit field in the HS. The asymmetric potential at the interface generates an out-of-plane electric field. In the rest frame of an electron, this electric field manifests as an in-plane effective magnetic field B_R acting on the electron spin. The Rashba Hamiltonian $H_R = \alpha_R(\sigma \times k).\hat{z}$ describes the orthogonal locking of electron spin and the wave vector for the in-plane motion of the electron. α_R, k, σ, and $\hat{z}$ represent the Rashba coupling constant, the wave vector of the electron, the vector of the Pauli spin matrices, and the direction of the inversion-symmetry breaking field, respectively. The proximity-induced exchange interactions at the interface also produce an effective magnetic field B_{ex} that acts in the direction of magnetization. It is worth noting that the presence of significant SOC, exchange interactions, and certain band structure features could all be leveraged to create topologically non-trivial states that can lead to QAHE[299,300]. The quantized version of the anomalous Hall effect, in which the Hall conductance is quantized in units of e^2/h without the necessity for an external magnetic field in the system, is known as QAHE. The appearance of a non-zero Chern number in the electronic bands due to broken time-reversal symmetry in the absence of Landau levels or the external magnetic field signifies quantized Hall conductance. It leads to topologically protected dissipationless chiral edge states with no backscattering of electrons, which is revolutionary for next-generation electronics. Highly celebrated 2D material graphene which sparked a chain of scientific discoveries and industrial applications displays some specific features in the band structure such as the Dirac cone. However, because it lacks the inherent magnetic ordering and has a low SOC strength, QAHE does not exist in the graphene. Inducing QAHE in several graphene-based heterostructures by the proximity effect of magnetic and high spin-orbit coupling materials is a current scientific research area of interest[301–304]. Furthermore, Rehman et al. theoretically reported the opening of a non-trivial SOC gap to produce QAHE in heavy-element atomic layers on monolayer CrI_3[305]. CrI_3/X (X = Bi, Sb, or As) systems are predicted to exhibit QAHE associated with the non-zero Chern number in the SO gaps. Berry curvature $\Omega(k)$ exhibiting sharp peaks at the momenta of SOC-induced gaps pointing to the presence of a Hall plateau and the non-zero Chern number indicating the existence of QAHE have been observed recently[306–309]. The presence of proximity-induced Zeeman exchange splitting and the Rashba spin-orbit field in the EuO/KTO HS warrants a thorough examination of the system's detailed electronic band structure using DFT calculations to look for the possibility of such quantum phenomena.

In this chapter, using a comprehensive DFT study, we examine the orbital, spintronic, and topological properties of the 2DEG with detailed electronic structure calculations in the EuO/KTO heterointerface. The non-stoichiometric geometry of the superlattice structure causes the charge transfer at the interface creating the 2DEG. The hybridization of Eu and Ta d orbitals causes spin splitting of the 2DEG due to the proximity effect of EuO. Magnetic ordering at the interface is related to the occupation of $5d_{xy}$ orbitals of Ta at the interfacial layer on the KTO side. The Rashba SOC opens the gap between the degenerate states at the crossing point of majority and minority spin bands in the conduction band region near the Fermi energy suggesting the possibility of non-trivial topology in the band structure. The non-zero Chern number and spikelike features of calculated Berry curvature at these SOC-induced gaps reveal that EuO/KTO system hosts non-trivial topological states. Negative magnetic anisotropy energy (MAE) indicates that the magnetic easy axis is perpendicular to the interfacial plane.

4.2 Computational Methodology

The first-principles calculations based on DFT were performed using the PAW method as implemented within the VASP[201,202,233]. GGA with PBE exchange-correlation functional was used[200]. Structure optimization and electronic properties were investigated within DFT+U formalism. In the DFT+U method, the Hubbard correction U was used to account for strong on-site Coulombic interactions between the localized d and f electrons of Ta and Eu, respectively within Dudarev's approach[164]. Values of 7.3 eV and 1.1 eV kept fixed for the Hubbard U correction and exchange interaction parameter J, respectively for the f orbitals of Eu are well reported in the literature[310]. The corresponding values of U and J used for the d orbitals of Ta were 5 eV and 1 eV, respectively. The structure optimization was done with the gamma-centered k-point mesh of $5 \times 5 \times 2$ to get more converged results. A kinetic energy cut-off of 520 eV was used for the plane-wave basis set. The superlattice structure of EuO/KTO was made up of two symmetric n-type interfaces $(EuO)^0/(TaO_2)^+$. Bulk KTO and the rock salt EuO have lattice constants of 3.98 and 5.14 Å, respectively. As a result, the EuO cell is rotated at a 45° angle to match the perovskite KTO (substrate) in [001] orientation. The successful growth of EuO films on KTO substrate by experimental groups justifies the high lattice mismatch of –8.8% between the EuO and KTO systems[13,122,123]. SOC was considered in the second-variational technique, which was implemented in VASP, with magnetization in the direction of the quantization axis along (001). The spin quantization axis was rotated from the x-y plane (in-plane) to the z-axis (perpendicular to the interface) for MAE calculations, where the magnetic moment values were kept constant. To get a more accurate value for MAE, the convergence criterion was raised to 10^{-6} eV for self-consistent calculations including SOC. To confirm the non-trivial topology of the electronic band structure, the Berry curvature and the Chern number were calculated with the VASPBERRY code[237] using the Bloch wavefunctions output by the VASP code. PyProcar code[203] was used to plot the spin texture on the constant energy contour in the reciprocal space considering the non-collinear SOC calculations using the VASP.

4.3 Electronic structure

Rare-earth monochalcogenide EuO in its bulk form has a rocksalt crystal structure and is a ferromagnetic semiconductor in the ground state. FM ordering is driven by the Heisenberg exchange coupling between the localized Eu-4f moments of 6.9 μ_B /Eu below its Curie temperature (T_C) of 69K[311]. The experimental electronic energy gap is 1.12 eV in EuO, at room temperature[312]. Due to its exceptional semiconducting and ferromagnetic (FM) properties, the rare-earth compound EuO has garnered considerable attention for a long time and has potential in semiconductor-based spintronics such as spin-filter tunnel barriers[313,314].

Using spin-polarized calculations, a magnetic moment value of 6.9 μ_B is observed on the localized 4f states of Eu. In order to get an idea of the relative position and occu-

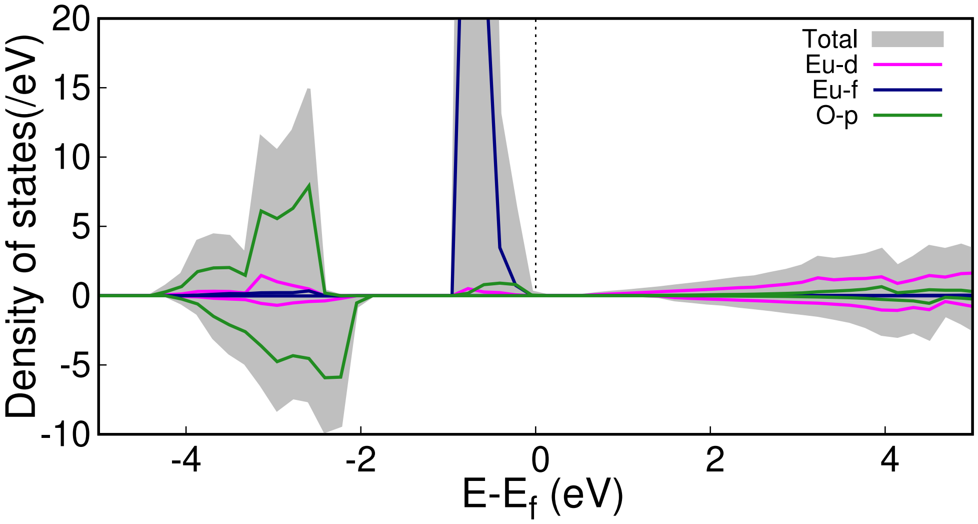

Figure 4.1: Total as well as atomic and orbital projected DOS in bulk EuO with spin-polarization.

pation of 5d and 4f orbitals, the total and orbital-projected DOS for the ferromagnetic EuO is calculated with spin-polarization and is shown in Fig. 4.1. A gap of 0.74 eV is found between the valence and conduction bands in our calculations. This calculated value is slightly lesser than the experimental reported value of 1.12 eV[315]. A sharp peak corresponding to Eu-4f spin-up states is observed just below the Fermi level. The conduction band is mainly composed of Eu-d states in addition to a small contribution from O-p states. On the other hand, the valence band below the Eu-4f peak is composed of O-p states with a major contribution, along with a small contribution from Eu-5d states. It is to be noted that in the Eu-4f peak, Eu-5d states are also there with lower density. The valence band is the admixture of p states of O and 5d and 4f states of Eu. Thus there is hybridization of the d and f states of Eu near the Fermi level. This causes the spin splitting of 5d states of Eu which is induced by the localized 4f spins. As a result, the ferromagnetic ordering in EuO is described by the super-exchange interactions between 4f and 5d orbitals of Eu. Next, the spin-polarized electronic band structure of bulk ferromagnetic EuO is calculated along the high symmetry path Γ-X-W-L-Γ-K-X and is illustrated in Fig. 4.2. It is observed that the semiconducting gap is a direct band gap with the valence band maximum and conduction band minimum at the Γ point. The nearly flat bands appearing right below the Fermi level corresponding to the sharp peak in the DOS plot, are formed by highly localized 4f spin-up states. In contrast, spin-split

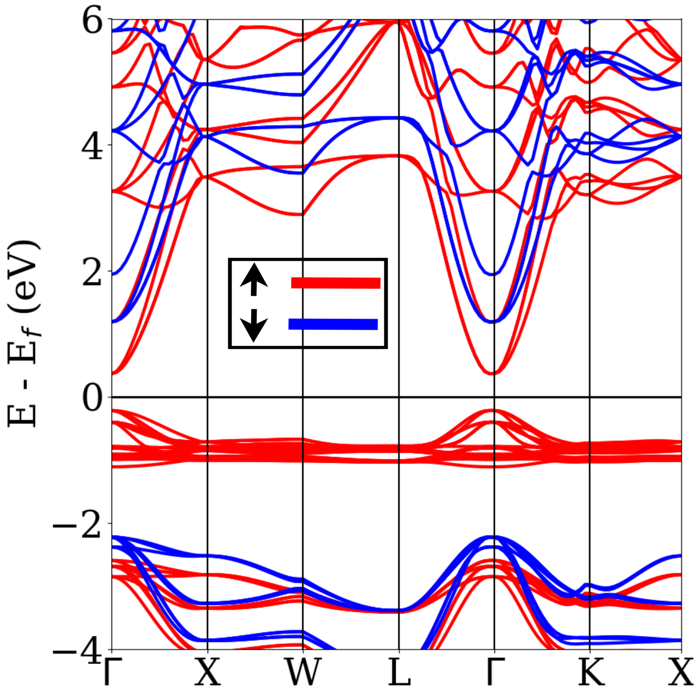

Figure 4.2: Spin-polarized electronic band structure of bulk EuO along the high symmetry path Γ-X-W-L-Γ-K-X. Red and blue lines correspond to the majority and minority spin states, respectively.

conduction band states above the Fermi level, which are produced by 5d states of Eu, are quite dispersive.

To determine the electronic properties of the EuO/KTO superlattice, we calculate the spin-polarized electronic structure using first-principles calculations. In Fig. 4.3 (a), the computed total DOS is displayed along with the orbital projection on the atoms. The plot illustrates the metallic n-type conducting heterointerface with partially occupied states at the Fermi level or 2DEG with the spin splitting of the electronic states. Polar KTO is made up of alternating $(KO)^-$ and $(TaO_2)^+$ charged planes whereas FM EuO consists of $(EuO)^0$ neutral planes. The HS is composed of nonstoichiometric KTO substrate terminated with the (TaO_2) monolayers on both sides to have two symmetric EuO/TaO_2 interfaces. The extra $(TaO_2)^+$ monolayer induces unbalance of charge, leading to electron doping in the HS giving rise to 2DEG.

To determine the spatial distribution of the 2DEG in the depth of the superlattice structure, we calculate the layer-wise DOS projected on the atomic layers. Due to the

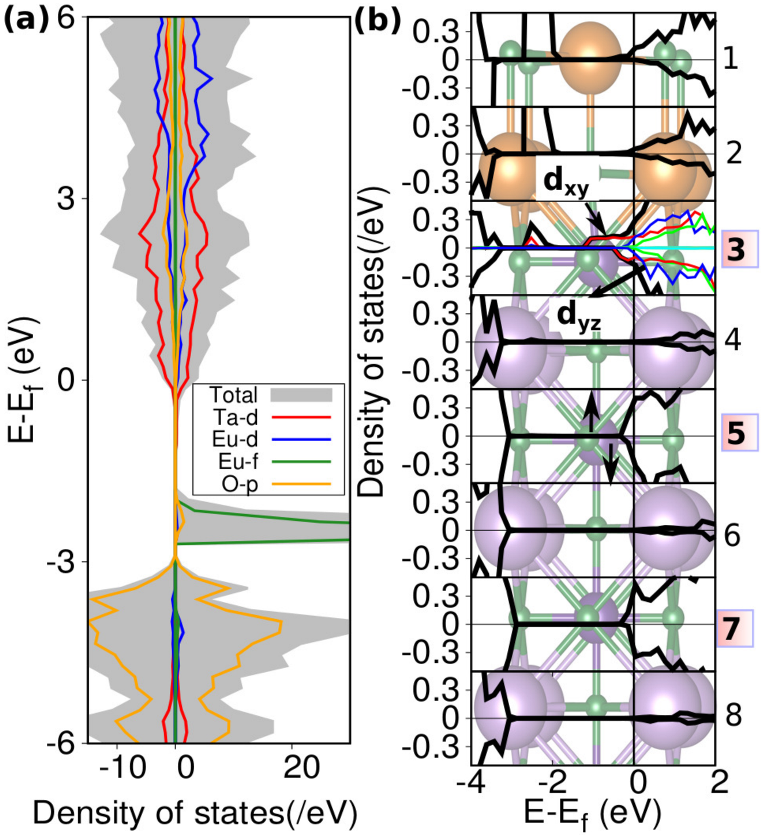

Figure 4.3: Spin-polarized DOS (a) Total DOS along with the orbital projection on the corresponding atoms, (b) Layer-wise projected DOS on the atomic layers shown in the background of the plot.

mirror symmetry of the superlattice structure used for the calculations, only the first 8 layers are shown in the DOS plot (Fig. 4.3 (b)), with the atomic layers shown in the background and the layer number marked on the right. The first two EuO layers contribute to the states at the Fermi level to some extent whereas the KO layers (numbered 4, 6, and 8) do not contribute to the conducting states at the Fermi energy. The TaO_2 layer at the interface (marked as 3) makes the most contribution to the 2DEG or states at the Fermi level. Furthermore, the projection on the d orbitals of Ta in the interfacial layer (numbered 3) as shown by colored lines depicts the major contribution from d_{xy} orbitals at the interface. As we go away from the interface, the contribution of TaO_2 layers starts to diminish. This illustrates the confinement of the 2DEG at the interfacial TaO_2 layer on the KTO side. The exchange splitting of electronic states follows a simi-

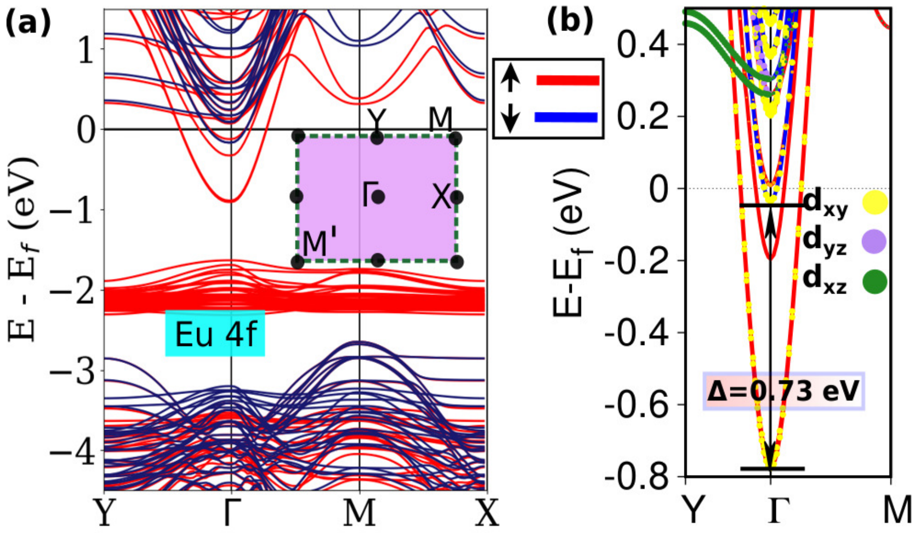

Figure 4.4: Spin-polarized electronic band structure (a) Band structure plot of the EuO/KTO superlattice along the high symmetry path Y-Γ-M-X in the 2D Brillouin zone as shown in the inset, with red and blue lines representing up and down spin, respectively. (b) d-orbital projected band structure plot along the path Y-Γ-M with the value of exchange splitting in the d$_{xy}$ orbitals indicated in the figure.

lar pattern, with the highest value found at the interfacial TaO$_2$ layer. As a result of lifted degeneracy caused by broken inversion symmetry at the interface, the light d$_{xy}$ band is split towards lower energy in comparison to the two heavier d$_{xz}$ and d$_{yz}$ bands. Only the d$_{xy}$ band is occupied at low carrier densities or at low Fermi levels, and therefore only one type of carrier is used for transport. Further, the spin-polarized band structure calculated along the high symmetry path Y-Γ-M-X as shown in Fig. 4.4 (a) reveals the parabolic bands near the Fermi level around Γ. There are multiple band crossing points between the majority and minority spin bands in Γ-M and Y-Γ directions. Along the Y-Γ-M path, we can see heavy bands somewhat above the Fermi level, in addition to the light parabolic bands. To investigate the orbital characteristics of these bands, band structure with projection on the 5d orbitals of Ta along the path Y-Γ-M around the Fermi level is shown in Fig. 4.4 (b). In the 2DEG, we see two types of charge carriers with different orbital characteristics. Due to the splitting of t$_{2g}$ states, the d$_{xy}$ orbitals primarily confined at the interfacial layer create the light parabolic bands closer to the Fermi energy, but the anisotropic heavy d$_{xz}$/d$_{yz}$ states are relatively away from the Fermi level. This is because of the reduction in symmetry and the orbital reconstruction at the interface. 2DEG involving the d_{xy} orbitals of interfacial Ta has a significant exchange splitting of 0.73 eV resulting in a spin-polarized interface channel. The substantial exchange splitting between the two spin channels of $5d_{xy}$ orbitals of interfacial Ta atom due to hybridization with the exchange-split d orbitals of Eu atoms caused by the proximity effect is the fundamental source of magnetism. To analyze the band crossing points along Γ-M direction with d_{xy} orbital character (responsible for interfacial magnetism) near the Fermi level, the band structure along the M'-Γ-M path is illustrated in Fig. 4.5. The oppositely polarized spin bands with the crossing points α_1 and α_2 near the Fermi level are zoomed in the inset of Fig. 4.5. These band crossing points appearing in the Ta states open up the possibility of creating a non-trivial topological gap as SOC is turned on, which will be addressed later.

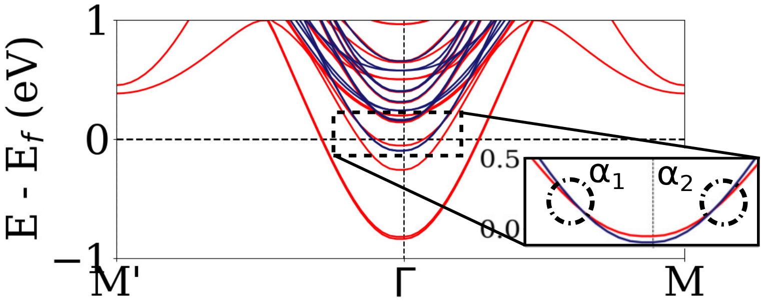

Figure 4.5: Band structure along M'-Γ-M path with the band crossing points of majority and minority spin states, α_1 and α_2 are zoomed in the inset.

4.4 Spin and Charge density

Bulk EuO is an FM semiconductor with a magnetic moment of 6.9 μ_B per Eu ion. The spin-polarized states localized on Eu 4f bands interact with the conduction band formed by 5d orbitals, resulting in a substantial exchange splitting of 0.6 eV of the empty conduction band. To calculate the magnetic moment on the individual atoms in the superlattice due to the proximity effect, we perform spin-polarized calculations. The magnetic moment generated on Eu atoms by f orbitals is calculated to be $6.9\mu_B$, which agrees well with the bulk value. We also observe an induced magnetic moment of $0.165\mu_B$ localized at the interfacial Ta atoms, originating from 5d orbitals. We calculate the spin polarization at the Fermi level using equation 4.1, where $\rho_\uparrow$ and $\rho_\downarrow$ are the total up and down spin DOS at the Fermi level, respectively. The spin polarization at the Fermi level is calculated to be 0.294, a positive value indicates that spin-up states dominate spin-down states at the Fermi level, implying ferromagnetism at the interface.

$$P = \frac{\rho_{\uparrow} - \rho_{\downarrow}}{\rho_{\uparrow} + \rho_{\downarrow}} \tag{4.1}$$

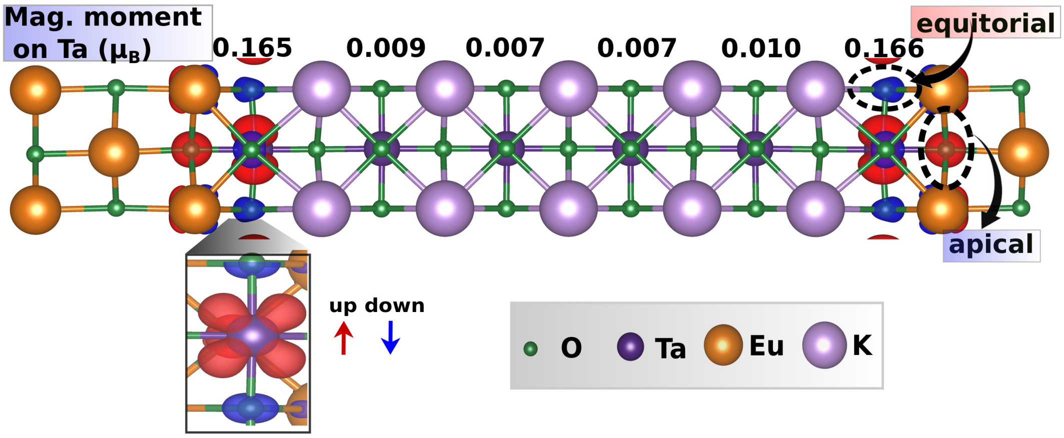

Figure 4.6: Spin density distribution of the EuO/KTO superlattice with red (up spin) and blue (down spin) isosurfaces. The inset of the figure shows the top view of the interfacial TaO_2 layer with the induced spin density in d_{xy} orbitals.

We have shown isosurface plots for spin density distribution in Fig. 4.6 to get information about the induced spin density at the interface. The net spin accumulation at the interface is seen in the isosurface plots with red and blue colors showing up and down spin densities, respectively. The spin density on the Ta atoms in the interfacial layer is seen as red hue isosurfaces. Planar oxygen atoms in the interfacial TaO_2 layer have a magnetic moment or spin density that is opposite to that of the Ta atoms, whereas apical oxygen atoms in the next EuO layer have a magnetic moment that is parallel to that of the interfacial Ta atoms. The induced spin density in the d_{xy} orbitals of the Ta atom responsible for the spin-polarized 2DEG is further confirmed in the top view of the interfacial TaO_2 layer in the inset of Fig. 4.6. Fig. 4.6 also shows the values of the induced magnetic moment on the Ta atoms in the TaO_2 layers in EuO/KTO superlattice. To get a quantitative picture of the spatial distribution of 2DEG with superlattice depth, we integrate the partial DOS projected on each layer from E-E_f = -0.77 eV (bottom of 2DEG) to E_f (Fermi energy) to get the electron number occupation of each layer, which produces the metallic states of 2DEG at the Fermi level, as shown in Fig. 4.7 (a).

This confirms that the electrons in the 2DEG are primarily localized on the KTO side, particularly at the interfacial TaO_2 layer, as previously stated. The number of electrons continues to drop as we go away from the interfacial layer. The charge carrier density of the 2DEG at the interface is calculated from the electron number occupation of the interfacial TaO_2 layer designated as 3. The corresponding values of carrier density of 2DEG at the interface n_{up} and n_{down} are 1.00×10^{14} cm^{-2} and 0.38×10^{14} cm^{-2} in the majority and minority spin states, respectively. The charge transfer at the interface is depicted by the differential charge density plots of the EuO/KTO superlattice, as illustrated in Fig. 4.7 (b). Accumulation (depletion) of electronic charge density is represented by the yellow (blue) color in the plot. There is relatively little variation on the Eu atom in terms of charge transfer, the interfacial Ta atom, on the other hand, shows significant accumulation and depletion of electrons in certain orbitals. The accumulated electrons in Ta occupy d_{xy} orbitals and d_{yz}/d_{xz} orbitals show depletion of electrons. As a result, there is a redistribution of charge in the 5d orbitals of interfacial Ta atoms. Also, charge accumulates in the p orbitals of O atoms in the interfacial EuO and TaO_2 layers due to the O atom's high electronegativity.

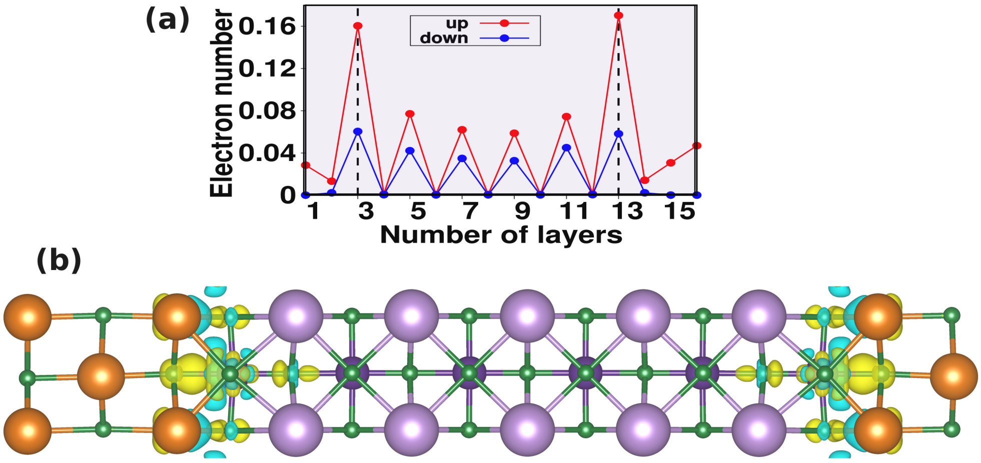

Figure 4.7: (a) Layer decomposition of electron occupation in the 2DEG (b) Differential charge density plot of the EuO/KTO superlattice. The yellow color represents electron accumulation, while the blue color represents electron depletion.

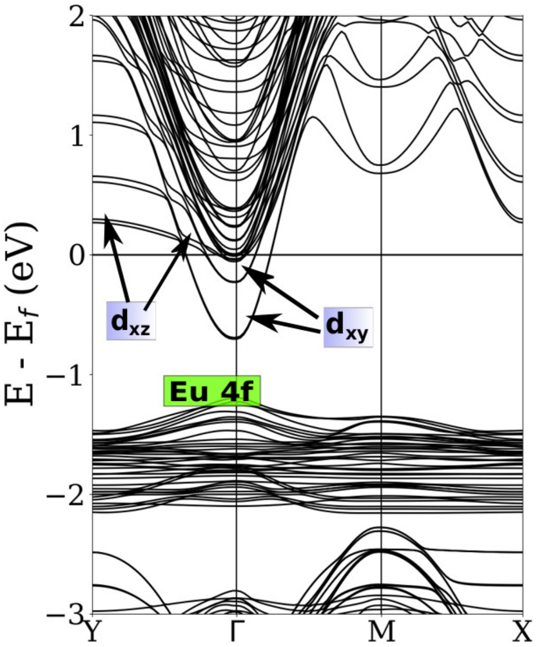

Figure 4.8: The band structure of the EuO/KTO superlattice with SOC with the orbital character of the bands marked in the figure.

4.5 Rashba SOC and Berry curvature

To investigate the effect of spin-orbit interaction, SOC is incorporated into the electronic structure calculations. Fig. 4.8 depicts the band structure with SOC in the 2D Brillouin zone displaying the orbital character of the bands. It is quite interesting to note that we do not see the conventional Rashba splitting in the bands, which consists of two parabolas that are offset horizontally. Next, we wish to see the influence of SOC on the band crossing points α_1 and α_2 around the Γ point towards the M' and M points, respectively near the Fermi level (as shown in the inset of fig. 4.5). It is noticed that the Rashba spin-orbit gap ($\sim$ 4.8 meV) appears to be opened at these band crossing points as seen in the inset of Fig. 4.9, whereas, the system remains metallic with two highly dispersive bands crossing the Fermi level. It is significant to notice that the bands in the graphene-BaMnO$_3$ system do not exhibit the conventional Rashba splitting (two horizontally displaced parabolas) as also seen in EuO/KTO HS here. Also, the crossing points of the majority and minority spin bands, create a Rashba spin-orbit gap including SOC[307]. The broken time-reversal symmetry induced by the interfacial magnetic ordering caused by the proximity effect of EuO in the superlattice could give rise to non-trivial topology around these SO-induced gaps. To confirm the non-trivial topology of the electronic structure, the Berry curvature Ω(k) is calculated along the high symmetry path M'-Γ-M for the bands around the Fermi level as shown in Fig. 4.9 together with the corresponding bands. The negative peaks of Ω(k) are observable at the momenta of SO gaps around the Γ point (Fig. 4.9). Further, the anomalous Hall conductivity (AHC) σ_{xy} is related to the Chern number C by σ_{xy}=Ce^2/h. We calculate the Chern number for the occupied bands with the VASPBERRY code based on Fukui's approach[316] by integrating the Berry curvature Ω_n(k) of each nth energy band over the entire BZ and summing over all occupied bands using equation (2),

$$C = \sum_n \frac{1}{2\pi} \int_{BZ} d^2k \Omega_n(k) \tag{4.2}$$

A general way to calculate the gap Chern number is to add the Chern numbers of all the bands below the band gap ($C_{gap} = \sum C_i$). We find the n-type metallic electronic structure with a gap between the valence and conduction bands and Fermi level crossing the conduction bands in EuO/KTO HS. We determine the Chern number of the SO gap by adding the Chern numbers C_i for all the bands up to the Fermi energy. We can incorporate the occupied states in the conduction bands below the Fermi level, by including the contribution from these bands to the Chern number as well. This also contains the two bands with the SOC-induced gaps at α_1 and α_2. With a magnitude of 6, the estimated Chern number, C=−6, indicates the existence of six topologically protected chiral edge states. In a few other systems, large Chern values up to C = 6 have already been reported[317,318].

Moreover, the idea that one can determine the Chern number of occupied states for semiconductors is generally understood. Whereas the metallic electronic structures like those in the current EuO/KTO instance are peculiar. Nonetheless, the Chern number has been calculated for metallic electronic states in a few previous studies[318,319]. Lukas et al.[318] reported two potential QAHE states in the 2D limit of magnetic Weyl semimetal $Co_3Sn_2S_2$ based on stoichiometry. The monolayer with the stoichiometry Co_3SnS_2 is found to be a semimetal with a Chern number of 6. The energy-dependent AHC for Co_3SnS_2 monolayer reaches up to almost 6e^2/h corroborating the quantization of the AHC. However, since Co_3SnS_2 lacks a global band gap, its AHC changes sharply as

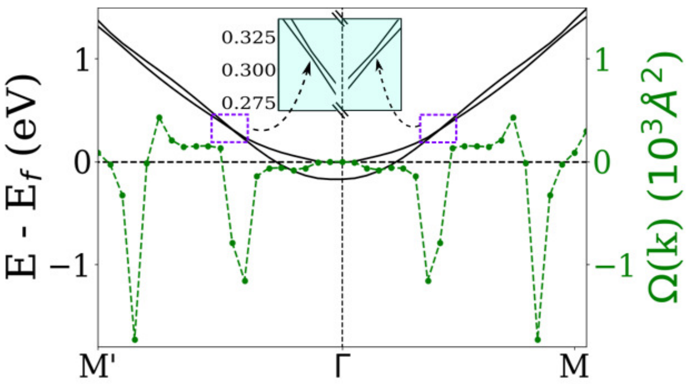

Figure 4.9: The Berry curvature along the high symmetry path M'-Γ-M along with the bands having the Rashba spin-orbit gap opened at the crossing points α_1 and α_2. The zoomed-in spin-orbit gaps are shown in the inset.

the energy varies around E$_f$. Because Co_3SnS_2 monolayer is semimetallic, the projections of the bulk conduction and valence are separated by a gap, which is joined by six edge bands. The aforementioned illustration vividly highlights the importance of obtaining a non-zero Chern number in a system that has the potential of hosting non-trivial topological chiral edge states but lacks the global gap. It is worth mentioning here that on the same grounds of obtaining non-zero Chern numbers, it was expected that ferromagnetic $RuCl_3$ and $RuBr_3$ monolayers and $BaTiO_3$/Ba_2FeReO_6/$BaTiO_3$ heterostructures would exhibit QAHE. But because the systems were overall metallic, a gap would need to be created, potentially with the help of strain engineering, to acquire the quantized portion of conductivity[319,320]. Additionally, the graphene-$BaMnO_3$ system realizes a hybrid QAH state with the trivial metallic states at the fermi level against the backdrop of topologically non-trivial bands with a robust quantized anomalous Hall conductivity[307]. Similar to the preceding point, strain engineering may be used to establish the gap necessary to produce this quantized portion of anomalous Hall conductivity in the EuO/KTO system by pushing apart the two additional bands that exist at the fermi level. As a result of proximity coupling between ferromagnetic insulator EuO and the perovskite oxide KTO containing heavy metal atom Ta, non-trivial topological states are found at the interface of EuO/KTO.

We also calculate the spin texture of the bands having SO gap on the constant energy contour in the reciprocal space. The constant energy contour has fourfold symmetry as seen in Fig. 4.10. A section of the in-plane counterclockwise tangent electron spins

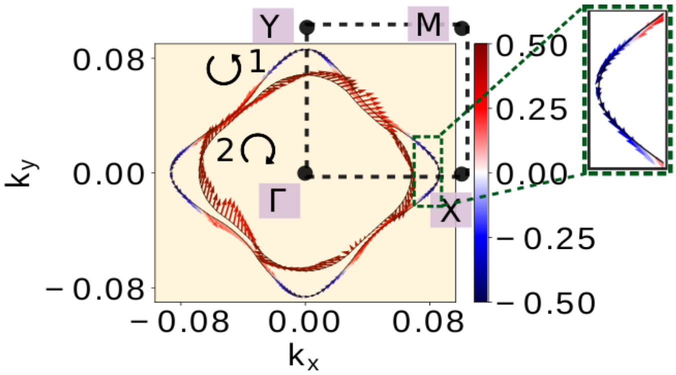

Figure 4.10: The spin texture of the bands with the Rashba spin-orbit gap on the constant energy contour in reciprocal space. A portion of the anticlockwise helical spin of the outer band labeled 1 is zoomed in the inset.

in a helical pattern signifying the linear Rashba effect for the outer band labeled 1 is zoomed in the inset of Fig. 4.10. The inner band marked as number 2 depicts a single winding of electron spin i.e. electron spin completes a single revolution by 2π without changing its chirality as it moves clockwise around constant energy contour in a helical pattern.

Finally, the value of the MAE has been obtained according to the expression $MAE = E_{\perp} - E_{||}$ to find the direction of the easy magnetization axis in the EuO/KTO heterointerface. In the above expression, the $E_{\perp}$ and $E_{||}$ are the total energies of the EuO/KTO superlattice determined with the magnetization direction perpendicular and parallel to the interfacial plane, respectively. The total energy values are calculated by changing the magnetization axis from the in-plane direction [100] to out-of-plane [001] direction. The MAE for this superlattice is determined to be -0.7 meV; a negative value indicating the PMA[321], which is important for spintronic and magnetoelectronic applications. Thus the spins are oriented out-of-plane or perpendicular to the interface. The computed MAE value in the EuO/KTO superlattice is comparable to that in the LSMO/LAO superlattice[321].

4.6 Conclusions

In conclusion, we investigate the spin-polarized 2DEG at the interface of the EuO/KTO superlattice using first-principles calculations. We show that the magnetic ordering at the interface is related to the occupation of more extended $5d_{xy}$ orbitals of Ta with

0.165 μ_B magnetic moment in the d orbitals per Ta atom. A substantial exchange splitting value of 0.73 eV larger than that of bulk EuO is observed. The gap-opening at the crossing point of majority and minority spin states, on incorporating the SOC raises hope for the presence of non-trivial topological states. The pronounced negative spikes of Berry curvature $\Omega(k)$ at the momenta of these SO gaps around the Fermi level and the integral value of Chern number confirms the non-trivial topology of the band structure. If the additional bands at the fermi level can be driven away such as through strain engineering, it can display QAH insulating characteristics. The spin texture of the bands with the SO gap on the constant energy contour in the reciprocal space reveals the helical spin texture with single spin winding having opposite chirality, characteristic of the Rashba effect. According to the negative MAE, the magnetic easy axis is perpendicular to the interfacial plane. As a result, our study adds a viable option to the list of magnetic oxide interfaces with PMA, the Rashba effect with a distinct helical spin texture as well as the non-trivial topological states, which are highly desirable in the low-power spintronics, spin-orbitronics, and nanoelectronics.

CHAPTER 5

Summary and Future Outlook

"I never think of the future – it comes soon enough."

Albert Einstein

5.1 Summary

This final Chapter of the thesis provides an overview of the key conclusions of the research work that have been provided in the form of individual chapters.

Chapter 1 begins with a succinct backdrop of the study. The next section of this chapter provides an overview of strongly correlated materials, including Mott-Hubbard and charge-transfer insulators. After that, it provides a quick review of 2D magnetic TMC and oxide heterostructures, two classes of strongly correlated materials. We have also included a brief history of magnetism in solids and the exchange interactions that mediate the magnetic ordering in order to provide some understanding of magnetism in solid-state systems. The concept of SOC has then been explained, with emphasis placed on the Rashba effect and its emergence in oxide heterostructures, followed by a short description of SOC-driven topological states, particularly the quantum anomalous Hall effect (QAHE). Towards the end of chapter 1, the theoretical background of various computational methods useful in understanding the calculation of results presented in this thesis has been provided.

Chapter 2 infers to the ab initio study of electronic and ground state magnetic properties in bulk and layered transition metal chalcogenides. In this context, the first section of this chapter investigates the electronic structure and magnetic ordering in triclinic $CuSeO_3$. The electronic structure suggests that $CuSeO_3$ in the triclinic phase is a charge-transfer insulator. We find the non-collinear antiferromagnetic configuration as the ground-state magnetic ordering. This can be attributed to the hybridization of Cu-d and O-p orbitals, giving rise to Cu-O-Cu superexchange interactions. We observe a spiral spin texture in the reciprocal space with a finite out-of-plane spin component. Spintronics of such non-collinear antiferromagnetic charge transfer insulating states is a relatively new and rapidly developing field of physics. In the following section of this chapter, the vdW layered transition metal ternary chalcogenide CoAsS with strong electron correlations is explored for its potential in spintronics. The dynamically stable CoAsS monolayer via its rich magnetic and electronic phase diagram has been demonstrated as a quasi-2D magnetic material. Because of the broken time-reversal symmetry and SOC, a topological state with a non-trivial Chern number is revealed at the critical Coulomb parameter using Kubo's approach. These results make the CoAsS monolayer very appealing for low-power-consumption nanoelectronics and spintronics.

Chapter 3 focuses on the emergent phenomena in perovskite oxide heterostructures based on polar perovskite oxide $LaVO_3$ (LVO). In this regard, the first section of the chapter explores the electronic properties in the heterostructure between a Mott insulator LVO and a band insulator $SrTiO_3$ (STO) with two distinct orientations (001) and (111). The electronic structure confirms that this heterointerface comprising two bulk insulators is n-type metallic in both orientations. Because of the peculiar orbital reconstruction at the two interfaces, we notice the difference in orbital occupation as well as orbital degeneracies. Furthermore, the Fermi surface reveals fourfold/sixfold symmetry as well as the presence/absence of open orbits in the (001)/(111) orientations. Thus, unique orbital-occupation and degeneracies due to orbital reconstruction as well as symmetry of Fermi surface highlights the important role played by crystal field in determining the electronic properties in LVO/STO heterostructure. In the subsequent section of this chapter, we have examined the (001) and (111) surfaces of polar perovskite oxide $KTaO_3$ (KTO) terminated with the Ta atoms for electronic and spintronic properties. We observed the presence of 2DEG with parabolic bands near the Fermi level at both the surfaces of KTO. The distribution of 2DEG is primarily contained in the surface layers of KTO in the 5d orbitals of Ta atoms. Due to the significant SOC of Ta atoms and the breaking of inversion symmetry at the surfaces, the Rashba spin splitting is visible in the bands. The spin texture on the Fermi surface and constant energy contours corroborate the 2D nature of the Rashba spin splitting on the (001) surface, While a complicated spin structure is seen on the surface of (111)-KTO. The final section of this chapter is devoted to the emergent properties in polar-polar heterostructure of perovskite oxides LVO and KTO depending on the crystal orientation. The charge transfer from the surface layers to the interfacial region due to the electronic reconstruction mechanism results in high carrier density 2DEG. Momentum-dependent Rashba spin splitting is seen in the electronic bands originating from the symmetry-breaking electric field. We demonstrate the orbital dependence of the Rashba effect in this heterostructure on account of orbital reconstruction at the interface. Spin-splitting is larger at the crossing regions of the d_{xy} and $d_{xz/yz}$ sub-bands. Further, the spin texture of the Rashba-split bands highlights the complexity of the orientation-dependence in the LVO/KTO heterostructure.

Chapter 4 is based on a theoretical understanding of high-mobility, conducting, and spin-polarized 2DEG at the EuO/TaO_2 interface of a ferromagnetic insulator EuO and non-magnetic polar perovskite KTO. The presence of proximity-induced Zeeman exchange splitting and the Rashba spin-orbit field in the EuO/KTO superlattice warrants a thorough examination of the system's detailed electronic band structure to look for the possibility of non-trivial quantum phenomena. 2DEG is confined on the KTO side particularly at the interfacial TaO_2 layer in the d_{xy} orbitals of Ta due to orbital reconstruction as confirmed by distributions of spin and charge density. The substantial exchange splitting (0.73 eV) between the two spin channels of interfacial Ta-5d_{xy} orbitals due to the proximity effect of ferromagnetic EuO results in a spin-polarized 2DEG at the interface. The band crossing points between the majority and minority spin bands open a gap when SOC is turned on. The large spikes of the Berry curvature at the momenta of SO-induced gaps and integral Chern number demonstrate the non-trivial band topology. We observe the Rashba-type spin texture of the bands having the SO-induced gap showing single spin winding of electron spin with opposite chirality without noticing the conventional Rashba splitting in the bands. The magnetic easy axis is perpendicular to the interfacial plane. Hence our findings suggest that EuO/KTO system has potential in low-power quantum electronics, spintronics, and spin-orbitronics.

5.2 Future Outlook

Strain engineering has been extensively employed to modulate physical properties, such as optical, electrical, and magnetic properties by altering the lattice and electronic structure of 2D materials. It appears to be a highly efficient method for controlling the properties of 2D materials due to their exceptional sensitivity to applied strain and ultrahigh flexibility relative to bulk materials. In addition to having the ability to influence the intrinsic vdW magnetism, the strain has the potential to induce magnetism in non-magnetic 2D materials. Another typical method for obtaining adjustable features is the application of an electric field. Since high electric fields (such as those from gates or interfaces) are common in nanosystems, this is especially appropriate for 2D materials. The energy levels of 2D materials can be changed and split by the electric field, which in turn finely controls the electronic structures. Further, charge transfer modifies the local spin population in 2D magnetic materials, modulating the magnetic properties. Therefore, in our future work, we will study the effect of strain and electric field in magnetic and non-magnetic 2D materials to enhance or induce magnetic properties.

Multiferroic behaviour is referred to the co-existence of two or more ferroic orders such as ferroelectricity, (anti-)ferromagnetism, and ferroelasticity. The magnetoelectric effect, which enables the control of electric polarization by a magnetic field and the control of magnetization by an electric field, is one of the functions that can be produced by the strong coupling between several ferroic orders. Therefore, the fervent research on multiferroics has been driven by both the fascinating physics underlying the complex spin-charge ordering in these materials as well as their intriguing potential for use in multifunctional computing and memory systems in the future. As a result, a lucrative research area has developed in conjunction with the consolidation of spintronics, owing to proliferation of spintronic functionalities in multiferroic materials. Oxides concentrate a lot of multiferroic examples, often with a strong magnetoelectric coupling. As a result, oxide heterostructures represent a fascinating platform for the demonstration of magnetoelectric coupling using spintronic functionalities such as magnetoresistance, anisotropic magnetoresistance, giant magnetoresistance, or tunnel magnetoresistance. Therefore, in our future work, multiferroic oxide heterostrutures will be explored for energy-efficient electric field control of magnetism for spintronics applications.

References

[1] P. Olalde-Velasco, J. Jiménez-Mier, J. D. Denlinger, Z. Hussain, and W. L. Yang, "Direct probe of Mott-Hubbard to charge-transfer insulator transition and electronic structure evolution in transition-metal systems," *Phys. Rev. B*, vol. 83, p. 241102, 2011.

[2] N. Nakagawa, H. Y. Hwang, and D. A. Muller, "Why some interfaces cannot be sharp," *Nat. Mater*, vol. 5, no. 3, pp. 204–209, 2006.

[3] S. Blundell, *Magnetism in condensed matter*. Oxford University Press, 2001, ch. 1, pp. 74–82.

[4] J. M. D. Coey, *Magnetism and Magnetic Materials*. Cambridge University Press, 2010, ch. 5, pp. 128–174.

[5] A. Manchon, H. C. Koo, J. Nitta, S. M. Frolov, and R. A. Duine, "New perspectives for Rashba spin–orbit coupling," *Nat. Mater*, vol. 14, no. 9, pp. 871–882, 2015.

[6] T. Uchihashi, "Surface atomic-layer superconductors with Rashba/Zeeman-type spin-orbit coupling," *AAPPS bull.*, vol. 31, no. 1, p. 27, 2021.

[7] H. Weng, X. Dai, and Z. Fang, "From anomalous Hall effect to the quantum anomalous Hall effect," *arXiv: Mater. Sci.*, 2015.

[8] C.-Z. Chang and M. Li, "Quantum anomalous Hall effect in time-reversal-symmetry breaking topological insulators," *J. Phys. Condens. Matter*, vol. 28, no. 12, p. 123002, 2016.

[9] J. M. D. Coey, *Magnetism and Magnetic Materials*. Cambridge University Press, 2010, ch. 1, pp. 1–19.

[10] M. N. Baibich, J. M. Broto, A. Fert, F. N. Van Dau, F. Petroff, P. Etienne, G. Creuzet, A. Friederich, and J. Chazelas, "Giant magnetoresistance of (001)Fe/(001)Cr magnetic superlattices," *Phys. Rev. Lett.*, vol. 61, pp. 2472–2475, 1988.

[11] A. Khvalkovskiy, D. Apalkov, S. Watts, R. Chepulskii, R. Beach, A. Ong, X. Tang, A. Driskill-Smith, W. Butler, P. Visscher, D. Lottis, V. Nikitin, and M. Krounbi, "Basic principles of STT-MRAM cell operation in memory arrays," *J. Phys. D: Appl. Phys.*, vol. 46, p. 074001, 2013.

[12] G. Macam, A. Sufyan, Z.-Q. Huang, C.-H. Hsu, S.-M. Huang, H. Lin, and F.-C. Chuang, "Tuning topological phases and electronic properties of monolayer ternary transition metal chalcogenides (ABX_4, A/B = Zr, Hf, or Ti; X = S, Se, or Te)," *Appl. Phys. Lett.*, vol. 118, no. 11, p. 111901, 2021.

[13] S. Zhang, R. Xu, W. Duan, and X. Zou, "Intrinsic half-metallicity in 2D ternary chalcogenides with high critical temperature and controllable magnetization direction," *Adv. Funct. Mater.*, vol. 29, no. 14, p. 1808380, 2019.

[14] M. M. Abd-Elmeguid, B. Ni, D. I. Khomskii, R. Pocha, D. Johrendt, X. Wang, and K. Syassen, "Transition from Mott insulator to superconductor in $GaNb_4Se_8$ and $GaTa_4Se_8$ under high pressure," *Phys. Rev. Lett.*, vol. 93, p. 126403, 2004.

[15] M. Tsurubayashi, K. Kodama, M. Kano, K. Ishigaki, Y. Uwatoko, T. Watanabe, K. Takase, and Y. Takano, "Metal-insulator transition in Mott-insulator $FePS_3$," *AIP Adv.*, vol. 8, no. 10, p. 101307, 2018.

[16] X. Li and J. Yang, "First-principles design of spintronics materials," *Natl. Sci. Rev.*, vol. 3, no. 3, pp. 365–381, 2016.

[17] C. Ahn, A. Cavalleri, A. Georges, S. Ismail-Beigi, A. J. Millis, and J.-M. Triscone, "Designing and controlling the properties of transition metal oxide quantum materials," *Nat. Mater*, vol. 20, no. 11, pp. 1462–1468, 2021.

[18] Y. Tokura and N. Nagaosa, "Orbital physics in transition-metal oxides," *Science*, vol. 288, no. 5465, pp. 462–468, 2000.

[19] E. Morosan, D. Natelson, A. H. Nevidomskyy, and Q. Si, "Strongly correlated materials," *Adv. Mater.*, vol. 24, no. 36, pp. 4896–4923, 2012.

[20] H. Jiang, "First-principles approaches for strongly correlated materials: A theoretical chemistry perspective," *Int. J. Quantum Chem.*, vol. 115, no. 11, pp. 722–730, 2015.

[21] E. Dagotto and Y. Tokura, “Strongly correlated electronic materials: Present and future,” *MRS Bull.*, vol. 33, p. 1037–1045, 2008.

[22] V. I. Anisimov, J. Zaanen, and O. K. Andersen, “Band theory and Mott insulators: Hubbard U instead of Stoner I,” *Phys. Rev. B*, vol. 44, pp. 943–954, 1991.

[23] A. Walsh, S.-H. Wei, Y. Yan, M. M. Al-Jassim, J. A. Turner, M. Woodhouse, and B. A. Parkinson, “Structural, magnetic, and electronic properties of the Co-Fe-Al oxide spinel system: Density-functional theory calculations,” *Phys. Rev. B*, vol. 76, p. 165119, 2007.

[24] S. S. Ataei, M. R. Mohammadizadeh, and N. Seriani, “Ab initio simulation of the effects of hydrogen concentration on anatase TiO_2,” *J. Phys. Chem. C*, vol. 120, no. 16, pp. 8421–8427, 2016.

[25] J. Zaanen, G. A. Sawatzky, and J. W. Allen, “Band gaps and electronic structure of transition-metal compounds,” *Phys. Rev. Lett.*, vol. 55, pp. 418–421, 1985.

[26] J. Zaanen, G. Sawatzky, and J. Allen, “The electronic structure and band gaps in transition metal compounds,” *J. Magn. Magn. Mater.*, vol. 54-57, pp. 607–611, 1986.

[27] K. S. Novoselov, A. K. Geim, S. V. Morozov, D. Jiang, Y. Zhang, S. V. Dubonos, I. V. Grigorieva, and A. A. Firsov, “Electric field effect in atomically thin carbon films,” *Science*, vol. 306, no. 5696, pp. 666–669, 2004.

[28] P. Johari and V. B. Shenoy, “Tuning the electronic properties of semiconducting transition metal dichalcogenides by applying mechanical strains,” *ACS Nano*, vol. 6, no. 6, pp. 5449–5456, 2012.

[29] B. Xia, D. Gao, and D. Xue, “Ferromagnetism of two-dimensional transition metal chalcogenides: both theoretical and experimental investigations,” *Nanoscale*, vol. 13, pp. 12 772–12 787, 2021.

[30] Y. Tong, Y. Guo, K. Mu, H. Shan, J. Dai, Y. Liu, Z. Sun, A. Zhao, X. C. Zeng, C. Wu, and Y. Xie, “Half-metallic behavior in 2D transition metal dichalcogenides nanosheets by dual-native-defects engineering,” *Adv. Mater.*, vol. 29, no. 40, p. 1703123, 2017.

[31] J. Ge, T. Luo, Z. Lin, J. Shi, Y. Liu, P. Wang, Y. Zhang, W. Duan, and J. Wang, “Magnetic moments induced by atomic vacancies in transition metal dichalcogenide flakes,” *Adv. Mater.*, vol. 33, no. 4, p. 2005465, 2021.

[32] Y. Li, Z. Zhou, S. Zhang, and Z. Chen, "MoS_2 nanoribbons: High stability and unusual electronic and magnetic properties," *J. Am. Chem. Soc.*, vol. 130, no. 49, pp. 16 739–16 744, 2008.

[33] H. Y. Lv, W. J. Lu, J. Y. Li, R. C. Xiao, M. J. Wei, P. Tong, X. B. Zhu, and Y. P. Sun, "Edge-controlled half-metallic ferromagnetism and direct-gap semiconductivity in ZrS_2 nanoribbons," *RSC Adv.*, vol. 7, pp. 33 408–33 412, 2017.

[34] Z. Yang, D. Gao, J. Zhang, Q. Xu, S. Shi, K. Tao, and D. Xue, "Realization of high Curie temperature ferromagnetism in atomically thin MoS_2 and WS_2 nanosheets with uniform and flower-like morphology," *Nanoscale*, vol. 7, pp. 650–658, 2015.

[35] Q. Zhou, S. Su, P. Cheng, X. Hu, M. Zeng, X. Gao, Z. Zhang, and J.-M. Liu, "Robust ferromagnetism in zigzag-edge rich MoS_2 pyramids," *Nanoscale*, vol. 10, pp. 11 578–11 584, 2018.

[36] Z. Zhang, X. Zou, V. H. Crespi, and B. I. Yakobson, "Intrinsic magnetism of grain boundaries in two-dimensional metal dichalcogenides," *ACS Nano*, vol. 7, no. 12, pp. 10 475–10 481, 2013.

[37] H. Shu, P. Luo, P. Liang, D. Cao, and X. Chen, "Layer-dependent dopant stability and magnetic exchange coupling of iron-doped MoS_2 nanosheets," *ACS Appl. Mater. Interfaces*, vol. 7, no. 14, pp. 7534–7541, 2015.

[38] Z. Xiang, Z. Zhang, X. Xu, Q. Zhang, Q. Wang, and C. Yuan, "Room-temperature ferromagnetism in Co doped MoS_2 sheets," *Phys. Chem. Chem. Phys.*, vol. 17, pp. 15 822–15 828, 2015.

[39] J. Wang, F. Sun, S. Yang, Y. Li, C. Zhao, M. Xu, Y. Zhang, and H. Zeng, "Robust ferromagnetism in Mn-doped MoS_2 nanostructures," *Appl. Phys. Lett.*, vol. 109, no. 9, p. 092401, 2016.

[40] P. Manchanda, A. Enders, D. J. Sellmyer, and R. Skomski, "Hydrogen-induced ferromagnetism in two-dimensional Pt dichalcogenides," *Phys. Rev. B*, vol. 94, p. 104426, 2016.

[41] D. Gao, S. Shi, K. Tao, B. Xia, and D. Xue, "Tunable ferromagnetic ordering in MoS_2 nanosheets with fluorine adsorption," *Nanoscale*, vol. 7, pp. 4211–4216, 2015.

[42] J. Luxa, O. Jankovský, D. Sedmidubský, R. Medlín, M. Maryško, M. Pumera, and Z. Sofer, "Origin of exotic ferromagnetic behavior in exfoliated layered transition metal dichalcogenides MoS_2 and WS_2," *Nanoscale*, vol. 8, pp. 1960–1967, 2016.

[43] V. Kanzyuba, S. Dong, X. Liu, X. Li, S. Rouvimov, H. Okuno, H. Mariette, X. Zhang, S. Ptasinska, B. D. Tracy, D. J. Smith, M. Dobrowolska, and J. K. Furdyna, "Structural evolution of dilute magnetic (Sn,Mn)Se films grown by molecular beam epitaxy," *J. Appl. Phys.*, vol. 121, no. 7, p. 075301, 2017.

[44] Y. Zhou, Z. Wang, P. Yang, X. Zu, L. Yang, X. Sun, and F. Gao, "Tensile strain switched ferromagnetism in layered NbS_2 and $NbSe_2$," *ACS Nano*, vol. 6, no. 11, pp. 9727–9736, 2012.

[45] P. Manchanda, V. Sharma, H. Yu, D. J. Sellmyer, and R. Skomski, "Magnetism of Ta dichalcogenide monolayers tuned by strain and hydrogenation," *Appl. Phys. Lett.*, vol. 107, no. 3, p. 032402, 2015.

[46] N. D. Mermin and H. Wagner, "Absence of ferromagnetism or antiferromagnetism in one- or two-dimensional isotropic Heisenberg models," *Phys. Rev. Lett.*, vol. 17, pp. 1133–1136, 1966.

[47] M. Lines, "Examples of two dimensional ordered magnetic systems," *Phys. Lett. A*, vol. 24, no. 11, pp. 591–592, 1967.

[48] R. J. Birgeneau, H. J. Guggenheim, and G. Shirane, "Neutron scattering from K_2NiF_4: A two-dimensional Heisenberg antiferromagnet," *Phys. Rev. Lett.*, vol. 22, pp. 720–723, 1969.

[49] R. Plumier, "Neutron diffraction study of magnetic stacking faults in antiferromagnetic K_2NiF_4," *J. Appl. Phys.*, vol. 35, no. 3, pp. 950–951, 1964.

[50] R. J. Birgeneau, H. J. Guggenheim, and G. Shirane, "Neutron scattering investigation of phase transitions and magnetic correlations in the two-dimensional antiferromagnets $K_2NiF_4, Rb_2MnF_4, Rb_2FeF_4$," *Phys. Rev. B*, vol. 1, pp. 2211–2230, 1970.

[51] Z. Q. Qiu, J. Pearson, and S. D. Bader, "Magnetic phase transition of ultrathin Fe films on Ag(111)," *Phys. Rev. Lett.*, vol. 67, pp. 1646–1649, 1991.

[52] W. Dürr, M. Taborelli, O. Paul, R. Germar, W. Gudat, D. Pescia, and M. Landolt, "Magnetic phase transition in two-dimensional ultrathin Fe Films on Au(100)," *Phys. Rev. Lett.*, vol. 62, pp. 206–209, 1989.

[53] M. Przybylski and U. Gradmann, "Ferromagnetic order in a Fe(110) monolayer on W(110) by Mössbauer spectroscopy," *Phys. Rev. Lett.*, vol. 59, pp. 1152–1155, 1987.

[54] H. J. Elmers, J. Hauschild, H. Höche, U. Gradmann, H. Bethge, D. Heuer, and U. Köhler, “Submonolayer magnetism of Fe(110) on W(110): Finite width scaling of stripes and percolation between islands,” *Phys. Rev. Lett.*, vol. 73, pp. 898–901, 1994.

[55] H. J. Elmers, G. Liu, and U. Gradmann, “Magnetometry of the ferromagnetic monolayer Fe(110) on W(110) coated with Ag,” *Phys. Rev. Lett.*, vol. 63, pp. 566–569, 1989.

[56] D. Kerkmann, D. Pescia, and R. Allenspach, “Two-dimensional magnet at Curie temperature: Epitaxial layers of Co on Cu(100),” *Phys. Rev. Lett.*, vol. 68, pp. 686–689, 1992.

[57] P. Krams, F. Lauks, R. L. Stamps, B. Hillebrands, and G. Güntherodt, “Magnetic anisotropies of ultrathin Co(001) films on Cu(001),” *Phys. Rev. Lett.*, vol. 69, pp. 3674–3677, 1992.

[58] C. A. Ballentine, R. L. Fink, J. Araya-Pochet, and J. L. Erskine, “Magnetic phase transition in a two-dimensional system: p(1×1)-Ni on Cu(111),” *Phys. Rev. B*, vol. 41, pp. 2631–2634, 1990.

[59] D. L. Cortie, G. L. Causer, K. C. Rule, H. Fritzsche, W. Kreuzpaintner, and F. Klose, “Two-dimensional magnets: Forgotten history and recent progress towards spintronic applications,” *Adv. Funct. Mater.*, vol. 30, no. 18, p. 1901414, 2020.

[60] Y. Ma, Y. Dai, M. Guo, C. Niu, Y. Zhu, and B. Huang, “Evidence of the existence of magnetism in pristine VX_2 monolayers (X = S, Se) and their strain-induced tunable magnetic properties,” *ACS Nano*, vol. 6, no. 2, pp. 1695–1701, 2012.

[61] N. Sivadas, M. W. Daniels, R. H. Swendsen, S. Okamoto, and D. Xiao, “Magnetic ground state of semiconducting transition-metal trichalcogenide monolayers,” *Phys. Rev. B*, vol. 91, p. 235425, Jun 2015.

[62] H. L. Zhuang, Y. Xie, P. R. C. Kent, and P. Ganesh, “Computational discovery of ferromagnetic semiconducting single-layer $CrSnTe_3$,” *Phys. Rev. B*, vol. 92, p. 035407, 2015.

[63] X. Li and J. Yang, “$CrXTe_3$ (X = Si, Ge) nanosheets: two dimensional intrinsic ferromagnetic semiconductors,” *J. Mater. Chem. C*, vol. 2, pp. 7071–7076, 2014.

[64] X. Chen, J. Qi, and D. Shi, “Strain-engineering of magnetic coupling in two-dimensional magnetic semiconductor $CrSiTe_3$: Competition of direct exchange interaction and superexchange interaction,” *Phys. Lett. A*, vol. 379, no. 1, pp. 60–63, 2015.

[65] X. Li, X. Wu, and J. Yang, “Half-metallicity in $MnPSe_3$ exfoliated nanosheet with carrier doping,” *J. Am. Chem. Soc.*, vol. 136, no. 31, pp. 11 065–11 069, 2014.

[66] M.-W. Lin, H. L. Zhuang, J. Yan, T. Z. Ward, A. A. Puretzky, C. M. Rouleau, Z. Gai, L. Liang, V. Meunier, B. G. Sumpter, P. Ganesh, P. R. C. Kent, D. B. Geohegan, D. G. Mandrus, and K. Xiao, “Ultrathin nanosheets of $CrSiTe_3$: a semiconducting two-dimensional ferromagnetic material,” *J. Mater. Chem. C*, vol. 4, pp. 315–322, 2016.

[67] W.-B. Zhang, Q. Qu, P. Zhu, and C.-H. Lam, “Robust intrinsic ferromagnetism and half semiconductivity in stable two-dimensional single-layer chromium trihalides,” *J. Mater. Chem. C*, vol. 3, pp. 12 457–12 468, 2015.

[68] M. A. McGuire, H. Dixit, V. R. Cooper, and B. C. Sales, “Coupling of crystal structure and magnetism in the layered, ferromagnetic insulator CrI_3,” *Chem. Mater.*, vol. 27, no. 2, pp. 612–620, 2015.

[69] J. Liu, Q. Sun, Y. Kawazoe, and P. Jena, “Exfoliating biocompatible ferromagnetic Cr-trihalide monolayers,” *Phys. Chem. Chem. Phys.*, vol. 18, pp. 8777–8784, 2016.

[70] J.-U. Lee, S. Lee, J. H. Ryoo, S. Kang, T. Y. Kim, P. Kim, C.-H. Park, J.-G. Park, and H. Cheong, “Ising-Type magnetic ordering in atomically thin $FePS_3$,” *Nano Lett*, vol. 16, no. 12, pp. 7433–7438, 2016.

[71] C. Gong, L. Li, Z. Li, H. Ji, A. Stern, Y. Xia, T. Cao, W. Bao, C. Wang, Y. Wang, Z. Q. Qiu, R. J. Cava, S. G. Louie, J. Xia, and X. Zhang, “Discovery of intrinsic ferromagnetism in two-dimensional van der Waals crystals,” *Nature*, vol. 546, no. 7657, pp. 265–269, 2017.

[72] B. Huang, G. Clark, E. Navarro-Moratalla, R. Cheng, K. L. Seyler, D. Zhong, E. Schmidgall, M. A. McGuire, D. H. Cobden, W. Yao, D. Xiao, P. Jarillo-Herrero, and X. Xu, “Layer-dependent ferromagnetism in a van der Waals crystal down to the monolayer limit,” *Nature*, vol. 546, no. 7657, pp. 270–273, 2017.

[73] X. Wang, K. Du, Y. Y. F. Liu, P. Hu, J. Zhang, Q. Zhang, M. H. S. Owen, X. Lu, C. K. Gan, P. Sengupta, C. Kloc, and Q. Xiong, “Raman spectroscopy of atomically thin two-dimensional magnetic iron phosphorus trisulfide ($FePS_3$) crystals,” *2D Mater.*, vol. 3, no. 3, p. 031009, 2016.

[74] D. J. O’Hara, T. Zhu, A. H. Trout, A. S. Ahmed, Y. K. Luo, C. H. Lee, M. R. Brenner, S. Rajan, J. A. Gupta, D. W. McComb, and R. K. Kawakami, “Room

temperature intrinsic ferromagnetism in epitaxial Manganese Selenide films in the monolayer limit," *Nano Lett.*, vol. 18, no. 5, pp. 3125–3131, 2018.

[75] Y. Deng, Y. Yu, Y. Song, J. Zhang, N. Z. Wang, Z. Sun, Y. Yi, Y. Z. Wu, S. Wu, J. Zhu, J. Wang, X. H. Chen, and Y. Zhang, "Gate-tunable room-temperature ferromagnetism in two-dimensional Fe_3GeTe_2," *Nature*, vol. 563, no. 7729, pp. 94–99, 2018.

[76] C. Tan, J. Lee, S.-G. Jung, T. Park, S. Albarakati, J. Partridge, M. R. Field, D. G. McCulloch, L. Wang, and C. Lee, "Hard magnetic properties in nanoflake van der Waals Fe_3GeTe_2," *Nat. Commun*, vol. 9, no. 1, p. 1554, Apr 2018.

[77] X. Duan, H. Wang, X. Chen, and J. Qi, "Multiple polarization phases and strong magnetoelectric coupling in the layered transition metal phosphorus chalcogenides $TMP_2X_6(T = \mathrm{Cu, Ag}; M = \mathrm{Cr, V}; X = \mathrm{S, Se})$ by controlling the interlayer interaction and dimension," *Phys. Rev. B*, vol. 106, p. 115403, 2022.

[78] M. J. Swamynadhan and S. Ghosh, "Designing multifunctional two-dimensional layered transition metal phosphorous chalcogenides," *Phys. Rev. Materials*, vol. 5, p. 054409, 2021.

[79] Z. Zhang, J. Li, M. Xie, W. Zhuo, D. T. Adroja, P. J. Baker, T. G. Perring, A. Zhang, F. Jin, J. Ji, X. Wang, J. Ma, and Q. Zhang, "Low-energy spin dynamics of the quantum spin liquid candidate $NaYbSe_2$," *Phys. Rev. B*, vol. 106, p. 085115, 2022.

[80] M. Aapro, M. N. Huda, J. Karthikeyan, S. Kezilebieke, S. C. Ganguli, H. G. Herrero, X. Huang, P. Liljeroth, and H.-P. Komsa, "Synthesis and properties of monolayer MnSe with unusual atomic structure and antiferromagnetic ordering," *ACS Nano*, vol. 15, no. 8, pp. 13 794–13 802, 2021.

[81] Y. L. Huang, W. Chen, and A. T. S. Wee, "Two-dimensional magnetic transition metal chalcogenides," *SmartMat*, vol. 2, pp. 139–153, 2021.

[82] P. Zubko, S. Gariglio, M. Gabay, P. Ghosez, and J.-M. Triscone, "Interface physics in complex oxide heterostructures," *Annu. Rev. Condens. Matter Phys.*, vol. 2, no. 1, pp. 141–165, 2011.

[83] C. L. Prajapat, H. Bhatt, Y. Kumar, T. V. C. Rao, P. K. Mishra, G. Ravikumar, C. J. Kinane, B. Satpati, A. Caruana, S. Langridge, S. Basu, and S. Singh, "Interface-induced magnetization and exchange bias in LSMO/BFO multiferroic heterostructures," *ACS Appl. Electron. Mater.*, vol. 2, pp. 2629–2637, 2020.

[84] A. Ohtomo and H. Y. Hwang, “A high-mobility electron gas at the $LaAlO_3/SrTiO_3$ heterointerface,” *Nature*, vol. 427, no. 6973, pp. 423–426, 2004.

[85] Z. Q. Liu, C. J. Li, W. M. Lü, X. H. Huang, Z. Huang, S. W. Zeng, X. P. Qiu, L. S. Huang, A. Annadi, J. S. Chen, J. M. D. Coey, T. Venkatesan, and Ariando, “Origin of the two-dimensional electron gas at $LaAlO_3/SrTiO_3$ interfaces: The role of oxygen vacancies and electronic reconstruction,” *Phys. Rev. X*, vol. 3, p. 021010, 2013.

[86] A. S. Kalabukhov, Y. A. Boikov, I. T. Serenkov, V. I. Sakharov, V. N. Popok, R. Gunnarsson, J. Börjesson, N. Ljustina, E. Olsson, D. Winkler, and T. Claeson, “Cationic disorder and phase segregation in $LaAlO_3/SrTiO_3$ heterointerfaces evidenced by medium-energy ion spectroscopy,” *Phys. Rev. Lett.*, vol. 103, p. 146101, 2009.

[87] A. Brinkman, M. Huijben, M. van Zalk, J. Huijben, U. Zeitler, J. C. Maan, W. G. van der Wiel, G. Rijnders, D. H. A. Blank, and H. Hilgenkamp, “Magnetic effects at the interface between non-magnetic oxides,” *Nat. Mater*, vol. 6, no. 7, pp. 493–496, 2007.

[88] N. Reyren, S. Thiel, A. D. Caviglia, L. F. Kourkoutis, G. Hammerl, C. Richter, C. W. Schneider, T. Kopp, A.-S. Rüetschi, D. Jaccard, M. Gabay, D. A. Muller, J.-M. Triscone, and J. Mannhart, “Superconducting interfaces between insulating oxides,” *Science*, vol. 317, no. 5842, pp. 1196–1199, 2007.

[89] A. D. Caviglia, M. Gabay, S. Gariglio, N. Reyren, C. Cancellieri, and J.-M. Triscone, “Tunable rashba spin-orbit interaction at oxide interfaces,” *Phys. Rev. Lett.*, vol. 104, p. 126803, 2010.

[90] M. Ben Shalom, M. Sachs, D. Rakhmilevitch, A. Palevski, and Y. Dagan, “Tuning spin-orbit coupling and superconductivity at the $SrTiO_3/LaAlO_3$ interface: A magnetotransport study,” *Phys. Rev. Lett.*, vol. 104, p. 126802, 2010.

[91] J. D. Burton and E. Y. Tsymbal, “Tunneling anisotropic magnetoresistance in a magnetic tunnel junction with half-metallic electrodes,” *Phys. Rev. B*, vol. 93, p. 024419, 2016.

[92] M. Bowen, A. Barthélémy, M. Bibes, E. Jacquet, J.-P. Contour, A. Fert, F. Ciccacci, L. Duò, and R. Bertacco, “Spin-polarized tunneling spectroscopy in tunnel junctions with half-metallic electrodes,” *Phys. Rev. Lett.*, vol. 95, p. 137203, 2005.

[93] Z. Liao, M. Huijben, Z. Zhong, N. Gauquelin, S. Macke, R. J. Green, S. Van Aert, J. Verbeeck, G. Van Tendeloo, K. Held, G. A. Sawatzky, G. Koster, and G. Rijnders, “Controlled lateral anisotropy in correlated manganite heterostructures by interface-engineered oxygen octahedral coupling,” *Nat. Mater*, vol. 15, no. 4, pp. 425–431, 2016.

[94] F. Y. Bruno, M. N. Grisolia, C. Visani, S. Valencia, M. Varela, R. Abrudan, J. Tornos, A. Rivera-Calzada, A. A. Ünal, S. J. Pennycook, Z. Sefrioui, C. Leon, J. E. Villegas, J. Santamaria, A. Barthélémy, and M. Bibes, “Insight into spin transport in oxide heterostructures from interface-resolved magnetic mapping,” *Nat. Commun*, vol. 6, no. 1, p. 6306, 2015.

[95] L. You, C. Lu, P. Yang, G. Han, T. Wu, U. Luders, W. Prellier, K. Yao, L. Chen, and J. Wang, “Uniaxial magnetic anisotropy in $La_{0.7}Sr_{0.3}MnO_3$ thin films induced by multiferroic $BiFeO_3$ with striped ferroelectric domains,” *Adv. Mater.*, vol. 22, no. 44, pp. 4964–4968, 2010.

[96] D. Pesquera, E. Khestanova, M. Ghidini, S. Zhang, A. P. Rooney, F. Maccherozzi, P. Riego, S. Farokhipoor, J. Kim, X. Moya, M. E. Vickers, N. A. Stelmashenko, S. J. Haigh, S. S. Dhesi, and N. D. Mathur, “Large magnetoelectric coupling in multiferroic oxide heterostructures assembled via epitaxial lift-off,” *Nat. Commun*, vol. 11, no. 1, p. 3190, 2020.

[97] F. Motti, G. Vinai, A. Petrov, B. A. Davidson, B. Gobaut, A. Filippetti, G. Rossi, G. Panaccione, and P. Torelli, “Strain-induced magnetization control in an oxide multiferroic heterostructure,” *Phys. Rev. B*, vol. 97, p. 094423, 2018.

[98] C.-P. Chang, J. G. Lin, H. T. Jeng, S.-L. Cheng, W. F. Pong, Y. C. Shao, Y. Y. Chin, H.-J. Lin, C. W. Chen, J.-R. Yang, C. H. Chen, and M.-W. Chu, “Atomic-scale observation of a graded polar discontinuity and a localized two-dimensional electron density at an insulating oxide interface,” *Phys. Rev. B*, vol. 87, p. 075129, 2013.

[99] C. He, T. D. Sanders, M. T. Gray, F. J. Wong, V. V. Mehta, and Y. Suzuki, “Metal-insulator transitions in epitaxial $LaVO_3$ and $LaTiO_3$ films,” *Phys. Rev. B*, vol. 86, p. 081401, 2012.

[100] D. F. Li, Y. Wang, and J. Y. Dai, “Tunable electronic transport properties of $DyScO_3/SrTiO_3$ polar heterointerface,” *Appl. Phys. Lett.*, vol. 98, no. 12, p. 122108, 2011.

[101] M. Zhang, K. Du, T. Ren, H. Tian, Z. Zhang, H. Hwang, and Y. Xie, “A termination-insensitive and robust electron gas at the heterointerface of two complex oxides,” *Nat. Commun*, vol. 10, pp. 1–6, 2019.

[102] S. Thiel, G. Hammerl, A. Schmehl, C. W. Schneider, and J. Mannhart, “Tunable quasi-two-dimensional electron gases in oxide heterostructures,” *Science*, vol. 313, no. 5795, pp. 1942–1945, 2006.

[103] M. Basletic, J.-L. Maurice, C. Carrétéro, G. Herranz, O. Copie, M. Bibes, E. Jacquet, K. Bouzehouane, S. Fusil, and A. Barthélémy, “Mapping the spatial distribution of charge carriers in $LaAlO_3/SrTiO_3$ heterostructures,” *Nat Mater*, vol. 7, pp. 621–625, 2008.

[104] P. Moetakef, D. G. Ouellette, J. R. Williams, S. James Allen, L. Balents, D. Goldhaber-Gordon, and S. Stemmer, “Quantum oscillations from a two-dimensional electron gas at a Mott/band insulator interface,” *Appl. Phys. Lett.*, vol. 101, no. 15, p. 151604, 2012.

[105] P. Moetakef, T. A. Cain, D. G. Ouellette, J. Y. Zhang, D. O. Klenov, A. Janotti, C. G. Van de Walle, S. Rajan, S. J. Allen, and S. Stemmer, “Electrostatic carrier doping of $GdTiO_3/SrTiO_3$ interfaces,” *Appl. Phys. Lett.*, vol. 99, no. 23, p. 232116, 2011.

[106] R. F. Need, B. J. Isaac, B. J. Kirby, J. A. Borchers, S. Stemmer, and S. D. Wilson, “Interface-driven ferromagnetism within the quantum wells of a rare earth titanate superlattice,” *Phys. Rev. Lett.*, vol. 117, p. 037205, 2016.

[107] P. Xu, T. C. Droubay, J. S. Jeong, K. A. Mkhoyan, P. V. Sushko, S. A. Chambers, and B. Jalan, “Quasi 2D ultrahigh carrier density in a complex oxide broken-gap heterojunction,” *Adv. Mater. Interfaces*, vol. 3, no. 2, p. 1500432, 2016.

[108] P. Perna, D. Maccariello, M. Radovic, U. Scotti di Uccio, I. Pallecchi, M. Codda, D. Marré, C. Cantoni, J. Gazquez, M. Varela, S. J. Pennycook, and F. M. Granozio, “Conducting interfaces between band insulating oxides: The $LaGaO_3/SrTiO_3$ heterostructure,” *Appl. Phys. Lett.*, vol. 97, no. 15, p. 152111, 2010.

[109] A. Annadi, A. Putra, A. Srivastava, X. Wang, Z. Huang, Z. Q. Liu, T. Venkatesan, and Ariando, “Evolution of variable range hopping in strongly localized two dimensional electron gas at $NdAlO_3/SrTiO_3$ (100) heterointerfaces,” *Appl. Phys. Lett.*, vol. 101, no. 23, p. 231604, 2012.

[110] P. Xu, W. Han, P. M. Rice, J. Jeong, M. G. Samant, K. Mohseni, H. L. Meyerheim, S. Ostanin, I. V. Maznichenko, I. Mertig, E. K. U. Gross, A. Ernst, and S. S. P. Parkin, “Reversible formation of 2D electron gas at the $LaFeO_3/SrTiO_3$ interface via control of oxygen vacancies,” *Adv. Mater.*, vol. 29, no. 10, p. 1604447, 2017.

[111] Y. Z. Chen, N. Bovet, F. Trier, D. V. Christensen, F. M. Qu, N. H. Andersen, T. Kasama, W. Zhang, R. Giraud, J. Dufouleur, T. S. Jespersen, J. R. Sun, A. Smith, J. Nygrd, L. Lu, B. Büchner, B. G. Shen, S. Linderoth, and N. Pryds, "A high-mobility two-dimensional electron gas at the spinel/perovskite interface of γ-$Al_2O_3/SrTiO_3$," *Nat. Commun*, vol. 4, no. 1, p. 1371, 2013.

[112] Y. Wang, W. Tang, J. Cheng, M. Behtash, and K. Yang, "Creating two-dimensional electron gas in polar/polar perovskite oxide heterostructures: First-principles characterization of $LaAlO_3/A^{+}B_5{}^{+}O_3$," *ACS Appl. Mater. Interfaces*, vol. 8, pp. 13 659–13 668, 2016.

[113] A. F. Santander-Syro, C. Bareille, F. Fortuna, O. Copie, M. Gabay, F. Bertran, A. Taleb-Ibrahimi, P. Le Fèvre, G. Herranz, N. Reyren, M. Bibes, A. Barthélémy, P. Lecoeur, J. Guevara, and M. J. Rozenberg, "Orbital symmetry reconstruction and strong mass renormalization in the two-dimensional electron gas at the surface of $KTaO_3$," *Phys. Rev. B*, vol. 86, p. 121107, 2012.

[114] N. Wadehra and S. Chakraverty, "Electrostatic memory in $KTaO_3$," *Appl. Phys. Lett*, vol. 114, no. 16, p. 163103, 2019.

[115] K. Ueno, S. Nakamura, H. Shimotani, H. T. Yuan, N. Kimura, T. Nojima, H. Aoki, Y. Iwasa, and M. Kawasaki, "Discovery of superconductivity in $KTaO_3$ by electrostatic carrier doping," *Nat. Nanotechnol*, vol. 6, pp. 408–412, 2011.

[116] K. V. Shanavas and S. Satpathy, "Electric field tuning of the Rashba effect in the polar perovskite structures," *Phys. Rev. Lett.*, vol. 112, p. 086802, 2014.

[117] N. Wadehra, R. Tomar, S. Halder, M. Sharma, I. Singh, N. Jena, B. Prakash, A. De Sarkar, C. Bera, A. Venkatesan, and S. Chakraverty, "Electronic structure modification of the $KTaO_3$ single-crystal surface by Ar^{+} bombardment," *Phys. Rev. B*, vol. 96, p. 115423, 2017.

[118] K. Zou, S. Ismail-Beigi, K. Kisslinger, X. Shen, D. Su, F. J. Walker, and C. H. Ahn, "$LaTiO_3/KTaO_3$ interfaces: A new two-dimensional electron gas system," *APL Mater.*, vol. 3, no. 3, p. 036104, 2015.

[119] H. Zhang, H. Zhang, X. Yan, X. Zhang, Q. Zhang, J. Zhang, F. Han, L. Gu, B. Liu, Y. Chen, B. Shen, and J. Sun, "Highly mobile two-dimensional electron gases with a strong gating effect at the amorphous $LaAlO_3/KTaO_3$ interface," *ACS Appl. Mater. Interfaces*, vol. 9, pp. 36 456–36 461, 2017.

[120] N. Wadehra, R. Tomar, R. M. Varma, R. K. Gopal, Y. Singh, S. Dattagupta, and S. Chakraverty, "Planar Hall effect and anisotropic magnetoresistance in polar-polar interface of $LaVO_3-KTaO_3$ with strong spin-orbit coupling," *Nat. Commun*, vol. 11, no. 1, p. 874, 2020.

[121] S. Goyal, N. Wadehra, and S. Chakraverty, “Tuning the electrical state of 2DEG at $LaVO_3$-$KTaO_3$ interface: Effect of light and electrostatic gate,” *Adv. Mater. Interfaces*, vol. 7, p. 2000646, 2020.

[122] H. Zhang, Y. Yun, X. Zhang, H. Zhang, Y. Ma, X. Yan, F. Wang, G. Li, R. Li, T. Khan, Y. Chen, W. Liu, F. Hu, B. Liu, B. Shen, W. Han, and J. Sun, *Phys. Rev. Lett.*, vol. 121, p. 116803, 2018.

[123] N. Kumar, N. Wadehra, R. Tomar, Shama, S. Kumar, Y. Singh, S. Dattagupta, and S. Chakraverty, “Observation of Shubnikov–de Haas oscillations, planar Hall effect, and anisotropic magnetoresistance at the conducting interface of EuO–$KTaO_3$,” *Adv. Quantum Technol.*, vol. 4, no. 1, p. 2000081, 2021.

[124] M. Wahler, N. Homonnay, T. Richter, A. Müller, C. Eisenschmidt, B. Fuhrmann, and G. Schmidt, “Inverse spin Hall effect in a complex ferromagnetic oxide heterostructure,” *Sci. Rep.*, vol. 6, no. 1, p. 28727, 2016.

[125] M.-J. Jin, S. Y. Moon, J. Park, V. Modepalli, J. Jo, S.-I. Kim, H. C. Koo, B.-C. Min, H.-W. Lee, S.-H. Baek, and J.-W. Yoo, “Nonlocal spin diffusion driven by giant spin Hall effect at oxide heterointerfaces,” *Nano Lett.*, vol. 17, pp. 36–43, 2017.

[126] S. Hurand, A. Jouan, C. Feuillet-Palma, G. Singh, J. Biscaras, E. Lesne, N. Reyren, A. Barthélémy, M. Bibes, J. E. Villegas, C. Ulysse, X. Lafosse, M. Pannetier-Lecoeur, S. Caprara, M. Grilli, J. Lesueur, and N. Bergeal, “Field-effect control of superconductivity and Rashba spin-orbit coupling in top-gated $LaAlO_3/SrTiO_3$ devices,” *Sci. Rep.*, vol. 5, p. 12751, 2015.

[127] A. Fête, S. Gariglio, A. D. Caviglia, J.-M. Triscone, and M. Gabay, “Rashba induced magnetoconductance oscillations in the $LaAlO_3 - SrTiO_3$ heterostructure,” *Phys. Rev. B*, vol. 86, p. 201105, 2012.

[128] D. Bucheli, M. Grilli, F. Peronaci, G. Seibold, and S. Caprara, “Phase diagrams of voltage-gated oxide interfaces with strong Rashba coupling,” *Phys. Rev. B*, vol. 89, p. 195448, 2014.

[129] H. Liang, L. Cheng, L. Wei, Z. Luo, G. Yu, C. Zeng, and Z. Zhang, “Nonmonotonically tunable Rashba spin-orbit coupling by multiple-band filling control in $SrTiO_3$-based interfacial *d*-electron gases,” *Phys. Rev. B*, vol. 92, p. 075309, 2015.

[130] S. Bandyopadhyay and M. Cahay, *Introduction to Spintronics*, 2015, ch. 6, pp. 129–137.

[131] G. Dresselhaus, “Spin-orbit coupling effects in zinc blende structures,” *Phys. Rev.*, vol. 100, pp. 580–586, 1955.

[132] Y. A. Bychkov and É. I. Rashba, “Properties of a 2D electron gas with lifted spectral degeneracy,” *Soviet Journal of Experimental and Theoretical Physics Letters*, vol. 39, p. 78, 1984.

[133] W. Lin, L. Li, F. Doğan, C. Li, H. Rotella, X. Yu, B. Zhang, Y. Li, W. S. Lew, S. Wang, W. Prellier, S. J. Pennycook, J. Chen, Z. Zhong, A. Manchon, and T. Wu, “Interface-based tuning of Rashba spin-orbit interaction in asymmetric oxide heterostructures with 3 d electrons,” *Nat. Commun.*, vol. 10, p. 3052, 2019.

[134] E. Lesne, Y. Fu, S. Oyarzun, J. C. Rojas-Sánchez, D. C. Vaz, H. Naganuma, G. Sicoli, J.-P. Attané, M. Jamet, E. Jacquet, J.-M. George, A. Barthélémy, H. Jaffrès, A. Fert, M. Bibes, and L. Vila, “Highly efficient and tunable spin-to-charge conversion through Rashba coupling at oxide interfaces,” *Nat. Mater*, vol. 15, pp. 1261–1266, 2016.

[135] J. Wang and S.-C. Zhang, “Topological states of condensed matter,” *Nat. Mater*, vol. 16, no. 11, pp. 1062–1067, 2017.

[136] L. Cheng, L. Wei, H. Liang, Y. Yan, G. Cheng, M. Lv, T. Lin, T. Kang, G. Yu, J. Chu, Z. Zhang, and C. Zeng, “Optical manipulation of Rashba spin–orbit coupling at $SrTiO_3$-based oxide interfaces,” *Nano Lett.*, vol. 17, pp. 6534–6539, 2017.

[137] Y. Gan, Y. Zhang, D. V. Christensen, N. Pryds, and Y. Chen, “Gate-tunable Rashba spin-orbit coupling and spin polarization at diluted oxide interfaces,” *Phys. Rev. B*, vol. 100, p. 125134, 2019.

[138] K. v. Klitzing, G. Dorda, and M. Pepper, “New method for high-accuracy determination of the fine-structure constant based on quantized Hall resistance,” *Phys. Rev. Lett.*, vol. 45, pp. 494–497, 1980.

[139] C.-X. Liu, S.-C. Zhang, and X.-L. Qi, “The quantum anomalous Hall effect: Theory and experiment,” *Annu. Rev. Condens. Matter Phys.*, vol. 7, no. 1, pp. 301–321, 2016.

[140] F. D. M. Haldane, “Model for a quantum Hall effect without Landau levels: Condensed-matter realization of the ”parity anomaly”,” *Phys. Rev. Lett.*, vol. 61, pp. 2015–2018, 1988.

[141] M. Kohmoto, “Topological invariant and the quantization of the hall conductance,” *Ann. Phys. (N. Y.)*, vol. 160, no. 2, pp. 343 – 354, 1985.

[142] Y. Yao, L. Kleinman, A. H. MacDonald, J. Sinova, T. Jungwirth, D.-s. Wang, E. Wang, and Q. Niu, “First principles calculation of anomalous hall conductivity in ferromagnetic bcc fe,” *Phys. Rev. Lett.*, vol. 92, p. 037204, 2004.

[143] D. J. Thouless, M. Kohmoto, M. P. Nightingale, and M. den Nijs, “Quantized hall conductance in a two-dimensional periodic potential,” *Phys. Rev. Lett.*, vol. 49, pp. 405–408, 1982.

[144] H.-J. Kim, C. Li, J. Feng, J.-H. Cho, and Z. Zhang, “Competing magnetic orderings and tunable topological states in two-dimensional hexagonal organometallic lattices,” *Phys. Rev. B*, vol. 93, p. 041404, 2016.

[145] E. Liu, Y. Sun, N. Kumar, L. Muechler, A. Sun, L. Jiao, S.-Y. Yang, D. Liu, A. Liang, Q. Xu, J. Kroder, V. Süß, H. Borrmann, C. Shekhar, Z. Wang, C. Xi, W. Wang, W. Schnelle, S. Wirth, Y. Chen, S. T. B. Goennenwein, and C. Felser, “Giant anomalous hall effect in a ferromagnetic kagome-lattice semimetal,” *Nat. Phys.*, vol. 14, no. 11, pp. 1125–1131, 2018.

[146] S. shen Chern, “On the curvatura integra in a riemannian manifold,” *Ann. Math.*, vol. 46, no. 4, pp. 674–684, 1945.

[147] C. L. Kane and E. J. Mele, “Quantum spin Hall effect in graphene,” *Phys. Rev. Lett.*, vol. 95, p. 226801, 2005.

[148] B. A. Bernevig, T. L. Hughes, and S.-C. Zhang, “Quantum spin Hall effect and topological phase transition in HgTe quantum wells,” *Science*, vol. 314, no. 5806, pp. 1757–1761, 2006.

[149] M. König, S. Wiedmann, C. Brüne, A. Roth, H. Buhmann, L. Molenkamp, X.-L. Qi, and S.-C. Zhang, “Quantum spin Hall insulator state in HgTe quantum wells,” *Science (New York, N.Y.)*, vol. 318, pp. 766–70, 12 2007.

[150] C. Liu, T. L. Hughes, X.-L. Qi, K. Wang, and S.-C. Zhang, “Quantum spin Hall effect in inverted type-ii semiconductors,” *Phys. Rev. Lett.*, vol. 100, p. 236601, 2008.

[151] I. Knez, R.-R. Du, and G. Sullivan, “Evidence for helical edge modes in inverted InAs/GaSb quantum wells,” *Phys. Rev. Lett.*, vol. 107, p. 136603, 2011.

[152] H. Zhang, J. Wang, G. Xu, Y. Xu, and S.-C. Zhang, “Topological states in ferromagnetic CdO/EuO superlattices and quantum wells,” *Phys. Rev. Lett.*, vol. 112, p. 096804, 2014.

[153] X. Hu, A. Rüegg, and G. A. Fiete, “Topological phases in layered pyrochlore oxide thin films along the [111] direction,” *Phys. Rev. B*, vol. 86, p. 235141, 2012.

[154] Y. Wang, Z. Wang, Z. Fang, and X. Dai, “Interaction-induced quantum anomalous Hall phase in (111) bilayer of $LaCoO_3$,” *Phys. Rev. B*, vol. 91, p. 125139, 2015.

[155] A. Rüegg, C. Mitra, A. A. Demkov, and G. A. Fiete, “Electronic structure of $(LaNiO_3)_2/(LaAlO_3)_N$ heterostructures grown along [111],” *Phys. Rev. B*, vol. 85, p. 245131, 2012.

[156] A. Rüegg and G. A. Fiete, “Topological insulators from complex orbital order in transition-metal oxides heterostructures,” *Phys. Rev. B*, vol. 84, p. 201103, 2011.

[157] I. Yakovkin and P. Dowben, “The problem of the band gap in LDA calculations,” *Surf. Rev. Lett.*, vol. 14, pp. 481–487, 06 2007.

[158] O. Gunnarsson and R. O. Jones, “Total-energy differences: Sources of error in local-density approximations,” *Phys. Rev. B*, vol. 31, pp. 7588–7602, 1985.

[159] D. C. Langreth and M. J. Mehl, “Beyond the local-density approximation in calculations of ground-state electronic properties,” *Phys. Rev. B*, vol. 28, pp. 1809–1834, 1983.

[160] C. Filippi, D. J. Singh, and C. J. Umrigar, “All-electron local-density and generalized-gradient calculations of the structural properties of semiconductors,” *Phys. Rev. B*, vol. 50, pp. 14 947–14 951, 1994.

[161] M. Stleäde, M. Moukara, J. A. Majewski, P. Vogl, and A. Görling, “Exact exchange Kohn-Sham formalism applied to semiconductors,” *Phys. Rev. B*, vol. 59, pp. 10 031–10 043, 1999.

[162] B. Himmetoglu, A. Floris, S. de Gironcoli, and M. Cococcioni, “Hubbard-corrected DFT energy functionals: The LDA+U description of correlated systems,” *Int. J. Quantum Chem.*, vol. 114, no. 1, pp. 14–49, 2014.

[163] V. I. Anisimov, F. Aryasetiawan, and A. I. Lichtenstein, “First-principles calculations of the electronic structure and spectra of strongly correlated systems: the LDA+U method,” *J. Phys. Condens. Matter*, vol. 9, no. 4, p. 767, 1997.

[164] S. L. Dudarev, G. A. Botton, S. Y. Savrasov, C. J. Humphreys, and A. P. Sutton, “Electron-energy-loss spectra and the structural stability of nickel oxide: An LSDA+U study,” *Phys. Rev. B*, vol. 57, pp. 1505–1509, 1998.

[165] A. I. Liechtenstein, V. I. Anisimov, and J. Zaanen, “Density-functional theory and strong interactions: Orbital ordering in Mott-Hubbard insulators,” *Phys. Rev. B*, vol. 52, pp. R5467–R5470, 1995.

[166] F. Aryasetiawan, K. Karlsson, O. Jepsen, and U. Schönberger, “Calculations of Hubbard U from first-principles,” *Phys. Rev. B*, vol. 74, p. 125106, 2006.

[167] M. Cococcioni and S. de Gironcoli, “Linear response approach to the calculation of the effective interaction parameters in the $\mathrm{LDA}+\mathrm{U}$ method,” *Phys. Rev. B*, vol. 71, p. 035105, 2005.

[168] A. A. Stekolnikov and F. Bechstedt, “Shape of free and constrained group-iv crystallites: Influence of surface energies,” *Phys. Rev. B*, vol. 72, p. 125326, 2005.

[169] Y. Singh and P. Gegenwart, “Antiferromagnetic Mott insulating state in single crystals of the honeycomb lattice material Na_2IrO_3,” *Phys. Rev. B*, vol. 82, p. 064412, 2010.

[170] J. B. Torrance, P. Lacorre, A. I. Nazzal, E. J. Ansaldo, and C. Niedermayer, “Systematic study of insulator-metal transitions in perovskites $RNiO_3$ (R=Pr,Nd,Sm,Eu) due to closing of charge-transfer gap,” *Phys. Rev. B*, vol. 45, pp. 8209–8212, 1992.

[171] Y. Wang, Q. He, W. Ming, M.-H. Du, N. Lu, C. Cafolla, J. Fujioka, Q. Zhang, D. Zhang, S. Shen, Y. Lyu, A. T. N’Diaye, E. Arenholz, L. Gu, C. Nan, Y. Tokura, S. Okamoto, and P. Yu, “Robust ferromagnetism in highly strained $SrCoO_3$ thin films,” *Phys. Rev. X*, vol. 10, p. 021030, 2020.

[172] H. Guo, Z. W. Li, L. Zhao, Z. Hu, C. F. Chang, C.-Y. Kuo, W. Schmidt, A. Piovano, T. W. Pi, O. Sobolev, D. I. Khomskii, L. H. Tjeng, and A. C. Komarek, “Antiferromagnetic correlations in the metallic strongly correlated transition metal oxide $LaNiO_3$,” *Nat. Commun*, vol. 9, no. 1, p. 43, 2018.

[173] R. R. Chen, Y. Sun, S. J. H. Ong, S. Xi, Y. Du, C. Liu, O. Lev, and Z. J. Xu, “Antiferromagnetic inverse spinel oxide $LiCoVO_4$ with spin-polarized channels for water oxidation,” *Adv. Mater.*, vol. 32, no. 10, p. 1907976, 2020.

[174] M. Alfredsson, G. David Price, C. R. A. Catlow, S. C. Parker, R. Orlando, and J. P. Brodholt, “Electronic structure of the antiferromagnetic $B1-\mathrm{structured FeO}$,” *Phys. Rev. B*, vol. 70, p. 165111, 2004.

[175] A. J. Williams, A. Gillies, J. P. Attfield, G. Heymann, H. Huppertz, M. J. Martínez-Lope, and J. A. Alonso, "Charge transfer and antiferromagnetic insulator phase in $SrRu_{1-x}Cr_xO_3$ perovskites: Solid solutions between two itinerant electron oxides," *Phys. Rev. B*, vol. 73, p. 104409, 2006.

[176] I. H. Lone, J. Aslam, N. R. E. Radwan, A. H. Bashal, A. F. A. Ajlouni, and A. Akhter, "Multiferroic ABO_3 transition metal oxides: a rare interaction of ferroelectricity and magnetism," *Nanoscale Res. Lett.*, vol. 14, no. 1, p. 142, 2019.

[177] T. Nakajima, S. Mitsuda, S. Kanetsuki, K. Prokes, A. Podlesnyak, H. Kimura, and Y. Noda, "Spin noncollinearlity in multiferroic phase of triangular lattice antiferromagnet $CuFe_{1-x}Al_xO_2$," *J. Phys. Soc. Japann*, vol. 76, no. 4, p. 043709, 2007.

[178] T.-h. Arima, "Ferroelectricity induced by proper-screw type magnetic order," *J. Phys. Soc. Japan*, vol. 76, no. 7, p. 073702, 2007.

[179] N. Terada, T. Nakajima, S. Mitsuda, H. Kitazawa, K. Kaneko, and N. Metoki, "Ga-substitution-induced single ferroelectric phase in multiferroic $CuFeO_2$," *Phys. Rev. B*, vol. 78, p. 014101, 2008.

[180] O. Aktas, K. D. Truong, T. Otani, G. Balakrishnan, M. J. Clouter, T. Kimura, and G. Quirion, "Raman scattering study of delafossite magnetoelectric multiferroic compounds: $CuFeO_2$ and $CuCrO_2$," *J. Phys. Condens. Matter*, vol. 24, no. 3, p. 036003, 2011.

[181] C. Zhong, H. Cao, J. Fang, X. Jiang, X. Ji, and Z. Dong, "Spin-lattice coupling and helical-spin driven ferroelectric polarization in multiferroic $CuFeO_2$," *Appl. Phys. Lett.*, vol. 97, no. 9, p. 094103, 2010.

[182] T. Nakajima, S. Mitsuda, K. Takahashi, M. Yamano, K. Masuda, H. Yamazaki, K. Prokes, K. Kiefer, S. Gerischer, N. Terada, H. Kitazawa, M. Matsuda, K. Kakurai, H. Kimura, Y. Noda, M. Soda, M. Matsuura, and K. Hirota, "Comprehensive study on ferroelectricity induced by a proper-screw-type magnetic ordering in multiferroic $CuFeO_2$: Nonmagnetic impurity effect on magnetic and ferroelectric order," *Phys. Rev. B*, vol. 79, p. 214423, 2009.

[183] S. Seki, J.-H. Kim, D. S. Inosov, R. Georgii, B. Keimer, S. Ishiwata, and Y. Tokura, "Formation and rotation of skyrmion crystal in the chiral-lattice insulator Cu_2OSeO_3," *Phys. Rev. B*, vol. 85, p. 220406, 2012.

[184] S. Seki, S. Ishiwata, and Y. Tokura, "Magnetoelectric nature of skyrmions in a chiral magnetic insulator Cu_2OSeO_3," *Phys. Rev. B*, vol. 86, p. 060403, 2012.

[185] M. C. Langner, S. Roy, S. K. Mishra, J. C. T. Lee, X. W. Shi, M. A. Hossain, Y.-D. Chuang, S. Seki, Y. Tokura, S. D. Kevan, and R. W. Schoenlein, "Coupled skyrmion sublattices in Cu_2OSeO_3," *Phys. Rev. Lett.*, vol. 112, p. 167202, 2014.

[186] V. Dyadkin, K. Prša, S. V. Grigoriev, J. S. White, P. Huang, H. M. Rønnow, A. Magrez, C. D. Dewhurst, and D. Chernyshov, "Chirality of structure and magnetism in the magnetoelectric compound Cu_2OSeO_3," *Phys. Rev. B*, vol. 89, p. 140409, 2014.

[187] J. S. White, I. Živković, A. J. Kruchkov, M. Bartkowiak, A. Magrez, and H. M. Rønnow, "Electric-field-driven topological phase switching and skyrmion-lattice metastability in magnetoelectric Cu_2OSeO_3," *Phys. Rev. Appl.*, vol. 10, p. 014021, 2018.

[188] J. Müller, J. Rajeswari, P. Huang, Y. Murooka, H. M. Rønnow, F. Carbone, and A. Rosch, "Magnetic skyrmions and skyrmion clusters in the helical phase of Cu_2OSeO_3," *Phys. Rev. Lett.*, vol. 119, p. 137201, 2017.

[189] H. Effenberger, "Die kristallstrukturen von drei modifikationen des $Cu(SeO_3)$," *Z. Kristallogr. Cryst. Mater.*, vol. 175, no. 1-4, pp. 61–72, 1986.

[190] G. Meunier and M. Bertaud, "Constantes cristallographiques de $CuSe_2O_5, CuSeO_3 et Cu_2SeO_4$," *J. Appl. Crystallogr*, vol. 9, no. 4, pp. 364–366, 1976.

[191] S. Lee, W.-J. Lee, J. van Tol, P. L. Kuhns, A. P. Reyes, H. Berger, and K.-Y. Choi, "Anomalous spin dynamics in the coupled spin tetramer system $CuSeO_3$," *Phys. Rev. B*, vol. 95, p. 054405, 2017.

[192] M. A. Subramanian and A. P. Ramirez, "Antiferromagnetic-ferromagnetic Cu-O-Cu coupljng change in copper oxides: $Se_1-xTexCuO_3$ perovskites," *MRS Proceedings*, vol. 547, p. 169, 1998.

[193] M. A. Subramanian, A. P. Ramirez, and W. J. Marshall, "Structural tuning of ferromagnetism in a 3D cuprate perovskite," *Phys. Rev. Lett.*, vol. 82, pp. 1558–1561, 1999.

[194] G. Lawes, A. P. Ramirez, C. M. Varma, and M. A. Subramanian, "Magnetodielectric effects from spin fluctuations in isostructural ferromagnetic and antiferromagnetic systems," *Phys. Rev. Lett.*, vol. 91, p. 257208, 2003.

[195] A. Villesuzanne, M.-H. Whangbo, M. A. Subramanian, and S. F. Matar, "Spin dimer and electronic band structure analyses of the ferromagnetism versus antiferromagnetism in $SeCuO_3$ and $TeCuO_3$," *Chem. Mater.*, vol. 17, pp. 4350–4355, 2005.

[196] I. Živković, D. M. Djokić, M. Herak, D. Pajić, K. Prša, P. Pattison, D. Dominko, Z. Micković, D. Cinčić, L. Forró, H. Berger, and H. M. Rønnow, "Site-selective quantum correlations revealed by magnetic anisotropy in the tetramer system $SeCuO_3$," *Phys. Rev. B*, vol. 86, p. 054405, 2012.

[197] M. Herak, A. Grubišić Čabo, D. Žilić, B. Rakvin, K. c. v. Salamon, O. Milat, and H. Berger, "Magnetic anisotropy of the spin tetramer system $SeCuO_3$ studied by torque magnetometry and ESR spectroscopy," *Phys. Rev. B*, vol. 89, p. 184411, 2014.

[198] K. Kohn, K. Inoue, O. Horie, and S.-I. Akimoto, "Crystal chemistry of $MSeO_3$ and $MTeO_3$ (M = Mg, Mn, Co, Ni, Cu, and Zn)," *J. Solid State Chem.*, vol. 18, no. 1, pp. 27–37, 1976.

[199] K. Kohn, "A new ferrimagnet Cu_2SeO_4," *J. Phys. Soc. Japan*, vol. 42, no. 6, pp. 2065–2066, 1977.

[200] J. P. Perdew, K. Burke, and M. Ernzerhof, "Generalized gradient approximation made simple," *Phys. Rev. Lett.*, vol. 77, pp. 3865–3868, 1996.

[201] P. E. Blöchl, "Projector augmented-wave method," *Phys. Rev. B*, vol. 50, pp. 17 953–17 979, 1994.

[202] G. Kresse and D. Joubert, "From ultrasoft pseudopotentials to the projector augmented-wave method," *Phys. Rev. B*, vol. 59, pp. 1758–1775, 1999.

[203] U. Herath, P. Tavadze, X. He, E. Bousquet, S. Singh, F. Muñoz, and A. H. Romero, "Pyprocar: A python library for electronic structure pre/post-processing," *Comput. Phys. Commun.*, vol. 251, p. 107080, 2020.

[204] R. Tomar, S. Kakkar, S. Goyal, M. Manolata Devi, C. Bera, and S. Chakraverty, "Multiple helimagnetic phases in triclinic $CuSeO_3$," *J. Magn. Magn. Mater.*, vol. 497, p. 165945, 2020.

[205] V. Carozo, Y. Wang, K. Fujisawa, B. R. Carvalho, A. McCreary, S. Feng, Z. Lin, C. Zhou, N. Perea-López, A. L. Elías, B. Kabius, V. H. Crespi, and M. Terrones, "Optical identification of sulfur vacancies: Bound excitons at the edges of monolayer tungsten disulfide," *Sci. Adv.*, vol. 3, no. 4, 2017.

[206] S. Shimizu, J. Shiogai, N. Takemori, S. Sakai, H. Ikeda, R. Arita, T. Nojima, A. Tsukazaki, and Y. Iwasa, "Giant thermoelectric power factor in ultrathin FeSe superconductor," *Nat. Commun*, vol. 10, no. 1, p. 825, 2019.

[207] J. Li, Y. Li, S. Du, Z. Wang, B.-L. Gu, S.-C. Zhang, K. He, W. Duan, and Y. Xu, "Intrinsic magnetic topological insulators in van der Waals layered $MnBi_2Te_4$-family materials," *Sci. Adv.*, vol. 5, no. 6, 2019.

[208] A. K. Geim, "Graphene: Status and prospects," *Science*, vol. 324, no. 5934, pp. 1530–1534, 2009.

[209] L. Song, L. Ci, H. Lu, P. B. Sorokin, C. Jin, J. Ni, A. G. Kvashnin, D. G. Kvashnin, J. Lou, B. I. Yakobson, and P. M. Ajayan, "Large scale growth and characterization of atomic hexagonal boron nitride layers," *Nano Lett.*, vol. 10, no. 8, pp. 3209–3215, 2010.

[210] Q. Peng, W. Ji, and S. De, "Mechanical properties of the hexagonal boron nitride monolayer: Ab initio study," *Comput. Mater. Sci.*, vol. 56, pp. 11 – 17, 2012.

[211] Y. Ma, L. Kou, X. Li, Y. Dai, S. C. Smith, and T. Heine, "Quantum spin Hall effect and topological phase transition in two-dimensional square transition-metal dichalcogenides," *Phys. Rev. B*, vol. 92, p. 085427, 2015.

[212] Q. H. Wang, K. Kalantar-Zadeh, A. Kis, J. N. Coleman, and M. S. Strano, "Electronics and optoelectronics of two-dimensional transition metal dichalcogenides," *Nat. Nanotechnol*, vol. 7, pp. 699–712, 2012.

[213] L. Kulyuk, D. Dumcehnko, E. Bucher, K. Friemelt, O. Schenker, L. Charron, E. Fortin, and T. Dumouchel, "Excitonic luminescence of the Br_2-intercalated layered semiconductors $2H-WS_2$," *Phys. Rev. B*, vol. 72, p. 075336, 2005.

[214] H. Kahnouji, S. J. Hashemifar, N. Rezaei, and M. Alaei, "Effects of strain on electronic and magnetic properties of Co/WS_2 nanolayer: A density functional and Monte Carlo study," *Phys. Rev. B*, vol. 100, p. 085423, 2019.

[215] Y. C. Cheng, Z. Y. Zhu, W. B. Mi, Z. B. Guo, and U. Schwingenschlögl, "Prediction of two-dimensional diluted magnetic semiconductors: Doped monolayer MoS_2 systems," *Phys. Rev. B*, vol. 87, p. 100401, Mar 2013.

[216] A. N. Andriotis and M. Menon, "Tunable magnetic properties of transition metal doped MoS_2," *Phys. Rev. B*, vol. 90, p. 125304, Sep 2014.

[217] X. Zhang and Q. Li, "Electronic and magnetic properties of nonmetal atoms adsorbed ReS_2 monolayers," *J. Appl. Phys.*, vol. 118, no. 6, p. 064306, 2015.

[218] J. He, K. Wu, R. Sa, Q. Li, and Y. Wei, "Magnetic properties of nonmetal atoms absorbed MoS_2 monolayers," *Appl. Phys. Lett.*, vol. 96, no. 8, p. 082504, 2010.

[219] J. Choe, K. Lee, C.-L. Huang, N. Trivedi, and E. Morosan, “Magnetotransport in Fe-intercalated $T\mathrm{S}_2$: Comparison between $T = \mathrm{Ti\,and\,Ta}$,” *Phys. Rev. B*, vol. 99, p. 064420, 2019.

[220] M. Habib, Z. Muhammad, R. Khan, C. Wu, Z. ur Rehman, Y. Zhou, H. Liu, and L. Song, “Ferromagnetism in CVT grown tungsten diselenide single crystals with nickel doping,” *Nanotechnology*, vol. 29, no. 11, p. 115701, 2018.

[221] D. Gao, Q. Xue, X. Mao, W. Wang, Q. Xu, and D. Xue, “Ferromagnetism in ultrathin VS_2 nanosheets,” *J. Mater. Chem. C*, vol. 1, pp. 5909–5916, 2013.

[222] T. Li, S. Jiang, N. Sivadas, Z. Wang, Y. Xu, D. Weber, J. E. Goldberger, K. Watanabe, T. Taniguchi, C. J. Fennie, K. Fai Mak, and J. Shan, “Pressure-controlled interlayer magnetism in atomically thin CrI_3,” *Nat. Mater*, vol. 18, pp. 1303–1308, 2019.

[223] S. Jiang, L. Li, Z. Wang, K. F. Mak, and J. Shan, “Controlling magnetism in 2D CrI_3 by electrostatic doping,” *Nat. Nanotechnol*, vol. 13, pp. 549–553, 2018.

[224] L. Thiel, Z. Wang, M. A. Tschudin, D. Rohner, I. Gutiérrez-Lezama, N. Ubrig, M. Gibertini, E. Giannini, A. F. Morpurgo, and P. Maletinsky, “Probing magnetism in 2D materials at the nanoscale with single-spin microscopy,” *Science*, vol. 364, no. 6444, pp. 973–976, 2019.

[225] N. Ru, J.-H. Chu, and I. R. Fisher, “Magnetic properties of the charge density wave compounds RTe_3(R=Y, La, Ce, Pr, Nd, Sm, Gd, Tb, Dy, Ho, Er, and Tm),” *Phys. Rev. B*, vol. 78, no. 1, 2008.

[226] H.-S. Kim and H.-Y. Kee, “Crystal structure and magnetism in $\alpha-\mathrm{RuCl}_3$: An ab initio study,” *Phys. Rev. B*, vol. 93, p. 155143, 2016.

[227] J. S. Oh, H.-S. Yu, C.-J. Kang, S. Sinn, M. Han, Y. J. Chang, B.-G. Park, K. Lee, B. I. Min, S. W. Kim, H.-D. Kim, and T. W. Noh, “Manifestations of quasi-two-dimensional metallicity in a layered ternary transition metal chalcogenide Ti_2PTe_2,” *Chem. Mater.*, vol. 28, no. 21, pp. 7570–7573, 2016.

[228] J. Chang, L. F. Register, S. K. Banerjee, and B. Sahu, “Density functional study of ternary topological insulator thin films,” *Phys. Rev. B*, vol. 83, p. 235108, 2011.

[229] J. Seo, D. Y. Kim, E. S. An, K. Kim, G.-Y. Kim, S.-Y. Hwang, D. W. Kim, B. G. Jang, H. Kim, G. Eom, S. Y. Seo, R. Stania, M. Muntwiler, J. Lee, K. Watanabe, T. Taniguchi, Y. J. Jo, J. Lee, B. I. Min, M. H. Jo, H. W. Yeom, S.-Y. Choi, J. H. Shim, and J. S. Kim, “Nearly room temperature ferromagnetism in a magnetic metal-rich van der Waals metal,” *Sci. Adv.*, vol. 6, no. 3, 2020.

[230] Z. Fei, B. Huang, P. Malinowski, W. Wang, T. Song, J. Sanchez, W. Yao, D. Xiao, X. Zhu, A. F. May, W. Wu, D. H. Cobden, J.-H. Chu, and X. Xu, "Two-dimensional itinerant ferromagnetism in atomically thin Fe_3GeTe_2," *Nat. Mater*, vol. 17, no. 9, pp. 778–782, 2018.

[231] B. L. Chittari, D. Lee, N. Banerjee, A. H. MacDonald, E. Hwang, and J. Jung, "Carrier- and strain-tunable intrinsic magnetism in two-dimensional MAX_3 transition metal chalcogenides," *Phys. Rev. B*, vol. 101, 2020.

[232] X. Chen, J. Qi, and D. Shi, "Strain-engineering of magnetic coupling in two-dimensional magnetic semiconductor $CrSiTe_3$: Competition of direct exchange interaction and superexchange interaction," *Phys. Lett. A*, vol. 379, no. 1, pp. 60 – 63, 2015.

[233] G. Kresse and J. Furthmüller, "Efficient iterative schemes for ab initio total-energy calculations using a plane-wave basis set," *Phys. Rev. B*, vol. 54, pp. 11 169–11 186, 1996.

[234] A.-L. Dalverny, J.-S. Filhol, F. Lemoigno, and M.-L. Doublet, "Interplay between magnetic and orbital ordering in the strongly correlated cobalt oxide: A DFT + U study," *J. Phys. Chem. C*, vol. 114, no. 49, pp. 21 750–21 756, 2010.

[235] H. Hsu, P. Blaha, R. M. Wentzcovitch, and C. Leighton, "Cobalt spin states and hyperfine interactions in $LaCoO_3$ investigated by $\mathrm{LDA}+U$ calculations," *Phys. Rev. B*, vol. 82, p. 100406, 2010.

[236] A. Togo and I. Tanaka, "First principles phonon calculations in materials science," *Scr. Mater.*, vol. 108, pp. 1–5, 2015.

[237] H.-J. Kim, "VASPBERRY," 2018.

[238] X. Kou, S.-T. Guo, Y. Fan, L. Pan, M. Lang, Y. Jiang, Q. Shao, T. Nie, K. Murata, J. Tang, Y. Wang, L. He, T.-K. Lee, W.-L. Lee, and K. L. Wang, "Scale-invariant quantum anomalous hall effect in magnetic topological insulators beyond the two-dimensional limit," *Phys. Rev. Lett.*, vol. 113, p. 137201, 2014.

[239] M.-h. Zhang, C.-w. Zhang, P.-j. Wang, and S.-s. Li, "Prediction of high-temperature chern insulator with half-metallic edge states in asymmetry-functionalized stanene," *Nanoscale*, vol. 10, pp. 20 226–20 233, 2018.

[240] S.-j. Zhang, C.-w. Zhang, S.-f. Zhang, W.-x. Ji, P. Li, P.-j. Wang, S.-s. Li, and S.-s. Yan, "Intrinsic dirac half-metal and quantum anomalous hall phase in a hexagonal metal-oxide lattice," *Phys. Rev. B*, vol. 96, p. 205433, 2017.

[241] Y.-p. Wang, W.-x. Ji, C.-w. Zhang, P. Li, P.-j. Wang, B. Kong, S.-s. Li, S.-s. Yan, and K. Liang, “Discovery of intrinsic quantum anomalous hall effect in organic mn-dca lattice,” *Appl. Phys. Lett.*, vol. 110, no. 23, p. 233107, 2017.

[242] H. Y. Hwang, Y. Iwasa, M. Kawasaki, B. Keimer, N. Nagaosa, and Y. Tokura, “Emergent phenomena at oxide interfaces,” *Nat. Mater.*, vol. 11, no. 2, pp. 103–113, 2012.

[243] C. Cancellieri, A. S. Mishchenko, U. Aschauer, A. Filippetti, C. Faber, O. S. Barišić, V. A. Rogalev, T. Schmitt, N. Nagaosa, and V. N. Strocov, “Polaronic metal state at the $LaAlO_3/SrTiO_3$ interface,” *Nat. Commun*, vol. 7, p. 10386, 2016.

[244] D.-S. Park, A. D. Rata, I. V. Maznichenko, S. Ostanin, Y. L. Gan, S. Agrestini, G. J. Rees, M. Walker, J. Li, J. Herrero-Martin, G. Singh, Z. Luo, A. Bhatnagar, Y. Z. Chen, V. Tileli, P. Muralt, A. Kalaboukhov, I. Mertig, K. Dörr, A. Ernst, and N. Pryds, “The emergence of magnetic ordering at complex oxide interfaces tuned by defects,” *Nat. Commun*, vol. 11, p. 3650, 2020.

[245] F. Lechermann, L. Boehnke, D. Grieger, and C. Piefke, “Electron correlation and magnetism at the $LaAlO_3/SrTiO_3$ interface: A DFT+DMFT investigation,” *Phys. Rev. B*, vol. 90, p. 085125, 2014.

[246] R. Pentcheva and W. E. Pickett, “Avoiding the polarization catastrophe in $LaAlO_3$ overlayers on $SrTiO_3(001)$ through polar distortion,” *Phys. Rev. Lett.*, vol. 102, p. 107602, 2009.

[247] S. Nazir, C. Bernal, and K. Yang, “Modulated two-dimensional charge-carrier density in $LaTiO_3$–layer-doped $LaAlO_3/SrTiO_3$ heterostructure,” *ACS Appl. Mater. Interfaces*, vol. 7, pp. 5305–5311, 2015.

[248] J. Lee and A. A. Demkov, “Charge origin and localization at the *n*-type $SrTiO_3/LaAlO_3$ interface,” *Phys. Rev. B*, vol. 78, p. 193104, 2008.

[249] K. Rubi, J. Gosteau, R. Serra, K. Han, S. Zeng, Z. Huang, B. Warot-Fonrose, R. Arras, E. Snoeck, Ariando, M. Goiran, and W. Escoffier, “Aperiodic quantum oscillations in the two-dimensional electron gas at the $LaAlO_3/SrTiO_3$ interface,” *npj Quantum Mater.*, vol. 5, p. 9, 2020.

[250] P. V. Ong and J. Lee, “Orbital-selective charge transfer at oxygen-deficient $LaAlO_3/SrTiO_3(001)$ interfaces,” *Phys. Rev. B*, vol. 87, p. 195212, 2013.

[251] Z. S. Popović, S. Satpathy, and R. M. Martin, “Origin of the two-dimensional electron gas carrier density at the $LaAlO_3$ on $SrTiO_3$ interface,” *Phys. Rev. Lett.*, vol. 101, p. 256801, 2008.

[252] L. Guan, F. Tan, G. Shen, Y. Liang, X. Xu, J. Guo, J. Wang, Z. Zhang, and X. Li, "Comparison of geometry models in the study of perovskite heterostructures," *Appl. Surf. Sci.*, 2019.

[253] Z. Zhong, A. Tóth, and K. Held, "Theory of spin-orbit coupling at $LaAlO_3$/$SrTiO_3$ interfaces and $SrTiO_3$ surfaces," *Phys. Rev. B*, vol. 87, p. 161102, 2013.

[254] G. Khalsa, B. Lee, and A. H. MacDonald, "Theory of t_{2g} electron-gas Rashba interactions," *Phys. Rev. B*, vol. 88, p. 041302, 2013.

[255] A. Ohtomo, D. A. Muller, J. L. Grazul, and H. Y. Hwang, "Artificial charge-modulationin atomic-scale perovskite titanate superlattices," *Nature*, vol. 419, no. 6905, pp. 378–380, 2002.

[256] B. I. Edmondson, S. Liu, S. Lu, H. Wu, A. Posadas, D. J. Smith, X. P. A. Gao, A. A. Demkov, and J. G. Ekerdt, "Effect of $SrTiO_3$ oxygen vacancies on the conductivity of $LaTiO_3$/$SrTiO_3$ heterostructures," *J. Appl. Phys.*, vol. 124, no. 18, p. 185303, 2018.

[257] F. Wen, Y. Cao, X. Liu, B. Pal, S. Middey, M. Kareev, and J. Chakhalian, "Evolution of ferromagnetism in two-dimensional electron gas of $LaTiO_3$/$SrTiO_3$," *Appl. Phys. Lett*, vol. 112, no. 12, p. 122405, 2018.

[258] S. Kumar, J. Kaswan, B. Satpati, A. K. Shukla, B. Gahtori, J. J. Pulikkotil, and A. Dogra, "$LaScO_3$/$SrTiO_3$: A conducting polar heterointerface of two 3d band insulating perovskites," *Appl. Phys. Lett*, vol. 116, no. 5, p. 051603, 2020.

[259] C. Li, Q. Xu, Z. Wen, S. Zhang, A. Li, and D. Wu, "The metallic interface between insulating $NdGaO_3$ and $SrTiO_3$ perovskites," *Appl. Phys. Lett*, vol. 103, no. 20, p. 201602, 2013.

[260] Y. Hotta, T. Susaki, and H. Y. Hwang, "Polar discontinuity doping of the $LaVO_3/SrTiO_3$ interface," *Phys. Rev. Lett.*, vol. 99, p. 236805, 2007.

[261] C. He, T. D. Sanders, M. T. Gray, F. J. Wong, V. V. Mehta, and Y. Suzuki, "Metal-insulator transitions in epitaxial $LaVO_3$ and $LaTiO_3$ films," *Phys. Rev. B*, vol. 86, p. 081401, 2012.

[262] S. Harashima, C. Bell, M. Kim, T. Yajima, Y. Hikita, and H. Y. Hwang, "Coexistence of two-dimensional and three-dimensional Shubnikov–de Haas oscillations in Ar^+-irradiated $KTaO_3$," *Phys. Rev. B*, vol. 88, p. 085102, 2013.

[263] A. Gupta, H. Silotia, A. Kumari, M. Dumen, S. Goyal, R. Tomar, N. Wadehra, P. Ayyub, and S. Chakraverty, "$KTaO_3$—the new kid on the spintronics block," *Adv. Mater.*, vol. 34, no. 9, p. 2106481, 2022.

[264] G. E. Jellison, I. Paulauskas, L. A. Boatner, and D. J. Singh, "Optical functions of $KTaO_3$ as determined by spectroscopic ellipsometry and comparison with band structure calculations," *Phys. Rev. B*, vol. 74, p. 155130, 2006.

[265] M. Tyunina, J. Narkilahti, M. Plekh, R. Oja, R. M. Nieminen, A. Dejneka, and V. Trepakov, "Evidence for strain-induced ferroelectric order in epitaxial thin-film $KTaO_3$," *Phys. Rev. Lett.*, vol. 104, p. 227601, 2010.

[266] H. Nakamura and T. Kimura, "Electric field tuning of spin-orbit coupling in $KTaO_3$ field-effect transistors," *Phys. Rev. B*, vol. 80, p. 121308, 2009.

[267] P. D. C. King, R. H. He, T. Eknapakul, P. Buaphet, S.-K. Mo, Y. Kaneko, S. Harashima, Y. Hikita, M. S. Bahramy, C. Bell, Z. Hussain, Y. Tokura, Z.-X. Shen, H. Y. Hwang, F. Baumberger, and W. Meevasana, "Subband structure of a two-dimensional electron gas formed at the polar surface of the strong spin-orbit perovskite $KTaO_3$," *Phys. Rev. Lett.*, vol. 108, p. 117602, 2012.

[268] F. Y. Bruno, S. McKeown Walker, S. Riccò, A. de la Torre, Z. Wang, A. Tamai, T. K. Kim, M. Hoesch, M. S. Bahramy, and F. Baumberger, "Band structure and spin–orbital texture of the (111)-$KTaO_3$ 2D electron gas," *Adv. Electron. Mater.*, vol. 5, no. 5, p. 1800860, 2019.

[269] S. Nazir, J. Cheng, and K. Yang, "Creating two-dimensional electron gas in nonpolar/nonpolar oxide interface via polarization discontinuity: First-principles analysis of $CaZrO_3/SrTiO_3$ heterostructure," *ACS Appl. Mater. Interfaces*, vol. 8, no. 1, pp. 390–399, 2016.

[270] A. Masuno, T. Terashima, and M. Takano, "Epitaxial growth of perovskite-type $LaVO_3$ thin films on various substrates by the PLD method," *Solid State Ion.*, vol. 172, pp. 275–278, 2004.

[271] Z. Zhong, L. Si, Q. Zhang, W.-G. Yin, S. Yunoki, and K. Held, "Giant switchable Rashba effect in oxide heterostructures," *Adv. Mater. Interfaces*, vol. 2, no. 5, p. 1400445, 2015.

[272] M. J. Veit, R. Arras, B. J. Ramshaw, R. Pentcheva, and Y. Suzuki, "Nonzero berry phase in quantum oscillations from giant Rashba-type spin splitting in $LaTiO_3/SrTiO_3$ heterostructures," *Nat. Commun.*, vol. 9, no. 1, p. 1458, 2018.

[273] H. J. H. Ma, J. Zhou, M. Yang, Y. Liu, S. W. Zeng, W. X. Zhou, L. C. Zhang, T. Venkatesan, Y. P. Feng, and Ariando, "Giant crystalline anisotropic magnetoresistance in nonmagnetic perovskite oxide heterostructures," *Phys. Rev. B*, vol. 95, p. 155314, 2017.

[274] Q.-F. Yao, J. Cai, W.-Y. Tong, S.-J. Gong, J.-Q. Wang, X. Wan, C.-G. Duan, and J. H. Chu, "Manipulation of the large Rashba spin splitting in polar two-dimensional transition-metal dichalcogenides," *Phys. Rev. B*, vol. 95, p. 165401, 2017.

[275] A. Janotti, L. Bjaalie, L. Gordon, and C. G. Van de Walle, "Controlling the density of the two-dimensional electron gas at the $SrTiO_3/LaAlO_3$ interface," *Phys. Rev. B*, vol. 86, p. 241108, 2012.

[276] D.-H. Choe, D. West, and S. Zhang, "Band alignment and the built-in potential of solids," *Phys. Rev. Lett.*, vol. 121, p. 196802, 2018.

[277] J. Junquera, M. H. Cohen, and K. M. Rabe, "Nanoscale smoothing and the analysis of interfacial charge and dipolar densities," *J. Condens. Matter Phys.*, vol. 19, no. 21, p. 213203, 2007.

[278] J.-S. Lee, Y. W. Xie, H. K. Sato, C. Bell, Y. Hikita, H. Y. Hwang, and C.-C. Kao, "Titanium dxy ferromagnetism at the $LaAlO_3/SrTiO_3$ interface," *Nat. Mater.*, vol. 12, no. 8, pp. 703–706, 2013.

[279] W. Kong, T. Yang, J. Zhou, Y. Z. Luo, T. Zhu, J. Chen, L. Shen, Y. Jiang, Y. P. Feng, and M. Yang, "Tunable Rashba spin-orbit coupling and its interplay with multiorbital effect and magnetic ordering at oxide interfaces," *Phys. Rev. B*, vol. 104, p. 155152, 2021.

[280] J. D. Burton and E. Y. Tsymbal, "Highly spin-polarized conducting state at the interface between nonmagnetic band insulators: $\mathrm{LaAlO_3/FeS_2}$ (001)," *Phys. Rev. Lett.*, vol. 107, p. 166601, 2011.

[281] R. Tomar, S. Kakkar, C. Bera, and S. Chakraverty, "Anisotropic magnetoresistance and planar hall effect in (001) and (111) $\mathrm{LaVO_3/SrTiO_3}$ heterostructures," *Phys. Rev. B*, vol. 103, p. 115407, 2021.

[282] M. Huijben, Y. Liu, H. Boschker, V. Lauter, R. Egoavil, J. Verbeeck, S. G. E. te Velthuis, G. Rijnders, and G. Koster, "Enhanced local magnetization by interface engineering in perovskite-type correlated oxide heterostructures," *Adv. Mater. Interfaces*, vol. 2, no. 3, p. 1400416, 2015.

[283] B. R. K. Nanda and S. Satpathy, "Effects of strain on orbital ordering and magnetism at perovskite oxide interfaces: $LaMnO_3/SrMnO_3$," *Phys. Rev. B*, vol. 78, p. 054427, 2008.

[284] M. Verissimo-Alves, P. García-Fernández, D. I. Bilc, P. Ghosez, and J. Junquera, "Highly confined spin-polarized two-dimensional electron gas in $SrTiO_3/SrRuO_3$ superlattices," *Phys. Rev. Lett.*, vol. 108, p. 107003, 2012.

[285] J. Betancourt, T. R. Paudel, E. Y. Tsymbal, and J. P. Velev, "Spin-polarized two-dimensional electron gas at $GdTiO_3/SrTiO_3$ interfaces: Insight from first-principles calculations," *Phys. Rev. B*, vol. 96, p. 045113, 2017.

[286] B. R. K. Nanda and S. Satpathy, "Spin-polarized two-dimensional electron gas at oxide interfaces," *Phys. Rev. Lett.*, vol. 101, p. 127201, 2008.

[287] H. X. Yang, A. Hallal, D. Terrade, X. Waintal, S. Roche, and M. Chshiev, "Proximity effects induced in graphene by magnetic insulators: First-principles calculations on spin filtering and exchange-splitting gaps," *Phys. Rev. Lett.*, vol. 110, p. 046603, 2013.

[288] H. Haugen, D. Huertas-Hernando, and A. Brataas, "Spin transport in proximity-induced ferromagnetic graphene," *Phys. Rev. B*, vol. 77, p. 115406, 2008.

[289] A. G. Swartz, P. M. Odenthal, Y. Hao, R. S. Ruoff, and R. K. Kawakami, "Integration of the ferromagnetic insulator EuO onto graphene," *ACS Nano*, vol. 6, no. 11, pp. 10 063–10 069, 2012.

[290] Q. Zhang, S. A. Yang, W. Mi, Y. Cheng, and U. Schwingenschlögl, "Large spin-valley polarization in monolayer $MoTe_2$ on top of EuO(111)," *Adv. Mater.*, vol. 28, no. 5, pp. 959–966, 2016.

[291] L. Gao and A. A. Demkov, "Spin-polarized two-dimensional t_{2g} electron gas: Ab initio study of EuO interface with oxygen-deficient $SrTiO_3$," *Phys. Rev. B*, vol. 97, p. 125305, 2018.

[292] J. Lee, N. Sai, and A. A. Demkov, "Spin-polarized two-dimensional electron gas through electrostatic doping in $LaAlO_3/EuO$ heterostructures," *Phys. Rev. B*, vol. 82, p. 235305, 2010.

[293] Y. Wang, M. K. Niranjan, J. D. Burton, J. M. An, K. D. Belashchenko, and E. Y. Tsymbal, "Prediction of a spin-polarized two-dimensional electron gas at the $LaAlO_3/EuO(001)$ interface," *Phys. Rev. B*, vol. 79, no. 21, 2009.

[294] K. J. Kormondy, L. Gao, X. Li, S. Lu, A. B. Posadas, S. Shen, M. Tsoi, M. R. McCartney, D. J. Smith, J. Zhou, L. L. Lev, M.-A. Husanu, V. N. Strocov, and A. A. Demkov, “Large positive linear magnetoresistance in the two-dimensional $t2g$ electron gas at the EuO/$SrTiO_3$ interface,” *Sci. Rep.*, vol. 8, no. 1, p. 7721, 2018.

[295] S. Kakkar and C. Bera, “Rashba spin splitting in two-dimensional electron gas in polar-polar perovskite oxide heterostructure $LaVO_3$/$KTaO_3$: A DFT investigation,” *Physica E Low Dimens. Syst. Nanostruct.*, vol. 144, p. 115394, 2022.

[296] S. Goyal, R. Tomar, and S. Chakraverty, “Photodynamics study of $KTaO_3$-based conducting interfaces,” *ACS Appl. Electron. Mater.*, vol. 3, no. 2, pp. 905–911, 2021.

[297] N. Kumar, S. Kakkar, and C. Bera, “High thermoelectric power factor in $LaVO_3$/$KTaO_3$ heterostructure,” *Physica E Low Dimens. Syst. Nanostruct.*, vol. 146, p. 115525, 2023.

[298] M. Dumen, A. Singh, S. Goyal, C. Bera, and S. Chakraverty, “Photoconductivity of the EuO–KTO interface: Effect of intrinsic carrier density and temperature,” *J. Phys. Chem. C*, vol. 125, no. 28, pp. 15 510–15 515, 2021.

[299] H. Fu, C.-X. Liu, and B. Yan, “Exchange bias and quantum anomalous Hall effect in the $MnBi_2Te_4$/CrI_3 heterostructure,” *Sci. Adv.*, vol. 6, no. 10, p. eaaz0948, 2020.

[300] C.-Z. Chang, J. Zhang, X. Feng, J. Shen, Z. Zhang, M. Guo, K. Li, Y. Ou, P. Wei, L.-L. Wang, Z.-Q. Ji, Y. Feng, S. Ji, X. Chen, J. Jia, X. Dai, Z. Fang, S.-C. Zhang, K. He, Y. Wang, L. Lu, X.-C. Ma, and Q.-K. Xue, “Experimental observation of the quantum anomalous Hall effect in a magnetic topological insulator,” *Science*, vol. 340, no. 6129, pp. 167–170, 2013.

[301] J. Zhang, B. Zhao, Y. Yao, and Z. Yang, “Robust quantum anomalous Hall effect in graphene-based van der Waals heterostructures,” *Phys. Rev. B*, vol. 92, p. 165418, 2015.

[302] Q. Cui, J. Liang, B. Yang, Z. Wang, P. Li, P. Cui, and H. Yang, “Giant enhancement of perpendicular magnetic anisotropy and induced quantum anomalous Hall effect in graphene/NiI_2 heterostructures via tuning the van der Waals interlayer distance,” *Phys. Rev. B*, vol. 101, p. 214439, 2020.

[303] C. Tang, B. Cheng, M. Aldosary, Z. Wang, Z. Jiang, K. Watanabe, T. Taniguchi, M. Bockrath, and J. Shi, “Approaching quantum anomalous Hall effect in

proximity-coupled YIG/graphene/h-BN sandwich structure," *APL Mater.*, vol. 6, no. 2, p. 026401, 2018.

[304] P. Högl, T. Frank, K. Zollner, D. Kochan, M. Gmitra, and J. Fabian, "Quantum anomalous Hall effects in graphene from proximity-induced uniform and staggered spin-orbit and exchange coupling," *Phys. Rev. Lett.*, vol. 124, p. 136403, 2020.

[305] M. U. Rehman, X. Dong, T. Hou, Z. Li, S. Qi, and Z. Qiao, "Quantum anomalous Hall effect by coupling heavy atomic layers with CrI_3," *Phys. Rev. B*, vol. 100, p. 195422, 2019.

[306] J. Zhang, B. Zhao, Y. Yao, and Z. Yang, "Quantum anomalous Hall effect in graphene-based heterostructure," *Sci. Rep.*, vol. 5, no. 1, p. 10629, 2015.

[307] Z. Zanolli, C. Niu, G. Bihlmayer, Y. Mokrousov, P. Mavropoulos, M. J. Verstraete, and S. Blügel, "Hybrid quantum anomalous Hall effect at graphene-oxide interfaces," *Phys. Rev. B*, vol. 98, p. 155404, 2018.

[308] K. Dolui, S. Ray, and T. Das, "Intrinsic large gap quantum anomalous Hall insulators in $\mathrm{La}X(X = \mathrm{Br,Cl,I})$," *Phys. Rev. B*, vol. 92, p. 205133, 2015.

[309] S. Kakkar, A. Sharma, and C. Bera, "Electronic, magnetic, and topological properties of layered ternary chalcogenide CoAsS: A first principles study," *J. Magn. Magn. Mater.*, vol. 536, p. 168133, 2021.

[310] W.-Y. Tong, H.-C. Ding, Y.-C. Gao, S.-J. Gong, X. Wan, and C.-G. Duan, "Spin-dependent optical response of multiferroic EuO: First-principles DFT calculations," *Phys. Rev. B*, vol. 89, p. 064404, 2014.

[311] T. R. McGuire and M. W. Shafer, "Ferromagnetic Europium compounds," *J. Appl. Phys.*, vol. 35, no. 3, pp. 984–988, 1964.

[312] J. O. Dimmock, "Optical properties of the europium chalcogenides," *IBM J. Res. Dev.*, vol. 14, no. 3, pp. 301–308, 1970.

[313] B. T. Matthias, R. M. Bozorth, and J. H. Van Vleck, "Ferromagnetic interaction in EuO," *Phys. Rev. Lett.*, vol. 7, pp. 160–161, 1961.

[314] A. Mauger and C. Godart, "The magnetic, optical, and transport properties of representatives of a class of magnetic semiconductors: The europium chalcogenides," *Phys. Rep.*, vol. 141, no. 2, pp. 51–176, 1986.

[315] A. Jayaraman, A. K. Singh, A. Chatterjee, and S. U. Devi, “Pressure-volume relationship and pressure-induced electronic and structural transformations in Eu and Yb monochalcogenides,” *Phys. Rev. B*, vol. 9, pp. 2513–2520, 1974.

[316] T. Fukui, Y. Hatsugai, and H. Suzuki, “Chern numbers in discretized brillouin zone: Efficient method of computing (spin) Hall conductances,” *J. Phys. Soc. Japan*, vol. 74, no. 6, pp. 1674–1677, 2005.

[317] Y.-F. Zhao, R. Zhang, R. Mei, L.-J. Zhou, H. Yi, Y.-Q. Zhang, J. Yu, R. Xiao, K. Wang, N. Samarth, M. H. W. Chan, C.-X. Liu, and C.-Z. Chang, “Tuning the Chern number in quantum anomalous Hall insulators,” *Nature*, vol. 588, no. 7838, pp. 419–423, 2020.

[318] L. Muechler, E. Liu, J. Gayles, Q. Xu, C. Felser, and Y. Sun, “Emerging chiral edge states from the confinement of a magnetic Weyl semimetal in $Co_3Sn_2S_2$,” *Phys. Rev. B*, vol. 101, p. 115106, 2020.

[319] S. Baidya, U. V. Waghmare, A. Paramekanti, and T. Saha-Dasgupta, “Controlled confinement of half-metallic two-dimensional electron gas in $BaTiO_3/Ba_2FeReO_6/BaTiO_3$ heterostructures: A first-principles study,” *Phys. Rev. B*, vol. 92, p. 161106, 2015.

[320] C. Huang, J. Zhou, H. Wu, K. Deng, P. Jena, and E. Kan, “Quantum anomalous Hall effect in ferromagnetic transition metal halides,” *Phys. Rev. B*, vol. 95, p. 045113, 2017.

[321] C. Song, X. Li, L. Shen, B. Cui, X. Xu, G. Yu, M. Liu, S. Meng, and K. Wu, “Emergent perpendicular magnetic anisotropy at the interface of an oxide heterostructure,” *Phys. Rev. B*, vol. 104, p. 115162, 2021.

List of Publications

Publications included in the thesis

1. **S. Kakkar**, A. Sharma, and C. Bera, “Electronic, magnetic, and topological properties of layered ternary chalcogenide CoAsS: A first principles study,” J. Magn. Magn. Mater., vol. 536, p. 168133, 2021.

2. **S. Kakkar** and C. Bera, “Rashba spin splitting in two-dimensional electron gas in polar-polar perovskite oxide heterostructure LaVO$_3$/KTaO$_3$: A DFT investigation,” Physica E Low Dimens. Syst. Nanostruct, vol. 144, p. 115394, 2022.

3. **S. Kakkar** and C. Bera, “Non-trivial topological states in spin-polarized 2D electron gas at EuO–KTO interface with the Rashba spin texture,” Adv. Phys. Res., p. 2200026., https://onlinelibrary.wiley.com/doi/abs/10.1002/apxr.202200026.

4. R. Tomar, **S. Kakkar**, C. Bera, and S. Chakraverty, “Anisotropic magnetoresistance and planar hall effect in (001) and (111) LaVO$_3$/SrTiO$_3$ heterostructures,” Phys. Rev. B, vol. 103, p. 115407, 2021.

5. R. Tomar, **S. Kakkar**, S. Goyal, M. M. Devi, C. Bera, and S. Chakraverty, “Multiple helimagnetic phases in triclinic CuSeO$_3$,” J. Magn. Magn. Mater., vol. 497, p. 165945, 2020.

Publications not included in the thesis

1. N. Kumar, **S. Kakkar**, and C. Bera, “High thermoelectric power factor in LaVO$_3$/KTaO$_3$ heterostructure,” Physica E Low Dimens. Syst. Nanostruct, vol. 146, p. 115525, 2023.

2. R. Gupta, **S. Kakkar**, B. Dongre, J. Carrete, and C. Bera, ”Enhancement in the thermoelectric performance of SnS monolayer by strain engineering,” ACS Appl. Energy Mater., vol. 6, p. 3944–3952, 2023.

3. N. Kumar, **S. Kakkar**, and C. Bera, ”Theoretical prediction of high thermoelectric power factor in EuO/KTO heterostructure” (manuscript under preparation).

4. T. Sarkar, S. Biswas, **S. Kakkar**, A. V. Raghu, K. Sharu, J. Mitra, C. Bera, and V. B. Kamble, ”Coexistence of multiple magnetic interactions in oxygen deficient V_2O_5 nanoparticles”, Phys. Rev. B (under review).

5. Y. Kumar, H. Bhatt, **S. Kakkar**, C. J. Kinane, A. Caruana, S. Langridge, C. Bera, S. Basu, and S. Singh, ”Emerging interfacial magnetization in isovalent manganite heterostructures driven by octahedral coupling”, (manuscript prepared).

6. N. Kumar, R. Gupta, R. Kaur, D. Oka, **S. Kakkar**, S. Kumar, S. Singh, T. Fukumura, C. Bera, and S. Chakraverty, ”B-site stoichiometry control of the magnetotransport properties of epitaxial Sr_2FeMoO_6 thin film”, ACS Appl. Electron. Mater., vol. 3, p. 597-604, 2021.

7. **S. Kakkar** and C. Bera, ”First principle study of magnetic properties of layered ternary chalcogenide CoAsS”, AIP Conf. Proc., vol. 2265, p. 030563, 2020.

Research Schools, Workshops and Conferences

1. Winter School on “Modelling and Simulations of Materials for Energy and the Environment: Dec 12-14, 2018” at JNCASR, Bangalore.

2. Oral presentation at Conference on “Strategies and Challenges in Computational Chemistry from Molecular Simulation to Quantum Crystallography”, PU Chandigarh (March 5-6, 2019).

3. Poster presentation in ”64th DAE Solid State Physics Symposium- 2019”, IIT Jodhpur.

4. Participation in conference “2D Materials for Spin-Orbitronics”, May 03-05, 2021, the Abdus Salam ICTP, Trieste, Italy.

5. Participation in the workshop on “Critical Reading and Effective Writing: The tools for research” held at the Department Of SAIF/CIL, PU Chandigarh (November 12-13, 2018).

6. Poster presentation in Indo-Japan Workshop on “Interface Phenomena for Spintronics (IJW-IPS 2022)” NISER, Bhubaneswar, India (March 8-10, 2022).

7. Short invited talk at the ”International Online Conference on Nanomaterials (ICN-2022)” held at Mahatma Gandhi University, Kottayam, Kerala, India (August 12-14, 2022).

8. Oral presentation in ”Physics of Nano Materials (PNM-2022)”, Institute of Nano Science and Technology, Mohali (July 7-8, 2022).

Appendix

Permissions for Content Reused

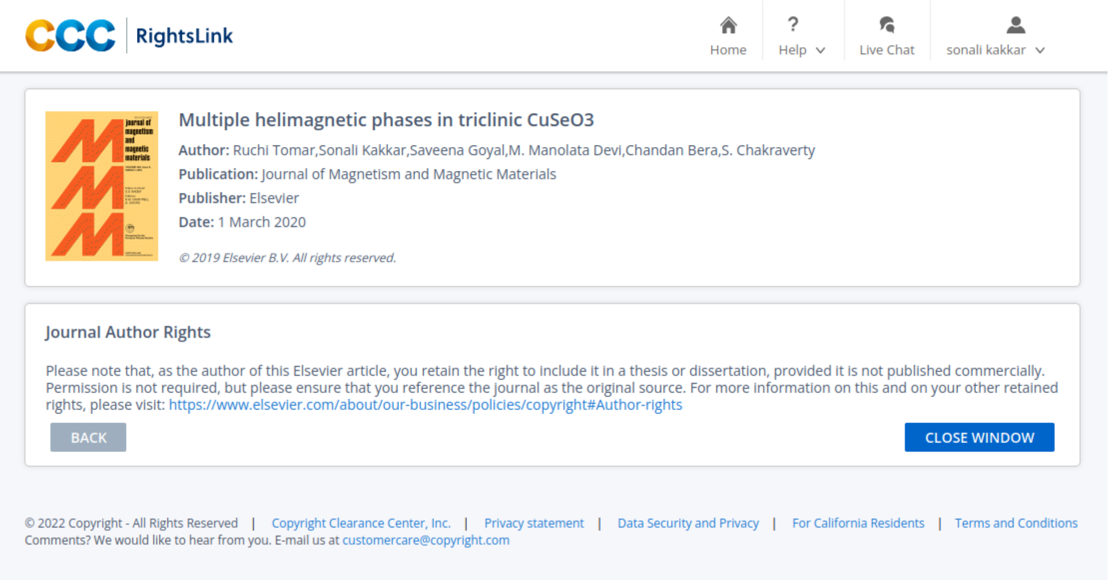

Multiple helimagnetic phases in triclinic CuSeO3

Author: Ruchi Tomar,Sonali Kakkar,Saveena Goyal,M. Manolata Devi,Chandan Bera,S. Chakraverty
Publication: Journal of Magnetism and Magnetic Materials
Publisher: Elsevier
Date: 1 March 2020

© 2019 Elsevier B.V. All rights reserved.

Journal Author Rights

Please note that, as the author of this Elsevier article, you retain the right to include it in a thesis or dissertation, provided it is not published commercially. Permission is not required, but please ensure that you reference the journal as the original source. For more information on this and on your other retained rights, please visit: https://www.elsevier.com/about/our-business/policies/copyright#Author-rights

© 2022 Copyright - All Rights Reserved | Copyright Clearance Center, Inc. | Privacy statement | Data Security and Privacy | For California Residents | Terms and Conditions
Comments? We would like to hear from you. E-mail us at customercare@copyright.com

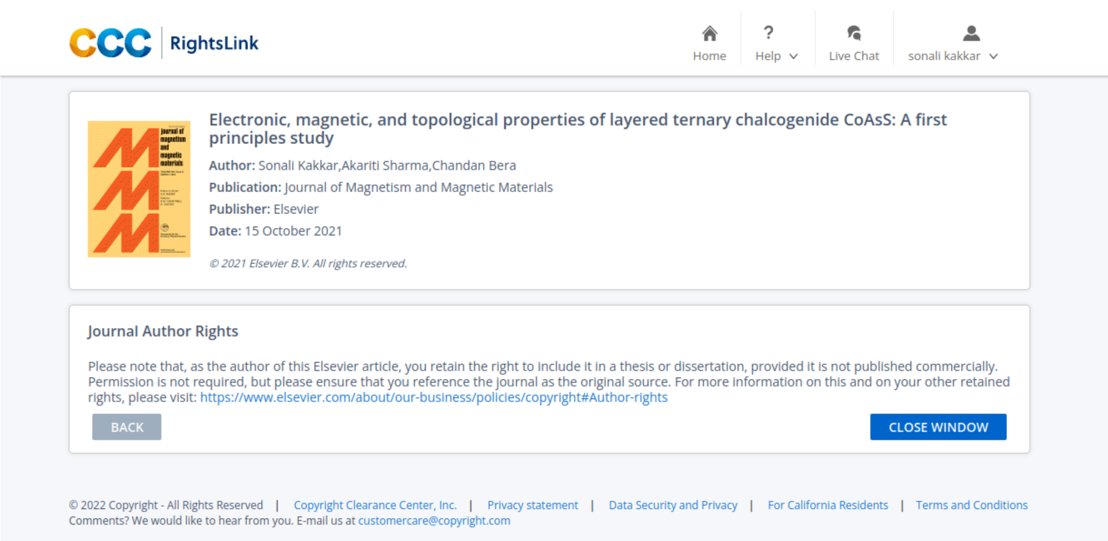

Electronic, magnetic, and topological properties of layered ternary chalcogenide CoAsS: A first principles study

Author: Sonali Kakkar,Akariti Sharma,Chandan Bera

Publication: Journal of Magnetism and Magnetic Materials

Publisher: Elsevier

Date: 15 October 2021

© 2021 Elsevier B.V. All rights reserved.

Journal Author Rights

Please note that, as the author of this Elsevier article, you retain the right to include it in a thesis or dissertation, provided it is not published commercially. Permission is not required, but please ensure that you reference the journal as the original source. For more information on this and on your other retained rights, please visit: https://www.elsevier.com/about/our-business/policies/copyright#Author-rights

© 2022 Copyright - All Rights Reserved | Copyright Clearance Center, Inc. | Privacy statement | Data Security and Privacy | For California Residents | Terms and Conditions
Comments? We would like to hear from you. E-mail us at customercare@copyright.com

American Physical Society
Reuse and Permissions License

23-Dec-2022

This license agreement between the American Physical Society ("APS") and sonali kakkar ("You") consists of your license details and the terms and conditions provided by the American Physical Society and SciPris.

Licensed Content Information

License Number:	**RNP/22/DEC/061340**
License date:	23-Dec-2022
DOI:	10.1103/PhysRevB.103.115407
Title:	Anisotropic magnetoresistance and planar Hall effect in (001) and (111) ${\mathrm{LaVO}}_{3}/{\mathrm{SrTiO}}_{3}$ heterostructures
Author:	Ruchi Tomar et al.
Publication:	Physical Review B
Publisher:	American Physical Society
Cost:	USD $ 0.00

Request Details

Does your reuse require significant modifications: No

Specify intended distribution locations:	Worldwide
Reuse Category:	Reuse in a thesis/dissertation
Requestor Type:	Student
Items for Reuse:	Whole Article
Format for Reuse:	Print and Electronic
Total number of print copies:	More Than 10000

Information about New Publication:

University/Publisher:	
Title of dissertation/thesis:	First-Principles Studies of Transition Metal Chalcogenides and Oxide Heterostructures for Spintronic Applications
Author(s):	
Expected completion date:	May. 2023

License Requestor Information

Name:	sonali kakkar
Affiliation:	Individual
Email Id:	sonalikakkar12@gmail.com
Country:	India

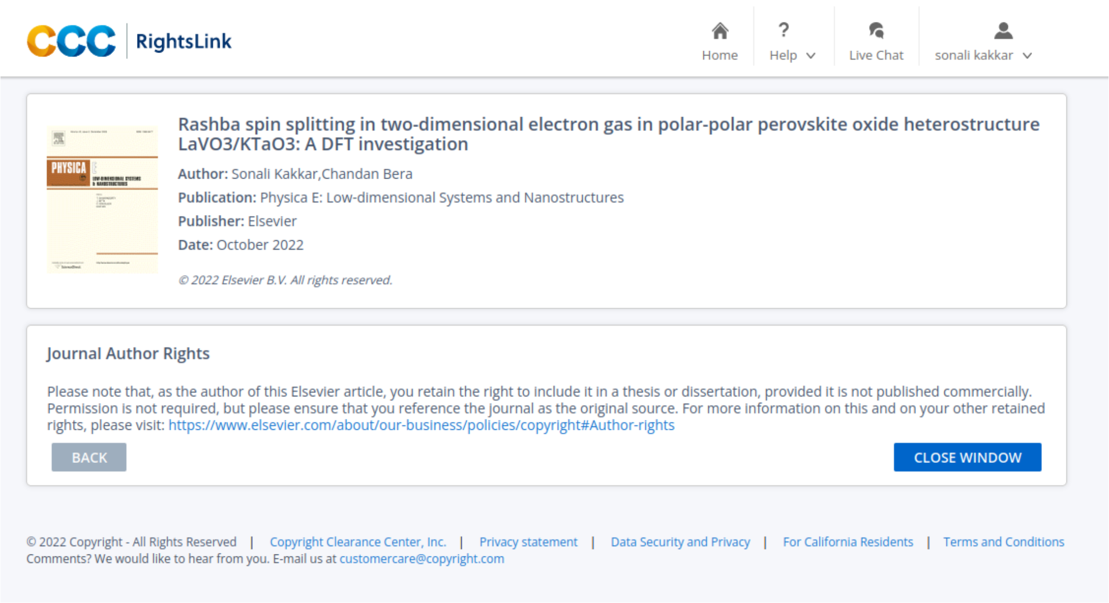

Rashba spin splitting in two-dimensional electron gas in polar-polar perovskite oxide heterostructure LaVO3/KTaO3: A DFT investigation

Author: Sonali Kakkar,Chandan Bera

Publication: Physica E: Low-dimensional Systems and Nanostructures

Publisher: Elsevier

Date: October 2022

© 2022 Elsevier B.V. All rights reserved.

Journal Author Rights

Please note that, as the author of this Elsevier article, you retain the right to include it in a thesis or dissertation, provided it is not published commercially. Permission is not required, but please ensure that you reference the journal as the original source. For more information on this and on your other retained rights, please visit: https://www.elsevier.com/about/our-business/policies/copyright#Author-rights

© 2022 Copyright - All Rights Reserved | Copyright Clearance Center, Inc. | Privacy statement | Data Security and Privacy | For California Residents | Terms and Conditions
Comments? We would like to hear from you. E-mail us at customercare@copyright.com

Wiley journals like Advanced Physics Research is **open- access journal** which permits unrestricted use, distribution, and reproduction, so that the whole article can be reused for **thesis/dissertation** as highlighted below. One article published in Advanced Physics Research have gone into the thesis.
Non-Trivial Topological States in Spin-Polarized 2D Electron Gas at EuO–KTO Interface with the Rashba Spin Texture S. Kakkar and C. Bera, (2022) Adv. Phys. Res. 2200026, https://doi.org/10.1002/apxr.202200026.

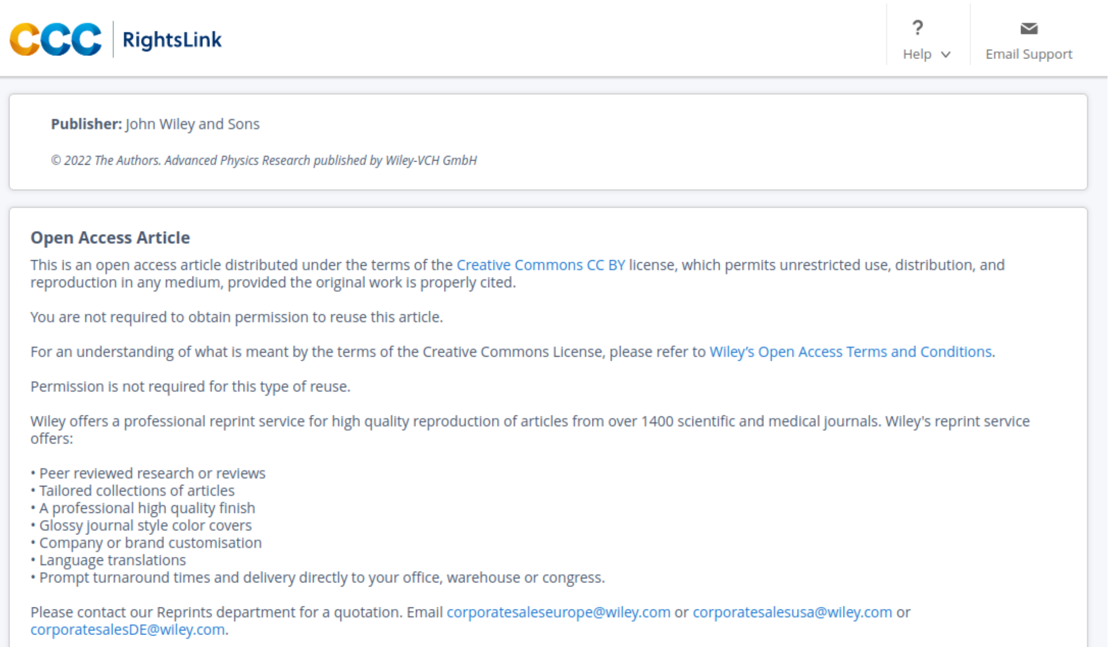

Publisher: John Wiley and Sons

© 2022 The Authors. Advanced Physics Research published by Wiley-VCH GmbH

Open Access Article

This is an open access article distributed under the terms of the Creative Commons CC BY license, which permits unrestricted use, distribution, and reproduction in any medium, provided the original work is properly cited.

You are not required to obtain permission to reuse this article.

For an understanding of what is meant by the terms of the Creative Commons License, please refer to Wiley's Open Access Terms and Conditions.

Permission is not required for this type of reuse.

Wiley offers a professional reprint service for high quality reproduction of articles from over 1400 scientific and medical journals. Wiley's reprint service offers:

- Peer reviewed research or reviews
- Tailored collections of articles
- A professional high quality finish
- Glossy journal style color covers
- Company or brand customisation
- Language translations
- Prompt turnaround times and delivery directly to your office, warehouse or congress.

Please contact our Reprints department for a quotation. Email corporatesaleseurope@wiley.com or corporatesalesusa@wiley.com or corporatesalesDE@wiley.com.

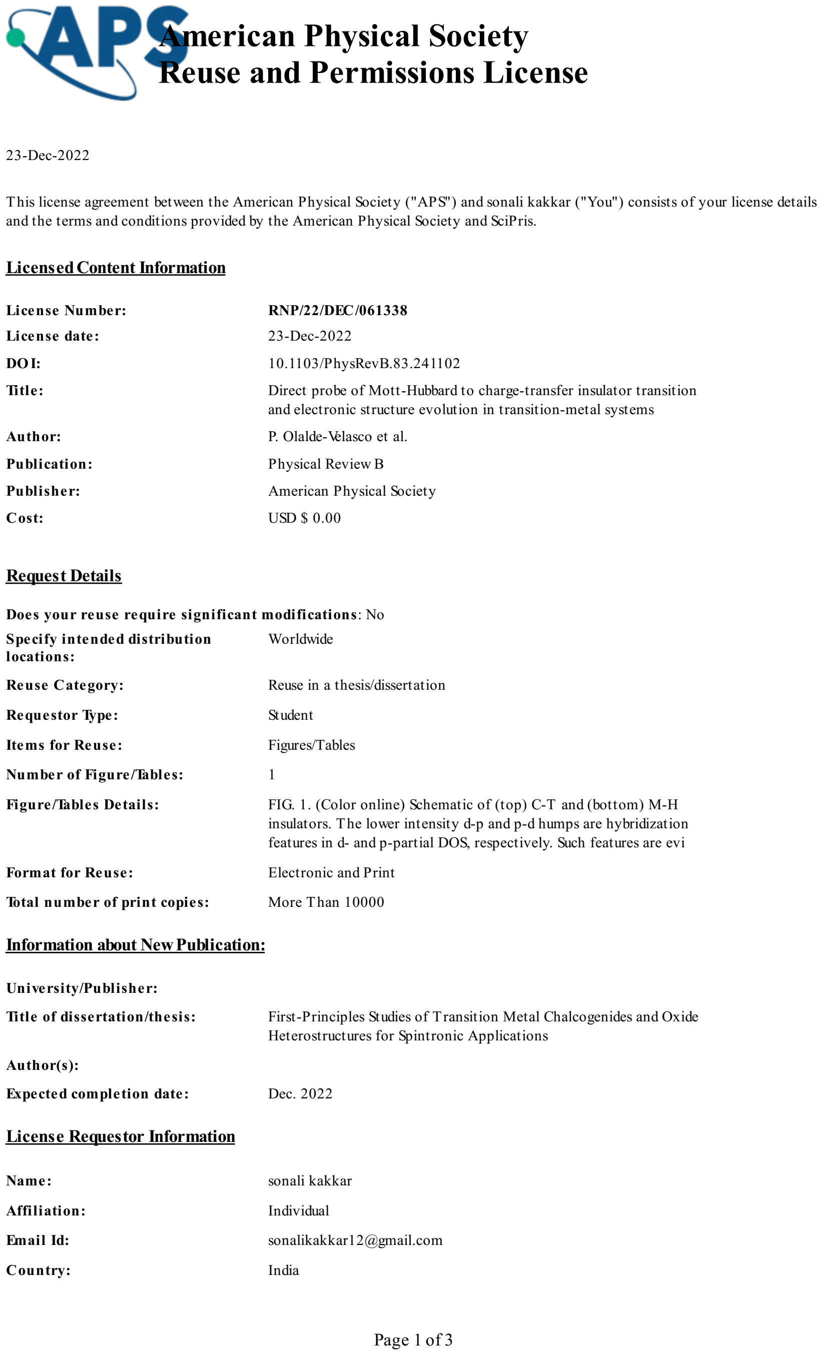

American Physical Society Reuse and Permissions License

23-Dec-2022

This license agreement between the American Physical Society ("APS") and sonali kakkar ("You") consists of your license details and the terms and conditions provided by the American Physical Society and SciPris.

Licensed Content Information

License Number:	**RNP/22/DEC/061338**
License date:	23-Dec-2022
DOI:	10.1103/PhysRevB.83.241102
Title:	Direct probe of Mott-Hubbard to charge-transfer insulator transition and electronic structure evolution in transition-metal systems
Author:	P. Olalde-Velasco et al.
Publication:	Physical Review B
Publisher:	American Physical Society
Cost:	USD $ 0.00

Request Details

Does your reuse require significant modifications: No

Specify intended distribution locations:	Worldwide
Reuse Category:	Reuse in a thesis/dissertation
Requestor Type:	Student
Items for Reuse:	Figures/Tables
Number of Figure/Tables:	1
Figure/Tables Details:	FIG. 1. (Color online) Schematic of (top) C-T and (bottom) M-H insulators. The lower intensity d-p and p-d humps are hybridization features in d- and p-partial DOS, respectively. Such features are evi
Format for Reuse:	Electronic and Print
Total number of print copies:	More Than 10000

Information about New Publication:

University/Publisher:	
Title of dissertation/thesis:	First-Principles Studies of Transition Metal Chalcogenides and Oxide Heterostructures for Spintronic Applications
Author(s):	
Expected completion date:	Dec. 2022

License Requestor Information

Name:	sonali kakkar
Affiliation:	Individual
Email Id:	sonalikakkar12@gmail.com
Country:	India

SPRINGER NATURE LICENSE
TERMS AND CONDITIONS

Dec 23, 2022

This Agreement between Ms. sonali kakkar ("You") and Springer Nature ("Springer Nature") consists of your license details and the terms and conditions provided by Springer Nature and Copyright Clearance Center.

License Number	5454820313425
License date	Dec 23, 2022
Licensed Content Publisher	Springer Nature
Licensed Content Publication	Nature Materials
Licensed Content Title	Why some interfaces cannot be sharp
Licensed Content Author	Naoyuki Nakagawa et al
Licensed Content Date	Jan 22, 2006
Type of Use	Thesis/Dissertation
Requestor type	non-commercial (non-profit)
Format	print and electronic
Portion	figures/tables/illustrations
Number of figures/tables /illustrations	1

High-res required	no
Will you be translating?	no
Circulation/distribution	50000 or greater
Author of this Springer Nature content	no
Title	First-Principles Studies of Transition Metal Chalcogenides and Oxide Heterostructures for Spintronic Applications
Institution name	institute of nano science and technology
Expected presentation date	May 2023
Portions	Figure1
Requestor Location	Ms. sonali kakkar institute of nano science and technology mohali, 140306 India Attn: Ms. sonali kakkar
Total	0.00 USD

Terms and Conditions

Springer Nature Customer Service Centre GmbH Terms and Conditions

The following terms and conditions ("Terms and Conditions") together with the terms specified in your [RightsLink] constitute the License ("License") between you as Licensee and Springer Nature Customer Service Centre GmbH as Licensor. By clicking 'accept' and completing the transaction for your use of the material ("Licensed Material"), you confirm your acceptance of and obligation to be bound by these Terms and Conditions.

Author's Biography

Sonali Kakkar (Reg. No. **PH17221**) joined the **Institute of Nano Science and Technology, Mohali** (INST-Mohali) in January 2018 for her doctoral dissertation by research and registered at the **Indian Institute of Science Education and Research Mohali** (IISER-Mohali) for the award of the ***Degree of Doctor of Philosophy***. She received a gold medal from Panjab University, Chandigarh for ranking first (three years in a row) in her B.Sc. (Non-medical) program. She earned her Master of Science (Hons. Physics) degree from Panjab University, Chandigarh. Her scientific expertise and area of research include: *ab initio study of Transition Metal Chalcogenides and Oxide Heterostructures* for potential spintronic applications.